

AD 608473

RADC-TDR-64-363

Final Report



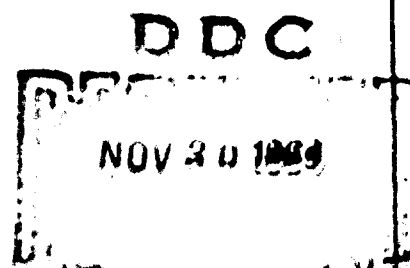
INVESTIGATION OF FOAM PLASTIC TECHNIQUES
FOR HARDENING GROUND RADOMES

COPY 1
HARD COPY
MICROFILM

TECHNICAL DOCUMENTARY REPORT NO. RADC-TDR-64-363

October 1954

Development Engineering Branch
Rome Air Development Center
Research and Technology Division
Air Force Systems Command
Griffiss Air Force Base, New York



Project No. 5579 , Task No. 557901

(Prepared under Contract No. AF 30(602)-3128 by Aeronca
Manufacturing Corporation, Middletown, Ohio.)

**Best
Available
Copy**

When US Government drawings, specifications, or other data are used for any purpose other than a definitely related government procurement operation, the government thereby incurs no responsibility nor any obligation whatsoever; and the fact that the government may have formulated, furnished, or in any way supplied the said drawings, specifications, or other data is not to be regarded by implication or otherwise, as in any manner licensing the holder or any other person or corporation, or conveying any rights or permission to manufacture, use, or sell any patented invention that may in any way be related thereto.

Qualified requesters may obtain copies from Defense Documentation Center.

Defense Documentation Center release to Office of Technical Services is authorized.

Do not return this copy. Retain or destroy.



FOREWORD

This report was prepared by the Middletown Division of the Aeronca Manufacturing Corporation on Air Force Contract No. AF30(602)-3128, "Investigation of Foamed Plastic Techniques for Hardening Ground Radomes". The work was performed for the Rome Air Development Center, Research and Technology Division, Air Force Systems Command, under the technical direction of Mr. Richard Mair, during the period 1 July 1963 to 31 May 1964.

The program was carried out under the technical direction of Mr. R. R. Jeffries, with Mr. B. B. Cahill as the principal investigator. Assistance in the pattern and dielectric measurements was given by Mr. G. K. Squire, Mr. J. E. Brunner, and Mr. J. L. Ecker; in the thermal shield studies by Mr. W. G. Voss and Mr. W. R. Niehaus; the structural analyses were performed by Mr. H. I. Dwyer; and the adhesive studies were performed by Mr. R. F. Latchaw.

Special acknowledgement is made to the outside agencies who unselfishly contributed their time and effort to help us achieve our goals. In particular, we wish to express our gratitude to Mr. R. A. Muldoon, M. I. T., Lincoln Laboratories; Mr. R. Ripperger, University of Texas; Mr. H. Schwartz and Mr. R. Farmer, Plastics Composites Section of Nonmetallics Plastics Laboratory, Wright-Patterson Air Force Base; Mr. G. C. Zellner, Melpar Research Division; and Mr. D. Nelson, Koppers Development Laboratories.

PUBLICATION REVIEW

This report has been reviewed and is approved. For further technical information on this project, contact Mr. Richard W. Mair, EMEAM, Extension: 22128

Approved:

R. W. Mair
RICHARD W. MAIR
Project Engineer
Engineering Division

Approved:

William S. Beeke
WILLIAM S. BEEKE
Chief, Engineering Division

FOR THE COMMANDER:

Irving J. Gabelman
IRVING J. GABELMAN
Chief, Advanced Studies Group

ABSTRACT

The investigation reported here was directed toward the determination of the feasibility of hardening above ground antenna installations, at the 75 psi free-field overpressure range for a one megaton nuclear burst, by means of pseudo-encapsulation with a foam plastic radome.

The problem was to determine if a foam plastic protection system could be designed to permit antenna survival to the blast, and if that design would permit efficient electrical transmission characteristics before and after the detonation occurred.

The overall survival problem was approached by treating the effects of the individual environments on foam plastics separately. Conclusions from the investigation of the effects of a nuclear detonation on the selected foam plastics are summarized as follows:

- (1) The nuclear radiation will have a negligible effect on the dielectric and mechanical properties.
- (2) Thermal radiation produces considerable physical changes in all foam plastic materials through ablation, burning and melting. The electrical properties of most foam plastics are affected as a result of charred composites on the residual surface. However, polyethylene foam was observed in thermal ablation tests to leave no charry residue. A thermal protection system using a polyethylene foam laminate was concluded feasible.
- (3) Mechanical shock effects due to the blast overpressure wave were inconclusive due to inadequate test data on the stress-strain response of foams to dynamic loading. Conditional feasibility can be assumed on the basis of anticipated foam plastic nonlinear viscoelastic response.

The electrical transmission efficiency of a foam encapsulated scale model antenna was observed for a 6 ft. parabolic dish encapsulated with low density polystyrene foam. These tests indicate that phase errors are the main contributors to degradation of the pattern; and these should be eliminated if possible by a symmetrical assembly. The attenuation and reflection losses in low density foam were small. Boresight shift was observed and agreed well with the calculated value. The experimental tests indicate that electrical performance can be predicted for a full scale model.

A program to acquire high energy, dynamic loading data on certain foam plastic materials such as polyethylene, polystyrene, and polyurethane seems warranted to complete the feasibility analysis for the foam plastic hardening concept.

| <u>ion</u> | <u>Title</u> | <u>Page</u> |
|------------|--|-------------|
| 3.8 | Electrical System Transmission Experiments | 69 |
| 3.8.1 | Objectives of Experimental Program | 69 |
| 3.8.2 | Predicted Results | 69 |
| 3.8.3 | Scale Model | 70 |
| 3.8.4 | Boresight Shift Analysis | 71 |
| 3.8.5 | Dielectric Attenuation Factor | 74 |
| 3.8.6 | Power Dissipation in Dielectric | 75 |
| 3.8.7 | Scale Model Transmission Testing Results | 76 |
| 3.9 | Bonding of Foamed Plastics | 85 |
| 3.9.1 | Introduction | 85 |
| 3.9.2 | Objectives of Study | 85 |
| 3.9.3 | Program Description | 86 |
| 3.9.4 | Evaluation of Processing Techniques | 88 |
| 3.9.5 | Mechanical Testing | 88 |
| 3.9.6 | Discussion of Results | 90 |
| 3.9.7 | Summary | 97 |
| | CONCLUSIONS AND RECOMMENDATIONS | 99 |
| 4.1 | Conclusions | 99 |
| 4.2 | Recommendations for Further Investigations | 100 |
| 4.2.1 | Experimental Studies | 100 |
| 4.2.2 | Analytical Studies | 100 |
| | REFERENCES | 102 |
| | APPENDICES | |
| | ANALYSIS OF A SQUARE PANEL | 105 |
| | ELEMENTS OF LINEAR VISCOELASTIC THEORY | 114 |
| | SUMMARY OF NUCLEAR WEAPONS CHARACTERISTICS | 134 |
| | STRESS-STRAIN DATA ON POLYMER FOAMS | 159 |
| | STRESS ANALYSIS COMPUTATIONS | 170 |
| | THERMAL ABLATION DATA | 187 |
| | MEASUREMENTS OF THE DIELECTRIC CON- STANTS OF FOAMED PLASTICS | 200 |
| | BORESIGHT SHIFT ANALYSIS | 218 |
| | SCALE MODEL ANTENNA PATTERNS | 221 |

TABLE OF CONTENTS

| <u>Section</u> | <u>Title</u> | <u>Page</u> |
|----------------|--|-------------|
| 1.0 | INTRODUCTION | 1 |
| 2.0 | SUMMARY OF RESULTS | 3 |
| 2.1 | General Summary | 3 |
| 2.2 | Analytical Results | 4 |
| 2.3 | Experimental Results | 5 |
| 3.0 | TECHNICAL DISCUSSION | 7 |
| 3.1 | Introduction | 7 |
| 3.2 | Phenomenological Behavior of Foamed Plastics | 8 |
| 3.2.1 | Introduction | 8 |
| 3.2.2 | Static Theory of Foamed Plastics | 9 |
| 3.2.3 | Dynamic Phenomena in Foamed Plastics | 16 |
| 3.2.4 | A Mathematical Model for A Foam | 19 |
| 3.3 | Effects of Nuclear Radiation on Polymer Plastics | 21 |
| 3.3.1 | Introduction | 21 |
| 3.3.2 | Nuclear Radiation Phenomena from A One Megaton Burst | 21 |
| 3.3.3 | Mechanisms of Damage | 22 |
| 3.3.4 | Effects of Irradiation on Mechanical Properties of Polymers | 25 |
| 3.3.5 | Effects of Irradiation on the Electrical Properties of Polymers | 25 |
| 3.3.6 | Conclusions | 27 |
| 3.4 | Effects of Thermal Radiation | 30 |
| 3.4.1 | Discussion of Thermal Damage Mechanism | 30 |
| 3.4.2 | Method of Solution | 31 |
| 3.5 | Thermal Shield Experimental Studies | 31 |
| 3.5.1 | Design Environment | 31 |
| 3.5.2 | Design Concepts | 32 |
| 3.5.3 | Testing Program | 34 |
| 3.6 | Thermal Shield Analytical Studies | 37 |
| 3.6.1 | Introduction | 37 |
| 3.6.2 | Ablation Analysis of an Opaque Solid | 37 |
| 3.6.3 | Ablation Analysis of Semi-Transparent Solid | 41 |
| 3.6.4 | Discussion of Effects of Semi-Transparency | 45 |
| 3.6.5 | Summary | 51 |
| 3.6.6 | Nomenclature | 51 |
| 3.7 | Structural Analysis of Foam Hardened Configuration | 52 |
| 3.7.1 | Introduction | 52 |
| 3.7.2 | Encapsulated Antenna Approach | 53 |
| 3.7.3 | Thick Shell Approach | 62 |
| 3.7.4 | Foundation Requirements | 64 |

LIST OF FIGURES

| <u>Figure</u> | <u>Title</u> | <u>Page</u> |
|---------------|---|-------------|
| 1 | Initial Gamma Radiation Dose vs Slant Range | 23 |
| 2 | Total Initial Radiation (Gamma and Neutron) | 24 |
| 3 | The Effect of Gamma Radiation on The Tensile Strength of Plastic Films | 26 |
| 4 | Loss Tangent of Polystyrene vs Integrated γ -ray Flux | 28 |
| 5 | Loss Tangent of Polyethylene vs Integrated γ -ray Flux | 28 |
| 6 | Loss Tangent of Polystyrene vs Integrated Fast Neutron Flux | 29 |
| 7 | Loss Tangent of Polyethylene vs Integrated Fast Neutron Flux | 29 |
| 8 | Heat of Ablation vs Initial Heat Flux for Polyethylene Foam | 36 |
| 9 | Surface Recession - Convective Heating - Thermal Thickness = 0 | 38 |
| 10 | Mass Recession Rate - Convective Heating - Thermal Layer = 0 | 39 |
| 11 | Effect of Attenuation Coefficient on Temperature Rise of Material | 46 |
| 12 | Temperature Rise vs Distribution from Surface for Steady State Ablation | 47 |
| 13 | Temperature Rise vs Time | 48 |
| 14 | Temperature Rise vs Time | 49 |
| 15 | Effect of Encapsulation on Wavefront | 72 |
| 16 | Calculated Phase Front Produced by Encapsulation | 73 |
| 17 | Pre-Test Assembly Side View (Left) | 77 |
| 18 | Pre-Test Assembly Cut-away View | 78 |
| 19 | Pre-Test Assembly Side View (Right) | 79 |
| 20 | Side View - Scale Model Antenna Encapsulation Configuration | 81 |
| 21 | Front View - Scale Model Antenna Encapsulation Configuration | 82 |
| 22 | Scale Model Antenna Encapsulation Configuration | 83 |
| I-1 | Speed of Sound vs Frequency | 112 |
| I-2 | Speed of Sound vs Density | 113 |
| II-1 | Simple Elements | 114 |
| II-2 | Simple Viscoelastic Systems | 114 |
| II-3 | Displacement During Creep | 116 |
| II-4 | Generalized Voigt Model | 117 |
| II-5 | Standard Linear Solid | 121 |

| <u>Figure</u> | <u>Title</u> | <u>Page</u> |
|---------------|--|-------------|
| II-6 | Comparison Between Response of Model Solids and Measured Values of Real Polymers | 129 |
| II-7 | Wave Propagation In Finite Rods of Viscoelastic Material | 133 |
| III-1 | Blast Characteristics vs Peak Overpressure | 136 |
| III-2 | Peak Overpressure on the Ground vs Distance from Ground Zero | 137 |
| III-3 | Peak Shock Velocity vs Distance from Ground Zero | 138 |
| III-4 | Peak Wind Velocity vs Distance from Ground Zero | 139 |
| III-5 | Reflected Overpressure Ratio vs Angle of Incidence | 141 |
| III-6 | Decay curves of Dynamic Pressure - Surface Burst | 142 |
| III-7 | Decay Curves of Overpressure - Surface Burst | 143 |
| III-8 | Positive Phase Duration on the Ground of Overpressure | 144 |
| III-9 | Positive Phase Duration on the Ground of Dynamic Pressure | 145 |
| III-10 | Duration of Positive Phase - Typical Air Burst | 146 |
| III-11 | Blast Energy Density vs Range | 148 |
| III-12 | 6000° Black Body Distribution | 150 |
| III-13 | Total Thermal Radiation Dose vs Distance from Ground Zero | 152 |
| III-14 | Percent of Thermal Radiation Emitted | 153 |
| III-15 | Heat Flux - Surface Burst - 3,850 ft. from Ground Zero | 154 |
| III-16 | Heat Flux - Surface Burst - 5,000 ft. from Ground Zero | 155 |
| III-17 | Heat Flux - Surface Burst - 10,000 ft. from Ground Zero | 156 |
| III-18 | Heat Flux - Surface Burst - 15,000 ft. from Ground Zero | 157 |
| III-19 | Heat Flux - Surface Burst - 20,000 ft. from Ground Zero | 158 |
| IV-1 | Polyurethane Compressive Strength vs Density | 160 |
| IV-2 | Polyurethane Tensile Strength vs Density | 161 |
| IV-3 | Foamed Polyurethane Stress-Strain Curve | 162 |
| IV-4 | Energy Absorption vs Strain of Foamed Polyurethane | 163 |
| IV-5 | Ultimate Compressive Strength vs Density - Rigid Polyurethane | 164 |
| IV-6 | X-Band Dielectric Measurements - Polyurethane Foam | 165 |
| IV-7 | Yield Stress vs Density - Polystyrene Foam | 166 |
| IV-8 | Yield Stress vs Yield Strain - Polystyrene Foam | 167 |

| <u>Figure</u> | <u>Title</u> | <u>Page</u> |
|---------------|--|-------------|
| IV-9 | Stress vs Strain - Polystyrene Foam | 168 |
| IV-10 | Energy Absorption vs Strain - Various Foam Materials | 169 |
| VI-1 | Heat Source Calibration Curve | 188 |
| VI-2 | Heat Source Calibration Curve | 189 |
| VI-3 | Thermocouple Time - Temperature Record - Sample # 1 | 192 |
| VI-4 | Thermocouple Time - Temperature Record - Sample # 2 | 193 |
| VI-5 | Thermocouple Time - Temperature Record - Sample # 3 | 194 |
| VI-6 | Thermocouple Time - Temperature Record - Sample # 4 | 195 |
| VI-7 | Thermocouple Time - Temperature Record - Sample # 5 | 196 |
| VI-8 | Thermocouple Time - Temperature Record - Sample # 6 | 197 |
| VI-9 | Thermocouple Time - Temperature Record - Sample # 8 | 198 |
| VI-10 | Thermocouple Time - Temperature Record - Sample # 9 | 199 |
| VII-1 | X-Band Dielectrometer Circuit | 207 |
| VII-2 | VSWR Measurement | 207 |
| VII-3 | Standing Wave Patterns | 207 |
| VII-4 | Transcendental Curves for Determination of γ_2 - Chart 1 | 213 |
| VII-5 | Transcendental Curves for Determination of γ_2 - Chart 2 | 214 |
| VII-6 | Transcendental Curves for Determination of γ_2 - Chart 3 | 215 |
| IX-1 | Unencapsulated Pattern - E - Plane cut - Bore-sight $\pm 6^\circ$ | 223 |
| IX-2 | Unencapsulated Pattern - E - Plane cut - Bore-sight $\pm 180^\circ$ | 225 |
| IX-3 | Unencapsulated Pattern - Cross Polarization cut - Bore-sight $\pm 6^\circ$ | 227 |
| IX-4 | Unencapsulated Pattern - H - Plane cut - Bore-sight $\pm 6^\circ$ | 229 |
| IX-5 | Unencapsulated Pattern - H - Plane cut - Bore-sight $\pm 180^\circ$ | 231 |

| <u>Figure</u> | <u>Title</u> | <u>Page</u> |
|---------------|---|-------------|
| IX-6 | Encapsulated Pattern - E - Plane cut - Bore-sight $\pm 6^\circ$ | 233 |
| IX-7 | Encapsulated Pattern - E - Plane cut - Bore-sight $\pm 180^\circ$ | 235 |
| IX-8 | Encapsulated Pattern - Cross Polarization cut - Boresight $\pm 6^\circ$ | 237 |
| IX-9 | Encapsulated Pattern - H-Plane cut Boresight $\pm 6^\circ$ | 239 |
| IX-10 | Encapsulated Pattern - H - Plane cut Boresight $\pm 180^\circ$ | 241 |
| IX-11 | Boresight Shift - E - Plane cut - Boresight $\pm 6^\circ$ | 243 |

LIST OF TABLES

| <u>Table</u> | <u>Title</u> | <u>Page</u> |
|--------------|---|-------------|
| 1 | Experimentally Determined Attenuation Coefficients | 50 |
| 2 | Allowable Bearing Capacity | 68 |
| 3 | Adhesives Evaluated | 87 |
| 4 | Processing Times and Cost Factors for Adhesives | 89 |
| 5 | Results of Compatibility Tests | 91 |
| 6 | Results of Flatwise Tension Tests | 92 |
| 7 | Results of Lap Shear Tests | 94 |
| 8 | Tensile Strengths vs Bondline Thickness | 95 |
| 9 | Diagonal Shear-Tension Tests of Promising Adhesives | 96 |
| II-1 | Simple Model Relationships | 122 |
| III-1 | Rankine - Hugoniot Equations | 135 |
| IV-1 | Material Constants - Polyurethane and Polystyrene | 159 |
| VI-1 | Results of Facility Calibration Tests | 190 |
| VI-2 | Test Results - Heat of Ablation | 191 |

1. INTRODUCTION

The principal objective of the study was to establish the feasibility of protecting an above-ground antenna against nuclear weapons by foamed plastic techniques. A solution to the problem of hardening existing antenna installations against the effects of nuclear weapons has been sought for some time by many investigators. The investigation reported herein treats the particular case of protecting a fixed antenna installation from the effects resulting from a surface or air burst of a one megaton weapon at the 75 psi free-field overpressure range. The protection scheme investigated in this study is a psuedo-encapsulation of the antenna with a foamed-plastic material which constitutes a solid radome. The hardening concept was based on the theory that the foamed-plastic, deforming under the blast loading, will absorb the bulk of the blast energy. As a result, the blast overpressure will be prevented from overstressing the antenna.

Existing foamed-plastic materials, such as polystyrene, polyethylene and polyurethane foams, were the prime materials considered because of their combined electrical and mechanical properties. The problem areas receiving the most attention in the study were:

- a. Stress-strain characteristics of the materials when subjected to a blast overpressure wave.
- b. Survivability in the thermal environment.
- c. Neutron and gamma radiation effects.
- d. Electrical transmission characteristics.
- e. Structural analysis techniques for foamed-plastic radomes.
- f. Adhesive bonding of foamed-plastic materials.

The effort was largely an analytical study of the effects of the adverse environment on the mechanical, electrical and thermal properties of the foamed plastic. Experimental work was performed to obtain data on the heat of ablation for polyethylene foam to be used for a thermal protection system and to confirm the calculated electrical effects on antenna gain and boresight error.

The state-of-the-art of foamed radomes has been restricted to the 10-25 psi range primarily due to the deleterious effects of the thermal pulse at higher shock overpressure ranges. An integrated thermal flux of 100 cal/cm² has been the threshold. (1)* A thermal shield concept based on an ablating polyethylene foamed plastic laminate has been developed however, and appears capable of accommodating an integrated thermal flux of 1000 cal/cm². Experimental observations on polyethylene foam during this investigation clearly indicate that polyethylene foam, after ablation, is left with a noncarbonaceous surface. This means that the inherently low dielectric loss factor (or loss tangent) is left unchanged after ablation.

Flying debris has not been considered, although a high degree of protection from flying objects should be inherent with foamed radomes.

This study has resulted in a preliminary antenna hardening concept, contributed a feasible thermal protective system for hardening structures, and outlined areas where additional work should be done.

This study leads to the conclusion that a foamed-plastic radome is a feasible technique for hardening antenna installations against a nuclear blast. Nuclear radiation effects are negligible. Adequate thermal protection is provided by the foamed-plastic radome. Absorption of overpressure energy can probably be effectively contained in the foam. Electrical radiation variations can be predicted and can be minimized by judicious design techniques. A complete demonstration of the extent of hardening which is possible will require additional experimental testing of foam materials in a dynamic environment such as a shock tube.

* Reference Number

2. SUMMARY OF RESULTS

2.1 GENERAL SUMMARY

This study has resulted in a conditionally feasible above-ground antenna hardening concept and has outlined areas where additional work should be done. The fundamental question of whether the foam encapsulated antenna could survive the blast wave could not be answered conclusively due to a lack of pertinent data on foamed plastics under simulated shock loading at energy levels associated with a nuclear burst. The existing data do show that foamed plastics are viscoelastic materials, and the response to loads, unlike elastic bodies, contains time as a parameter. This means that the stress-strain law contains partial time derivatives of stress and/or strain. This is significant, particularly when the energy absorption capabilities of the material are considered. The energy absorption process will obey an exponential decay law with the decay factor being a function of the material parameters. This decay factor must be determined by experimental observation of the propagation of stress waves under dynamic loading. Knowledge of the exponential factor for foams then allows a prediction of the bulk quantity of foam material necessary to reduce the incident load to a safe level. Based on the present knowledge of the properties of foamed plastic, the concept which offers the most probable feasibility is a thick-shell encapsulation. This permits that portion of the loading that is transmitted elastically, without attenuation, to be transmitted to the foundation without stressing the antenna dish, while the balance of energy is absorbed in the foamed shell.

Three foamed-plastic materials, viz., polystyrene, polyurethane, and polyethylene, were considered to offer the best chances for success due to their combined cushioning and dielectric properties. All three incur significant changes and deformations on the exposed surface when subjected to the thermal radiation from the bomb, but only polyethylene foam has been shown to be suitable as a low temperature, ablating thermal shield. An experimental analysis to demonstrate the nature of the surface after exposure exhibited a surface free of carbonaceous residues or other lossy, dielectric residues. An analytical analysis indicates 1.5 ft. of polyethylene foam

would be ablated in the environment of a one megaton burst at the 75 psi range.

The electrical transmission tests performed on a six-foot dish encapsulated with polystyrene foam, of 2 lb. per cu. ft. density, demonstrated that the phase variations due to an asymmetrical arrangement of foam about the optical axis accounts for the change in pattern shape and bore-sight shift. Attenuation and reflection losses were too small to be observed with the experimental setup employed. They may be calculated, however, from the measured loss tangent and radome geometry. Experimental studies of adhesives to determine the feasibility of bonding foams for large scale assemblies were made. It was concluded that several adhesives and application techniques are acceptable for field use.

2.2 ANALYTICAL RESULTS

2.2.1 Dynamic Analysis

It was ascertained during this study that no mathematical model capable of predicting foam response to arbitrary dynamic loading is available. However, two concepts for hardening a structure against mechanical shock were advanced:

- a. Total encapsulation
- b. A thick shell

A total encapsulation model is difficult to analyze completely. When the blast loading on a foamed plastic is considered, the foam will absorb the transient load but transmit, with lesser attenuation, the quasi-static drag load. Qualitatively, these conclusions are based on the probable viscoelastic action of the foamed plastic. The foam most suitable for total encapsulation is a low density foam where the expected absolute quantity of elastic energy stored in the foam is a minimum.

A thick-shell approach was analyzed on the basis of pure elastic action, which leads to a conservative estimate of the foam dimensional requirements of a viscoelastic shell. On the basis of the approximations that (1) the stress-strain response is linear (elastic) and (2) the loading is nearly static and of a magnitude equal to the sum of the transient peak and drag

overpressures, then a configuration may be advanced. The shell was made of rigid polyurethane foam of 25 pcf, with a Poisson ratio of .15, an allowable stress of 800 psi and a modulus of 10,000 psi. The critical shell thickness, based on an external radius of 50 ft., was 10 ft. A composite structure made of concrete with an R. F. window material was conceived as a possibly lower cost design. The optimal foam for a thick-shell radome will depend upon the desired elasticity.

2.2.2 Nuclear Effects Analysis

The nuclear radiation effects on polymers, especially polystyrene, are unnoticed for dosages up to 10^6 roentgen, which is well above the environment to be expected from a one megaton bomb at the 75 psi overpressure level.

2.2.3 Thermal Shield Analysis

The thermal shield analysis was based on ablation of an opaque and semi-transparent solid exposed to a radiant flux. The conservative value of foam thickness, for polyethylene under the specified thermal load, to undergo ablation is 1.48 ft. A laminate thickness of polyethylene foam of two to three feet would protect a shielded polystyrene plastic from reaching 150° F since the substrate temperature reaches 150° F maximum, 4.5 inches below the interface.

2.3 EXPERIMENTAL RESULTS

2.3.1 Polyethylene Ablation Tests

The heat of ablation for polyethylene was determined to be a function of the incident heat flux only if ignition occurs. The heat of ablation, although measured under experimental thermal fluxes which were below that of the 1,000 BTU/ft.² estimated thermal flux from the specified nuclear blast level, was extrapolated to a value of approximately 4,700 BTU/lb. for an incident flux of 1,000 BTU/ft.². The temperature of ablation was observed to be approximately 900° F.

2.3.2 Electrical Scale Model Transmission Tests

The effects that were observed in the scale model tests were as follows:

- a. A boresight shift of 0.66° occurred, which agreed well with the calculated value, 0.707° .
- b. Pattern variations occurred due to phase variations across the aperture of the reflector.
- c. Improved VSWR from 1.1:1 to 1.05:1.

2.3.3 Dielectric Measurements of Foam Samples

Using an X-band short circuit dielectrometer technique, the index of refraction and loss tangent of polystyrene (2 pcf) foam and polyethylene foam (1 pcf) were measured. These results were:

| | $\tan \delta$ | ϵ' |
|-------------------|---------------|-------------|
| Polyethylene Foam | .0004 | 1.040 |
| Polystyrene Foam | .00025 | 1.028 |

where $\tan \delta$ is the loss tangent and ϵ' is the real part of the complex dielectric constant.

3. TECHNICAL DISCUSSION

3.1 INTRODUCTION

The technical objectives of this investigation were to evaluate the effects of a nuclear blast on the pre-blast characteristics of foamed-plastics to determine the feasibility of protecting an above-ground antenna against the environment associated with the 75 psi overpressure range of a one megaton bomb by a psuedo-encapsulation. The electrical transmission characteristics of a foamed, encapsulated scale model were analyzed for the following:

- a. Boresight shift
- b. VSWR reflection losses in the feedhorn
- c. Pattern distortion
- d. Electrical transmission efficiency.

The effort is primarily analytical using existent data on nuclear weapons effects, foam characteristics, and structural evaluation methods. The experimental portion of the work was essentially: (1) the electrical measurements of a foamed, encapsulated scale model, (2) thermal ablation measurements of polyethylene foam for post-ablation characteristics, and (3) an adhesive experimental study to determine suitable bonding techniques and adhesives for the construction of foamed structures. In order to study the feasibility of foams for hardening, there are many considerations involved. It was necessary to break up the overall problem into many subtasks. Some tasks gave conclusive and complete answers, others partially complete, and still others were not resolvable. In order to give a complete and unconditional feasibility argument, all of the problem aspects must be completely answerable, or, at least, trends must be indicated where an exact number cannot be obtained.

The following subsections comprise the Technical Discussion:

- Phenomenological Behavior of Foamed Plastics
- Effects of Nuclear Radiation on Foamed Plastics
- Effects of Thermal Radiation on Foamed Plastics
- Thermal Shield Design Experimental Studies

Analytical Studies of Thermal Shield Design
Study of Foamed Hardened Radome Configurations
Electrical Transmission Experiments
Adhesives Study for Foamed Plastics
Technical Appendices

3.2 PHENOMENOLOGICAL BEHAVIOR OF FOAMED PLASTICS

3.2.1 Introduction

The phenomenological behavior of plastic foams has been investigated for some time, but the analysis of the mechanical response of these materials to arbitrarily given loads has not progressed to a stage which permits general predictability of response except in the narrow range of loading conditions found in the cushioning industry. These sources are listed in the bibliography. Some success has been achieved, but since no experimental data utilizing simulated nuclear blast loading has been reported, experimentation using shock waves of high dynamic overpressures is necessary to validate the conclusions drawn from these analyses. Foamed plastics are two-phased media; i. e., they contain both entrapped gases and solid polymeric fibril walls. They should be expected to exhibit, in their stress-strain relationships, constants of both gas and solid moduli, modified by geometric factors. In the limit of dense foams, near solid polymeric behavior might be expected. The material constants of the foam have been found to be dispersive, and this accounts for the rate sensitivity of the response to different modes of loading. The gas entrapped in the cells undergoes a pneumatic effect due to the adiabatic compression, which will vary with the time of delivery. The non-linearity of the response of the foam is most likely accounted for by the non-linear relations of a gas under loading. The difficulty which arises with non-linear relations is that there is no general mathematical treatment which handles large deformations in non-linear response systems.

In classical theory of elasticity, stress-strain relations are both linear and independent of time. The assumption of small deformations must also be made in order to apply the superposition principle to analyze various types of loading functions. However, when time is introduced into the loading,

all bodies are expected to show some deviation from the static behavior and some more than others. Even after the stress is removed, the deformations vary in time. To account for these time variations of the mechanical properties, the linear viscoelastic theory is useful as a tool. Viscoelastic theory treats a medium as being made up of viscous elements (dashpots) and elastic elements (springs). This means that such a theory handles a mechanical response which includes time. Such phenomena are described by the relation:

$$f(\sigma, \epsilon, t) = 0 \quad (1)$$

This relation in the linear theory has the form of a linear differential or integral equation. A foam response to a given load, if known experimentally, may be fitted to some linear model. However, the stress-strain relationship will be expected to vary for different stress-time functions. This is a manifestation of the dispersive properties of the media.

The objective of the following discussion is to deduce an intuitive model which is "linearized" and agrees with the available data. In the absence of behavioral data on foamed plastics under loads simulating the nuclear burst environment, this model is required in order to theorize about the response to nuclear burst loadings.

3.2.2 Static Theory of Foamed Plastics

There exists no satisfactory classification of foamed plastics. There are several sets of categories which serve only to name some classes:

- a. The continuum of stiffness is divided into "rigid", "semirigid", and "flexible" (or "resilient"). Presumably, these designations refer to ranges of values of elastic moduli.
- b. The continuum of wall thickness to fibril diameter ratio is divided into "open cell" (all fibrils, no walls) and "closed cell" (all cells fully walled, plus fibrils along the wall intersections) as extreme cases. There are also foams in which only some walls exist.
- c. The continuum of foam density (lbs/ft.³) is divided into "light" and "dense".

- d. Other classes are defined on the basis of the chemical composition of the ingredients of the foam (e.g., polystyrene, polyurethane, etc.).

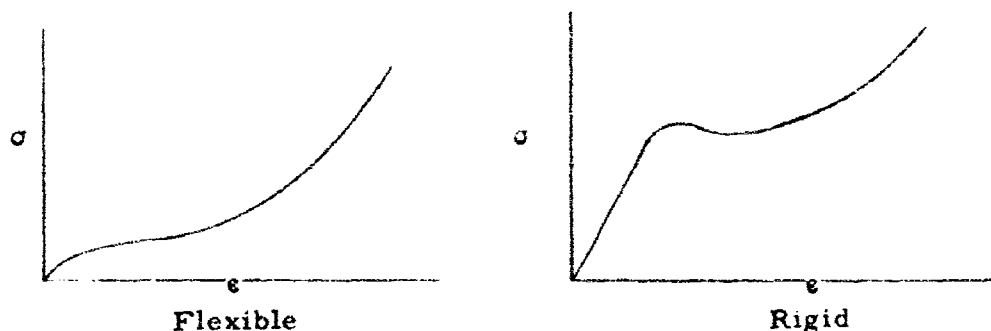
The foregoing classes are found to overlap. One of the functions of theory is to isolate the key variables which best serve in a classification. This is a task for future work in the case of foamed plastics because of the limited data available at the present time.

An attempt to correlate the rigid-flexible classification with the open-closed cell classification provides a good example of the difficulties encountered. Flexible urethanes, usually open cell, suggest that flexibility is a property to be ascribed to an open-cell structure only. However, resilient, polystyrene foam, being closed cell, confutes this premise. Another example pertains to the correlation of open-closed cell classification with density; the lower densities usually being open cell. Yet, there exists a closed-cell, polystyrene, resilient foam at very low density ($1/2$ lb/ft.³) to reject this conclusion. On the other hand, since this low density foam derives its resilient property from special processing after foaming, the foregoing correlations might be positive if the post-foaming processes were ruled out.

Polyurethane foams exist over the whole range from rigid to flexible. Flexible polyurethanes can be made at densities up to 20 lbs/ft.³. They are not processed further after foaming. Degree of flexibility can be controlled by processing in such a way that side branching of the polymer is controlled. If there is relatively little side branching, the foam is flexible; increased chain rigidity or side branching gives a rigid foam. Apparently this can be done independent of density. Even though open-closed cell does not correlate well with density, there is a tendency for higher density foams to have thicker cell walls, as well as thicker fibrils.

Recovery without permanent set correlates well with flexibility. A rigid foam cannot recover from a moderate strain, whereas a flexible foam can be compressed to half its volume many times with nearly perfect recovery (this is connoted by the term "resilient", often used as a synonym for "flexible").

The most striking dichotomy of foamed plastics is between the rigid and flexible types. Their static stress-strain curves look entirely different. Yet, the two curves have much in common and differ only in degree. This suggests that a single theory should serve for both. The curves look, roughly, like those in the sketches below:



The approach taken here was to consider the two types of foam separately and then weld the two theories together. Eventually, theories describing the behavior of open and closed cell foams should also be developed. The data are insufficient to permit this at the present time. The work reported herein concentrates upon the cell walls, but future work should restore balance by equal inquiry into fibril networks.

3.2.2.1 Rigid Foamed Plastics

Some of the qualitative characteristics of a rigid, foamed plastic are as follows:

- a. At low stress levels, it is linearly elastic with a relatively high value of Young's modulus.
- b. At strains in the vicinity of .05, the foam's stress-strain curve exhibits a sudden flattening which, in the case of a metal, would be called yielding. Some permanent set, though small, is present.
- c. Relief of load after that point leads to permanent set. There is evidence of internal damage such as crushing. Permanent deformation has occurred.

- d. When the strain is so large that the material crumples across cells, it gets stiffer progressively, like a wadded up piece of paper.
- e. The tensile modulus is generally greater than the compressive modulus.
- f. There is no loss of strength at temperatures as low as -100° F , and a rigid foam is dimensionally stable up to temperatures on the order of 175° F .
- g. The tensile strength is about twice the compressive or shear strength.
- h. A rigid foam can be either closed or open cell. This suggests that the fibrils are responsible for the rigidity.
- i. It has a negative Poisson ratio (as determined from its modulus and its compliance).
- j. Its strength is directly proportional to density.

Perhaps the first characteristic which requires explanation is the sharp corner in the stress-strain curve of a rigid, foamed plastic. A natural hypothesis is that most of the fibrils which are loaded axially buckle at that condition, leaving the material with a flat, stress-strain curve (no stiffness at all). However, buckling alone does not account for the internal damage associated with the observed permanent set. It is probably necessary to postulate also that buckling causes increased stresses in the fibrils, resulting in fracture. This point of view might be implemented by means of the Euler buckling load formula, which gives a critical load proportional to the fourth power of the fibril radius, or diameter (hence, proportional to the square of the foam density if increased density all goes into the fibrils), and inversely proportional to the square of the fibril length. If the cell walls were critical in buckling, the critical compressive stress would be proportional to the square of the wall thickness and inversely proportional to the square of the edge length, so walls and fibrils would act somewhat similarly, their relative importance depending upon their relative thickness. It has been stated that the fibrils are responsible for the strength properties of rigid foams. Probably the truth is that the walls, too, may have a role,

depending upon the surface tension of the wet foam, the density, etc.

The buckling stress for a fibril is proportional to the square of the diameter. But the diameter increases as the square root of the foam density, hence, the buckling stress would be directly proportional to the foam density if all additional density went into the fibrils. The buckling stress for a wall is proportional to the square of the thickness and, hence, proportional to the square of foam density if all additional density went into the walls. A thorough analysis of buckling stress as a function of foam density is required to indicate which of these two possibilities is the more valid.

The concept of buckling followed by fracture of fibrils and walls may be applied to account also for the "explosion" phenomenon observed in University of Texas drop tests.⁽³⁾ Probably the explosions take place throughout the material, but are noticed only around the edge. Small pieces of plastic would fly as the result of edge walls and fibrils fracturing while buckled. Each such fracture origin would send out stress waves, just as occurs in breaking glass, with the result that cracks would form and fairly large chunks could break off. Fragments are literally catapulted.

The observed fact that tensile strength exceeds compressive strength, reference 2, 4, and 5, may be understood in terms of the fact that only fiber or membrane axial stresses act in the case of tensile load, whereas in the case of compressive load there are additional stresses arising from the bending stiffness of the fibrils and walls when they are buckled.

The negative Poisson ratio⁽²⁾ is an interesting puzzle. It lies at the heart of the problem of understanding the mechanical behavior of foamed plastics. A value of about $-.18$ for Poisson's ratio for rigid styrofoam has been calculated.⁽²⁾

3.2.2.2 Flexible Foamed Plastics

Some of the qualitative characteristics of a flexible, foamed plastic are:

- a. In contrast to a rigid foam, there is no sharp elbow in the stress-strain curve. Instead, there is only a barely perceptible S-curvature.

- b. Over the entire range of strains, the trend is a gentle curvature upward. This is true of all densities and all temperatures.
- c. There is a moderate dependance of stiffness upon temperature; the stiffness increasing with decrease of temperature.

A rather simple approach to analyze flexible foam behavior can be employed. The stiffness of the foam is thought to arise from both the gas and solid phases, their moduli assumed to add parallel to each other. The foam geometry is assumed to be a cubical egg crate to permit visualization and analysis. When loaded, the stresses act along one of the egg crate axes. Then the fibrils and walls are either heavily or lightly loaded, depending upon their orientation with respect to the loading.

Two extreme cases can be analyzed; namely:

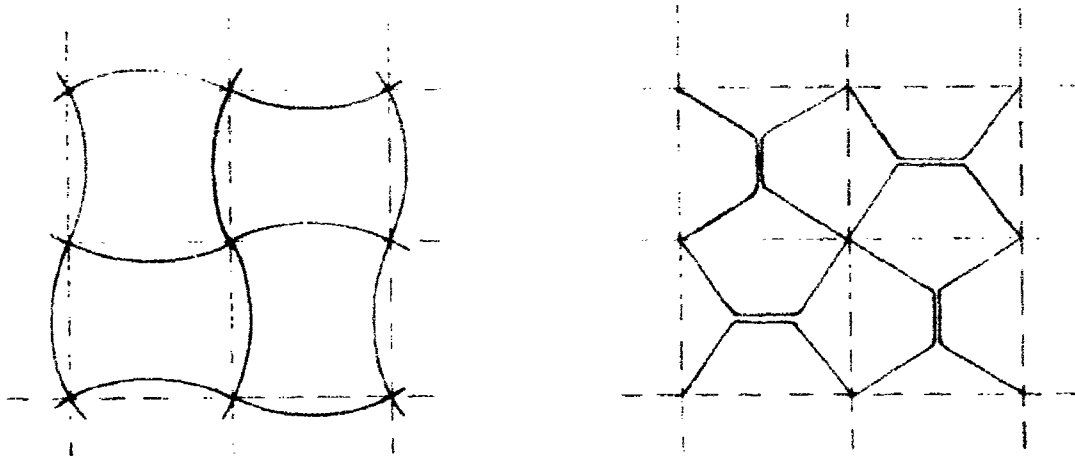
- a. A buckled wall panel surrounded by unbuckled fibrils
- b. A buckled fibril constrained by unbuckled wall panels.

In a flexible foam, both the fibrils and the walls must buckle to accommodate large strains. The stiffness and strength of a plastic solid would not comply to large strains without drastic modification or fracturing of the internal configuration. Fracture does not occur at large strains in a flexible foam, whereas it does in rigid foams as soon as internal buckling occurs. The difference may lie in the thickness to length ratio of the fibrils and walls for rigid versus flexible foams. The geometry factor is inherently important to distinguish the variation in flexible and rigid foam behavior since the solid substance of which the walls and fibrils are made is the same.

The fibrils and walls aligned with the load will buckle initially. In a rigid foam, these would soon fracture or yield, thereby increasing the portion of the load carried by the next most nearly aligned members. A progressive avalanche of failures occurs, making a sharp elbow in the stress-strain curve for a rigid foam. In a flexible foam, however, the buckled members continue to carry about half of their unbuckled load. Hence, smaller increase of load is transferred to the misaligned members, delaying their buckling. This lengthens the buckling process along the strain axis of the stress-strain plot. A very gradual decrease in slope occurs in place of a sharp elbow. This accounts for the early stage of the stress-strain curve for

a flexible foam.

It is enlightening to visualize an egg crate foam, if it were to buckle in such a way that fibrils remain straight but alternate walls buckle in opposite directions like a checkerboard in three dimensions. The following sketches indicate successive stages of the process as seen in a slice through the center of an echelon of cells. The dashed lines represent the fibrils half a cell away along the direction of view.



The bulging of the walls does not affect cell volume directly because of symmetry. Fibril torsion occurs since alternate fibril intersections are rotated in opposite directions. Furthermore, the bulging of all walls tends to make the space grid of fibrils contract in all directions while the edge and corner angles are preserved. Hence, this buckling mode of the egg crate is plausible provided that the fibrils will withstand large axial compression. Finally, the egg crate would display a negative Poisson ratio.

The situation suffered by one panel in such an egg crate is analyzed in Appendix 1. The displacements, stresses, stiffness, and Poisson ratio are calculated there. The findings are in qualitative agreement with the physical theory of flexible foams discussed in this section. In reality, the three-dimensional buckling situation is much more complicated--even in an egg crate--since the fibrils, too, must buckle. Then the edges of the panels are no longer straight, and the stress synthesis is much more difficult.

Interestingly, when a fibril buckles, it is not free to bulge as it pleases because it is constrained elastically by wall panels. Thus, the panels and fibrils, although both buckled, offer each other elastic foundations. Therefore, the stress-strain curve for a flexible foam should be nearly constant for very substantial strains. It approximates a linear elastic system in spite of the large deflections.

The stiffness contribution of the gas in the cells may be accounted for by assuming an adiabatic compression process. The results can be modified to apply to an isothermal process simply by replacing the ratio of specific heats everywhere by unity. The isothermal assumption would apply to a quasi-static process; the adiabatic assumption would apply to a very sudden compression. It is likely that the gas stiffness is negligible in a rigid foam, but may be relatively large compared with plastic stiffness in a flexible foam, especially at low foam densities. The way the gas interplays with the cellular geometry is unknown. The approach that seems best is to not try to understand physically what occurs but treat the composite behavior purely mathematically by the use of a pure mathematical model of springs and dashpots.

3.2.3 Dynamic Phenomena in Foamed Plastics

When a flexible foamed plastic is compressed suddenly in one direction, most of the mass accelerates in that direction. However, due to internal buckling, some of the resulting kinetic energy appears in the lateral directions. The average lateral motions of fibrils and walls over a volume element of several cells will have no net inertial reaction. However, a single fibril or wall will exert an inertial reaction opposing buckling. This shows up as a greater slope of the stress-strain curve obtained under dynamic conditions. That is, the lateral inertia opposes longitudinal motion much as if the foam density were greater. The effect is expected to be non-linear because the lateral acceleration of a point varies as the square root of the longitudinal acceleration. The equations for the dynamic buckling of a column or plate may provide a mathematical model of some plausibility for this phenomenon of apparent increase in inertia.

When a rigid plastic is compressed suddenly in one direction, the outer layer crumples almost immediately and picks up velocity. The pressure is communicated to successively deeper layers. Cumulative crumpling occurs. The crumpled layer gathers mass as it moves. It can accumulate a large momentum, eventually, if the body of foam is thick enough. Even if the forcing function is removed, the crumpled mass must be brought to rest by the remaining intact foam, which causes further crumpling. Depending upon the density and stiffness of the foam, this process might or might not stop. In the event that it has not stopped before reaching the antenna location, the antenna structure would receive the impact load.

A dynamic stress-strain curve is higher than a static one, not only because of inertia effects, but also because of damping effects. Internal energy dissipation increases with both amplitude and rate (or frequency) of deformation in some nonlinear fashion. The complexity of this effect arises from the fact that there may be many distinct damping mechanisms at work within the material. Three categories of mechanisms may be recognized.

- a. Mechanisms causing damping in the gas, such as viscosity.
- b. Mechanisms causing damping within the solid material.
- c. Mechanisms of interaction between gas and solid (such as acoustic damping of a panel) or between two solid members (such as dry friction).

The significance of each one will depend upon some time constant associated with their frequency response.

The heat liberated by a gas when suddenly (adiabatically) compressed in a foamed plastic is not necessarily a contribution to energy dissipation. Heat is pretty well trapped in a foamed plastic. If a sudden expansion (tension) were to follow a sudden compression, no energy would be lost.

One of the most common damping phenomena is the slow springback after removal of a compression load. If the compression is small and slow, the springback can be complete. In a rapid compression, however, heat is generated in the gas and also in the solid members (due to material damping mechanisms). If this heat is sufficient to raise the temperature of the thin solid members to their slumping point under load, the solid material will

deform to relieve the stresses in itself. This causes permanent set after springback. There will be residual stresses in the material also, which could weaken it against later loading. For small displacements, a foamed plastic obeys the wave equation. The one-dimensional wave equation is the well-known relation,

$$\frac{\partial^2 \xi}{\partial t^2} = C^2 \frac{\partial^2 \xi}{\partial X^2} \quad (2)$$

where ξ is the displacement of an incremental mass of the medium, C is the speed of propagation of sound in the medium. C^2 is proportional to the modulus and inversely proportional to the density. For shock conditions in a gas, the equation is roughly of the same form, except C^2 is replaced by $C^2(1 + S)^{\gamma + 1}$, where S is the change in density per initial density before the shock and is called the condensation, and γ is the adiabatic constant of the gas. In nonshock conditions, $\xi = f(X \pm ct)$ is a solution to the wave equation. Under shock, however, C is, in general, an integral function of space and time. The function, S , must be determined experimentally before the general solution of the shock wave equation can be obtained. The interesting consideration is the details of the passage of a stress wave through the solid and gas phases of a foamed plastic. Velocity is highest along a solid path. The velocity is lower through the gas, especially considering the inertia of cell walls between cells along a gas path. This would help to spread out an incident shock into a progressively thicker and weaker pressure gradient since the multiple interfaces would result in a multiple path traversal.

The primary problem with dynamic phenomenon is the necessary inclusion of time into the analysis. Static theories do not include time. Viscoelastic theories, however, do, in fact, include time but have been limited for the most part to linear behavior (small strains) only. The stress propagation waves and their effects that are prominent in dynamic problems are treated in the latter part of Appendix II. Unfortunately, only a few dynamic problems have been solved with this technique.

3.2.4 A Mathematical Model for A Foam

The mathematical model, which is just right for a given problem, is one which:

- a. Contains no negligible terms.
- b. Omits no terms which would contribute significantly relative to the accuracy requirements of the problem.
- c. Contains no terms which are unnecessary from the standpoint of the range of forcing functions of concern (spectra and spatial distributions), the degrees of freedom of concern, the parameter ranges of concern, etc.
- d. Requires computing facilities and time which are compatible with practical considerations associated with the problem, the project in which it occurs, and the stage of the project in which it occurs.
- e. Permits acceptable simulation of all phenomena of concern.
- f. Has as few nonlinearities as possible.
- g. Has as much physical significance as possible for ease of understanding and evaluating results.

The model must be very general and fundamental in order to account for the roles of all important parameters. That is, it would be less than satisfactory to have an empirical model fitted to a narrow range of materials and conditions, the extrapolation of which would be risky. The model must be simple in order to be tractable. This requires some idealization of the truth, which weakens generality. Likewise, some factors must be omitted lest analytical complications arise. A nonlinear response must be fitted to a linearized equation.

Mathematical model design is an art just like any other design skill. It must proceed by iteration. It also has practical aspects. For example, if a model containing N terms gives a certain accuracy, then there exists, in principle, a model containing less than N terms which produces little error in the results of chief concern. This means that in a big problem, remarkable economy of technical effort can be achieved by eliminating a factor or two in the accuracy requirement.

The greatest difficulty lies in selecting stress-strain relations. Here

is the heart of the problem of the mathematical modeling of foamed plastics (or any other nonclassical material). In the simplest case, a conventional elastic body under small loads, the stress-strain relations reduce to Hooke's law.

The stress-strain relation of a foam material under load will contain up to N order time derivatives of stress and strain, the time derivatives associated with the damping mechanisms. The possible approaches to solve for these terms are as follows:

- a. Choose a model representation from the developed linear viscoelastic theory. If stress and stress rate terms proportional to stress and strain rate terms are added, a general viscoelastic stress-strain relation results; i.e.:

$$P\sigma = Q\epsilon \quad (3)$$

where

$$P = \sum_{i=0}^n P_i \frac{\partial^i}{\partial t^i}$$

and

$$Q = \sum_{i=0}^n q_i \frac{\partial^i}{\partial t^i}$$

The coefficients are established by model fitting to observed stress-strain relation. The model may be visualized as a complex or simple arrangement of springs and dashpots in series and/or parallel configurations.

- b. Apply a Laplacian transformation to the dynamic (time-dependent) stress-strain relationship to obtain the frequency response. This permits direct comparison with linear idealized models whose behavior is well founded. The complex compliance and modulus is then derived as a function of frequency and also, through

transformation, time. The real part of the modulus is equal to the stiffness, and the imaginary part, the viscous damping.

The most time-saving approach appears to be response fitting to a linear viscoelastic model. This approach has been the only one seriously considered in this contractual effort. The elements of the viscoelastic theory are briefly described in Appendix II.

3.3 EFFECTS OF NUCLEAR RADIATION ON POLYMER PLASTICS

3.3.1 Introduction

The effects of high energy radiations on polymer plastic materials have been extensively investigated.^(6, 7, 8, 9, 10) The electrical and mechanical properties of polymers as dielectrics in electronic apparatus subject to nuclear and space environments have been a prime area of interest in these investigations. The data have been collected from irradiation experiments using high intensity radiation sources such as particle accelerators, reactors, cobalt pools, etc. Actually, none of these sources produce pulsed radiation of the same characteristics as a nuclear weapon. For this reason, the rate sensitivity is an unknown parameter. The integrated doses and the average rate of delivery, however, can easily be simulated. Integrated flux, or dosage, is the common linkage between the experimental tests and the atomic blast effects predictions. This discussion is not intended to be a survey of all radiation effects experiments on polymers, but, rather, only that extraction from the reported work necessary to indicate that polymer foams will be electrically and mechanically stable against the neutron and gamma dosages prevailing at or below the 75 psi incident overpressure range.

3.3.2 Nuclear Radiation Phenomena from A One Megaton Burst

Approximately 15% of the yield of a typical air burst results in the emission of nuclear radiation. The prompt or initial radiation is defined as that received directly from the initial reactions in the first minute following the detonation. Residual radiation, because most of it is dissipated in the upper atmosphere, does not constitute serious hazard to a ground structure. The nuclear radiation consists of charged particles, neutrons, and gamma radiation, but only the neutrons and gamma rays, because they have a long

range in air and are very penetrating, are to be of concern.

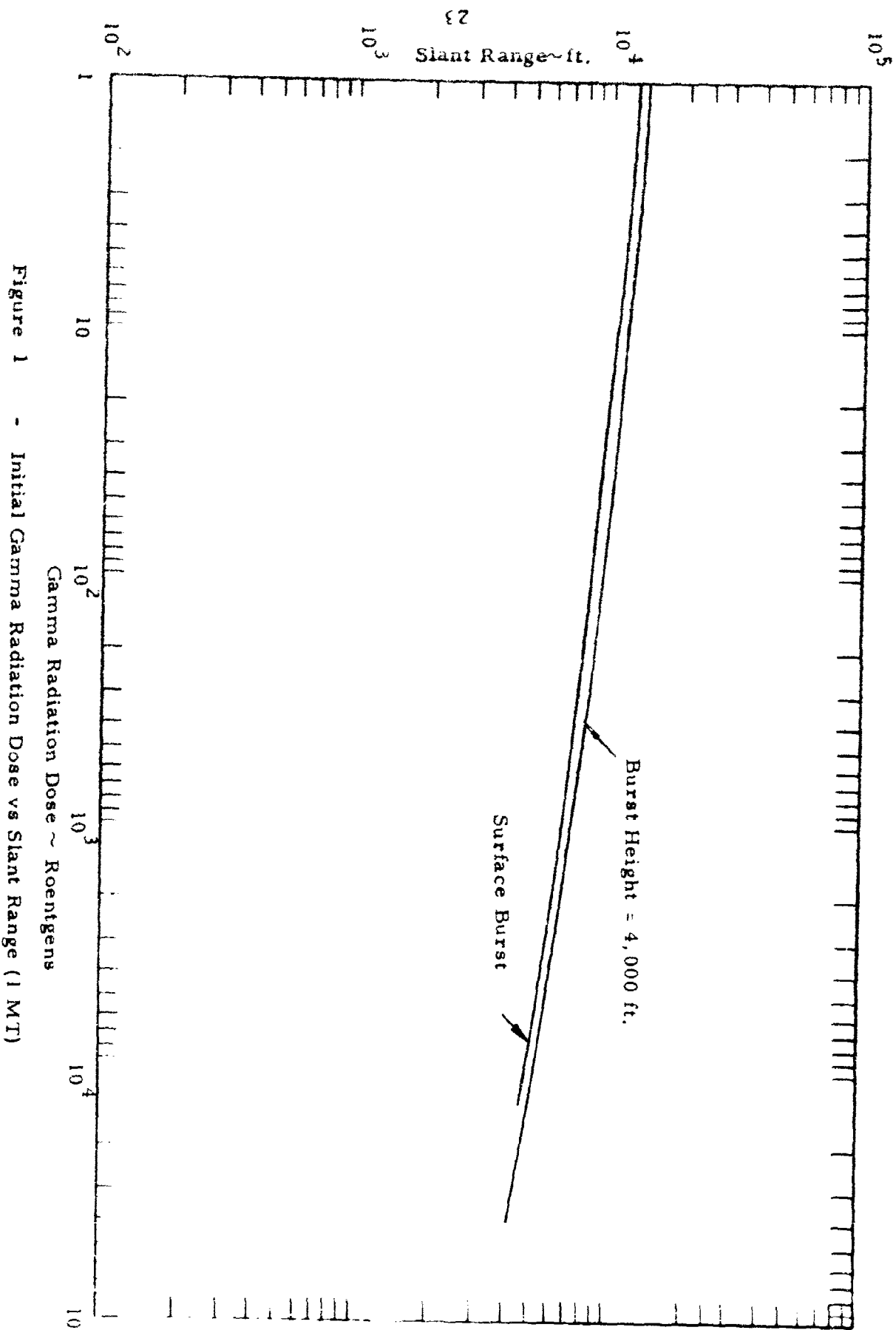
Gamma radiation dosage is usually measured in roentgens, r, which is the standard measure of the ionization caused by gamma rays interacting in matter. Figure 1 gives the intensity of initial gamma radiation at any distance from ground zero for a one megaton surface burst.⁽¹¹⁾

Neutron radiation dosage is measured in rem, which is the amount of energy absorbed in mammal tissue and is biologically equivalent in mammals to one roentgen of gamma rays. Figure 2 gives the intensity of the combined gamma and neutron radiation at any distance from ground zero for a one megaton surface burst.⁽¹¹⁾

Note that these quantities of radiation are integrated amounts over one minute. The range corresponding to the 75 psi peak overpressure is approximately 4,000 feet, at which the gamma and neutron dosages are 40,000 r and 10,000 rem, respectively. The radiation rates are 40,000 r/min. and 10,000 rem/min. Typical cobalt well (gamma) irradiation facilities deliver a gamma radiation dose at the rate of 1.3×10^4 r/min. to $.3 \times 10^4$ r/min. Hence, it is seen that materials irradiated in a cobalt well have been subjected to average dose rates comparable to the average rate of the nuclear bomb-delivered radiant energy.

3.3.3 Mechanisms of Damage

The mechanisms by which the effects of radiation in polymer plastics are produced are primarily ionization and excitation due to gamma radiation and displacement of atoms by neutrons which indirectly also result in ionization and excitation. Following these events, complex chemical reactions can take place and many changes in the physical properties may result from such reactions. In these materials, no simple picture for the effects has been found in the literature. In an atomic blast neutron and gamma rays are the agents causing damage. Fast neutrons produce damage mainly by light atom displacement. The displaced, energetic atom ionizes and excites neighboring molecules while slowing down to an interstitial or defect position. Gamma rays interact with electrons directly (Compton effect) and the result is molecular ionization and excitation. Equal fluxes of gamma rays are



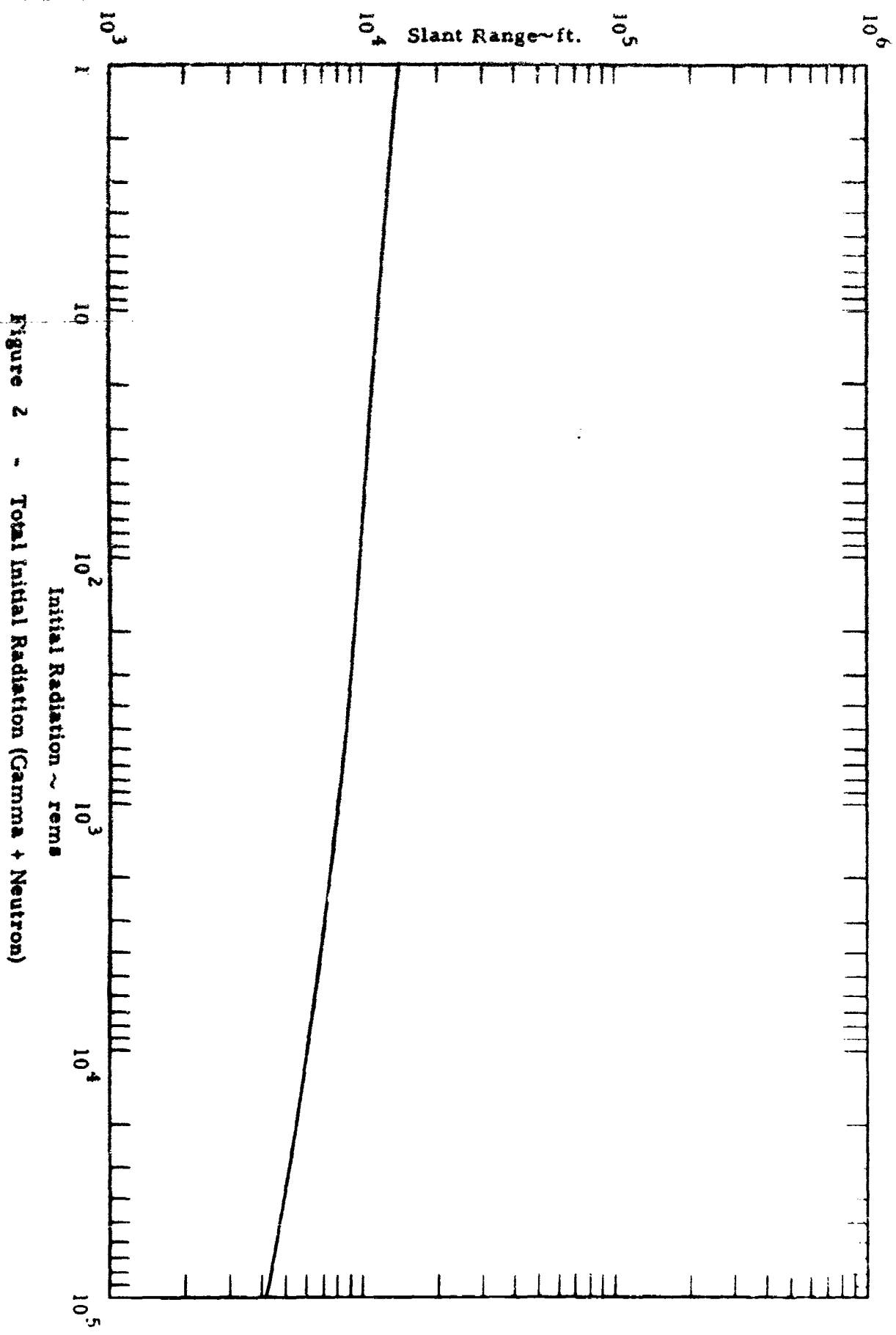


Figure 2 - Total Initial Radiation (Gamma + Neutron)

considered less damaging than neutrons in polymeric plastic materials. Other particles emitted from the bomb can cause damage, but they are not important at 4,000 feet from ground zero; i.e., that distance characterized by the 75 psi peak overpressure. The chemical, mechanical and electrical degradations in the irradiated organic polymers result directly from the ionization, displacement and excitation caused by only the gamma and neutron radiations from the bomb. The chemical and mechanical changes are time-consuming reactions producing essentially permanent results. The possible chemical and physical changes in irradiated polymers are many-fold, but the principal physical effects, for example, in polystyrene are cross-linking, gas evolution, molecular weight change and reduction in impact strength. These changes have not been observed, however, until gamma doses of 10^9 roentgens are absorbed. The presence of a benzene ring in the styrene monomer accounts for its resistance to irradiation effects. Most polymers cross link at 22 ev, but the polystyrene cross links at about 1800 ev. Therefore, the amount of cross linking in polystyrene for equal dosages will be less than other polymers.

The theoretical explanations for cross linking, molecular weight change, gas formation, etc., are controversial and are outside the scope of the present study. The primary concern in this study is the effect these phenomena have on the electrical and mechanical properties of polystyrene and other polymer materials which may be applicable to the hardened antenna concept.

3.3.4 Effects of Irradiation on Mechanical Properties of Polymers

Figure 3 describes the effects of gamma irradiation on the tensile strength of selected polymer films. The curve is self-explanatory. It should be noted that the effect is especially unnoticed in polystyrene before 10^7 r has been absorbed.

3.3.5 Effects of Irradiation on the Electrical Properties of Polymers

Although much work had been done on the effects of radiation on the mechanical properties of polymers, only limited studies have been made on their electrical properties. The effects on the loss tangent and dielectric

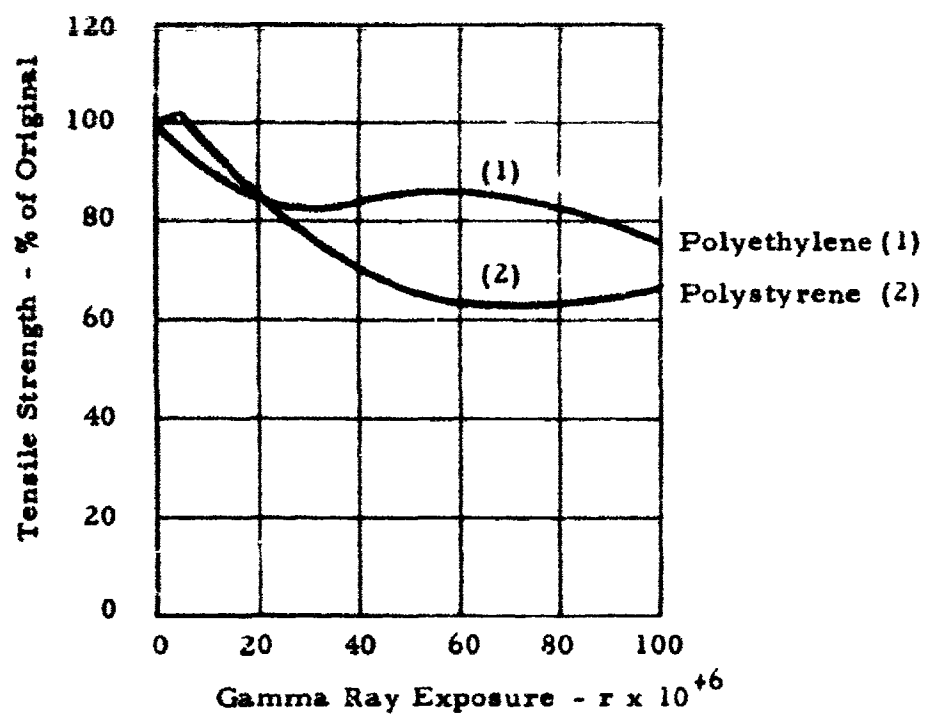


Figure 3 - The Effect of Gamma Radiation on the Tensile Strength of Plastic Films

constant have been principally observed over a frequency range from 10 to 10,000 mc/s. The effects will exist over a broader spectral range (10^{15} c/s to d.c.), i.e., effects such as radiation induced coloration, changes in the infrared and microwave absorption spectra, and photoconductivity and luminescence changes. Molecular changes resulting from the ionization and excitation phenomena will degrade, to some extent, the electrical insulation efficiency. The electrical changes are generally transitory unless severe dosages are absorbed. It is important to stress this distinction for the consideration of polymers in a system concept of a hardened antenna. Figures 4 and 5 describe the change in the loss tangent of polymers under gamma irradiation. Figures 6 and 7 describe the effects of neutrons on the same. The variation in the dielectric constant of the polymers, described in the above figures under the irradiation levels designated therein, was within the experimental range of error. (6, 9, 10)

3.3.6 Conclusions

The electrical properties of polystyrene resist degradation within experimental error for absorbed dosages up to 10^8 to 10^9 roentgens gamma radiation and 10^9 rem of neutrons (10^{18} neutrons/cm²). The radiation levels from the bomb are several orders of magnitude below this criteria. Hence, no appreciable electrical changes should be observed in polystyrene as a result of the atomic blast nuclear radiation.

The tensile strength of polystyrene has been observed not to degrade up to 10^6 roentgens. Again, dosage levels near this criterion are not expected for a one megaton burst, therefore, no mechanical degradation should occur due to the nuclear radiation.

It should be noted that polystyrene is the most radiation resistive of all polymers owing to its benzene ring structure. However, other polymers are nearly equal in response; e.g., polyethylene, which constitutes part of the thermal shield. It, too, is expected to incur no serious degradation from the nuclear radiant energy. In general, polymer plastics considered applicable for this effort are not expected to degrade from the nuclear radiation at the levels specified.

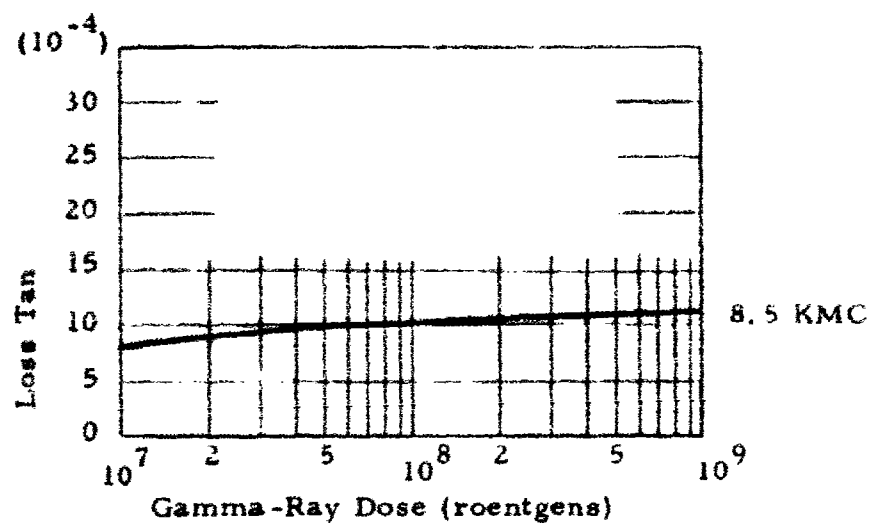


Figure 4 - Loss Tangent of Polystyrene vs Integrated γ - ray Flux

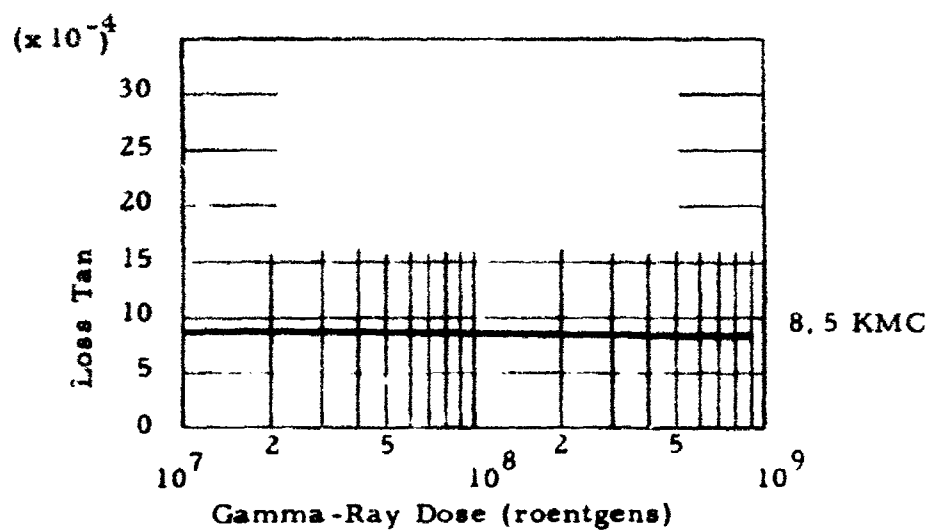


Figure 5 - Loss Tangent of Polyethylene vs Integrated γ - ray Flux

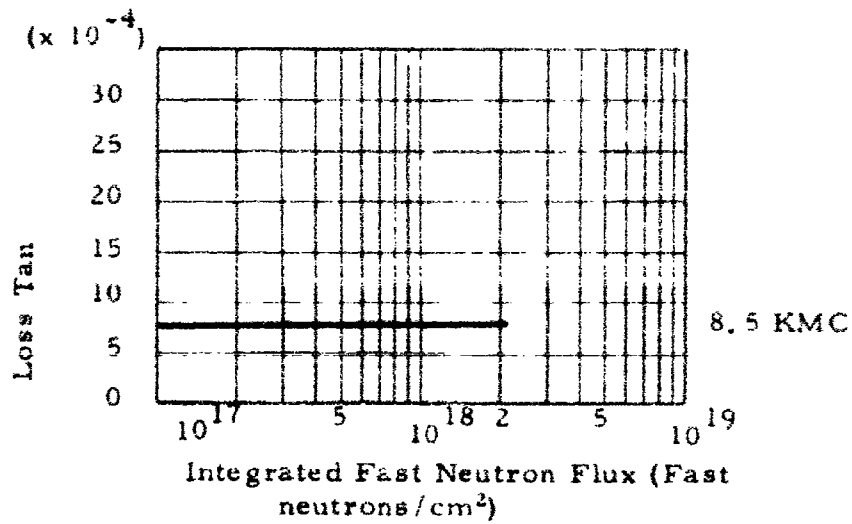


Figure 6 - Loss Tangent of Polystyrene vs Integrated Fast Neutron Flux

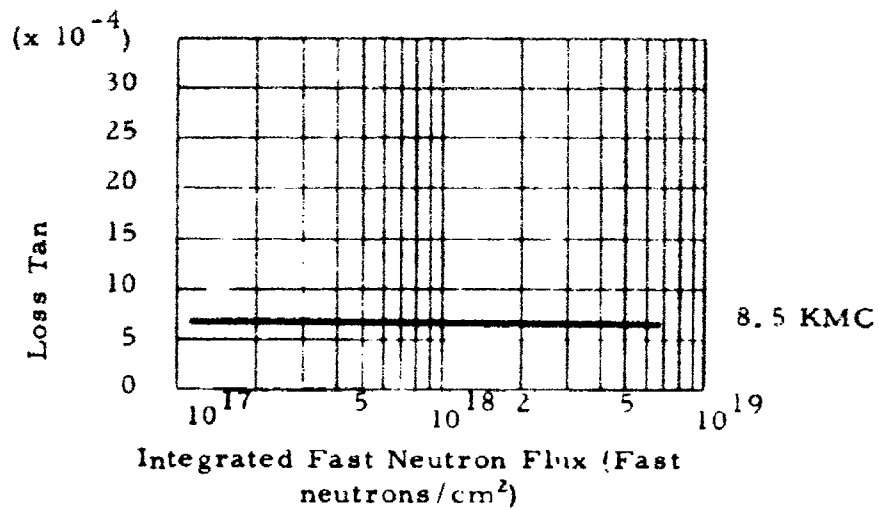


Figure 7 - Loss Tangent of Polyethylene vs Integrated Fast Neutron Flux

3.4 EFFECTS OF THERMAL RADIATION

3.4.1 Discussion of Thermal Damage Mechanism

The thermal yield of a one megaton nuclear blast is about 3×10^{14} calories. The energy density arriving at a target depends on the yield, the atmospheric transmittance, and the square of the inverse distance from the detonation. Figures III-12 through III-19 of Appendix III characterize the thermal radiation from a nuclear one megaton burst. Although the spectral energy distribution of the thermal radiation is not blackbody, a blackbody distribution corresponding to about 6,000° K coheres to the observed distribution reasonably well. The importance of this assumption is that material effects are strongly, spectrally dependent. The time rate of the delivery of energy to a target is also important. The thermal characteristics of a nuclear blast are treated in more detail in Appendix III, Section III.2.

Therefore, an interaction between radiation and matter will involve the radiation spectrum, the materials absorption spectrum, reflection smoothness and spectral response, and the time rate of delivery. Since a good portion of the 6,000° K spectral distribution is visible, this exhibits the importance of the color of an interacting medium.

All thermo-plastic foams, being quite unstable under thermal loading, will, due to their low temperature range of utilization (50 - 100° C), undergo extensive surface degradation and reduction in overall size. The degradation will consist of (1) liberation of gaseous or volatile decomposition components, (2) charred layers due to the nonvolatile, carbonized residues, and (3) ignition and surface flames.

The thermal effects are most serious to the utility of foamed plastics for hardening against nuclear bursts. The charred or carbonized residues are lossy dielectric substances and the reduction in size may seriously reduce the necessary quantity of foamed plastic to absorb the mechanical shock. Excessive temperatures in the residual foam also affect reduced mechanical strength.

3.4.2 Method of Solution

The knowledge about the instability of foamed plastics to thermal loading is based on the findings in the literature, ^(26, 27) experimental thermal testing at the Aeronca Manufacturing Corporation facility on polystyrene and polyethylene low density foams, and technical discussions of the problem with recognized experts in the field.

The conclusion, based on the above developments, was that a thermal shielding concept should be developed. The most useful and compatible concept is to employ polyethylene foam, which ablates readily under the intense thermal loading of the bomb (about 1,000 calories/cm² over a period of about 20 seconds) but leaves, in addition to a cooled substrate, no charred residue or lossy dielectric on the surface. Because of the cooled substrate, the mechanical energy absorbing portion of the structure should suffer no loss in strength and, because there is no charred residue, the electrical degradation effects should be small.

In order to assess the capabilities of polyethylene foam as a thermal shield, and to observe the behavior of foamed plastics under thermal exposure, experimental and analytical studies were undertaken with this objective. The following sections, 3.5 and 3.6, describe that technical effort.

3.5 THERMAL SHIELD EXPERIMENTAL STUDIES

3.5.1 Design Environment

The sought after thermal shield must be designed for the following environmental conditions and performance criteria:

- a. Absorb, reflect or otherwise dissipate the thermal radiation resulting from a one megaton surface burst 4,000 feet from the hardened site. The spectral distribution of the radiant energy is assumed to be equivalent to a 6,000° K blackbody.
- b. Atmospheric conditions are assumed to be such that the integrated heat flux to the thermal shield will be 1,000 cal/cm² (~3700 BTU/ft.²) with a peak rate of 425 cal/cm²-sec. (~1570 BTU/ft.²-sec.).
- c. 60% of the integrated heat flux must be dissipated prior to the arrival of the mechanical shock or blast wave.

- d. The interface between the thermal barrier and the primary structure has an allowable temperature limit of 150° F.
- e. The thermal shield, in both the pre- and post-blast conditions, must have a combined thickness and dielectric loss tangent that permits a minimum power transmission of 90%.

3.5.2 Design Concepts

Three concepts were considered for the design of the thermal shield:

- a. A combination reflective, radiative and ablative shield fabricated from fused silica.
- b. A high density organic polymer shield (ablative heat absorption) in which infrared absorption is achieved through diffusion and diffraction in the pore structure.
- c. A low density organic polymer shield (ablative heat absorption).

The relative merits of each concept are discussed in the following sections.

3.5.2.1 Fused Silica Thermal Shield

The general requirements for ceramic thermal shielding are chemical stability at high temperatures, low thermal conductivity, high resistance to thermal shock, and high thermal emittance. For this application, the most critical requirement is resistance to thermal shock because of the extremely high incident heat flux. In applications with high heat transfer rates, thermal shock resistance of ceramics is described by a factor R given by:

$$R = \frac{S_t (1 - \mu)}{E \alpha} \quad (4)$$

where

S_t = breaking tensile stress

μ = Poisson's ratio

E = modulus of elasticity

α = coefficient of thermal expansion.

Based on this measurement, the ceramic material most likely to survive a severe thermal shock condition is fused silica because of its extremely low coefficient of expansion, 5×10^{-7} , as opposed to a range of

$80-140 \times 10^{-7}$ for most ceramic materials. While fused silica might meet the requirement for thermal shock resistance, fused silica and other ceramic radome materials do not have sufficient strength to withstand an overpressure level of 75 psi. Loss of the thermal shielding during exposure to peak overpressure would expose the substructure to 40% of the total thermal radiation with a probable destruction of the system. On this basis, the use of ceramic thermal shielding does not appear feasible for this application.

3.5.2.2 High Density Organic Thermal Shield

The fabrication of a high density organic thermal shield probably requires no extension of existing technology. In this concept, energy dissipation would be achieved through the mechanism of ablation. While most organic polymers are relatively transparent to infrared radiation, opacity could be achieved through the use of reflective filler materials, powdered metals or crystalline materials such as titanium and zinc oxides.

The most suitable organic materials would be those such as polyethylene or teflon which melt and vaporize and leave no carbonaceous residues. The absence of a residue in the post-blast configuration is important to maintain efficient electrical transmission properties in the shielding system.

The principal difficulty associated with the dense organic shield is the maintenance of 150° F temperature at the interior interface with the structural material to be shielded. The use of sufficiently dense material to insulate the interface would also add excessive weight and cost to the overall system.

3.5.2.3 Low Density Organic Thermal Shield

With this concept, the mechanisms of energy dissipation and the material selections are the same as for the high density shield. However, in the low density system, infrared opacity can be achieved through diffusion and diffraction within the pore structure of the material. A survey of the available foams of polyethylene and teflon showed that polyethylene could be obtained in densities as low as 2 lbs/ft.³. The minimum available density for teflon is 83 lbs/ft.³ (40% porosity). This level of porosity for teflon does

not appear to be sufficiently high to insure infrared opacity and bond-line insulation.

Thus, the preferred concept for the thermal shield from compatible electrical and thermal considerations is the use of polyethylene foam of 2 lbs/ft.³ density. The multiplicity of pores at this density creates an effective network for infrared opacification as well as providing a highly efficient insulating medium of minimum weight.

3.5.3 Testing Program

3.5.3.1 Equipment and Calibration

The radiant heat source selected for the experimental program was a bank of 3600 watt quartz lamps with individual water-cooled reflectors. In order to measure the heat of ablation of foamed polyethylene, it was necessary to determine the relationship between the heat flux output of the lamps and the distance from the lamps at varying power inputs to the lamps. This calibration was made using a metallic sensing element of known emittance. The metallic element used in the calibration was Inconel X which had been oxidized in air at 2,000° F for 30 minutes. The emittance of Inconel X, oxidized in this manner, has been shown⁽¹²⁾ to vary from only .90 to .92 over the temperature range of 600 to 2,000° F.

In the calibration procedure, an oxidized Inconel X specimen of dimensions 2" by 2" by .032" was heated by the quartz lamps until equilibrium temperatures were achieved. Temperatures were measured with a Pt-Pt 10 Rh thermocouple. Incident heat fluxes were then calculated using known relationships⁽¹³⁾ between radiated heat flux and equilibrium temperature. Results of the calibration tests and the graphical relationships between heat flux, power input and distance from the lamps are summarized in Appendix VI.

3.5.3.2 Heat of Ablation - 2 lbs/ft.³ Polyethylene

Heat of ablation was measured on 2" by 2" by 8" samples of foamed polyethylene (2 lbs/ft.³). Two chromel-alumel thermocouples were embedded in each sample. Both thermocouples were placed at the center of the 8" dimension. Thermocouple No. 1 was 1" below the exposed surface

and Thermocouple No. 2 was 1-1/2" below the exposed surface. Continuous plots of thermocouple output versus time were made; in addition, times were recorded for ablation of a 1" depth of sample and complete ablation of the sample. Based upon the calibration curves from Figures VI-1 and VI-2 of Appendix VI and the times required for ablation, integrated heat inputs and heats of ablation were calculated. A summary of the testing for heat of ablation is shown in Table VI-2 of Appendix VI. Thermocouple readings, temperature versus time, are also found in the Appendix.

Two significant conclusions can be drawn from the experimental data with regard to heat of ablation: (1) if the sample does not ignite, heat of ablation is independent of heat flux, and (2) ignition of the sample increases the heat of ablation; with ignition, the heat of ablation is dependent upon the heat flux. Figure 8 shows a log-log plot of heat of ablation versus initial heat flux for the range of heat fluxes employed. Extrapolation of this curve to a heat flux of 1,000 BTU/ft.²-sec. would give a heat of ablation of approximately 4700 BTU/lb.

A comparison of the time-temperature curves in Appendix VI shows the measured temperature of ablation varying between 850 and 950° F. Hanst and Walker⁽¹⁴⁾ used radiation techniques to measure the ablation temperature of polyethylene and reported a value of approximately 920° F. Measured values of 850 to 950° F at the Aeronca facility are within the limits of accuracy for a thermocouple measurement.

3.5.3.3 Post-Ablation Sample Observations

The samples tested in the ablation studies did, in fact, ablate readily, and the surface of the samples, after ablation and the thermal loading ceased, were found to be relatively free of carbonaceous products. The appearance of foamed polyethylene in the pre-ablation state was characterized by a clean, white, sponge-like surface. After ablation, the exposed frontal surface had the appearance of a slightly yellow, glossy, resolidified molten solid. Only at a few dispersed points was a black or charred element observed. This suggests that the chemical decomposition temperature and the ablation temperature are so close to each other that ablation will, in practice, predominate over chemical decomposition. However, no exact analysis of the

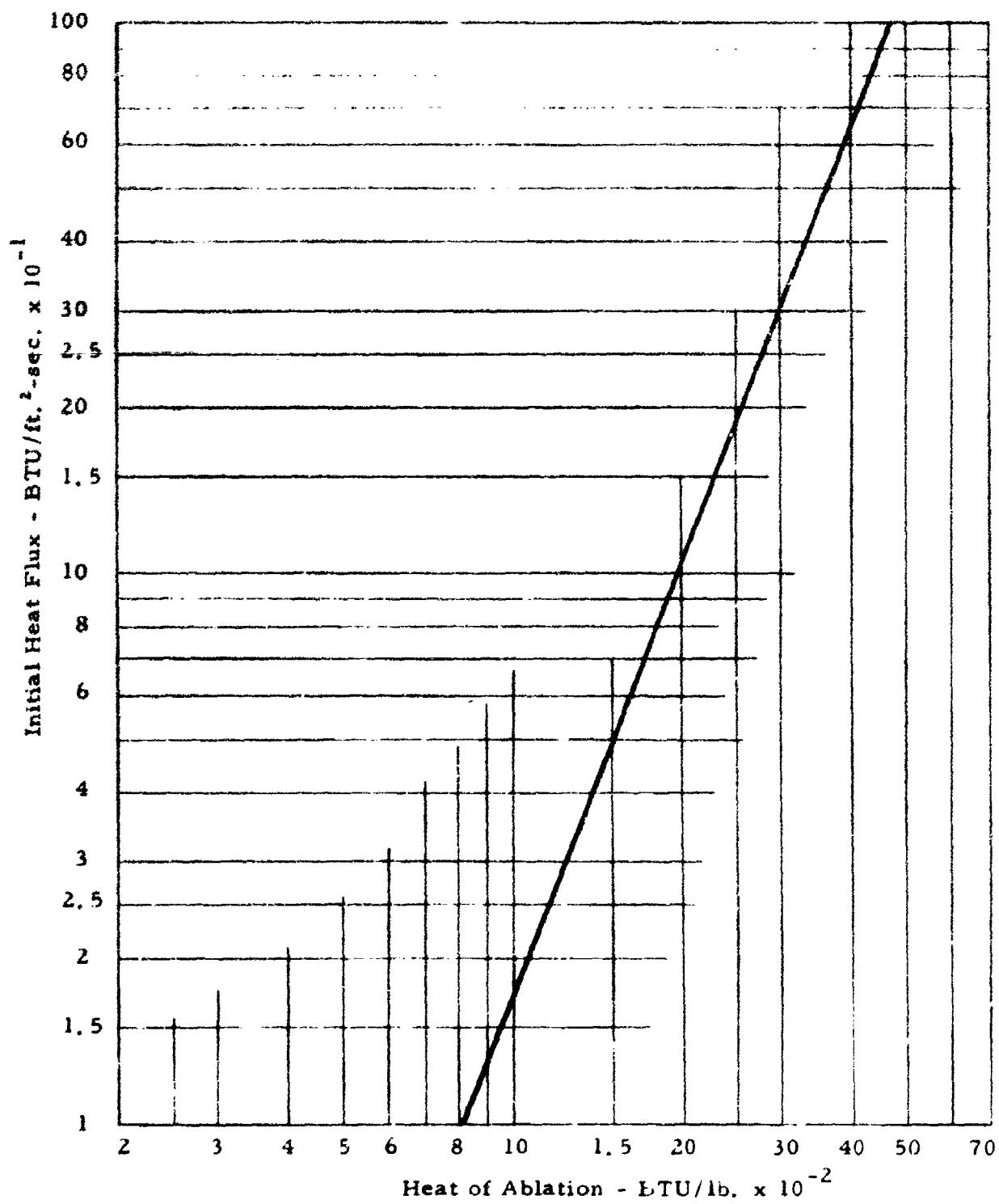


Figure 8 - Heat of Ablation vs Initial Heat Flux for Polyethylene Foam - 2 lb./ft.³

behavior was attempted in this effort. This observation, although contrary to what is observed for polystyrene, polyurethane, etc., under thermal loading, is not unique to polyethylene. Teflon, while not tested, is also expected to have a similar post-ablation surface condition.

3.6 THERMAL SHIELD ANALYTICAL STUDIES

3.6.1 Introduction

The analytical investigations of the thermal protection system for a hardened above-ground antenna consisted of the following tasks:

- a. A transient steady-state ablation analysis performed for an "opaque" ablating material, i.e., one which absorbs energy primarily on the surface. The thermal properties to be given to the material are that of polyethylene foam. Surface recession rates, mass recession rates and transient temperature profiles are to be computed for an integrated total heat load of 1,000 calories/cm² over a heating time of 26 seconds.
- b. A transient steady-state ablation analysis of a semi-transparent ablating material having the thermal properties of polyethylene foam. Transient steady-state ablation temperature profiles are to be computed for a range of attenuation coefficients ranging from 5 to 100 ft.⁻¹ in order to show the effect on the internal temperature distributions in the semi-transparent ablating material. Included would be the determination of the attenuation coefficients of polyethylene from experimental data taken at the Aeronca facility.

3.6.2 Ablation Analysis of An Opaque Solid

The results of this task are shown in Figures 9 and 10. These curves demonstrate the surface recession rates and mass ablation rates for a range of effective heats of ablation for foamed polyethylene. The curves indicate the largest rates occur during the initial four to five seconds of heating.

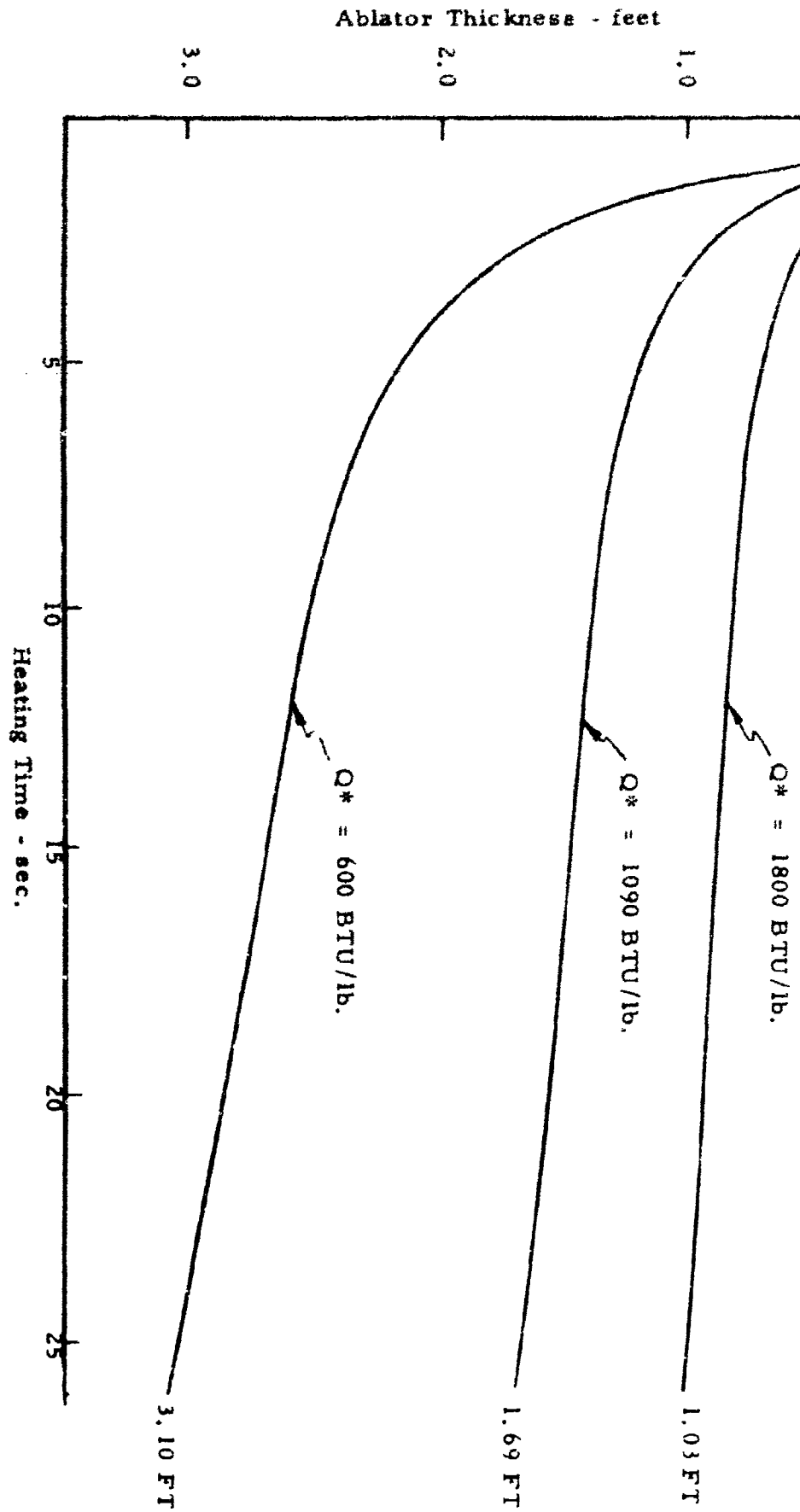


Figure 9 - Surface Recession - Convective Heating - Thermal Thickness = 0

Mass Ablation Rate
 \dot{m} - lb/FT²-sec.

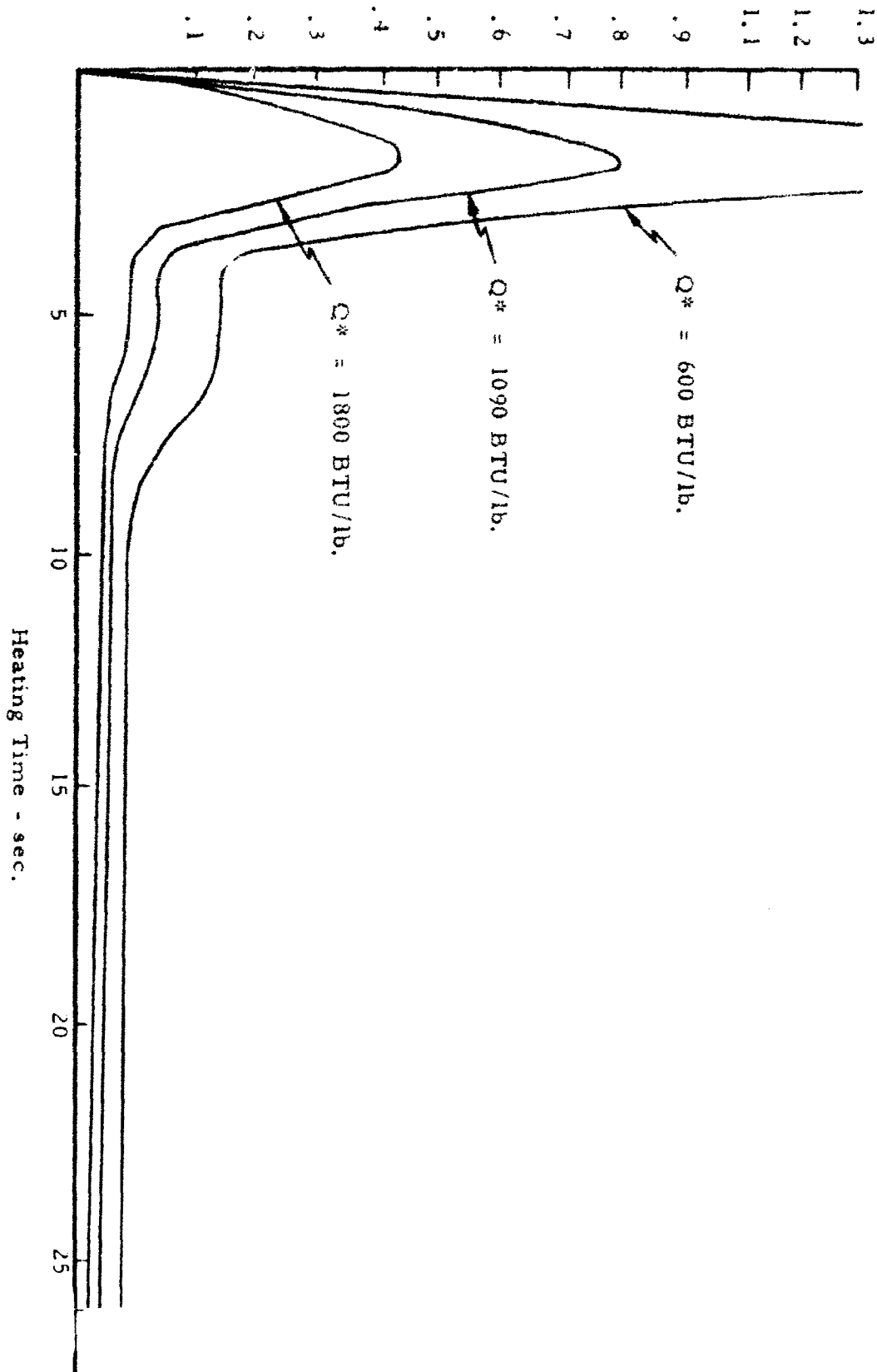


Figure 10 - Mass Recession Rate - Convective Heating - Thermal Layer - 0

The temperature distribution at any point within the thermally irradiated material has been found⁽¹⁵⁾ to obey

$$T(x, t) = T_i + (T_s - T_i) \exp \left[- \frac{x - s(t)}{\delta(t)} \right] \quad (5)$$

where

T_i = the initial surface temperature

T_s = the ablation temperature

$S(t)$ = the position of the receding surface with respect to a coordinate system whose origin is such that $x - s(t) > 0$

$$\delta(t) = \frac{K}{C_p \dot{m}}$$

K = thermal conductivity

C_p = specific heat

\dot{m} = mass ablation rate.

For a temperature rise of 50° F at some point (x, t) inside the solid of ablation temperature, T_s , where T_s is chosen as 900° F to represent polyethylene, the relationship $\frac{x - s(t)}{\delta(t)}$ must satisfy.

$$\frac{x - s(t)}{\delta(t)} = 2.81 \quad (6)$$

For $x - s(t) = .20$ inches, which is chosen arbitrarily, $\delta(t) = .712$ inches. Assuming that k and C_p are constants, and that $\delta(t) = (k/C_p) 1/\dot{m}$, \dot{m} can be determined for polyethylene foam; i. e.,

$$\dot{m} = (k/C_p) 1/\delta(t) = (k/C_p) (1/.712) = 2.6667 \times 10^{-5} / .712/12 = 4.5 \times 10^{-4} \text{ lb/ft.}^2 \text{ - sec.} \quad (7)$$

Therefore, for a temperature of 50° F in the solid material at a distance of 0.20 inch, or less, from the melting surface under steady-state ablation conditions, \dot{m} must be in the order of 4.5×10^{-4} lb/ft.²-sec.

Since it is evident from Figure 10 that the mass recession rate (ablation rate) is never this small when the material is considered as an opaque

medium, then the total required thickness of ablator for the effective heats of ablation as shown in Figure 9 would be approximately 1.23, 1.89, and 3.30 ft., respectively.

Figures 9 and 10 also show the mass recession rates and the surface recession rates for a range of experimentally determined effective heats of ablation ranging from 600 BTU/lb. to 1800 BTU/lb. Also given are the maximum thicknesses of the ablator for each experimentally determined effective heat of ablation based on the total time of irradiation (26 sec.).

The assumptions made in this thermal analysis were:

- a. There is no transmission of the radiant heat flux into the interior.
- b. There is a negligible thermal layer thickness and negligible temperature rise in the nonablating material.
- c. All the incident heat is dissipated in the ablation process.

In effect, the results of this analysis give the maximum thickness of ablator material that would be completely ablated if all of the heat generated by the thermal environment is absorbed by the ablation process. Since polyethylene foam is somewhat transparent to a radiant incident flux (attenuation coefficient of approximately 20 FT^{-1}), the preceding analysis gives a conservative quantity for the amount of material actually lost through mass transfer or ablation. In other words, for a transparent material, the surface recession rate will be less than that for an opaque material. This is caused by some of the incident heat penetrating into the material and creating a temperature rise at a relatively great depth.

On the other hand, the preceding analysis indicates bond line temperature lower than that to be expected for a transparent material. The necessity of the thermal analysis of a semi-transparent solid is to show, through parameter studies, the effects of penetration in depth of the heat flux on the temperature rise at various depths in the material.

3.6.3 Ablation Analysis of Semi-Transparent Solid

Many of the materials used for thermal protection are semi-transparent; consequently, a sizable fraction of the incident radiant flux may

flow through the material, heating it from within. This results in an earlier temperature response in depth than would otherwise be the case, e.g., that of Section 3.6.2. As a consequence, thermal protection systems designed for short time performance may be adversely affected.

The problem herein considered is that of a semi-transparent absorbing and scattering material heated by a transient radiant convective input. The heat equation is formulated so as to include the effect of absorption-in-depth of the radiant energy and the effects of ablation are included.

Assuming that the material does not decompose and that one-dimensional energy transport takes place by means of conduction and radiation fluxes, the heat equation in a laboratory coordinate system is:

$$\rho C \frac{\partial T}{\partial t} = \frac{\partial}{\partial x} \left(k \frac{\partial T}{\partial x} \right) - \frac{\partial F}{\partial x} \quad (8)$$

The radiant flux F at any point x may be represented by the following expression:

$$F(x) = (1 - R) F_1 e^{-a(x-s)} \quad (9)$$

the quantity R is the diffuse reflectivity of the material to the incident radiant flux F_1 . Both the flux attenuation coefficient and the diffuse reflectivity are considered as average values taken over the band of wavelengths of the radiant source. Accordingly, a and R are not only properties of the material, but also functions of the spectral distribution of the radiant source. Results presented herein are applicable only to a very thick sample or to one with a perfectly transparent rear boundary. Equations 8 and 9 may be combined, yielding the following differential equation:

$$\rho C \frac{\partial T}{\partial t} = \frac{\partial}{\partial x} \left(k \frac{\partial T}{\partial x} \right) + a(1 - R)F_1 e^{-a(x-s)} \quad (10)$$

Transforming from the laboratory coordinate system to the ablating surface, let

$$y = (x - s) \quad (11)$$

Equation 10 transforms as

$$\rho C \frac{\partial T}{\partial t} = \frac{\partial}{\partial y} \left(k \frac{\partial T}{\partial y} \right) + \rho C \dot{s} \frac{\partial T}{\partial y} + a F_o e^{-ay} \quad (12)$$

where

$$F_o = (1 - R) F_i(t) \quad (13)$$

In the steady-state limit, with constant thermal and optical properties, equation 12 reduces to the following:

$$\frac{d^2 T}{dy^2} + \frac{\dot{s}}{\alpha} \frac{dT}{dy} = -a \frac{F_o}{k} e^{-ay} \quad (14)$$

where α represents the thermal diffusivity and F_o is constant. The integral of (6) is:

$$\frac{dT}{dy} + \frac{\dot{s}}{\alpha} T = \frac{F_o}{k} e^{-ay} + K_1 \quad (15)$$

The integral solution to equation 15 is:

$$T = \frac{F_o}{k(\dot{s}/\alpha - a)} e^{-ay} + K_2 e^{-(\dot{s}/\alpha)y} + K_1 \quad (16)$$

Defining the temperature rise by $\theta = (T - T_o)$, the solution to equation 14 is found to be the following:

$$\frac{\theta}{\theta_w} = e^{-(\dot{s}/\alpha)y} + \frac{F_o}{k \theta_w (a - \dot{s}/\alpha)} \left[e^{-(\dot{s}/\alpha)y} - e^{-ay} \right] \text{ for } 0 < a \quad (17)$$

To use equation 17, one must evaluate \dot{s} from differentiating equation 17 with respect to y .

$$\frac{d\theta}{dy} = \frac{\dot{s}}{\alpha} \theta_w e^{-(\dot{s}/\alpha)y} + \frac{F_o}{k(a - \dot{s}/\alpha)} \left[a e^{-ay} - \frac{\dot{s}}{\alpha} e^{-(\dot{s}/\alpha)y} \right] \quad (18)$$

Thus at $y = 0$

$$\left(\frac{dT}{dy} \right)_{y=0} = \frac{F_o}{k} - \frac{\dot{s}}{\alpha} \theta_w \quad (19)$$

\dot{s} is then found to be the following:

$$\dot{s} = \frac{\dot{q}_{OR} + \left[k(\partial T / \partial y) \right]_{y=0}}{\rho \psi} = \frac{\dot{q}_{OR} + F_o}{\rho (C\theta_w + \psi)} \quad (20)$$

where ψ is the heat absorbed per unit mass ablated, given by

$$\psi = \Delta h_v + \eta (H_\infty - H_w) \quad (21)$$

Equations 17 and 20 completely specify the steady-state temperature distribution in a semi-infinite bar heated by constant radiative and aerodynamic inputs for constant thermal and optical properties. The first term on the right of equation 20 is the usual steady-state temperature distribution due to the aerodynamic heating, and the second term is the perturbation due to the radiant input.

For pure radiant heating

$$\left(\frac{dT}{dy} \right)_{y=0} = \frac{F_o}{k} \left(1 - \frac{C}{C\theta_w + \psi} \right) \quad (22)$$

Thus, a positive surface gradient always exists in steady-state ablation for radiant heating. The value of y (the distance from the surface of the material at which the temperature is calculated) at which this maximum occurs is:

$$y_{\max} = \frac{1}{(\dot{s}/\alpha - a)} \ln \left\{ \frac{\dot{s}/\alpha}{a} \left[1 + \left(a - \frac{\dot{s}}{\alpha} \right) \frac{k\theta_w}{F_o} \right] \right\} \quad (23)$$

q^* is never the same for aerodynamic heating as it is for radiant heating due to the transpiration contribution that is absent for pure radiant heating. Generally speaking, for the same net input, i.e., for $\dot{q}_{OR} = F_o$, a greater ablation rate results from radiant heating than for aerodynamic. This is due to the lower q^* value associated with the pure radiant input.

It is shown that during ablation, in a combined radiative and convective heating environment, it is possible to obtain a positive temperature gradient at the surface. It is also shown that, for pure radiative heating, the steady-state ablation rate is greater than for a net convective input

4 OR numerically equal to the magnitude F_j of the radiant input. This is due to the lower value of q^* appropriate to radiant heating.

From a thermal protection system point of view, it is clear that it is desirable to develop materials with as high an attenuation coefficient as possible in order to provide suitable thermal protection from a radiant heating environment. One technique that may be used to accomplish this is to opacify the materials by the addition of large numbers of scattering centers. The effect of this is to force the radiation to travel a very long optical path in traversing the material. Thus, even if the optical absorption coefficient is small, the attenuation of the radiant flux is large due to the long path traveled.

3.6.4 Discussion of Effects of Semi-Transparency

The heat transfer analysis in Section 3.6.3 treated a semi-transparent ablator heated by a radiant heat flux. Figures 11 and 12 give the relative temperature distribution in a semi-transparent polyethylene foam for a heat of ablation of 1100 BTU/lb., a radiant heat flux greater than 50 BTU/FT²-sec., and a surface recession rate equal to that given in Section 3.6.2 (which is considered conservative for this analysis in view of the assumptions made). Curves are given for different values of the attenuation coefficients above 10 FT⁻¹, the radiant flux heating penetrates no greater than approximately 4.5 inches, at which point a temperature of 150° is reached.

Figure 13 gives the back-face temperature rise history and the temperature rise history at a point five inches from the back-face for attenuation coefficients of 20 FT⁻¹ and 50 FT⁻¹ for an initial 2 FT ablator thickness. Figure 14 gives these temperature rise histories for attenuation coefficients of 5 FT⁻¹ and 10 FT⁻¹, respectively, for the same ablator thickness. Only for an attenuation coefficient less than 10 FT⁻¹ does the back-face temperature exceed 150° F.

The required thickness of the ablator heat shield, therefore, depends upon the value of the attenuation coefficient for the foamed polyethylene. Table 1 gives the value of the attenuation coefficient for nine samples based on tests that were made at the Aeronca facility. In all cases, the temperature of ablation was 200° F and the total thickness of the sample was 1.0 inch.

Material Properties & Parameters

$$\rho = 2 \text{ lb/ft}^3$$

$$C_p = .30 \text{ BTU/lb.}^\circ \text{F}$$

$$k = .8 \cdot 10^{-5} \text{ BTU/sec.}^\circ \text{F}^\circ \text{F}$$

$$T_{ABL} = 900^\circ \text{F to } 100^\circ \text{F (init. cond.)}$$

$$L_{ABL} = 860 \text{ BTU/ft.}$$

$$H_{ABL} = (T_A - T_o) C_p + L_{ABL} = 1,100 \text{ BTU/lb.}$$

$$\theta_w = (T_A - T_o) \text{ at surface}$$

$$\theta_y = (T_y - T_o) \text{ at distribution } y \text{ from surface}$$

$$a = \text{Atten. coeff. of radiant flux thru mat. (ft}^{-1}\text{)}$$

$$F_w = \text{Radiant flux thru surface layer}$$

$$F_y = \text{Radiant flux at dist. } y \text{ from surface reduced formula for } F_w \geq 50, a \leq 100$$

$$\frac{\theta_y}{\theta_w} = 4.6 e^{-ay} \quad \text{and } y \geq 1/4 \text{ in.}$$

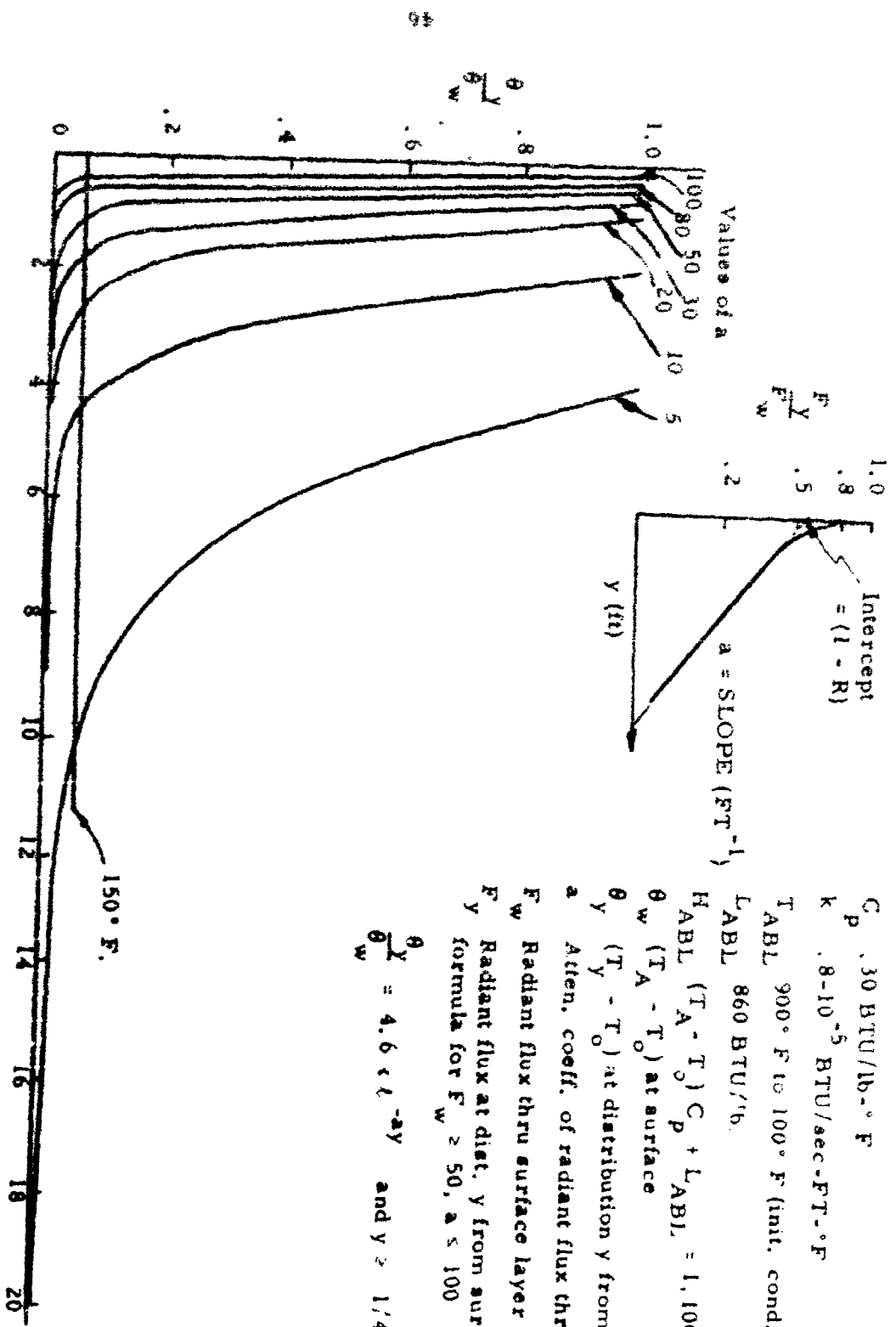


Figure 11 - Effect of Attenuation Coefficient on Temperature Rise of Material

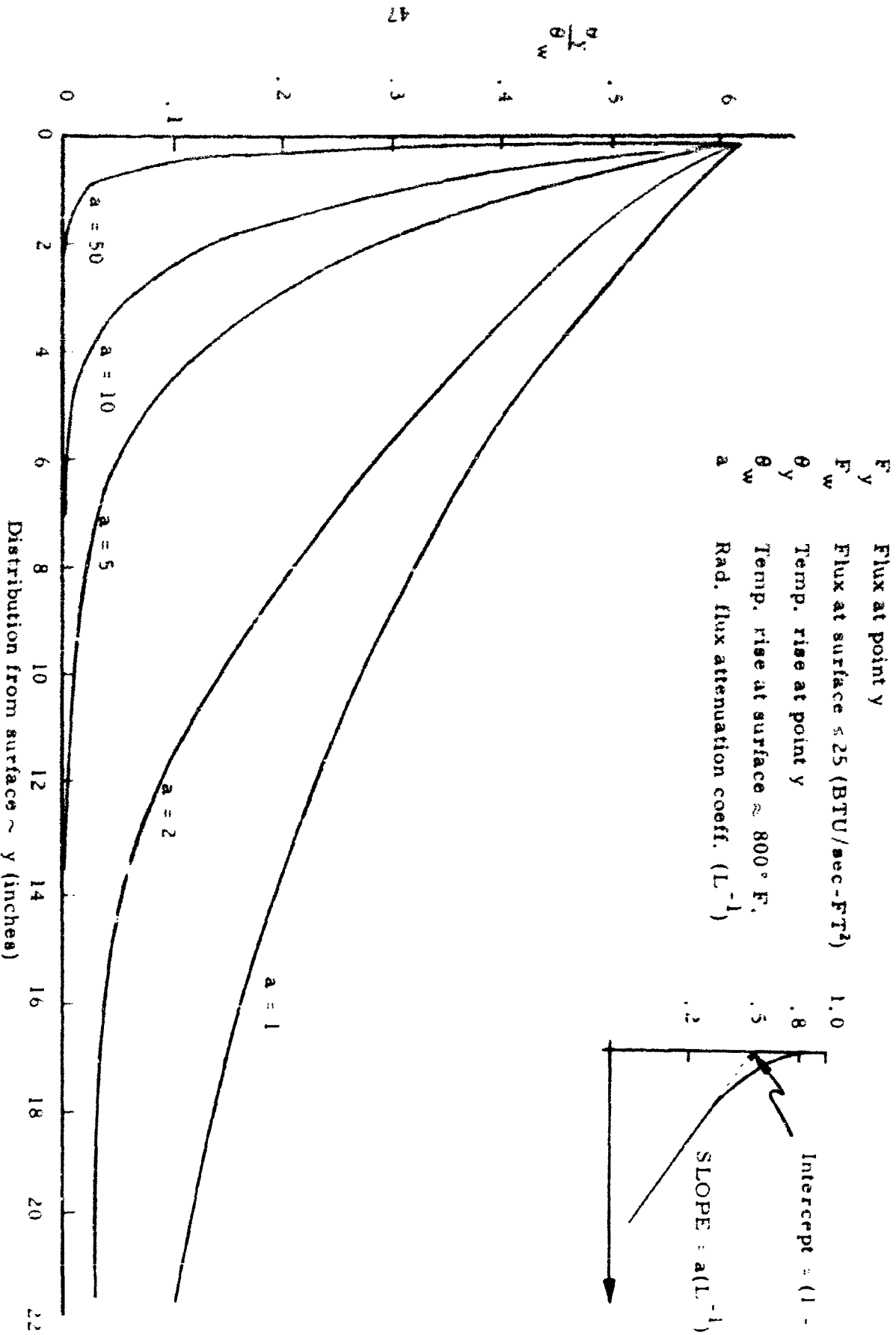


Figure 12 - Temperature Rise vs. Distribution from Surface for Steady State Ablation

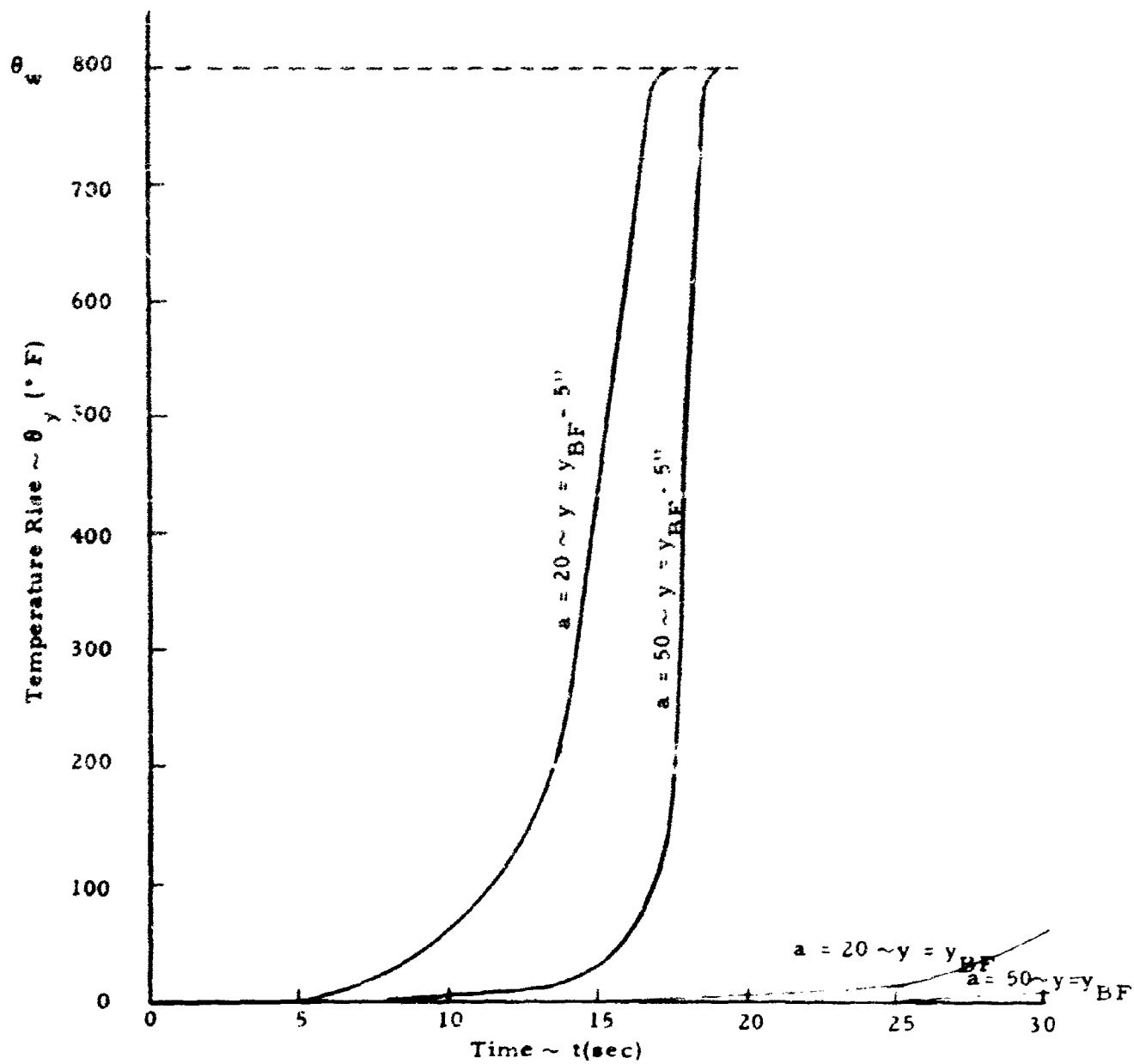


Figure 13 - Temperature Rise vs. Time for $y = y_{BF}$ and $y = y_{BF} - 5''$ for Radiant Attenuation $a = 20 \text{ (ft}^{-1}\text{)}$ and $50 \text{ (ft}^{-1}\text{)}$

$a = 5$
 $a = 10$

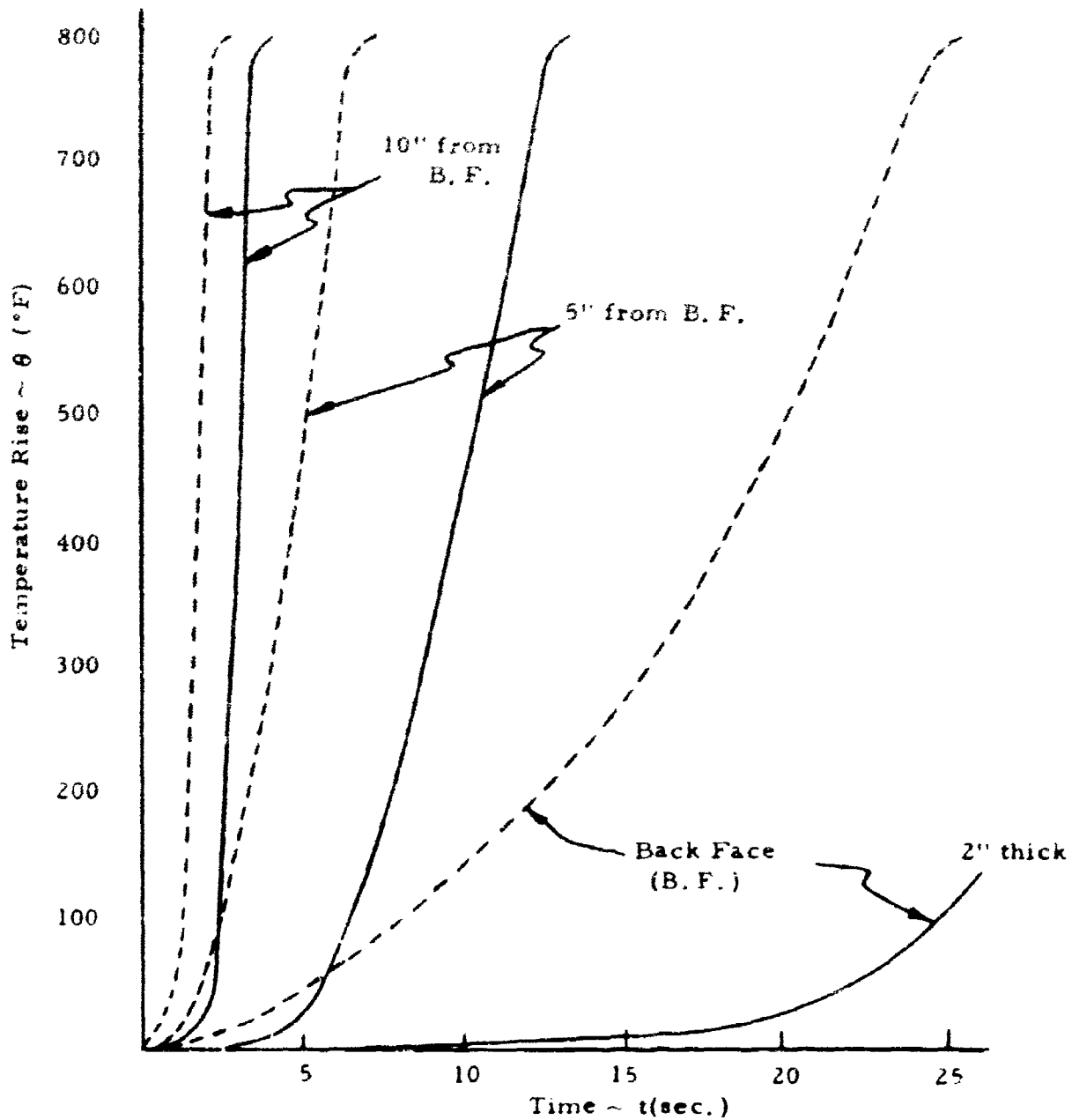


Figure 14 - Temperature Rise vs. Time at Back Face and Other Layers
 for Radiant Attenuation Coefficient $a = 5 \text{ \& } 10 (\text{FT}^{-1})$ & Ablation Heat
 $H_A = 1100 (\text{BTU/lb})$

TABLE 1

Experimentally Determined Attenuation Coefficients

| Sample No. | T_o (°F) | $T_{.5}$ (°F) | θ_o/θ_A | $\theta_{.5}/\theta_A$ | Ignition | $\frac{a}{-1}$ (ft) |
|---------------|---------------|------------------|---------------------|------------------------|----------|------------------------|
| 1 | 475 | 187 | .45 | .09 | No | 30 |
| 2 | 695 | 190 | .74 | .09 | No | 50 |
| 3 | 875 | 262 | .97 | .20 | Yes | 50 |
| 4 | 945 | 275 | ≈ 1 | .21 | Yes | 50 |
| 5 | 635 | 358 | .67 | .32 | Yes | 17 |
| 6 | 625 | 254 | .66 | .20 | Yes | 20 |
| 8 | 615 | 253 | .65 | .19 | No | 20 |
| 9 | 595 | 236 | .62 | .17 | Yes | 30 |

$$T_A \approx 900^\circ \text{ F} : \theta_A = 800^\circ \text{ F.} \sim s \approx 1.0''$$

The data indicates that the measured values for the attenuation coefficient range from 17 to 50 FT^{-1} , and with one exception, is always equal to or greater than 20 FT^{-1} . For purposes of defining a required thickness of ablator, a value of 20 FT^{-1} is used for the attenuation coefficient for polyethylene.

3.6.5 Summary

The following recapitulation is made concerning the thermal analysis of the heat shield for the hardened antenna system:

- a. For the selected value of the attenuation coefficient of 20 FT^{-1} , and using the maximum experimental value of 1800 BTU/lb. for the effective heat of ablation, the thickness of the ablator is 1.48 ft. (based on Figures 9 and 10).
- b. This value of ablator thickness is considered conservative in that -
 - (1) values of the effective heat of ablation reported in the literature are higher than 1800 BTU/lb. for the heating environments of this design problem,
 - (2) the thickness is based on an average recession rate for an opaque material plus an added thickness to account for penetration of the radiant flux at the instant when ablation (and heating) ceases, and
 - (3) the value of the attenuation coefficient used is the lowest measured value and is based on limited experimental data at relatively low heating rates.

3.6.6 Nomenclature

| | |
|-------------|-------------------------------------|
| H_w | air enthalpy at wall |
| H_∞ | enthalpy of freestream |
| K_n | integration constants |
| \dot{q}_c | convective heat flux to a cold wall |
| s | ablated length |
| ϵ | effective emissivity |
| σ | Stefan-Boltzmann constant |

| | |
|--------------|--|
| F_x | incident radiant flux |
| k | thermal conductivity |
| C_p | specific heat |
| q^* | ablation parameter |
| Δh_v | heat of vaporization |
| η | transpiration parameter |
| ϕ, τ | LaPlace transformed time and temperature |
| T | temperature |
| x | position coordinate |
| a | attenuation coefficient |
| α | thermal diffusivity |
| ρ | density |
| R | diffuse reflectance |

3.7 STRUCTURAL ANALYSIS OF FOAM HARDENED CONFIGURATIONS

3.7.1 Introduction

There has been advanced, in this program, several concepts whereby a foam hardened antenna configuration may have utility. The original concept that led to the feasibility considerations of foam materials in hardening existent above-ground antennas was an encapsulation scheme. The foam response under blast loading was envisaged as undergoing large deformations on the exterior surface resulting in permanent compression set and, perhaps, crushing. As a result of the huge energy absorption, the question was then to ascertain whether transmitted shock to the antenna location was reduced to a safe level. In particular, the question dealt with the physical quantity of foam that would be required to withstand and protect at the 75 psi incident overpressure range. In addition, that same quantity of foam would have to withstand other serious environments from the nuclear blast, such as thermal and nuclear radiations. The final, but yet most serious consideration, was whether or not that quantity of hardening foam would seriously degrade the electrical performance of the antenna.

The first order feasibility of hardening an antenna with a hemispherical configuration of foam at severe overpressure levels can be assessed only on the basis of the experimental or environmental testing data available on foams. The most severe mechanical testing on foamed plastics has been exclusively limited to drop tests or cushioning tests except for some efforts in evaluating foamed plastics for hardened space frame radomes.⁽¹⁶⁾ Because the existing data on foams is rather limited in scope, and observed under conditions far removed from a simulated nuclear blast, the results herein developed are not conclusive but indicate the configuration and dimensional characteristics suitable for experimental undertaking in a shock tube analysis. Furthermore, the philosophy of hardening is not limited to only one type of foam, or one possible configuration, or concept.

Another concept besides total encapsulation is possible; namely, a thick foamed shell. This shell may be elastic or deformable. A thick shell, as well as a total encapsulation configuration, utilizes a foam with a response that characterizes the mode of hardening; i.e., elastic or viscoelastic. This section is a discussion of the feasibility of each configuration concept. Only blast or shock environment will be of concern in this section. The contribution or the effects of nuclear radiation on plastic foams are negligible for this problem. The thermal effects are serious to thermoplastic foams but have been treated separately in Sections 3.4, 3.5 and 3.6. The thermal aspects have been treated with a "thermal shield" approach. The thermal shield must also be compatible with the blast and electrical aspects of the design.

3.7.2 Encapsulated Antenna Approach

The basis of a foamed, encapsulated antenna is to choose a sufficient quantity of foam which, when loaded, would absorb the bulk of the energy in the shock wave before it arrives at the antenna location. The foam selection must be based on electrical transmitting efficiency as well as shock energy absorption capacity. The blast characteristics described in Appendix III indicate that the loading on a structure due to the shock wave

will consist of two parts; the transient or diffraction loading from the arrival of the instantaneous shock peak overpressure, and the quasi-static loading due, in part, to the peak overpressure and, in part, to the wind or drag loading. The bulk of the energy is in the transient peak overpressure wave. The energy in the wind pressure that follows the shock front is severe but much less. Hence, if elastic structural designs were advanced which would withstand the transient loading, the drag loading that follows would normally be of no consequence. However, this may not be true for viscoelastic foams. Reasons should be evident in the ensuing discussion.

This study is concerned with analyzing dynamic response of a hemispherical foamed-plastic structure which is subjected to the intense, external, short-duration load due to the blast wave. In this case, the dominant response involves the effects of stress propagation, elastic and inelastic deformation, and the combined effects of deformation and stress propagation. The analysis should also be capable of predicting severe damage. The loading modes are buckling, bending and pulling of the structural material. If the stress compression wave arrives at an interior interface and reflects as a tension wave from the free surface, short-duration tensile fracturing or spalling of the foamed structure may occur. The material included in the region between the free surface, or interface, and the fracture point may come off as a spall or as a scab. In addition to this type of damage, the passage of intense waves can also produce internal changes. The severe modes of damage are fracture, crushing and tearing away of the material. (23)

3.7.2.1 Viscoelastic Considerations

It is important to accurately describe the stress wave propagation in a material in order to assess some criteria for what actually will occur. Intense stress wave propagation is a complicated, nonlinear phenomenon. Solutions to simple cases of rods and plates under elastic action are the only ones which have been advanced. (17, 18, 19) The assumption that no rate terms are present in the basic stress strain relation leads to unsatisfactory results for explaining the observed behavior of plastics under impact. The only consistent theory as yet developed to handle rate effects is

the linear viscoelastic theory. The basic assumption of small strains in the development, however, makes it very limited in scope. No suitable non-linear viscoelastic theory, which is what is actually needed, has been formulated. ⁽²⁴⁾ The chief difficulty is that one has no stress-strain relation available to predict the true behavior of foamed plastics under the very intense blast loading.

For example, a material that is purely elastic obeys the uniaxial stress law

$$\sigma = E \epsilon \quad (24)$$

where

σ = the uniaxial applied stress

ϵ = the strain

E = the ratio of σ / ϵ , normally called elastic modulus.

However, for a linear viscoelastic material, the relationship involves time differential operators; i.e., the generalized linear equation

$$P \left(a_n \frac{\partial^n}{\partial t^n} \right) \sigma = Q \left(b_n \frac{\partial^n}{\partial t^n} \right) \epsilon, \quad n = 0, 1, \dots \quad (25)$$

where the ratio $P/Q = E$. The value of E is dispersive, i.e., the frequency transform of equation 25 yields

$$\bar{a}_n (i\omega)^n \bar{\sigma} = \bar{b}_n (i\omega)^n \bar{\epsilon} \quad (26)$$

where

$$E = E(i\omega) = \frac{\bar{a}_n (i\omega)^n}{\bar{b}_n (i\omega)^n} \quad (27)$$

$$\bar{a}_n (i\omega)^n = \bar{a}_0 + a_1 (i\omega) + a_2 (i\omega)^2 + \dots, \quad (28)$$

and

$$\bar{b}_n (i\omega)^n = \bar{b}_0 + b_1 (i\omega) + b_2 (i\omega)^2 + \dots, \quad (29)$$

Note that all materials are characterized by their coefficients, a_n , and b_n . The bars above the function signify the frequency transform of that function in the time domain.

The velocity of propagation in these materials, then, is dispersive, i.e., $c^2 = \frac{1}{\rho_0} E(i\omega)$. Upon rapid loading, the high frequency components of the input will travel with markedly different speeds than the lower.

This theory, within the bounds of its assumptions, allows the material strain-rate effects to be explained physically through the motion of dislocations in the body which allow the material to flow plastically and mathematically through the dispersive terms in the generalized model. The distinction of the viscoelastic treatment from the elastic is that time now enters into the relationship explicitly. It can be shown, then, that the equation of motion of the material sections at every point (r, t) in the body obeys the relationship

$$\frac{\partial^2 u}{\partial t^2} = c^2(t) \frac{\partial^2 u}{\partial r^2} \quad (30)$$

as distinct from the equation of motion in a purely elastic body where c is a constant.

3.7.2.2 Thermodynamic Considerations

The linear viscoelastic theory is useful and meaningful if the strains are small, but this is not the case when considering the intense loadings associated with a nuclear burst. Since the nonlinear viscoelastic theory has not progressed satisfactorily, at the present time, a different approach should be considered.

a. Conservation of mass:

$$\frac{\partial}{\partial t} \left(\rho \frac{\partial \mu}{\partial r} \right) = 0 \quad \text{or} \quad \rho \frac{\partial \mu}{\partial r} = \rho_0 \quad (31)$$

b. Conservation of momentum:

$$\rho_0 \frac{\partial^2 \mu}{\partial t^2} = \frac{\partial \sigma}{\partial r} + \frac{\partial}{\partial r} (q) \quad (32)$$

where

$$\frac{\partial \sigma}{\partial r} = \text{elastic force per unit volume, and}$$

$$\frac{\partial q}{\partial r} = \text{viscous force per unit volume.}$$

c. Conservation of energy:

$$\rho_0 \frac{\partial W}{\partial t} = \sigma \frac{\partial^2 \mu}{\partial r \partial t} + q \frac{\partial^2 \mu}{\partial r \partial t} + \frac{\partial Z}{\partial r} \quad (33)$$

where

W = internal energy of an isolated segment of the body,

Z = energy exchange from thermal conduction to outside.

d. Characteristic energy--stress equation:

$$\sigma = f(\rho, W) \quad (34)$$

If equation 33 can be determined, then one can use thermodynamic considerations to evaluate the stress density relationship of the solid. The problem, however, is simplified only when the stresses involved are hydrostatic; otherwise, all of the stress tensor component equations must be satisfied simultaneously with the yielding and rate terms present in the formulation.

If, however, the applied stress is greater than the yield stress, the difference between components is negligible and the assumption of a hydrostatic state is useful. In fact, this is the basis for which experimental determinations of equations of state for measured shock and material velocities have been made. This is to say that the change in internal energy can be determined as a function of the stress propagated into the medium and the correct phenomenological behavior is incorporated into the formulation. This is the thermodynamic approach which has not yet been carried out for foamed plastics. It does, in general, predict that the shock phenomenon in a foam will be similar to that of a shock wave in air, whereas only the attenuation and propagation constants differ.

This approach has particular merit for the encapsulation problem at high pressures where the material strength becomes insignificant and dissipative action is predominant. Restrictive assumptions about the thermodynamic properties are not necessary. However, the linear approach is adequate when the stresses are not as severe.

3.7.2.3 Fracture Prediction

The problem of predicting fractures at low strain rates, where the fractures are brought about by bending or stretching, is usually solved by an elastic analysis utilizing static constants. Fractures associated with spalling occur at high strain rates due to stress waves of high intensity, short duration. However, under rapid plastic flow, the fracture strength usually increases due to internal changes and the localized load could fall to a safe level before the fracture propagates to any appreciable extent. But, one way to protect against spalling is to choose a thick enough viscoelastic medium, such that the compressive wave will be attenuated sufficiently by the time it reaches the free surface. Then the resultant combination of the reflected and incident stresses will be below the fracture stress. Fractures have a tendency to occur at weak points in the material bonding where the atom-atom interaction strength is some value V_{ij} . If the value V_{ij} is expressed as a function of the applied stress, the probability of fracture will be some function of $V_{ij}(\sigma)$. From a consideration of experimentally determined stress propagation histories in various sections of a structure, the region of fracture can be predicted. ⁽²³⁾

The analysis of what takes place during transient loading, while difficult, is not impossible. Even where viscoelastic theories become inadequate, hydrodynamic analysis methods are useful. The major difficulty in evaluating the response of a foam material to a nuclear blast input lies not in the analysis method, but in the lack of sufficient testing data on foamed plastics.

3.7.2.4 Foam Selection for Encapsulation

Foams and their properties have been discussed in Section 3.2. The cushioning data on foam is summarized in Appendix IV. The important consideration is that the static and dynamic behaviors of foams are markedly different. Both the static and dynamic stress strain curves possess elastic and viscous flow regions, but the dynamic curves have more hysteresis or energy absorption in compression set. The elastic yield stress for foams is directly proportioned to the density. Low density foams, for example,

have very low elastic yields and for that reason are suitable for cushioning even the smallest objects. High density foams will cushion, but only if the elastic stress limit is exceeded. Whether high or low density foam is used, the prime consideration, as far as the encapsulation problem is concerned, deals with the magnitude of the stress propagated through the foam back to the antenna location. A pure elastic wave suffers no attenuation. However, in a viscoelastic foam medium, the stress will most likely be attenuated exponentially. The dispersive behavior of solid plastic rods of polyurethane and polystyrene has been observed but not for the foams of those plastics (references 19 and 25). The observed stress-strain relations are similar to that of a standard linear solid (Appendix II). These curves are somewhat useful for assessing foam behavior since the limiting case of a high density foam is a solid. It can be concluded that all foams are viscoelastic in nature, but when subjected to intense input stresses, they are likely to be non-linear also.

The limiting energy absorption capacity of cushioning foams thus far observed is about 10^4 ft-lbs/ft³ (Appendix IV). However, from the considerations of the energy from a nuclear bomb (see Figure III-11, Appendix III), it is seen that about $10^6 \frac{\text{ft-lb}}{\text{ft}^2}$ of shock energy is available, even at the 10 psi overpressure range. This means that if the foam uniformly absorbed the total energy, a structural thickness of about 100 feet of foam would be required. On the basis of the analysis of small impact stresses in semi-infinite viscoelastic rods (see Appendix II), the stress distribution will obey an exponential law of the form $\exp - \frac{E}{2\eta} \frac{x}{c}$ where E is the elastic modulus, η is the viscosity, c is the speed of propagation of sound in the rod, and x is the lineal dimension. If the stress at any point in the rod $\sigma(x, t)$ exceeds ultimate, there exists a probability for failure to occur at that point and that time.

To over-simplify the problem in order to get an insight to the energy absorption phenomenon, suppose $\sigma(x, t)$ is proportional to $\sigma(0, t)e^{-xE/2\eta c}$ where $\sigma(0, t)$ is the loading on the free end due to a step impact at $t = 0$. The energy dissipation, ϕ^* , per unit volume at a position x in a Maxwellian type rod, due to the step input, is given by:

$$\varphi(x) = \int_0^{x/c} \frac{\sigma^2(o, t)}{\eta} I_0 \left(\frac{E}{2\eta} \sqrt{t^2 - x^2/c^2} \right) \exp \left\{ -\frac{Et}{\eta} \right\} dt \quad (35)$$

where I_0 is the zero order Bessel function of imaginary argument. This integral is not readily amenable to solution. However, if it is assumed that $t = x/c$, then $I_0 = 1$, and

$$\begin{aligned} \varphi^*(t = x/c) &= -\frac{\sigma^2(o, t)}{E} \left(\exp \left\{ -\frac{Ex}{\eta c} \right\} - 1 \right) \\ &= \frac{\sigma^2}{E} (o, t) \left(1 - \exp \left\{ -\frac{Ex}{\eta c} \right\} \right) \end{aligned} \quad (36)$$

The important aspects here deal with exponential absorption versus the linear dimensions. If the exponential factor $\frac{-E}{\eta c}$ is very small, i.e., the material highly absorbs, then for large x , there will be no concern for spalling effects at the far extremities of the material. However, failure may occur near the surface of incidence. On the other hand, if the factor $\frac{-E}{\eta c}$ is large, then spalling will be very likely at the inner free surface; i.e., the foam-antenna interface.

The most promising foam for encapsulation would seem to be the former case which is most suggestive of low density foam. The fact that spalling may occur in the latter case also implies that the stress at the foam antenna interface will be excessive.

The difficulty with equation 36 is that it is not readily adaptable to predictions for a hemispherical configuration. The transient loading will probably be absorbed just the same as the rod, i.e., in a small surface segment as equation 36 suggests, but the quasi-static, or uniform, drag loading that follows the transient loading is a different phenomenon. Another facet for consideration is that in linear viscoelastic theories, ideal viscoelastic models are chosen. A model for foam must await experimentation. Thus, the values of c , E , and η , which are representative of an arbitrary foamed plastic with which to compute the attenuation factor, are not available. Existing data on foams are too incomplete to determine these dispersive constants. Even in the static case, when the yield stress is exceeded, time should enter into the analysis to account for the viscous energy absorption.

Present static treatments, by intent, do not contain time as a parameter.

3.7.2.5 Feasibility of Encapsulation Configurations

Positive feasibility of hardening an antenna by encapsulation with foam is not resolvable with the data available. On the basis of uniform energy absorption, the concept would involve unreasonable dimensions (100 feet) even at low overpressures of about 10 psi because the limiting energy absorption capacity of foamed plastics is about 10^4 ft-lb per cubic foot. But foams are more likely to yield exponential absorption. When the blast loading characteristics are considered, the foam, because of stress propagation effects, will absorb the transient load but transmit, with less attenuation, the quasi-static drag load. The quasi-static drag load will not be attenuated by the same exponential factor as the reflected overpressure or transient load. Again, no treatment is available for a static deformation analysis to assess what that quasi-static factor is. However, some rules of thumb can be derived. Since the yield stress varies directly with density and the loading must be such that the load exceeds the yield to get absorption, the selection of a low density foam for encapsulation configuration is likely. This insures that plastic flow deformation will occur in the foam and the elastic wave will undergo attenuation as it propagates through the foam. For high overpressure regions, some of the lower valued "high density" foams may be applicable, although low density foams should always work better.

High density, rigid foams are, in general, not suitable for encapsulation applications since they are expected to transmit the quasi-static load elastically. The issue of what density to use cannot be resolved until additional test data are available. The antenna, by being in contact with the foam, is vulnerable if an overpressure stress in excess of the antenna design value arrives at the antenna interface. The encapsulation concept requires an exact account of a foam's response to a nuclear blast, an accurate description of the loading, and a careful consideration of the geometry. All of these considerations are, within the present state-of-the-art, impossible to handle without controlled experimentation.

3.7.3 Thick-Shell Approach

Thick shells in the shape of bodies of revolution avoid one problem of the complete encapsulation concept. The shell can be permitted to deflect under the applied blast load without damage to the antenna provided a sufficient space is left between the shell and the antenna to preclude contact. The design of the protective system is then reduced to the problem of survival of the shell.

From an analytical standpoint, a hemispherical dome consisting of a single uniform and homogeneous shell is the simplest to analyze. Foamed plastic material is necessary for efficient R. F. transmission through the shell, but a composite dome consisting of a reinforced concrete shell and a foamed plastic R. F. window in the path of the antenna beam would probably be more economical to build. The discontinuities at the edge of the window complicate the analysis and design of a composite structure. In both cases, the shell can be designed to act in either the elastic range or in the visco-elastic range.

3.7.3.1 Thick Shell Design Considerations

The design concept chosen for this preliminary study simplifies the structural analysis. The objective of the study is to develop an approximate method and a tentative approach to the design problem in spite of the incomplete data now available on the various plastic materials. A hemispherical shell constructed of a foamed polyurethane plastic having property values chosen arbitrarily from the range of values given in the available data was selected for investigation. The method used is described briefly in the next section.

3.7.3.2 Simplified Stress Analysis

The analysis method in this preliminary design study consisted of three axial solution for idealized and simplified shell structures. The prototype dome design would be based on the results of the trial which gave the highest stresses in the material. Material property values were assumed on the basis of reasonable values obtained from published data. Both the structural response and the blast loading were simplified and idealized to permit

elastic-type solutions. Plastic deformations were not considered. However, the viscoelastic arguments applying to total encapsulated bodies should apply equally well to a thick shell.

A hemispherical dome resting on and restrained by a rigid foundation was analyzed. Material properties were assumed for the study as follows:

| | |
|------------------|-----------------------------|
| Young's Modulus | 10,000 lbs/in. ² |
| Allowable Stress | 800 lbs/in. ² |
| Poisson's Ratio | 0.15 |
| Density | 25 lbs/ft. ³ |

The structure was assumed to act linearly; thus, permitting superposition of stresses. Three trial approximations were made to consider how the shell would respond to three different modes. The first mode of interest was a dome restrained at the base and subjected to a uniform external pressure. The pressure load was assumed to be the maximum overpressure due to the blast wave, exclusive of reflection effects due to the dome. In other words, the pressure was the sum of the maximum free field overpressure and the dynamic wind overpressure. Effects due to the actual nonuniform distribution of the dynamic overpressure were neglected. Considering the effects of both membrane action and bending action in the restrained thick shell, the model showed that a thickness of approximately 81 inches was required.

The second approximation investigated the elastic stability of the model defined by the first approximation. The critical buckling stress was determined and compared with the stress induced by the uniform load of the first approximation. By this criterion, the shell thickness found in the first approximation was inadequate. The shell was then revised to a thickness of approximately 140 inches.

The third trial approximation investigated the effects of the transient impulsive loading due to the reflected overpressure component which had previously been neglected. The natural period of the dome vibrating in the fundamental mode was determined roughly by means of classical expressions. A more correct approach using an energy solution and assumed mode shape was setup, but was not carried to a solution because of time

limitations. A dynamic load factor was calculated to permit replacing the impulsive load with an equivalent static load. The solution of this approximation showed the criterion of elastic stability investigated in the second approximation to be critical for the simplified assumptions used. The detailed calculations of all three approaches are given in Appendix V.

3.7.3.3 Summary

The simplified analysis performed in this study has led to a significant conclusion. The study indicates that an approximate elastic solution is possible. It further indicates that the solution is a conservative one since foams are viscoelastic, not elastic, materials. Assumptions or numerical constants, which should be checked and improved, include the following:

- a. Material properties
- b. Possibility of separating transient and quasi-steady-state pressure load
- c. Uniform pressure distributions
- d. Neglect of shell shear stresses implicitly in (c)
- e. Validity of the criteria for elastic stability
- f. Effects of compression wave stress reinforcement and reversals due to propagation of the wave through the material.

The methods developed for a homogeneous shell can be extended in principle to a composite concrete and foam shell. Local effects at the material interfaces, however, must then be evaluated carefully.

3.7.4 Foundation Requirements

3.7.4.1 Design Philosophy

The foundation design considerations for any arbitrary structure will involve the dead load of the structure (weight), the dynamic or static applied loads, the earth pad or soil where the footing is to be set, and the ground movement or shock, if envisaged. The structures normally encountered in foundation work are elastic structures, i.e., structures whose stress-strain response is predominantly elastic. Thus, loads on these structures are transferred through elastic deformation to the foundation pad. Any

inelastic deformation results in energy absorption in the structural material and, consequently, cannot be transferred to the foundation. In other words, only the elastic stresses or loads are transferred to the foundation.

This is an important consideration for designing foundations for foam radomes which will experience dynamic loads. If the response of the foam to the dynamic load is highly inelastic, and if the foam structure is of sufficient thickness between the loading surface and the foundation line, the foundation will experience but a fraction of the dynamic load. Only the unattenuated portion of the elastic stress wave will be transferred to the base. This means that the foam response to a dynamic loading must be clearly defined before a foundation can be designed. The foundation for a foam structure to contain the dead loads involves a straight forward design approach. It is the consideration of the dynamic loading and the foam response to the dynamic loading that complicates the foundation design analysis. Dynamic loading refers in this problem to the nuclear mechanical shock overpressure wave.

It should be concluded that foamed plastic structures under dynamic loading will impose less foundation requirements than similar elastic structures due to the energy absorbing mechanisms. However, it is premature without the foam stress-strain response to specify what the foundation design should be. The foundation design, based on the dead load, would be too optimistic, and the design based on the dynamic load, assuming a purely elastic response, would be highly unreasonable.

It should be pointed out that foundation engineering has, thus far, been restricted to foundations for structures subjected to normal environments; i.e., large static but small dynamic loads. Even for pure elastic structures, a large dynamic loading from high energy shock waves or earthquakes introduces complications into the analysis for foundation design which are not analytically resolved. Rather, these complications are circumvented by a qualified foundation engineer's experience with such problems. The consideration of what happens at a foamed plastic foundation interface has been neglected, although it will introduce complications into a stress analysis. However, the magnitude of this problem is speculative until a firm

understanding of foam response to nuclear shock loading has been achieved. Also, the problem of the geological conditions for an arbitrary site location is exemplified in the footing analysis of the following section, 3.7.4.3.

3.7.4.2 Foundation Design Rules

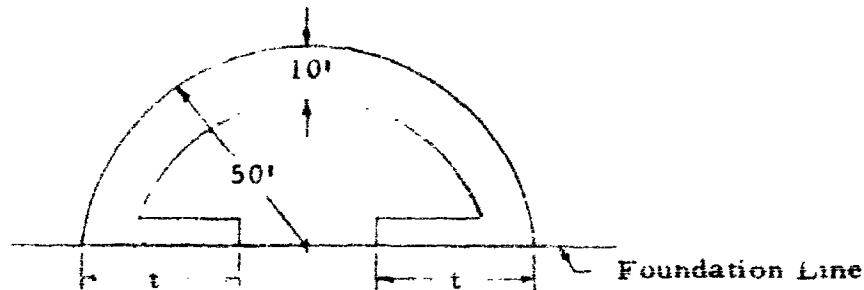
A blast wave traveling in the horizontal direction will tend to cause sliding and rotation of the dome. Foundation design must be such as to support both the dead load and the live load and to prevent or to limit the shock wave from contacting or excessively displacing the protected antenna.

Passive pressure on the vertical faces of the foundation and soil friction compose the resistive forces to the structure's sliding motion. It is, therefore, desirable to obtain a large resistive surface. In cases where maximum surface is required, deep beam floor slabs and auxiliary foundation struts are plausible. In all types of buildings, the horizontal blast loads tend to overturn the structure, thereby causing unequal pressure distribution on the foundation with higher pressures occurring on the leeward side. Since frictional forces are proportional to foundation pressure, the resistance at the blast approach side of the structure is small relative to that of the leeward side. This difference in frictional resistance at the footing, or base, makes it necessary to design for continuous load capacity across the structure. This permits transfer of forces to the leeward footing where the passive soil pressure can react to the sliding load. For a thick-shell configuration, the overturning tendency can be neglected because of the moment dead-weight relationship.

3.7.4.3 Footing Calculations

A rough approximation for sizing the footings is obtained from the total load equal to the dead load plus live load, where the instantaneous live load will be assumed as an equivalent static load and equal to the maximum blast pressure. The line, in the sketch below, at the foundation is considered as the interface between the thick-shell base and the footing. No allowance is made for ground motion since, under most geological conditions, the air blast and ground shock do not arrive simultaneously and

normally are not additive.



The thick-shell configuration for protecting a 30 ft. antenna is envisaged as a 50 ft. radius hemispherical shell with a foam or shell thickness of approximately 10 ft. The vertical live load will be given by

$$V. L. = P_{\max} \times A_b \quad (37)$$

where P_{\max} = maximum external design pressure equal to 154 psi and A_b = surface area = $2500 \pi \text{ ft.}^2$.

$$\therefore V. L. = 1.74 \times 10^8 \text{ lbs.} \quad (37a)$$

The dead load is the weight of the foam. If 25 pcf foam is used, 2×10^6 lbs. will be the dead load which can be neglected.

The total bearing area $\approx \pi (R - (R - t)^2)$, If $t = 30 \text{ ft.}$,

$$B. A. = 2100 \pi \text{ ft.}^2 \quad (38)$$

The stress at the base is then $\frac{V. L.}{B. A.}$ or

$$\sigma_{\text{base}} = \frac{P_{\max} A_b}{A_b} = 154 \text{ psi} \times \frac{2500 \pi}{2100 \pi} \approx 185 \text{ psi} \quad (39)$$

or, in terms of psf (pounds per square foot),

$$\sigma_{\text{base}} \approx 2.66 \times 10^4 \text{ psf} \approx 13 \text{ tons/ft.}^2 \quad (40)$$

The allowable bearing capacity of foundation footings are given in Table 2. Note that some rock content in the foundation appears mandatory from this data. However, it is not suggested that this be conclusive until more refinement in the analysis can be made. The validity of treating the instantaneous dynamic load as a static load has not yet been justified.

TABLE 2
Allowable Bearing Capacity*

| <u>Foundation Material</u> | <u>Tons per sq. ft.</u> |
|--|-----------------------------|
| Hard sound rock | 100 |
| Soft rock | 12 |
| Hardpan overlying rock; very compact clay, sand and gravel | 10 |
| Compact, sandy gravel; very compact clay, sand and gravel | 6 |
| Firm, sandy gravel; compact clay, sand, gravel | 5 |
| Loose, sandy gravel; firm, coarse, or medium sand | 4 |
| Loose, coarse, or medium sand; compact, fine sand, stiff clay | 3 |
| Firm, fine sand; compact inorganic silt, firm sand, clay soil | 2 |
| Loose, fine sand; firm inorganic silt | 1-1/2 |
| Loose, sand-clay soil; loose, inorganic silt, soft clay | 1 |

* From Building Code of the City of Detroit - 1955 Edition

Furthermore, on the basis of a foamed-plastic structure, it is likely that the required bearing capacity computed in this analysis is conservative.

3.7.4.4 Summary

A foundation design for a hardened, foamed structure is not warranted since the foam response to dynamic shock loadings is unknown. This essentially results from the uncertainty of: (1) the elasticity of the foam to the dynamic shock overpressure loading, and (2) the optimum hardening philosophy. Both are to be resolved in future work. Yet, once the foundation geometry and the material response are known, a foundation design can be advanced according to the state-of-the-art techniques. (20, 21)

3.8 ELECTRICAL SYSTEM TRANSMISSION EXPERIMENTS

3.8.1 Objectives of Experimental Program

The electrical operational characteristics of an antenna encapsulated in a foam or insulation medium must be evaluated to ascertain that a pre-blast encapsulation hardening configuration suitable for nuclear blast resistance is compatible from electrical aspects. The program was designed to determine, by scale model experimentation and analysis, the effects of encapsulation on the electrical efficiency of a 30-foot antenna. The required measurements were:

- a. Pattern measurements with and without the encapsulated foam.
- b. VSWR changes in the feedhorn termination.
- c. Gain reduction from the inclusion of the foamed dielectric.
- d. The boresight shift.

3.8.2 Predicted Results

The operational electrical characteristics of an antenna system totally encapsulated in a dielectric medium will be altered for the following reasons:

- a. The far-field pattern of the antenna will be shifted and distorted in a manner depending upon the shape and dielectric constant of the encapsulating material.
- b. The addition of the encapsulating dielectric medium will add an attenuation constant reducing the gain of the antenna system.

- c. The VSWR at the aperture of the feedhorn will be altered due to reflections from the interface of the dielectric medium and air. However, reflections of the interfaces remote from the feedhorn will be reduced by the space attenuation and by the attenuation constant of the dielectric medium. The interface that will be dominant in producing reflections may possibly act with the feedhorn aperture VSWR in such a manner as to reduce the overall VSWR. Where two discrete mismatches are present in a transmission system, the maximum possible VSWR is the product of the individual VSWR's and the minimum possible VSWR is the quotient of the two individual VSWR's.
- d. The maximum power handling capability of the antenna system will be altered by two factors. First, an increase in VSWR at the aperture of the feedhorn will increase the voltage maximum along the transmission line and thereby increase the chances of arcing in the waveguide. If the addition of the dielectric material does not increase the VSWR of the feedhorn above its design limits, this problem is of little consequence. The second limit in the power handling capability of the antenna system is the maximum temperature rise of the dielectric material. This limit is due to the heat dissipation properties of the dielectric material and is placed below the temperature where the dielectric material will change its physical or electrical properties.

3.8.3 Scale Model

The antenna system used in the investigation of the encapsulation effects was a scale model of a 30-foot diameter circular, parabolic antenna with a 137.5 inch focal length operating at 2400 mc. By maintaining a constant ratio of distance to wavelength, the antenna system may be scaled without altering the gain, far-field pattern or total attenuation. A scale factor of five was used such that the reflector diameter was reduced to six feet and the operating frequency increased to 12 kmc. The encapsulating material used was 2 lb/ft.³ foamed polystyrene with a measured

dielectric constant (ϵ_R) of 1.026 and a measured loss tangent ($\tan \delta$) of 0.00025. The details of the measurements and calculations of the dielectric constants are given in Appendix VII.

3.8.4 Boresight Shift Analysis

The far-field pattern distortion and boresight shift of such an antenna system as described in 3.8.3 and encapsulated in the dielectric material may be estimated by determining the phase front alteration produced by the dielectric material and its configuration.

First to be considered is the refraction of the individual rays across the reflector aperture. Snell's refraction law for an air dielectric interface is given by $\sin \phi = k \sin \psi$, where ϕ is the angle of incidence at the air dielectric interface with respect to the normal to the surface, ψ is the angle of refraction at the same point with respect to the normal to the surface, and k is the ratio of the propagation constant of the dielectric to that of the air. For the material used in this investigation, k is approximately 1.013. The phase front distortion produced by this k in the configuration shown in Figure 15 is negligible.

The second consideration is the distance each ray across the reflector aperture must travel to a point of constant phase outside of the encapsulation. The distorted phase front will be the surface described by points where the number of wavelengths traveled by each ray from the aperture plane through the dielectric and air is constant.

Referring to Figure 16, which describes the motion of the ray front,

$$N = \frac{X_d}{\lambda_d} + \frac{X_a}{\lambda_o} = \frac{R \cos \theta_A}{\lambda_d} \quad (41)$$

$$X = X_d + X_a \quad (42)$$

combining equations (41 and 42)

$$X = X_d + \lambda_a \left[\frac{R \cos \theta_A}{\lambda_d} - \frac{X_d}{\lambda_d} \right] \quad (43)$$

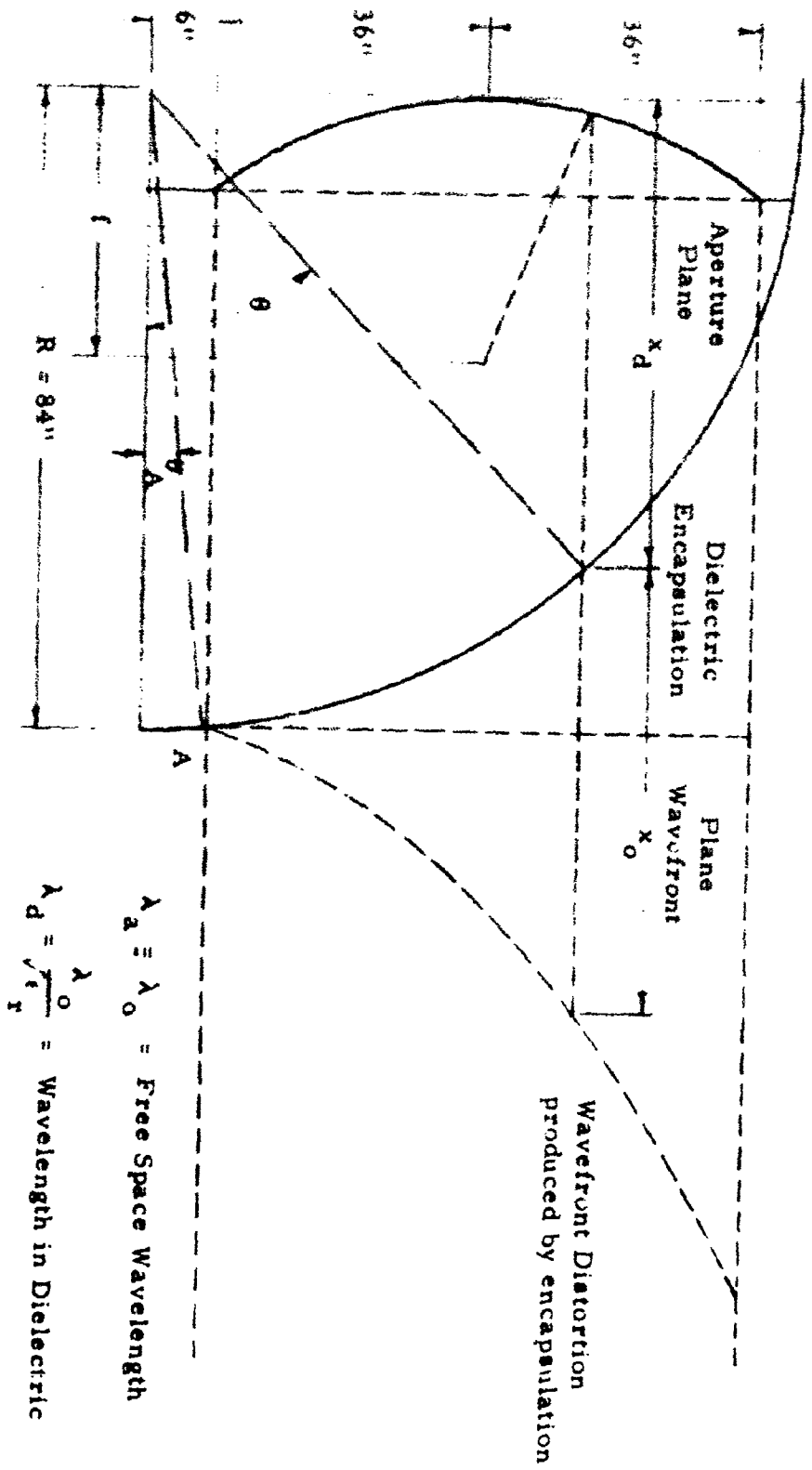


Figure 15 - Effect of Encapsulation on Wavefront

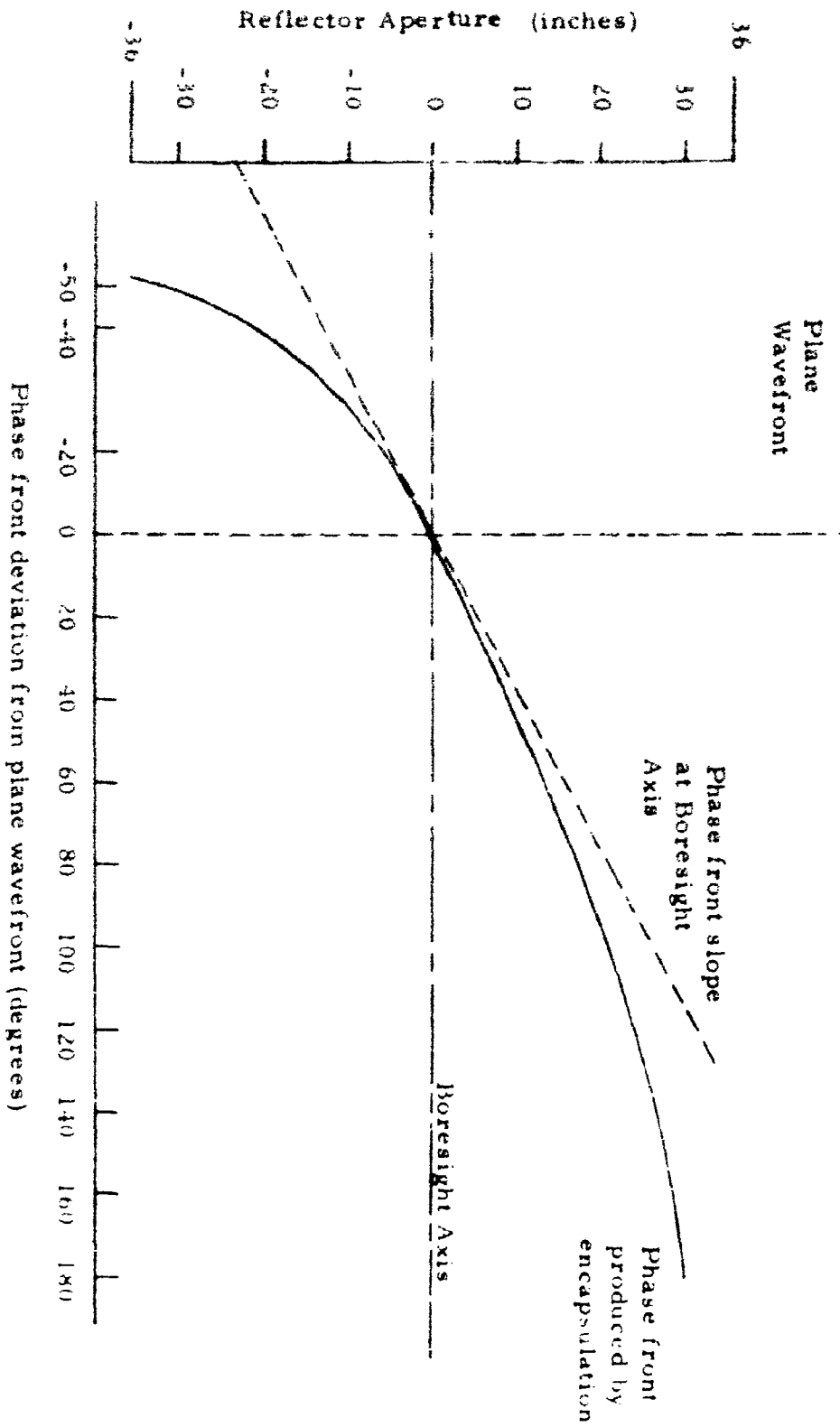


Figure 1b - Calculated Phase Front Produced by Encapsulation

From Figure 15, it is clear that $X_d = R \cos \theta$. Therefore,

$$X = R \cos \theta + \frac{\lambda}{2} \left[R \cos \theta_A - R \cos \theta \right] \quad (44)$$

Figure 16 shows the calculated phase front deviation with respect to the ideal plane phase front and the boresight axis of the antenna reflector. The portion of the phase front curve having the major influence on the boresight shift is that intersecting the boresight axis. The slope of the phase front curve at the boresight axis is 32° per foot or a total of 192° across the reflector aperture. The boresight shift angle (α) is a function of the displacement of the feed location, δ , of a parabolic reflector as seen by the boresight shift equation

$$\alpha = B. F. \tan^{-1} (\delta/f) \quad (45)$$

where

B. F. = the beam deflection factor, and

f = the focal length of the dish

and the phase front is also a function of δ (see Appendix VIII). By finding the δ that produces the same boresight phase front slope as is produced by the encapsulation dielectric material, the boresight shift α may also be found.

This is carried out in detail for the scale model in Appendix VIII and δ was found to be approximately 0.4 inches. For the parabolic reflector used in the scale model tests, the focal length f was 27.5 inches, the focal length to diameter ratio f/D was .382, and the beam deviation factor, B. F., for the illumination taper used in the tests was approximately 0.85. Substituting into the boresight shift equation, (45), and solving for the theoretical boresight shift, α ,

$$\alpha = B. F. \tan^{-1} \left(\frac{\delta}{f} \right) = .85 \tan^{-1} \left(\frac{.4}{27.5} \right) = 42.42' = 0.707^\circ \quad (45a)$$

3.8.5 Dielectric Attenuation Factor

The attenuation factor for the encapsulating dielectric material is dependent upon the material loss tangent, $\tan \delta$, its relative dielectric

constant, ϵ_R , and the operating wavelength, λ_o , in the following manner:

$$\alpha = \frac{8.686 \pi \sqrt{\epsilon_R} \tan \delta}{\lambda_o} \frac{\text{DB}}{\text{ft}} \text{ with } [\lambda_o \text{ in feet}] \quad (46)$$

The values for the foam used in the investigation were:

$$\epsilon_R = 1.026, \tan \delta = 0.00025, \text{ and } \lambda_o = 0.0819 \text{ ft. (X-band)}$$

Substituting these values into equation 46, one obtains

$$\alpha = 0.0844 \frac{\text{DB}}{\text{ft}} \quad (46a)$$

The total distance, S , from the focal point to the reflector and back to the surface of the encapsulation along the boresight axis for the scale model antenna is 8.3 feet. The attenuation, as a result of propagation through the encapsulation, is:

$$\alpha_T = \alpha S = 8.3 \text{ ft.} \times 0.0844 \frac{\text{DB}}{\text{ft}} = 0.70 \text{ DB} \quad (47)$$

3.8.6 Power Dissipation in Dielectric

The maximum power dissipated per unit volume (P_d) in the dielectric will be immediately in front of the feedhorn. At any point in this vicinity, the incident power, P_i , per unit area is given approximately by:

$$P_i = \frac{PG}{4\pi R^2} \quad (48)$$

where

P = total power radiated from the feedhorn

G = gain of the feedhorn

R = distance between the feedhorn and dielectric along the boresight axis

The power density transmitted through the first unit distance (d) in the dielectric will be given by:

$$P_o = P_i \left[10^{-\alpha d/10} \right] \quad (49)$$

The power dissipated in the first unit volume is given by:

$$P_d = \frac{PG}{4\pi R^2} \left[1 - 10^{-\alpha d/10} \right] \quad (50)$$

where

$$\alpha = \frac{8.686 \pi \sqrt{\epsilon_R} \tan \delta}{\lambda_0} \frac{\text{DB}}{\text{IN}} \left[\lambda_0 \text{ in inches} \right] \quad (51)$$

As an example of the probable magnitude of the maximum dissipated power in the dielectric of a full-scale antenna system, the following typical values are assumed:

$$\begin{aligned} \epsilon_R &= 1.026 & G &= 10 \\ \tan \delta &= 0.00025 & P &= 20,000 \text{ watts} \\ \lambda_0 &= 4.917 \text{ inches} & R &= 36 \text{ inches} \\ f_0 &= 2.4 \text{ kmc} & d &= 1 \text{ inch} \end{aligned}$$

One obtains:

- a. For α ; $\alpha = .001405 \frac{\text{db}}{\text{in}}$, and
- b. For the dissipated power per unit volume

$$P_d = 0.00368 \frac{\text{watts}}{\text{in}^3}$$

Since this is the maximum dissipated power in the dielectric, it can be seen that the power handling problem would not be difficult to circumvent for low dielectric-low loss materials. Also, the dissipated power in the dielectric material may be further controlled by the separation distance between the feedhorn aperture and the dielectric air interface.

3.8.7 Scale Model Transmission Testing Results

3.8.7.1 Description of Tests

A six-foot diameter circular parabolic reflector with a f/D ratio of .382 was used in making the encapsulated antenna tests. Polystyrene foam of 2 lbs/ft.³ density was used for the tests. The foam was purchased in slabs and assembled in front of the testing dish with the exterior surface cut into an approximate spherical contour of curvature .14 ft.⁻¹. The assembly, before it was placed on a tower for antenna measurements, is shown in Figures 17 through 19. The antenna transmission tests were made with this assembly atop a 25-foot tower. The characteristics of the

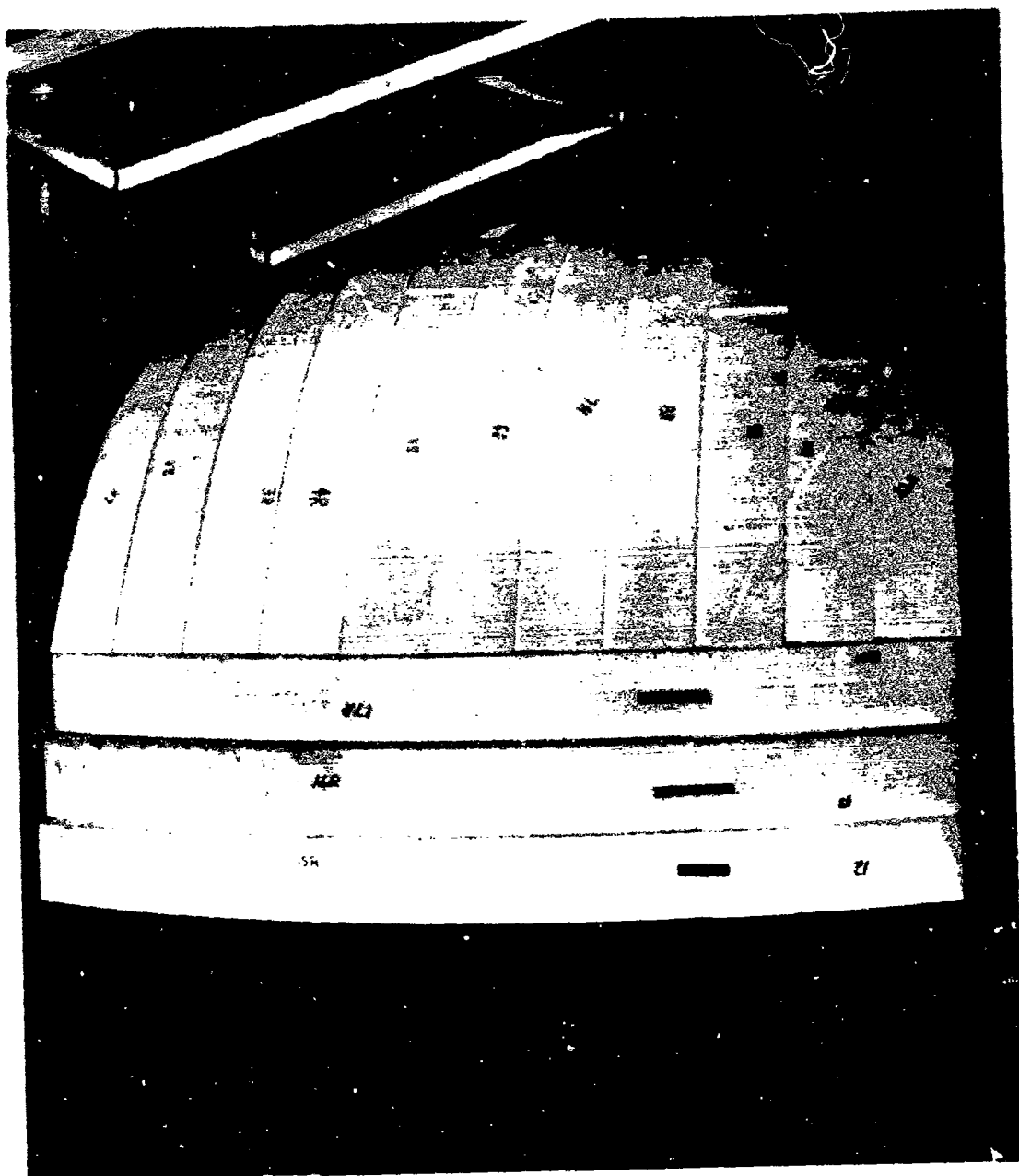


Figure 17 - Pre-Test Assembly - Side View (Left)

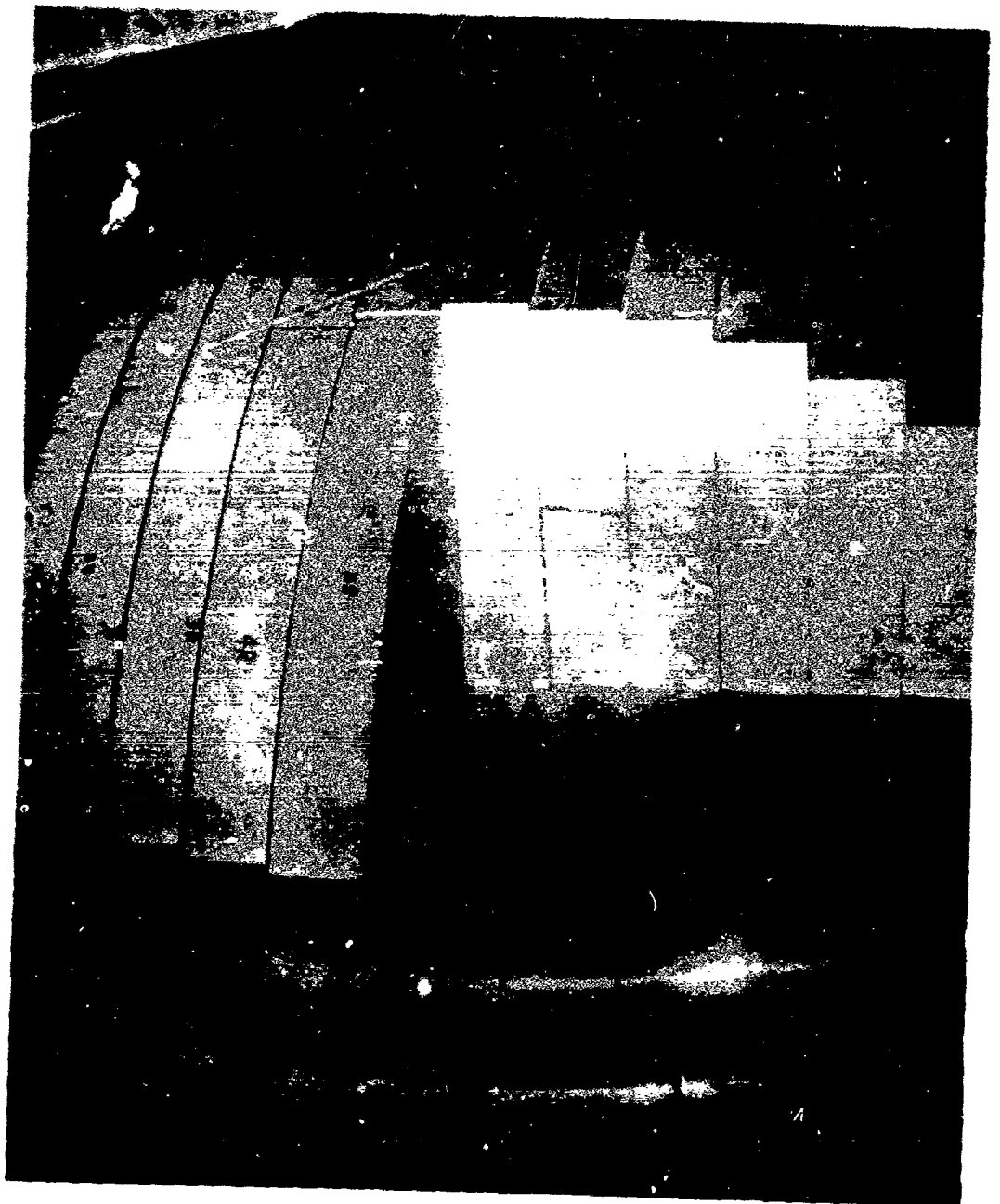


Figure 18 - Pre-Test Assembly - Cutaway View

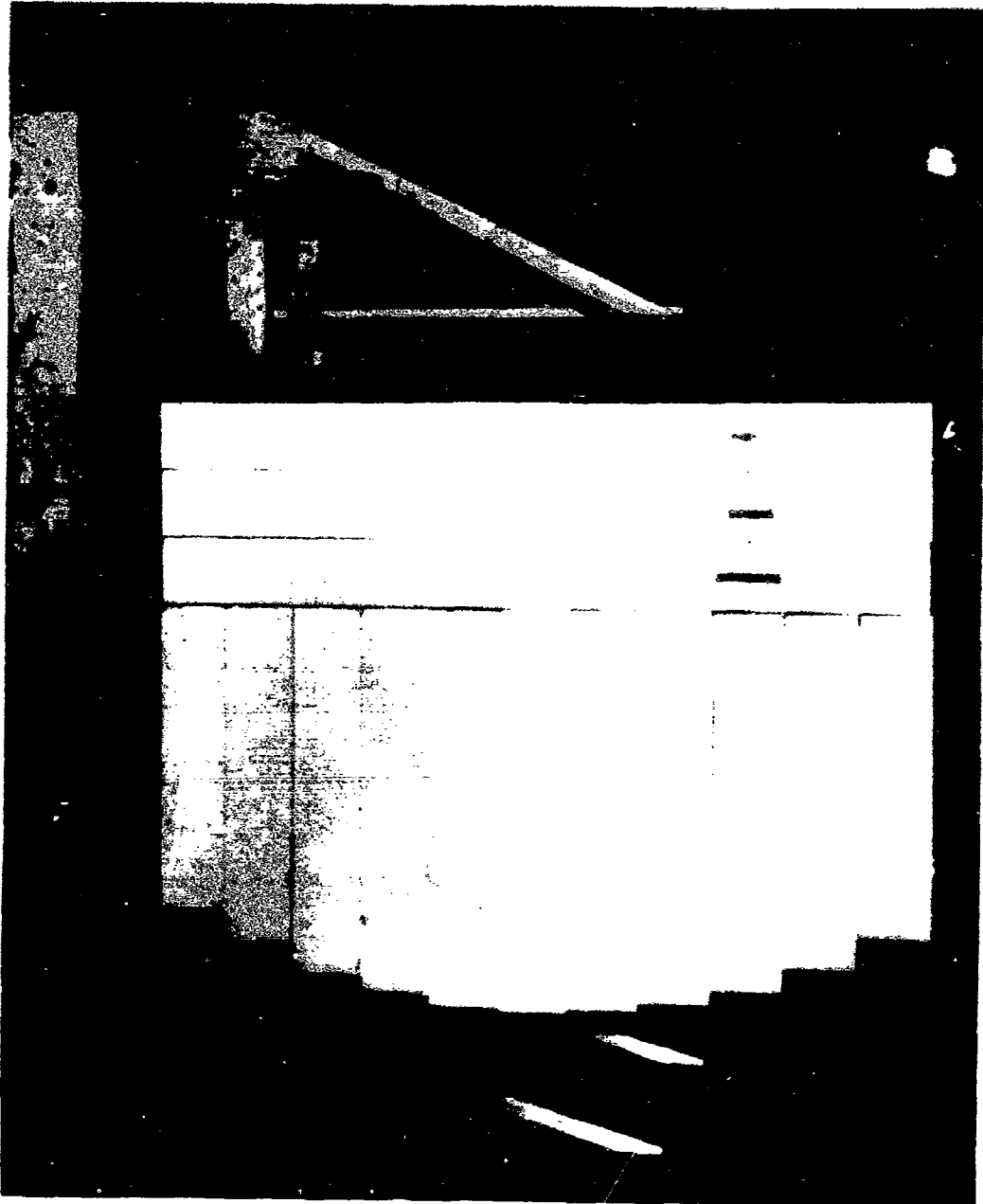


Figure 19 - Pre-Test Assembly - Side View (Right)

feedhorn designed for these tests were determined in the anechoic chamber. Edge illumination of the reflector with the feed pattern used was approximately -18 DB. The measured characteristics of this reflector, without the foamed dielectric encapsulation, are given in the tabulated data of Section 3.8.7.3. The measurements were always made with and without the foamed encapsulation in order to assess the relative effects of the addition of the dielectric on the dielectric-free antenna characteristics. The arrangement of the foam with respect to the reflector dish and the axis of rotation is shown in Figures 20, 21 and 22.

3.8.7.2 Measurement Accuracies

The accuracies of the measurements given in the tables and charts of Section 3.8.7 are as follows:

| | |
|----------------------------|--------------------------|
| Frequency | $\pm .1\%$ |
| Relative azimuth angle | $\pm .5\%$ of full scale |
| VSWR | $\pm .02$ |
| Gain | $\pm .5$ DB |
| Pattern calibration points | $\pm .1$ DB |

3.8.7.3 Tabulated Data

| <u>Measurement</u> | <u>Unencapsulated Antenna</u> | <u>Encapsulated Antenna</u> |
|--------------------|-----------------------------------|---------------------------------|
| Gain | 41.3 DB | 42.2 DB |
| VSWR | 1.1 : 1 | 1.05 : 1 |
| Boresight Axis | Reference Axis | Shifted C. W. .66° |
| -3 DB beamwidth | | |
| E-Plane | 1.2° | 1.2° |
| H-Plane | 1.35° | 1.2° |
| E-Plane | | |
| 1st Sidelobe Max. | -20.2 DB | -14.5 DB |
| H-Plane | | |
| 1st Sidelobe Max. | -24 DB | -14.5 DB |
| Cross-Polarization | | |
| Maximum | -16.3 DB | -14 DB |

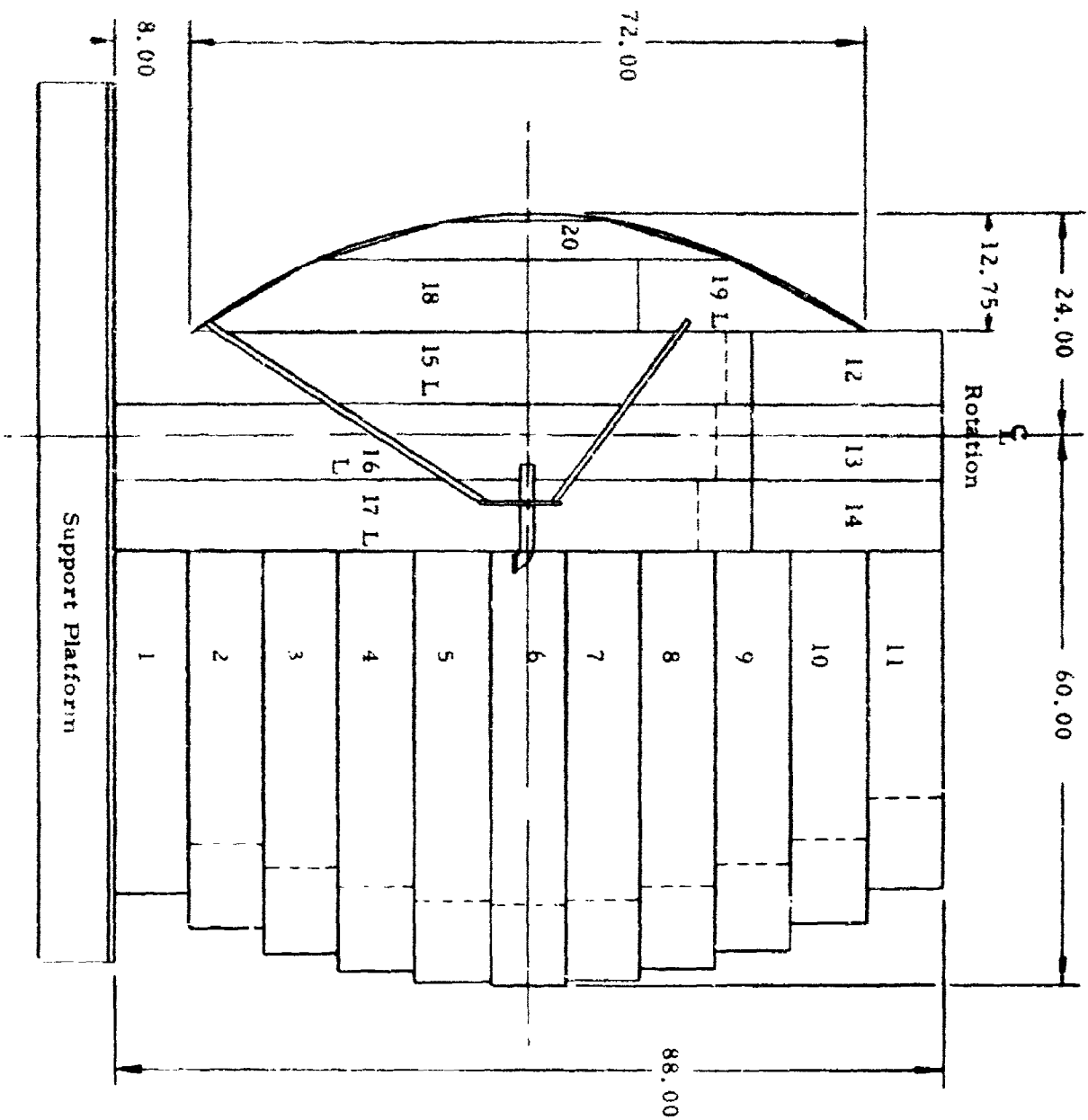
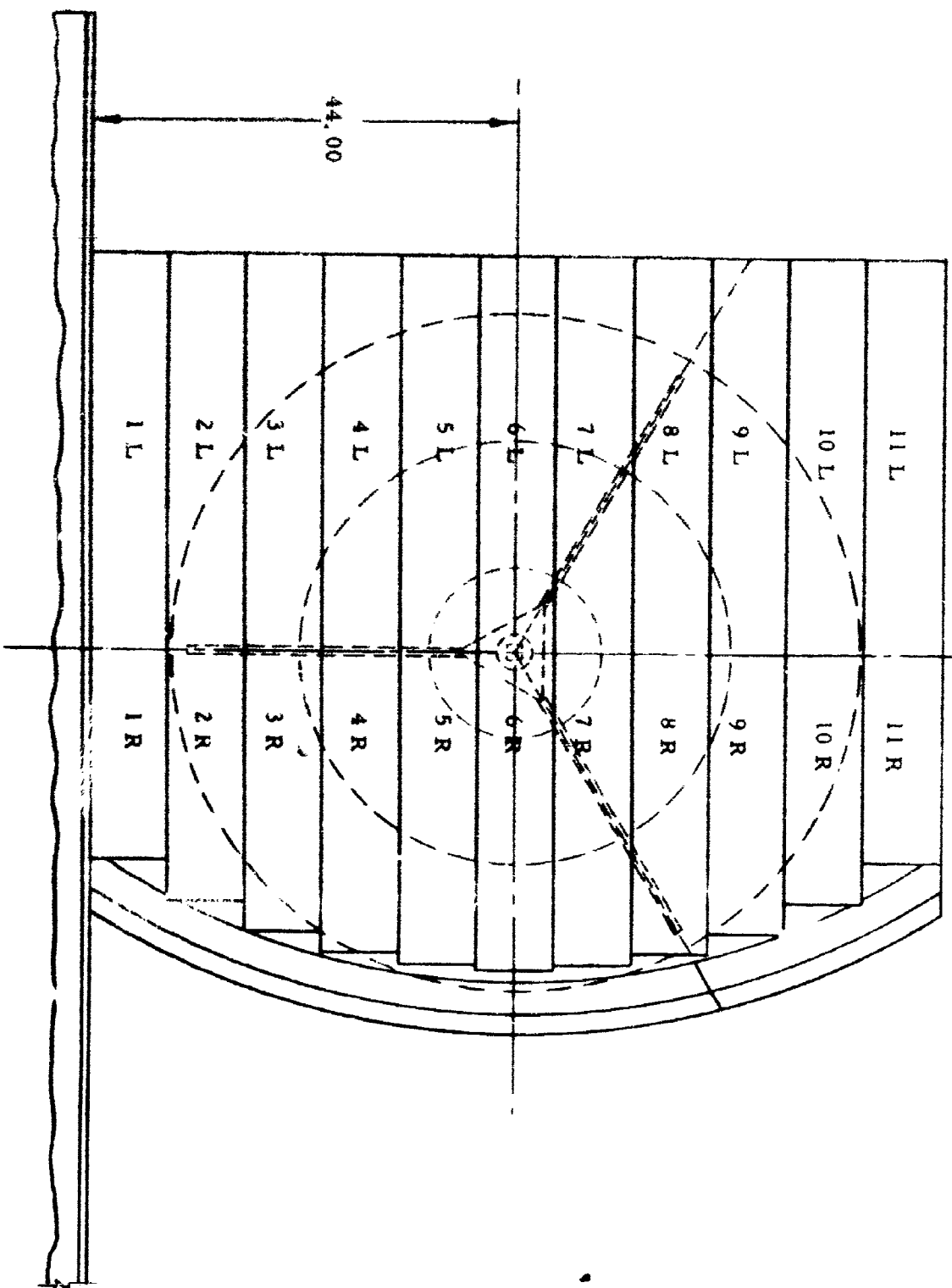


Figure 20 - C. W. Side View - Scale Model Antenna Encapsulation Configuration

G_L
Rotation



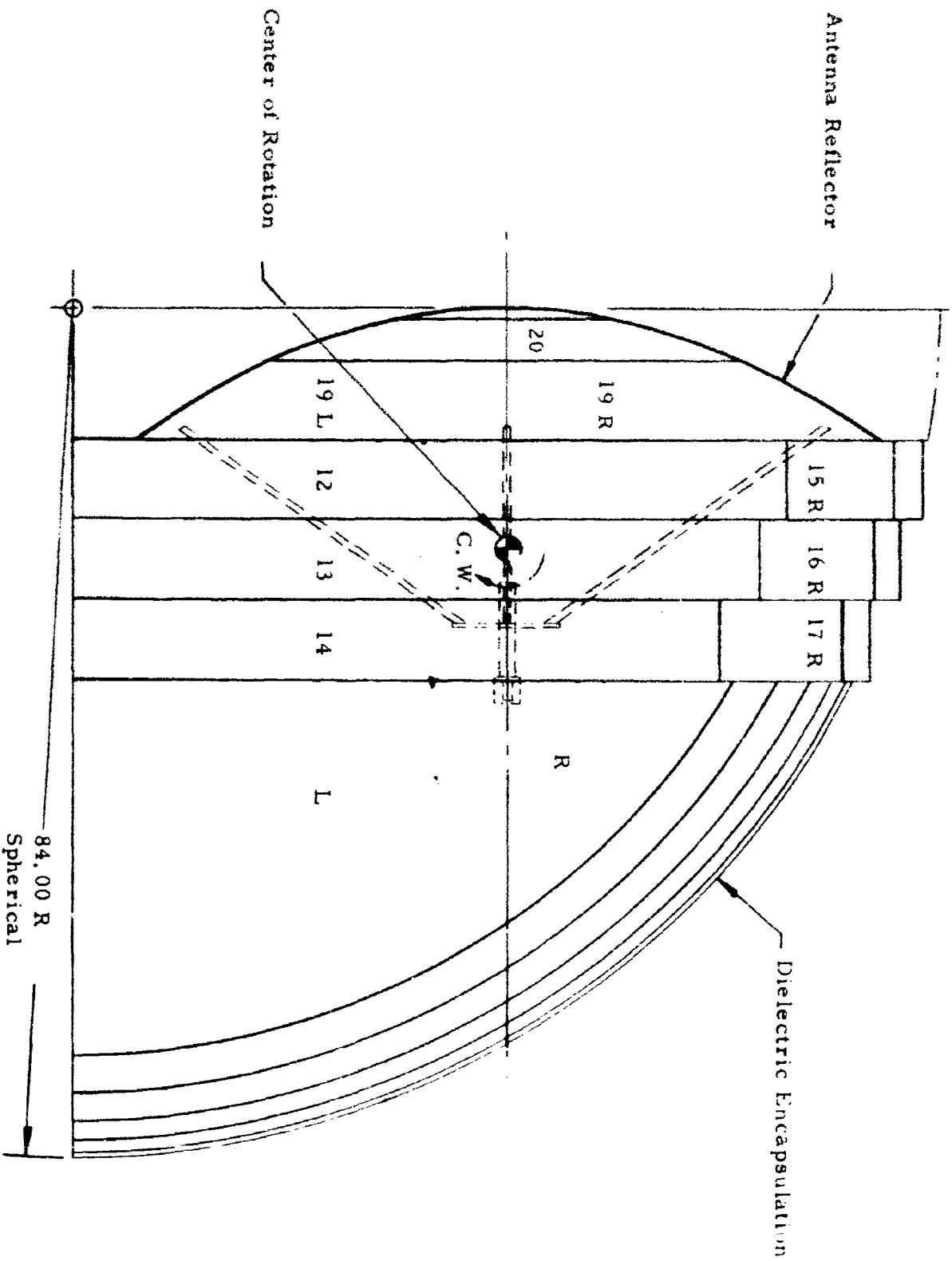


Figure 22 - Scale Model Antenna Encapsulation Configuration

The above table represents a summary of the information obtained from the measured antenna characteristics or raw data given in Appendix IX.

3.8.7.4 Gain Measurements

The measured gain of the scale model antenna system, with and without the encapsulation, is shown in Section 3.8.7.3. The measured gain with the encapsulation is shown to be 0.9 DB greater than that without the encapsulation. This would normally not be expected, yet it must be remembered that the accuracy of the gain measurements is $\pm .5$ DB. To explain the apparent gain increase, there may have been a small increase in H-plane edge illumination as evidenced by the decrease in the H-plane -3 DB beamwidth when the encapsulation was added. This would tend to increase the gain slightly. The loss in gain due to the addition of the encapsulation, if the illumination were constant in both planes, would not likely have been detectable.

3.8.7.5 VSWR Measurements

The addition of the dielectric material in front of the feedhorn improved the input VSWR from 1.1:1 to 1.05:1. This was not anticipated. The input VSWR should vary with the amplitude and phase of the reflected signal from the air dielectric interface immediately in front of the feedhorn aperture in conjunction with the amplitude and phase of the reflected signal from the feedhorn aperture. The resultant VSWR may be greater or less than the two component VSWR's.

3.8.7.6 Pattern Measurements

The addition of the dielectric encapsulation to the antenna system affected the following parameters:

- a. Half power (-3 DB) - the encapsulation material produced no change in the E-plane -3 DB beamwidth. The H-plane -3 DB beamwidth was reduced by 0.1° . This is probably due to a slight broadening of the H-plane feed pattern by the dielectric interface immediately in front of the feedhorn. It should be possible to eliminate this effect by making the immediate

interface a spherical surface across the aperture angle with its center approximately coincident with the phase center of the feedhorn.

- b. Sidelobes - the E-plane first sidelobes were increased by approximately 5.5 DB to a value of -14.5 DB and the H-plane first sidelobes were increased by 9.5 DB to a value of -14.5 DB. The reason for the difference in increase of the E- and H-plane sidelobes is probably the same as for the decrease in the H-plane -3 DB beamwidth; i.e., the edge illumination. The clockwise sidelobes should have been higher than the counterclockwise sidelobes with the addition of the encapsulation due to the phase errors across the aperture of the reflector. It is possible that the flat air dielectric interface on the clockwise side of the reflector configuration acted as a lossy wave radiator to alter the clockwise sidelobes while also acting as a scattering and reflecting surface to alter the counterclockwise sidelobes.
- c. Boresight shift measurements - the measured boresight shift as shown in pattern 5.4.1 was 0.66° . This value compares well with the calculated boresight shift of 0.707° . The boresight shift was measured in the E-plane. It is unlikely that the boresight shift would be any different if measured in the H-plane, since the angle of incidence of the wavefront, with respect to the outer air dielectric interface surface, is relatively small across nearly all of the reflector aperture.

3.9 BONDING OF FOAMED PLASTICS

3.9.1 Introduction

An experimental program to determine the feasibility of bonding foamed plastics, particularly expanded bead polystyrene foam and polyethylene foam, was performed at the Aeronca facility.

3.9.2 Objectives of Study

The objectives of this program were the following:

- a. To determine the compatibility of various types of adhesives with the foamed-plastic materials.
- b. To determine the bond strengths obtainable when bonding the foamed plastics in combination or to themselves with various types of adhesives.
- c. To evaluate such factors as surface preparation for bonding, method of adhesive application, bond line thickness requirements and adhesive costs.
- d. To determine those factors which might preclude or limit the use of adhesives for use in a field erection capacity.

3.9.3 Program Description

The materials tested in this program consisted of the following:

- a. Expanded bead polystyrene - Koppers "Dylite" nominal density 2 lbs/ft.³.
- b. Polyethylene foam - Dow "Ethafoam" nominal density 2 lbs/ft.³.
- c. Adhesives - Table 3 lists the adhesives which were used in this program.

The procedures employed to determine the optimum adhesives for use in this program were based on suppliers' recommendations, when available, to determine the most promising adhesives for evaluation in this program and to establish methods of use. The polystyrene foam was bonded in the "as received" condition. The polyethylene foam was bonded both "as received" and after sanding to remove surface gloss. All adhesives were mixed and applied per adhesive manufacturers' instructions. The drying times prior to assembly and cure times prior to test, as well as cost factors for each adhesive, are shown in Table 4. In all cases, only contact pressure was used to hold the adherents in place during bonding. Each of the recommended adhesives were applied to pieces of the polystyrene and polyethylene foam, prior to their use for mechanical testing, to determine if any adverse effects occurred. Selected adhesives were also evaluated for room temperature mechanical bonding properties when used to bond the foamed-plastic materials. These tests are discussed further in Section 3.9.5

TABLE 3
Adhesives Evaluated

| <u>Adhesive</u> | <u>Type</u> | <u>Manufacturer</u> |
|---------------------------|--|-----------------------|
| R-923-T | Contact (solvent base) | B. F. Goodrich |
| R-1078-T | Contact (solvent base) | B. F. Goodrich |
| R-1083-T | Contact (solvent base) | B. F. Goodrich |
| A-1178-B | Contact (solvent base) | B. F. Goodrich |
| A-1192-B | Contact (solvent base) | B. F. Goodrich |
| G-310 | Contact (solvent base) | Armstrong Cork Co. |
| LD-780 | Contact (water base) | Armstrong Cork Co. |
| G-1288 | Resorcinol-phenol-formal- dehyde (two components) | Koppers Company |
| 88 x 571 | Epoxy (two components) | General Adhesives Co. |
| Styrene Plastic Cement | Polystyrene (solvent base) | Ambroid Company |

3.9.4 Evaluation of Processing Techniques

Foams and adhesives were evaluated to determine the effects of the following processing factors:

- a. Surface preparation - tests were made to determine the adhesion-to-foam surfaces as molded and after sanding the molded surface to remove surface gloss.
- b. Adhesive application - promising adhesives were applied manually (by brush) and mechanically (by spray) to determine the best method of adhesive application. In most cases, the adhesive suppliers' recommended procedures were used.
- c. Film thickness requirements - tests were performed to determine the effect of different adhesive thicknesses on bond strengths.
- d. Applicability of adhesive to outside usage - the effects of outdoor environmental conditions on the usage of selected adhesive were evaluated.

3.9.5 Mechanical Testing

The test used to determine bond strengths consisted of the following:

- a. Lap shear - 1/8" thick by 2" wide pieces of the foamed materials were bonded with a 1/4" overlap. A tensile shear test, similar to that described in MIL-A-5090D, was employed to determine shear properties of the bond.
- b. Flatwise tension - 2" by 2" by 2" thick pieces of the foam were bonded together and tested in tension as described in MIL-STD-401A.
- c. Shear tension - 2" by 2" pieces of the foam were diagonally cut at a 45° angle and bonded together to give a shear tension type of loading upon testing. In some respects, this test was quite similar to a tensile test whereby a scarf joint is used to join the adherents.

TABLE 4

Processing Times and Cost Factors for Adhesives Evaluated

| Adhesive | Work Life at 75° F (1) | Drying Time at 75° F (2) | Cure Time (Days) ⁽³⁾ | Adhes. Cov. (Sq. Ft. / Gallon) ⁽⁴⁾ | Cost Per Gallon ⁽⁵⁾ |
|----------|---------------------------|-----------------------------|------------------------------------|---|-----------------------------------|
| R-923-T | NA | 20 min. | 4 | 85 | \$ 2.70 |
| R-1078-T | NA | 1 min. | 5 | 75 | \$ 2.35 |
| R-1083-T | NA | 20 min. | 3 | 75 | \$ 2.65 |
| A-1178-B | NA | 20 min. | 3 | 140 | \$ 8.65 |
| A-1192-B | NA | 20 min. | 3 | 140 | \$ 8.05 |
| G-310 | NA | 20 min. | 3 | 150 | \$ 4.30 |
| LD-780 | NA | 45 min. | 3 | 150 | \$ 4.65 |
| G-1288 | 3 hours | 25 min. | 6 | 150 | \$ 5.10 |
| 88 x 571 | 2 hours | None | 6 | 160 | \$10.00 |

(1) Work Life - time from joining two components until adhesive is no longer spreadable. NA - not applicable.

(2) Drying Time - time allowed to permit solvents to evaporate before assembly.

(3) Cure Time - times noted are those recommended by adhesive manufacturers for full cure and are those used in this program.

(4) Adhesive Coverage - quantities are based on an adhesive thickness of .005" on each surface for contact type adhesives and a .010" thickness for two component adhesives.

(5) Costs are based on 55 gallon drum quantities.

3.9.6 Discussion of Results

Table 5 gives the results of compatibility tests. As shown, there was no noticeable solvent attack from any of the adhesives on the polyethylene foam. However, there were adhesives, as noted, which severely attacked the polystyrene foam. The results of flatwise tension tests are given in Table 6. These results show that the 88 x 571 and G-1288 adhesives were the only adhesives which produced bonds of sufficient strength to fail the polystyrene foam. There were several adhesives (R-923-T, R-1083-T, G-310, and 88 x 571) which produced bond strengths in excess of the tensile strength of the polyethylene foam. However, this was not accomplished until the molded surfaces of the polyethylene foam were sanded to remove all surface gloss.

The results of lap shear tests are shown in Table 7. This test was discontinued after testing two adhesives because of erratic results. In all tests, the foam failed, thereby giving no indication of the shear strength of the bond.

In an effort to determine the best method of adhesive application, and to judge the effect of bond line thickness on bond strengths, flatwise tension tests, as shown in Table 8, were performed. From the limited number of tests performed, it is readily evident that a thinner bond line with equivalent or better resultant bond strengths can be obtained by spraying the adhesives. There is also less chance of trapping residual solvents (contact type adhesives only) in the bond line when spraying. However, there are inherent disadvantages in spraying these adhesives, such as control of overspray, need for specialized personnel and equipment, and the possibility that the adhesives (solvent base) may dry so readily that resultant weak bonds are obtained on assembly.

The diagonal shear tension type tests, as shown in Table 9, indicated that this test was nothing more than a tension type test. The values obtained were, in all respects, similar to those for tension tests when foam failure was obtained.

TABLE 5

Results of Compatibility Tests

| <u>Adhesive</u> | <u>Affect on Polystyrene Foam</u> | <u>Affect on Polyethylene Foam</u> |
|-----------------|---------------------------------------|--|
| R-923-T | None | None |
| R-1078-T | None | None |
| R-1083-T | None | None |
| A-1178-B | Severe | None |
| A-1192-B | None | None |
| G-310 | Very Slight | None |
| LD-780 | None | None |
| G-1288 | None | None |
| 88 x 571 | None | None |
| Ambroid Cement | Severe | None |

TABLE 6

Results of Flatwise Tension Tests

| Adhesive | Adherents ⁽¹⁾ | Tensile Strength(psi) ^(2 & 6) | | Type of Failure ⁽⁴⁾ |
|----------|--------------------------|--|---------------------|--------------------------------|
| R-923-T | PS to PS | 18.2 | | 1 |
| | PE to PE | 9.2 | 23.5 ⁽³⁾ | 1, 2 |
| | PS to PE | 8.0 | 22.8 | 1, 2 |
| R-1078-T | PS to PS | 22.5 | | 1 |
| | PE to PE | 7.1 | 21.3 | 1, 1 |
| | PS to PE | 7.8 | 17.7 | 1, 1 |
| R-1083-T | PS to PS | 16.8 | | 1 |
| | PE to PE | 12.9 | 23.9 | 1, 2 |
| | PS to PE | 11.6 | 24.2 | 1, 2 |
| A-1178-B | PS to PS | (5) | | |
| | PE to PE | 12.1 | 20.2 | 1, 1 |
| | PS to PE | (5) | | |
| A-1192-B | PS to PS | 2.2 | | 1 |
| | PE to PE | 10.3 | 11.2 | 1, 1 |
| | PS to PE | 11.2 | 18.9 | 1, 1 |
| G-310 | PS to PS | 15.2 | | 1 |
| | PE to PE | 13.4 | 22.2 | 1, 2 |
| | PS to PE | 8.3 | 21.2 | 1, 2 |
| LD-780 | PS to PS | 38.2 | | 1 |
| | PE to PE | 7.3 | 12.5 | 1, 1 |
| | PS to PE | 10.9 | 13.4 | 1, 1 |
| G-1288 | PS to PS | 46.0 | | 2 |
| | PE to PE | 10.2 | 14.8 | 1, 1 |
| | PS to PE | 12.6 | 19.9 | 1, 1 |
| 88 x 571 | PS to PS | 48.1 | | 2 |
| | PE to PE | 4.0 | 26.9 | 1, 2 |
| | PS to PE | 4.8 | 27.0 | 1, 2 |

(1) Abbreviations: PS = polystyrene foam, PE = polyethylene foam.

(2) Stress values are average values for three specimens.

(3) First column of values obtained when bonding polyethylene foam "as received". Second column of values obtained after sanding molded surfaces of polyethylene foam.

- (4) Types of Failure: 1 = bond failure; 2 = foam failure.
- (5) No tests made due to solvent attack on polystyrene foam.
- (6) From foam suppliers data, tensile strength of polystyrene foam (40 - 50 psi) for polyethylene foam 20 - 30 psi.

TABLE 7

Results of Lap Shear Tests on Promising Adhesives

| <u>Adhesives⁽¹⁾</u> | <u>Adherents</u> | <u>Failing Load(#)</u> | <u>Type of Failure⁽²⁾</u> |
|--------------------------------|------------------|------------------------|--------------------------------------|
| 88 x 571 | PS to PS | 14.7 | 1 |
| | PE to PE | 7.6 | 1 |
| R-1083-T | PS to PS | 4.8 | 1 |
| | PE to PE | 12.6 | 1 |

⁽¹⁾ Test discontinued because of erratic values and foam failures.

⁽²⁾ Type of Failure: 1 = foam failure.

TABLE 8

Comparison of Tensile Strengths Versus Bond Line
Thickness for Promising Adhesives

| Adhesive Application Method | Adhesive | Bond Line Thickness(in) ⁽¹⁾ | Adherents | Tensile Strength (psi) ⁽²⁾ | Type of Failure ⁽³⁾ |
|-----------------------------------|----------|---|-----------|---|-----------------------------------|
| Brush | R-923-T | .020 | PS to PS | 18.2 | 1 |
| Spray | R-923-T | .012 | PS to PS | 26.1 | 2 |
| Brush | 88 x 571 | .020 | PS to PS | 48.1 | 3 |
| Spray | 88 x 571 | .010 | PS to PS | 47.5 | 3 |
| Brush | R-1083-T | .018 | PS to PS | 16.8 | 1 |
| Spray | R-1083-T | .012 | PS to PS | 15.2 | 1 |
| Brush | G-310 | .015 | PS to PS | 15.2 | 1 |
| Spray | G-310 | .010 | PS to PS | 25.4 | 1 |

⁽¹⁾ Bond line thickness = total of wet film thickness on each bond surface.

⁽²⁾ Values are an average of three tests each.

⁽³⁾ Types of Failure: 1 = bond failure; 2 = bond line and foam failure combined; 3 = foam failure.

TABLE 9

Results of Diagonal Shear Tension Tests of Promising Adhesives

| <u>Adhesive</u> | <u>Adherents</u> | <u>Failing Stress (psi)</u> | <u>Type of Failure</u> ⁽¹⁾ |
|-----------------|------------------|-----------------------------|---------------------------------------|
| R-923-T | PS to PS | 31.7 | 1 |
| | PS to PE | 20.6 | 2 |
| | PE to PE | 24.4 | 2 |
| 88 x 571 | PS to PS | 35.5 | 2 |
| | PS to PE | 27.9 | 2 |
| | PE to PE | 27.0 | 2 |

⁽¹⁾ Type of Failure: 1 = bond line failure; 2 = foam failure.

3.9.7 Summary

The results of this investigation indicate the following:

- a. The epoxy-type adhesive (88 x 571) was the only adhesive capable of producing tension failures for any combination of foam adherents.
- b. The G-1288 adhesive is capable of producing tension failures in the foam when used for bonding polystyrene to polystyrene. However, it does not adhere well to the polyethylene foam.
- c. For bonding the polyethylene foam to itself, contact adhesives such as R-923-T, R-1083-T and G-310 are acceptable.
- d. It is necessary to remove the surface gloss from the polyethylene foam "as received" in order to obtain strong bonds with any adhesive. This may be accomplished by hand sanding or by the use of a wire brush. The polystyrene foam may be bonded in the "as received" condition.
- e. The spray application method worked best for the contact type adhesives. The epoxy and resorcinol type adhesives may be spray or brush applied. The spray method could give better glue line uniformity and permit less adhesive to be used. However, the spray application method requires specialized equipment, particularly for the two component type adhesives, and well-trained personnel. Brush or paint-roller application methods are by far the most practical.
- f. With respect to costs, the contact type adhesives are less expensive on a unit volume basis. However, on a coverage basis, the cost of the two component adhesives is comparable to that of the contact type.
- g. The use of the adhesives evaluated in this program for field usage is limited by the following:
 - (1) temperatures above 70° F are required to obtain full cure of the adhesives,
 - (2) the presence of moisture on the surfaces of the adherents is highly detrimental to the obtainment of strong bonds,

- (3) extremely high ambient temperatures (in excess of 100° F) may cause some adhesives to be nonusable due to limited work life and rapid drying times, and
- (4) adherents joined with contact type adhesives are almost impossible to reposition once they are bonded. On the other hand, adherents joined with two component adhesives must be held in position until curing is sufficient to maintain alignment (normally eight hours).

4. CONCLUSIONS AND RECOMMENDATIONS

4.1 CONCLUSIONS

It can be concluded from this program that a foamed-plastic radome does have merit as a technique for hardening above-ground antennas. The aspects of nuclear radiation, thermal loading and electrical radiation are considered adequate, and only the material response to the dynamic loading of a shock overpressure needs further evaluation.

The investigation of the effects of a nuclear detonation of a one megaton bomb, characterized by the 75 psi overpressure environment on a foamed plastic, has led to the following conclusion:

- a. Nuclear radiation effects on polystyrene or polyethylene foam will be negligible for dosages up to 10^6 roentgens. Since this dosage exceeds the specified level of interest (about 10^4 roentgens), no nuclear effects are foreseen.
- b. The thermal radiation can be resisted by the action of a polyethylene thermal ablative shield. Although additional experimental work would lead to an exact dimensional solution, on the basis of a theoretical thermal analysis using the measured heat of ablation and attenuation factor, a thickness of two to three feet of low density polyethylene foam should suffice for a thermal shield.
- c. Additional data on the response of foam plastics to dynamic shock loading is necessary before the mechanical shock wave effects can be defined.

From the scale model tests, it was concluded that the electrical transmission through a foamed-radome results in predictable pattern variations and boresight shift. Impedance mismatches introduced by the encapsulating foam are negligibly small.

It has been established that, under certain approximations concerning the loading, an elastic shell protective structure, made of rigid polyurethane of 50 ft. radius and 10 ft. thick with an assumed elastic response to the loading, would survive. While approximations were used, the dimensional requirements were deemed conservative, and if the foam response is

viscoelastic, these requirements would include a safety margin. An experimental program is needed before this design can be accepted as a conclusive hardening approach.

In a foamed-plastic structure, the foundation requirements can be resolved after the mechanics of the foamed-plastic response are known.

A composite structure, that is, one containing concrete and an R.F. window, is a possible approach. However, this is a premature consideration until foam is definitely proven as a hardening material for radomes in these specified environments.

4.2 RECOMMENDATIONS FOR FURTHER INVESTIGATION

4.2.1 Experimental Studies

A definitive approach to firmly establish the foam hardening concept requires dynamic foam response data. This is the most significant factor to establish the feasibility. The present program has served to demonstrate the parameters of interest; these are energy absorption or attenuation, fracture, stress propagation effects, transmitted elastic stress and the deformation history of a shock loaded foam material. The use of dynamic loading machines and shock tubes with strain and strain-rate instrumentation is suggested.

A scale model shock tube test of a foam configuration would also be highly desirable to firm up a configuration design.

4.2.2 Analytical Studies

An analytical analysis of the data obtained from shock tests is necessary to determine the mathematical model for a foam; i.e., to predict foam response and energy absorption capabilities. It is also necessary to derive a scaling law for viscoelastic configurations. It is probably not acceptable to use elastic scaling laws since the stress-strain law for a foamed plastic is described by a nonlinear differential equation. An effort should also be made to fill some gaps in the theory of nonlinear viscoelasticity which would permit the investigation of foam hardening capabilities for other potentially vulnerable structures.

An analysis of the electrical transmission characteristics should be made for the final design in both the pre- and post-blast conditions. Previous effort has shown that the electrical characteristics of an encapsulated antenna can be predicted with a knowledge of the dielectric constants of the foam material and the geometry of the configuration.

Some further experimental work is advisable to better define the radiant thermal energy attenuation coefficients for polyethylene foam. A better definition of the thermal flux dependency of the heat of ablation is also warranted. This knowledge is necessary to confidently predict required thicknesses of ablator material.

5. REFERENCES

1. Report of 14 July, 1962, IDA Panel on Hardening of Radomes, ASTIA 334727, Confidential.
2. Resnick, I., "Rigid Foam Plastics Information Manual". Material Laboratory, N. Y. Naval Shipyard, December 1960.
3. R. Shield, C. Covington, "High Velocity Impact Cushioning", U. Texas, Structural Mechanics Research Laboratory, September, 1960.
4. "Design Criteria for Plastic - Cushioning Materials", Picatinny Arsenal, Dover, N. J., December 1961, ASTIA 273400.
5. Doherty, D., Hurd, R., and Lester, G. R., "Physical Properties of Rigid Polyurethane Foams", Chem and Industry, 30, 38 July 1962, pp. 1340-56.
6. R. A. Weeks, D. Binder, Oak Ridge National Labs., "Effects Neutron and Gamma Ray Irradiation on the Dielectric Constant and Loss Tangent of Some Plastic Materials".
7. A. Charlesby, "Beneficial Effects Radiation on Polymers" Nucleonics, Volume 14, No. 9, September 1956, pp. 82-85.
8. R. F. Cox, "Effects of Ionizing Radiation on Synthetic and Natural Polymers", AERE-R-3208, July 1960.
9. H. G. Le Clair, W. H. Cobbs, Jr., "Effects of Radiation on Plastic Packaging Films" Ind. and Eng. Chemical, Pt. 1, Volume 50, No. 3 March 1958.
10. F. Clark, "Insulating Materials for Design and Engineering Practice", John Wiley, New York, 1962, pp. 429-436.
11. S. Glasstone, "Effects of Nuclear Weapons", AEC, 1962.
12. W. J. O'Sullivan, Jr., W. R. Wade, "Theory and Apparatus for Measurement of Emissivity for Radiative Colling of Hypersonic Aircraft with Data for Iconel and Iconel X", NASA TN-4121.
13. W. Hankey, R. Neuman, E. H. Flinn, "Design Procedures for Computing Aerodynamic Heating at Hypersonic Speeds", WADC TR 59-610, June 1960.
14. Haust, Walker, WADD TR 60-101, p. 309.

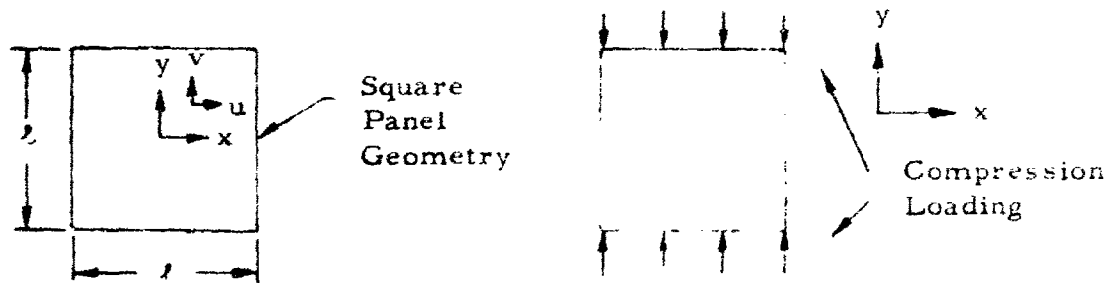
15. Constantino Economos "Results of Ablation Tests on Several Plastic Models in a Hypersonic Wind Tunnel" July 1961, Polytechnic Institute of Brooklyn, WADD TN 60-273
16. R. A. Muldoon, "Dynamic Buckling of Space Frame Radome Models", MIT Lincoln Labs 71-G-3, February 1962.
17. Bland, "Theory of Linear Viscoelasticity".
18. Nowacki, "Dynamics of Elastic Systems, Wiley, 1963.
19. H. Kalsky, "Viscoelastic Waves", International Symposium on Stress Wave Propagation in Materials, Interscience, 1960.
20. Newmark, N. M. ; J. D. Haultiwanger, "Principles and Practices for Design of Hardened Structures", AFSWC-TDR-62-138, AD295408, December 1962.
21. Urquhard, L. C. , "Civil Engineering Handbook", McGraw-Hill.
22. Design of Structure to Resist the Effects of Atomic Weapons - Structural Elements Subjected to Dynamic Loads, EM-1110-345-415, Corp of Engineers, March 1957.
23. E. Witmer, W. Hermann, J. Zuch, T. Pian, "Responses of Plates and Shells to Intense External Loads of Short Duration", WADD TR 60-433, April 1960.
24. S. C. Hunter, "An Account of the Dynamic Properties of Solids", (1961), R. A. R. D. E. Memorandum (MX) 8/62, ASTIA 274754.
25. M. L. Williams, R. J. Arenz, "Dynamic Analysis in Viscoelastic Media", Firestone Flight Sciences Laboratory, C. I. T. , ASD-TR 63-140.
26. O. Hill, E. Kerlin, "Experimental Investigation of Radiation Heating in Materials" General Dynamics/Ft. Worth. 1961, AD-270806.
27. H. Schwartz, R. Farmer "Thermal Irradiation of Plastic Materials", 1961 WADD TR 60-647.
28. Timoshenko "Theory of Plates and Shells", McGraw-Hill 1940.
29. Lee, Kanter "Wave Propagation In Finite Rods of Viscoelastic Material", J Appl. Physics, 24, 9. (1953).

30. Norris, Hansen, et al. , "Structural Design for Dynamic Loads", McGraw-Hill, 1959.
31. Hetenyi, M. , "Beams on Elastic Foundations," U. of Michigan Press, 1961.
32. Burton, R. , "Vibration and Impact", Addison-Wesley, 1958.
33. Sechler, E. E. , "Elasticity in Engineering", Wiley, 1952.
34. Love, A. E. H. , "Mathematical Theory of Elasticity", 4th Edition, 1927, (Dover Reprint).
35. A. Von Hippel "Dielectric and Waves" MIT Technology Press John Wiley, 1954.
36. A. Von Hippel "Dielectric Materials and Applications" MIT Technology Press, John Wiley, 1954.
37. S. Silver, "Microwave Antenna Theory and Design", MIT Radiation Laboratory Series, 1947.

APPENDIX I ANALYSIS OF A SQUARE PANEL

Consider a square plate having zero flexural rigidity but finite in-plane stiffness. Let it be loaded in its own plane on two opposite edges. Require that all edges remain straight, although they may translate and change length. Require that there be no net load on the two unloaded sides; although there may be stresses normal to the edge to hold the edge straight, these stresses must integrate to zero along either side. Let the load be compression, and permit the panel to bulge out of its plane, but with its edges coplanar.

It is required to investigate the deformation of the panel to find the stresses, deflections in all directions, the apparent stiffness seen by the load, and the apparent Poisson's ratio of the panel as a whole.



The boundary conditions are as follows:

1. $\bar{\sigma}_x = 0$
 $x = \pm \frac{l}{2}$
2. $\frac{\partial u}{\partial y} = 0$
 $x = \pm \frac{l}{2}$
3. $\frac{\partial v}{\partial x} = 0$
 $y = \pm \frac{l}{2}$
4. $w(\pm \frac{l}{2}, y) = w(x, \pm \frac{l}{2}) = 0$

A rigorous solution would also prohibit shear stresses along the edges, but this condition will not be enforced in the interest of simplicity of analysis. In fact, the entire approach used is approximate, being an assumed mode method with very few modes assumed. Although an exact solution is not attempted, it is believed that the approximate solution obtained should be reasonably valid.

The simplest plausible functions satisfying boundary conditions No. 2, 3, and 4 are:

$$u(x, y) = Bx \quad (I-1)$$

$$v(x, y) = Cy \quad (I-2)$$

$$w(x, y) = A \cos \frac{\pi x}{l} \cos \frac{\pi y}{l}, \quad (I-3)$$

where u is the displacement in the x direction, v in the y direction, and w in the direction normal to the xy plane, and where A , B , and C are constants.

In order to satisfy boundary condition No. 1, it is necessary to have equations for the stresses in terms of the displacements. The linear stress-strain relations are:

$$\sigma_x = \frac{E}{1 - \nu^2} (\epsilon_x + \nu \epsilon_y) \quad (I-4)$$

$$\sigma_y = \frac{E}{1 - \nu^2} (\epsilon_y + \nu \epsilon_x) \quad (I-5)$$

$$\tau_{xy} = \frac{E}{2(1 + \nu)} \gamma_{xy} \quad (I-6)$$

The strain-displacement relations for large deflections are given by Timoshenko (28) (Theory of Plates and Shells, 1940, p. 342):

$$\epsilon_x = \frac{\partial u}{\partial x} + \frac{1}{2} \left(\frac{\partial w}{\partial x} \right)^2 \quad (I-7)$$

$$\epsilon_y = \frac{\partial v}{\partial y} + \frac{1}{2} \left(\frac{\partial w}{\partial y} \right)^2 \quad (I-8)$$

$$\gamma_{xy} = \frac{\partial u}{\partial y} + \frac{\partial v}{\partial x} + \frac{\partial w}{\partial x} \frac{\partial w}{\partial y} \quad (I-9)$$

Eliminating the strains by substituting for strain in terms of displacements

equations (I-4) through (I-6) become

$$\sigma_x = \frac{E}{1-\nu^2} \left[\frac{\partial u}{\partial x} + \frac{1}{2} \left(\frac{\partial w}{\partial x} \right)^2 + \nu \frac{\partial v}{\partial y} + \frac{1}{2} \nu \left(\frac{\partial w}{\partial y} \right)^2 \right] \quad (I-10)$$

$$\sigma_y = \frac{E}{1-\nu^2} \left[\frac{\partial v}{\partial y} + \frac{1}{2} \left(\frac{\partial w}{\partial y} \right)^2 + \nu \frac{\partial u}{\partial x} + \frac{1}{2} \nu \left(\frac{\partial w}{\partial x} \right)^2 \right] \quad (I-11)$$

$$\tau_{xy} = \frac{E}{2(1+\nu)} \left[\frac{\partial u}{\partial y} + \frac{\partial v}{\partial x} + \frac{\partial w}{\partial x} \frac{\partial w}{\partial y} \right] \quad (I-12)$$

Substituting the assumed expression for u , v , and w into the equation (I-10) for the stress in the x direction, one then finds the average stress along either side edge:

$$\bar{\sigma}_x \Big|_{x=\pm \frac{l}{2}} = \frac{E}{1-\nu^2} \left[B + \nu C + \frac{\pi^2 A^2}{4 l^2} \right] \quad (I-13)$$

But this must vanish, according to boundary condition No. 1. Therefore,

$$B + \nu C + \frac{\pi^2 A^2}{4 l^2} = 0 \quad (I-14)$$

Therefore A can be expressed in terms of B and C .

$$A = \pm \frac{2l}{\pi} \sqrt{-B - \nu C} \quad (I-15)$$

If C is considered to be a prescribed edge displacement, then only B need yet be found. This will be done by Rayleigh-Ritz energy method, (28) i. e., one requires that the strain energy be a minimum with respect to B . According to Timoshenko (Theory of Plates and Shells, 1940, p. 345), the strain energy is:

$$\begin{aligned} V = & \frac{Eh}{2(1-\nu^2)} \iint \left\{ \left(\frac{\partial u}{\partial x} \right)^2 + \frac{\partial u}{\partial x} \left(\frac{\partial w}{\partial x} \right)^2 + \left(\frac{\partial v}{\partial y} \right)^2 + \frac{\partial v}{\partial y} \left(\frac{\partial w}{\partial y} \right)^2 \right. \\ & + \frac{1}{4} \left[\left(\frac{\partial w}{\partial x} \right)^2 + \left(\frac{\partial w}{\partial y} \right)^2 \right]^2 + 2\nu \left[\frac{\partial u}{\partial x} \frac{\partial v}{\partial y} + \frac{1}{2} \frac{\partial v}{\partial y} \left(\frac{\partial w}{\partial x} \right)^2 + \frac{1}{2} \frac{\partial u}{\partial x} \left(\frac{\partial w}{\partial y} \right)^2 \right] \\ & \left. + \frac{1-\nu}{2} \left[\left(\frac{\partial u}{\partial y} \right)^2 + 2 \frac{\partial u}{\partial y} \frac{\partial v}{\partial x} + \left(\frac{\partial v}{\partial x} \right)^2 + 2 \left(\frac{\partial u}{\partial y} + \frac{\partial v}{\partial x} \right) \frac{\partial w}{\partial x} \frac{\partial w}{\partial y} \right] \right\} dx dy \end{aligned} \quad (I-16)$$

Plugging in the expressions for u , v , and w in terms of B and C , and integrating over the surface of the panel, one obtains:

$$V = \frac{Eh\ell^2}{2(1-\nu^2)} \left[\left(\frac{5}{4} - \nu\right) B^2 + \left(1 - \nu + \frac{1}{4}\nu^2\right) C^2 + \left(-1 + \frac{5}{2}\nu - \nu^2\right) BC \right] \quad (I-17)$$

To find the B which makes V a minimum, differentiate V with respect to B and equate $\frac{\partial V}{\partial B}$ to zero. This yields

$$B = \left[\frac{2 - 5\nu + 2\nu^2}{5 - 4\nu} \right] C \quad (I-18)$$

Note that the apparent Poisson ratio of the panel is by definition;

$$\nu_p = -\frac{B}{C} = -\frac{2 - 5\nu + 2\nu^2}{5 - 4\nu} \quad (I-19)$$

It is always negative. Its value depends only upon the value of Poisson's ratio for the material of which the panel is made. For most plastics Poisson's ratio is about .3 or .4, so the apparent Poisson ratio for a plastic panel would be about -.1 to -.2. Note that this means that compression of the panel in one direction is accompanied by a significant contraction in the other direction. This finding may be explained by an explanation of what happens to the panel in detail:

1. The load causes buckling of y fibers near the y axis.
2. Bulging of the y fibers stretches the x fibers, since they too must bulge.
3. The side edges must move closer to each other in order to relieve some of the tension of the x fibers. QED.

To find the apparent stiffness of the panel as seen by the load, the stress in the y direction is written in terms of the given strain C , and averaged along the top or bottom edge of the panel.

$$\bar{\sigma}_y \Big|_{y=\pm \frac{\ell}{2}} = \frac{EC}{1-\nu^2} \left[\frac{3 - 2\nu - 3\nu^2 + 2\nu^3}{5 - 4\nu} \right] = E_f \epsilon_y \quad (I-20)$$

This is only about 60% of the stress developed by the same C in an unbuckled panel. Hence the apparent stiffness of the buckled panel is only about 60% of that of the unbuckled panel, depending slightly upon the Poisson ratio of the

material. It can be clearly seen that

E = foam material modulus

ν = foam plastic Poisson's ratio

E_f = geometry modified foam modulus

$$= \frac{E}{1 - \nu^2} \left[\frac{3 - 2\nu - 3\nu^2 + 2\nu^3}{5 - 4\nu} \right]$$

and

ϵ_y = strain in the y direction.

To determine what E to use in the buckled panel analysis:

The stiffness will be essentially that of a gas filled cellular system. The E that is chosen is quite essential to the correct viscoelastic description of the foam response. The buckled panel model conveniently accounts for the negative Poisson's ratio of the foam due to geometrical interaction between the gas and fibril members.

A perfect gas compressed suddenly (adiabatically) obeys the following equation:

$$\frac{p}{p_o} = \left(\frac{\rho}{\rho_o} \right)^\gamma \quad (I-21)$$

where p is pressure, ρ is density, γ is the ratio of specific heats, and subscript, o, refers to some reference condition.

Therefore, considering a gas in a cell of a foam plastic due to a small compressive strain ϵ and the apparent Poisson ratio of the foam ν , there will be an increase in gas density:

$$\frac{\rho}{\rho_o} = \frac{1}{(1-\epsilon)(1+\nu\epsilon)^2} \quad (I-22)$$

Then the ratio of new to old pressure is:

$$\frac{p}{p_o} = \left[\frac{1}{(1-\epsilon)(1+\nu\epsilon)^2} \right]^\gamma \approx 1 + (1-2\nu)\gamma\epsilon$$

The pressure increase is $(1 - 2\nu) \gamma \epsilon$, and so the gas stiffness is

$$E_G = \frac{\Delta p}{\epsilon} = (1 - 2\nu) \gamma p_0 \quad (1-20)$$

The order of magnitude is:

$$E_G \approx 1.4 \times 1.2 \times 15 = 25 \text{ psi, assuming } p_0 \approx 15 \text{ psi.}$$

But in a rigid foam, such as rigid styrofoam, the observed compression modulus can be on the order of 1,000 psi. Hence, the gas stiffness probably can be neglected for pre-failure compression of a rigid foam plastic of any density. However, in a resilient foam plastic, such as resilient polystyrene at .8 lb/ft.³, the compression modulus (secant modulus) at 40% strain is also about 25 psi. Hence, in a resilient foam of low density, at a large enough strain to buckle most fibrils and cell walls, the gas stiffness is most of the observed total stiffness of the foam. In general, it would be unwise to neglect gas stiffness a priori in calculating a foam stiffness.

An intuitive viscoelastic model to test the responses which have been observed, averaged out in time, would be comprised of a gas spring E_g , a fibril spring E_f , and a fibril dashpot, η . Unfortunately without the time dependent stress and strain functions that describe the loading under which the actual data has been taken, one can only conjecture about the model that would fit the response of the foam. A complex modulus measurement of polystyrene foam should permit model fitting. This, however, has not appeared in the literature. The closest facsimile of such data is the speed of sinusoidal propagation C_f in foam which can be computed from acoustic data taken for dylite, (See Figure I-1). Note that at high frequencies, the speed of propagation in foam is less than that for air, C_{air} . This implies from the analytical expression for C_f ,

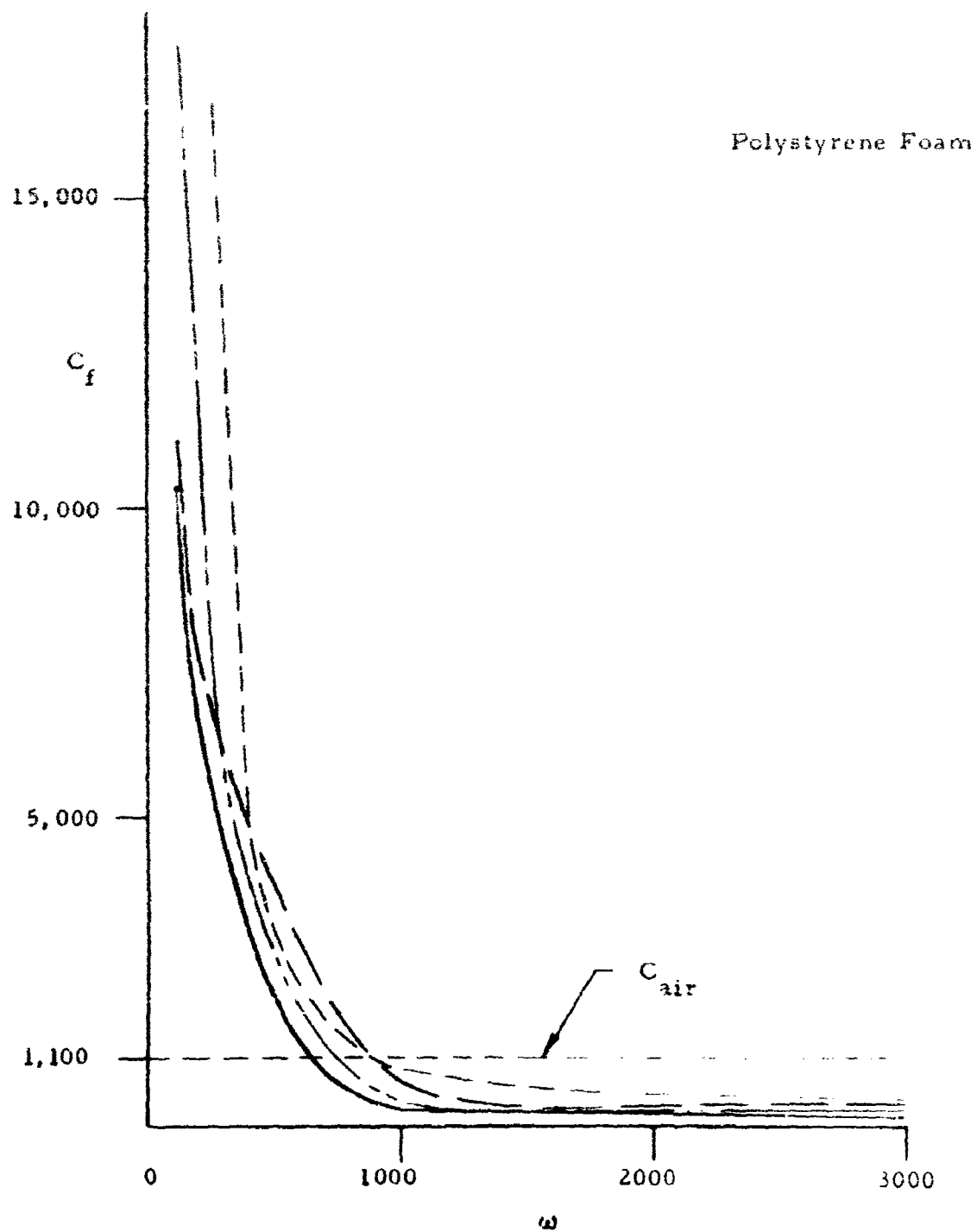
$$C_f = \frac{E^*(\omega)}{\rho}$$

that $E^*(\omega) = \sqrt{E_1^2 + E_2^2}$ is reduced at high ω .

A form of modulus that would account for such behavior is

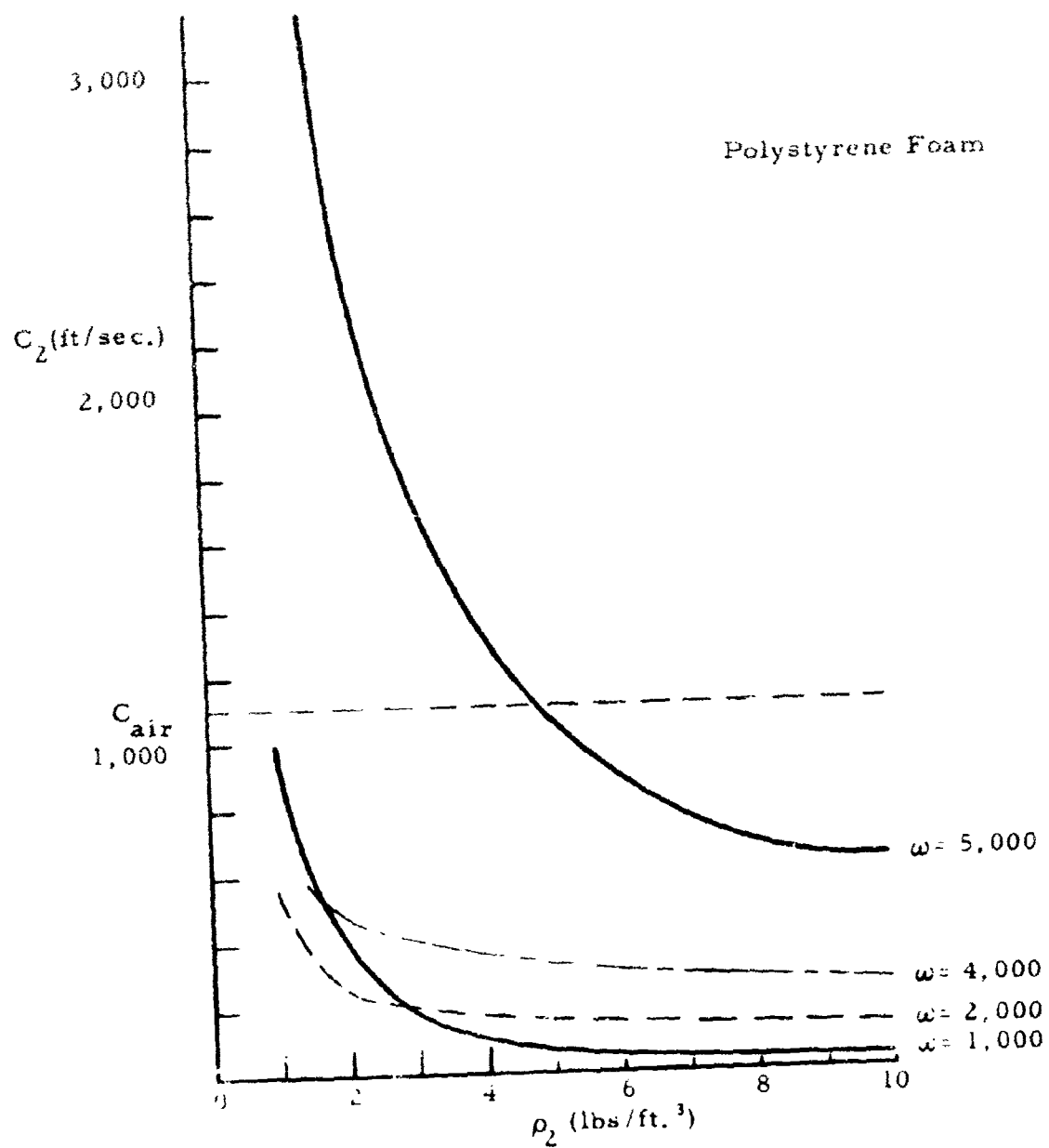
$$E^* = E_F + E_g + \eta \omega = \frac{\eta^2 \omega^2}{E_F} \quad (I-24)$$

In the limit of small ω , $E^* = E_F + E_g$ and $C_l > C_{air}$. However, at larger ω , if $\frac{\eta^2 \omega^2}{E_F} = E_F + \eta \omega$, then $E^* = E_g$ and $C_l = C_{air}$. But at higher ω , $E^* < E_g$ and $C_{air} > C_l$. The problem is finding a viscoelastic model that fits over the entire frequency range and yields the above modulus. The high frequency information would also have to be known (i.e., the $\omega \rightarrow \infty$ limit). The dependence of the foam speed of propagation on the density is described in Figure I-2. The observed increase with density follows from the fact that denser foams have more stiffness.



Speed of Sound vs Frequency

Figure I-i



Speed of Sound vs Density

Figure 11-2

APPENDIX II

Elements of Linear Viscoelastic Theory

1 General Features of Linear Viscoelastic Theory:

The generalizations of viscoelasticity are based on the response of a network consisting of linear springs and dashpots. Figure II-1 represents schematically a spring and dashpot.



Figure II-1 - Simple Elements

The force equations for these elements are given by

$$F = Ea \quad (\text{II-1})$$

$$F = \eta Da \quad (\text{II-2})$$

where E is the modulus of the spring, η is the viscosity coefficient of the dashpot and D is the time differential operator, $D \equiv \frac{\partial}{\partial t}$. Two useful combinations are the Maxwell and Voigt elements, shown in Figure II-2.

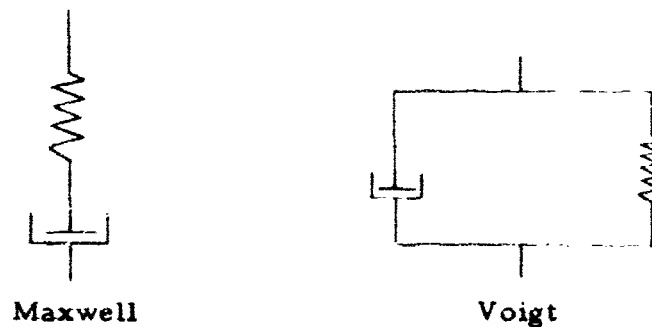


Figure II-2 - Simple Viscoelastic Systems

For the series combination (Maxwell element) one obtains the force equation,

$$F = \left(\frac{1}{\eta} + \frac{D}{E} \right) \dot{a} \quad (II-3)$$

and for the parallel combination (Voigt element) the force equation

$$F = (E + \eta D) a \quad (II-4)$$

2. Creep and Relaxation Response:

Other multi-element combinations of springs and dashpots have been generated, but the discussion will be limited to simple elements. The responses of the simple models to creep and relaxation are considered. Creep is the time elongation of an element exposed to a constant load, given mathematically by

$$a(t) = \frac{1}{E} F(t) = \frac{C}{E} H(t) \quad (II-5a)$$

$$\text{or} \quad Da(t) = \frac{F(t)}{\eta} = \frac{CH(t)}{\eta} \quad (II-5b)$$

where C is a constant and $H(t)$ is the Heaviside unit function. Equation (II-5b) when integrated yields

$$a(t) = \frac{C}{\eta} t H(t) \text{ since } a(0) = 0$$

For the Maxwell element (II-3),

$$a(t) = \int \frac{1}{\eta} CH(t) dt + \int \frac{D}{E} CH(t) dt = \frac{t}{\eta} CH(t) + \frac{C}{E} H(t)$$

$$\text{or} \quad a(t) = C \left(\frac{1}{E} + \frac{t}{\eta} \right) H(t) \quad (II-6)$$

For the Voigt element,

$$Ea + \eta Da = CH(t)$$

which can be integrated.

$$\therefore a(t) = \frac{C}{E} H(t) \left\{ 1 - \exp \left(-\frac{E}{\eta} t \right) \right\} \quad (II-7)$$

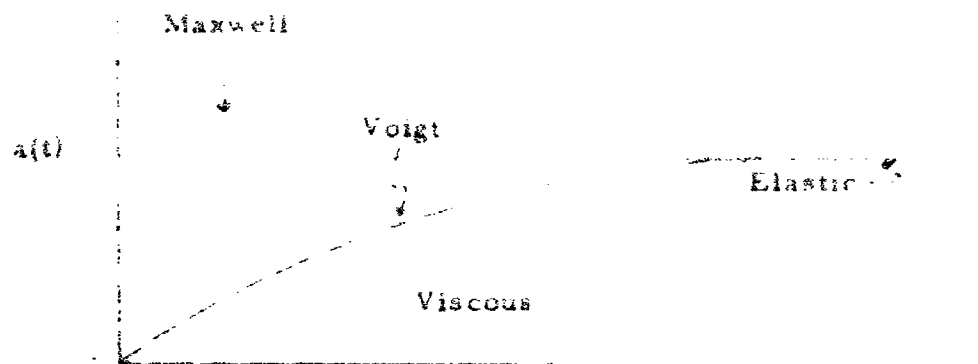


Figure II-3 - Displacement During Creep

These creep results are shown for each of the simple elements in Figure II-3. Note that in the Maxwell element the response is additive, whereas in the Voigt element the response is elastic in the limit of long time.

$a(t)$ is called extension response. The extension response to unit force when the contribution from instantaneous elasticity and long term viscous flow are excluded, is known as the "Creep Function". From (II-7) the creep characteristic time for $a(t)$ to reach $1-1/e$ of its maximum value is

$$\tau = \eta/E \quad (II-8)$$

which is called retardation time.

The reciprocal of the spring modulus is known as compliance and is denoted by J .

$$J = 1/E$$

The creep function can then be written for a Voigt element as

$$\psi(t) = J (1 - e^{-t/\tau}) H(t)$$

Of a generalized Voigt model (See Figure II-4) consisting of a large number of Voigt elements and a Maxwell element, the extension response is given by

$$a(t) = CH(t) \left(\frac{1}{E_1} + \frac{1}{\eta_2} \right) t + CH(t) \sum_{r=3}^n E_r^{-1} \left\{ 1 - \exp\left(-\frac{E_r}{\eta_r} t\right) \right\} \quad (II-9)$$

Figure II-4 - Generalized Voigt Model

The creep function is

$$\psi(t) = \sum_{r=1}^n J_r \left\{ 1 - \exp(-t/\tau_r) \right\} H(t) \quad (II-10)$$

where $J_r = \frac{1}{E_r}$ and $\tau_r = \eta_r / E_r$.

The creep function for a generalized Voigt model contains a spectrum of discrete retardation times. Considering a model consisting of a continuous distribution of retardation times, the creep function becomes

$$\psi(t) = H(t) \int_0^{\infty} J(\tau) \left\{ 1 - \exp(-t/\tau) \right\} d\tau \quad (II-11)$$

Consider keeping the extension response constant by determining the necessary variations of force to obtain what is called the relaxation force response. For an elastic element

$$F(t) = E a(t) = K E H(t) \quad (II-12)$$

and for a viscous element,

$$F(t) = \eta \dot{a}(t) = K \eta \delta(t) \quad (II-13)$$

where $\delta(t)$ is the Dirac δ function, and may be given by

$$\delta(t) = D H(t) \quad (II-14)$$

For a Maxwell element (II-3)

$$F(t) = K E \exp\left(-\frac{E}{\eta} t\right) H(t) \quad (II-15)$$

and for the Voigt element

$$F(t) = K E H(t) + K \eta \delta(t) \quad (II-16)$$

The viscous responses contain δ functions, that is, the stress goes to infinity at the instant of application of strain. A dashpot cannot give a finite instantaneous extension response to a finite instantaneous change in Force. A finite instantaneous extension imposed on a dashpot requires an infinite force

The force response to unit extension, $a(t) = H(t)$ excluding the constant and viscous terms, is known as the relaxation function, denoted by $X(t)$.

$$X(t) = \sum_{r=1}^n E'_r \exp \left(-\frac{E'_r}{\eta'_r} t \right)$$

or

$$X(t) = \sum_{r=1}^n E'_r \exp \left(-t/\tau'_r \right) H(t) \quad (\text{II-17})$$

where

$$\tau'_r = E'_r{}^{-1} \eta'_r$$

The summation is present for a generalized Maxwell model. The elasticities of the model determine the magnitudes in the relaxation function corresponding to the relaxation times τ'_r .

Again a continuous model would correspondingly appear as

$$X(t) = H(t) \int_0^\infty E(\tau) \exp \left(-t/\tau \right) d\tau \quad (\text{II-18})$$

3. Complex Modulus and Compliance:

If the applied loads are oscillatory, the strain is also oscillatory but in general lags in phase, e. g., if

$$F(t) = F_0 \exp(i\omega t) \quad (\text{II-19})$$

then

$$a(t) = a_0 \exp \left[i(\omega t - \delta) \right] \quad (\text{II-20})$$

By definition

$$\frac{F}{a} = \frac{F_0}{a_0} e^{i\delta} = E_1 + iE_2 = \frac{F_0}{a_0} \cos \delta + i \frac{F_0}{a_0} \sin \delta$$

is the complex modulus, $\gamma(i\omega)$.

If the model is a spring

$$E_1 = F_0/a_0; \quad E_2 = 0$$

If the model is a dashpot

$$F_2 = i \omega \eta = \frac{F_0(\omega)}{a_0(\omega)} ; E_1 = .$$

For Maxwell and Voigt models,

$$Y(i\omega) = (E^{-1} + (i\omega\eta)^{-1})^{-1} \quad \text{Maxwell element} \quad (II-21)$$

$$Y(i\omega) = E + i\omega\eta \quad \text{Voigt element} \quad (II-22)$$

Reciprocal complex modulus is called the complex compliance, $J(i\omega)$

For a generalized Voigt model,

$$J(i\omega) = E_1^{-1} + (i\omega\eta_2)^{-1} + \sum_{r=3}^n (E_r + i\omega\eta_r)^{-1} \quad (II-23)$$

4. Stored and Dissipated Energies;

Springs store energy and dashpots dissipate energy as heat. The energy stored in a spring is given by

$$V = \frac{Ea^2}{2} = \frac{F^2}{2E} = \frac{1}{2} Fa \quad (II-24)$$

and the rate of dissipation in a dashpot is given by

$$\phi = \eta (Da)^2 = \frac{1}{\eta} F^2 = F Da \quad (II-25)$$

Hence for a multiplex system, the total energy is summed over all the elements.

$$V = \frac{1}{2} \sum_i E_i a_i^2 = \frac{1}{2} \sum_i F_i a_i \quad (II-26)$$

and

$$\phi = \sum_i \eta_i (Da_i)^2 = \sum_i F_i Da_i \quad (II-27)$$

5. Theory of Linear Viscoelastic Behavior;

The mathematical theory has been formulated in terms of the principle of linear superposition. When a specimen is subjected to an arbitrary three dimensional load, both shear and dilational strains result. The viscoelastic basis is that their relationship involves time differential operators. The stress

is written in terms of the relaxation function.

$$\sigma = \epsilon_0 X(t) \quad (\text{II-28})$$

and the strain in terms of the creep function,

$$\epsilon = \sigma_0 \psi(t) \quad (\text{II-29})$$

The principle of superposition can be stated as follows:

Given $\epsilon(t)$, $\sigma(t)$ is a function of its entire previous loading history, given by the integral expression

$$\sigma = \epsilon(t) E + \int_{-\infty}^t X(t-\tau) \frac{d\epsilon}{d\tau} d\tau \quad (\text{II-30})$$

E is the instantaneous elastic modulus, and $E\epsilon(t)$ gives the elastic contribution to the stress while the integral gives the effects of the specimens history. For strain

$$\epsilon = \sigma(t) E^{-1} + E^{-1} \int_{-\infty}^t \psi(t-\tau) \frac{d\sigma}{d\tau} d\tau \quad (\text{II-31})$$

The majority of stress-strain problems for linear viscoelastic bodies are based on the linear partial differential equation involving strain and stress rather than the integral representation. The general form of the p. d. e. is

$$P\sigma = Q\epsilon \quad (\text{II-32})$$

where P and Q are the stress and strain time differential operators. If one employs simple, generalized models using dashpots and springs, one has only low order operators. These equations one recalls are in terms of the unit Heaviside extension function or unit Heaviside force function.

For the Maxwell model (II-32) takes the form

$$\sigma + \eta E_m^{-1} \frac{\partial \sigma}{\partial t} = \eta \frac{\partial \epsilon}{\partial t} \quad (\text{II-33})$$

where the generalized operators are given by

$$P = 1 + \eta E_m^{-1} D; \quad Q = \eta D$$

For the Voigt model it is given by

$$\sigma = E_v \epsilon + \eta \frac{d\epsilon}{dt} \quad (\text{II-34})$$

where

$$P = 1 \text{ and } Q = E_v (1 + \eta E_v^{-1} D)$$

According to Kolsky, the model that solid polymers are assumed to follow is the standard linear solid shown schematically in Figure II-5.

The stress-strain relationship is given by:

$$\sigma + \tau \frac{d\sigma}{dt} = E_a \epsilon + \tau (E_m + E_a) \frac{d\epsilon}{dt} \quad (\text{II-35})$$

where $\tau = E_m^{-1} \eta$.

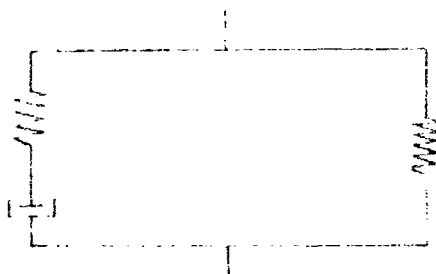


Figure II-5 - Standard Linear Solid

Of particular interest is the dissipation energy from measured parameters. The dissipated energies can be expressed in terms of stress and strain, in terms of the strain and relaxation function, or in terms of the stress and creep function.

The dissipation energy rate tabulated for the six simplest models from Bland, "Viscoelastic Theory", p. 49, 1960, is shown in Table II-1. That for the standard linear solid is found using the stress-strain law of (II-35). ϕ is obtained from Bland's table for a three element elastic stress-strain law, i.e.,

$$p_1 D\sigma + p_0 \sigma = q_1 D\epsilon + q_0 \epsilon$$

where

$$p_1 = \tau, p_0 = 1, q_0 = E_a, q_1 = \tau (E_m + E_a)$$

TABLE II-1
Simple Model Relationships

| Stress-Strain Law | Model Representation (In general, not unique) | Stored Energy, V | Rate of Dissipation, $\dot{\phi}$ |
|--|--|---|--|
| $\sigma = E\epsilon$, elastic | | $\frac{1}{2} E \epsilon^2 = \frac{1}{2E} \sigma^2$ | 0 |
| $\sigma = \eta \dot{\epsilon}$, viscous | | 0 | $\eta (D\epsilon)^2 = \frac{1}{\eta} \sigma^2$ |
| $\frac{1}{E} D\sigma + \frac{1}{\eta} \sigma = D\epsilon$, Maxwell | | $\frac{1}{2E} \sigma^2$ | $\frac{1}{\eta} \sigma^2$ |
| $\sigma = \eta D\epsilon + E\epsilon$, Voigt | | $\frac{1}{2} E \epsilon^2$ | $\eta (D\epsilon)^2$ |
| $P_1 D\sigma + P_0 \sigma = q_1 D\epsilon + q_0 \epsilon$, three-element elastic | | $\frac{P_0 P_1 \sigma^2 - 2P_1 q_0 \sigma \epsilon + q_0 q_1 \epsilon^2}{2(P_0 q_1 - P_1 q_0)}$ | $\frac{P_0^2 \sigma^2 - 2P_0 q_0 \sigma \epsilon + q_0^2 \epsilon^2}{P_0 q_1 - P_1 q_0}$ |
| $P_1 D\sigma + P_0 \sigma = q_2 D^2 \epsilon + q_1 D\epsilon$, three-element viscous | | $\frac{P_1^2 \sigma^2 - 2P_1 q_2 \sigma D\epsilon + q_2^2 (D\epsilon)^2}{2(P_1 q_1 - P_0 q_2)}$ | $\frac{P_0 P \sigma^2 - 2P q_2 \sigma D\epsilon + q_1 q_2 (D\epsilon)^2}{P_1 q_1 - P_0 q_2}$ |

From Table II-1, the value for φ is

$$\varphi = (p_o^2 \sigma^2 - 2p_o q_o \sigma \epsilon + q_o^2 \epsilon^2) / (p_o q_1 - p_1 q_o) \quad (\text{II-36})$$

By substitution of the values for the operators,

$$\varphi = (\sigma - E_a \epsilon)^2 / [\tau (E_m + E_a) - \tau E_a]$$

which reduces to

$$\varphi = (\sigma - E_a \epsilon)^2 / \tau E_m = \frac{(\sigma - E_a \epsilon)^2}{\eta}$$

or

$$\varphi = \frac{(\sigma - E_a \epsilon)^2}{\eta} \quad (\text{II-37})$$

The utility of Table II-1 is that when the stress-strain relationship can be reduced to one of these forms, the dissipation, or stored energy, can be determined by simple algebraic manipulation and substitution. For example, the stored energy, V , for this model is given by

$$V = \frac{p_o p_1 \sigma^2 - 2p_1 q_o \sigma \epsilon + q_o q_1 \epsilon^2}{2(p_o q_1 - p_1 q_o)} \quad (\text{II-38})$$

Substitution of parameters yields

$$\begin{aligned} V &= \tau \sigma^2 - 2\tau E_a \sigma \epsilon + E_a \tau (\Sigma_m + E_a) \epsilon^2 / 2\tau E_m \\ &= [\sigma^2 - 2E_a \sigma \epsilon + E_a^2 \epsilon^2 + E_a E_m \epsilon^2] / 2E_m \\ V &= \frac{(\sigma - E_a \epsilon)^2}{2E_m} + \frac{E_a \epsilon^2}{2} \end{aligned} \quad (\text{II-39})$$

The conservation of energy equation for a visco-elastic body is

$$DV + \varphi = \sigma_{ij} D\epsilon_{ij} \quad (\text{II-40})$$

Where σ_{ij} , ϵ_{ij} are the stress and strain tensors To explain briefly the

tensors consider some U_i which are components of the displacement vector $\bar{U} = (U_i, U_j, U_k)$.

If

$$U_i = U_i(x_k)$$

and

$$du_i = \frac{\partial U_i}{\partial x_k} dx_k$$

where the repeated k index indicates summation.

U_{ik} is a tensor of rank which for small deformations is defined as

$$U_{ik} = \frac{1}{2} \left(\frac{\partial U_i}{\partial x_k} + \frac{\partial U_k}{\partial x_i} \right) = \epsilon_{ik} \quad (\text{II-41})$$

U_{ik} gives the magnitude of extension in the \bar{j} direction; similarly U_{ij} gives the magnitude of extension in the \bar{k} direction. The stress tensor σ_{ij} is defined in a similar manner. $F_i = \frac{\partial \sigma_{ik}}{\partial x_k}$ is the force per unit volume component in the \bar{i} direction. σ_{ik} is symmetric and indicates that i 'th component of force per unit area normal to the \bar{k} axis.

In expression (II-40) the repeated indices also imply a summation over the i, j indices, from $i = 1, 2, 3$, and from $j = 1, 2, 3$.

Substitution of (II-37), (II-39) into (II-40) with the use of relation (II-35) verifies the energy balance equation.

6. Stress equations for Viscoelastic Continuous Media - The consideration of a stress problem involves the simultaneous solution of three sets of equations subject to given boundary conditions.

(1) Strain Equations:

$$D \epsilon_{ij} = \frac{1}{2} (\dot{U}_{ji} + \dot{U}_{ij}) \quad (\text{Small Strains}) \quad (\text{II-42})$$

(2) Stress Equations:

$$\sigma_{ij,j} + \rho X_i = \rho f_i \quad (\text{II-43})$$

X_i is the body force, ρ is the density, and g_i the acceleration. If g_i is small,

$$g_i \approx \frac{\lambda^2 U_i}{\lambda t^2}$$

(3) Stress-strain relationships

$$P'(D) \sigma_{kk} = Q'(D) \epsilon_{kk} \quad (\text{Dilation mode}) \quad (\text{II-44})$$

$$P''(D) S_{ij} = Q''(D) e_{ij} \quad (\text{Deviatoric mode}) \quad (\text{II-45})$$

where by definition

$$e_{ij} = \epsilon_{ij} - \frac{1}{3} \delta_{ij} \epsilon_{kk}$$

$$S_{ij} = \sigma_{ij} - \frac{1}{3} \delta_{ij} \sigma_{kk}$$

It is the dilational components that represent pure hydrostatic compression deformation whereas deviatoric components represent pure shear (the sum of the diagonal components is zero). It is often convenient to decompose a compression of a linear solid into pure shear and pure compression.

7. Dynamic Problems - In problems of impact, a fourier time analysis of the applied forces generally exhibits a large contribution from components of high frequency or of small characteristic time. One uses the one-sided fourier transform of $b(t)$ defined by

$$\bar{f}(\omega) = \int_0^{\infty} \exp(-i\omega t) b(t) dt \quad (\text{II-47})$$

The inverse is

$$b(t) = \frac{1}{\pi} R \left[\int_0^{\infty} \exp(i\omega t) \bar{f}(\omega) d\omega \right] \quad (\text{II-48})$$

where $R[X]$ denotes the real part of X .

If $b(t) = 0$ for $t < 0$, then

$$\int_0^{\infty} e^{-i\omega t} \frac{db(t)}{dt} dt = b(t) e^{-i\omega t} \Big|_0^{\infty} + i\omega \int_0^{\infty} e^{-i\omega t} b(t) dt = i\omega \bar{f}(\omega)$$

provided $b(t) e^{-i\omega t} \rightarrow 0$ as $t \rightarrow \infty$. The important thing to observe is that the transform of $\frac{d^n b}{dt^n} = (i\omega)^n \bar{f}(\omega)$.

The significance of the one sided fourier transform is that the stress equations (II-43) and (II-44) can be expressed in linearized form.

Substitution of (II-47) into (II-44) and (II-45) yields

$$P'(i\omega) \bar{\sigma}_{kk} = Q'(i\omega) \bar{\epsilon}_{kk} \quad (\text{II-49})$$

$$P''(i\omega) \bar{S}_{ij} = Q''(i\omega) \bar{e}_{ij} \quad (\text{II-50})$$

But $\frac{Q'(i\omega)}{P'(i\omega)} = Y'(i\omega)$, and $\frac{Q''(i\omega)}{P''(i\omega)} = Y''(i\omega)$ where Y' and Y'' are complex moduli; therefore

$$\bar{\sigma}_{kk} = Y'(i\omega) \bar{\epsilon}_{kk} \quad \bar{S}_{ij} = Y''(i\omega) \bar{e}_{ij} \quad (\text{II-51})$$

Substitution of the one sided fourier transform into (I-42) and (II-43) yields

$$\bar{\epsilon}_{ij} = \frac{1}{2} (\bar{U}_{ji} + \bar{U}_{ij}) \quad (\text{II-52})$$

and

$$\bar{\sigma}_{ij} + \rho \bar{X}_i + \rho \omega^2 \bar{U}_i = 0 \quad (\text{II-53})$$

8. Dynamic Correspondence Principle - The equations for an elastic solid differ from (II-42) through (II-45) only in that $Y'(i\omega)$ and $Y''(i\omega)$ are replaced by $3k$ and 2μ , respectively, where k is the modulus of compression and μ is the modulus of rigidity. Therefore, the correspondence principle states that the solution for a dynamic problem involving a viscoelastic body can be obtained from the solution for the corresponding problem for an elastic body by applying the one sided fourier transform to the elastic solution, replacing the elastic constants by viscoelastic complex constants and inverting the transform. Here is stated the powerful theorem of linear viscoelastic theory. It is the most basic description of the utility of the theory.

9. Application of Dynamic Analysis to Viscoelastic Media - The plastic foam is distinguished by its sensitivity to loading rate. The rate dependent effect is characterized by time dependent coefficients in the stress-strain equation. One should, however, realize that foams are more likely to be non-linear than linear; however, no suitable way of handling non-linear viscoelastic stress problems has been advanced. The stress-strain relationships represent an array of dashpot and spring elements whose spring moduli and dashpot viscosities are in fact those constants (see equations (II-44) and (II-45)). When a LaPlace transform is applied to equations (II-44) and (II-45) for initial conditions, we get:

$$\bar{\sigma}(\omega) = G^{\sigma}(\omega) \bar{\epsilon}(\omega) \quad (II-54)$$

$$\bar{S}(\omega) = G^S(\omega) \bar{e}(\omega) \quad (II-55)$$

where $G(\omega)$ relates the transformed stress to its transformed strain. The correspondence between elastic and viscoelastic equations permits one to deduce the viscoelastic stresses and strains from elastic solutions of any problem provided the LaPlace transformation is possible and a known elastic solution is available. Therefore, while the method of measuring applied stresses and time dependent strains could be complex, the procedure for their determination is identical to that for elastic processes.

The viscoelasticity of materials has been often described in terms of lag angle. The response of a shear specimen to a sinusoidal applied stress is exemplified by the following stress and strain identities:

$$\tau = \tau_o e^{i\omega t} \quad (II-56)$$

$$\gamma = \gamma_o e^{i(\omega t - \delta)} \quad (II-57)$$

where the complex compliance is given by

$$K(i\omega) = \frac{1}{G(i\omega)} = \bar{\gamma}(\omega) / \bar{\tau}(\omega)$$

or

$$K(i\omega) = K'(i\omega) - iK''(\omega) = \frac{\gamma_o}{\tau_o} e^{-i\delta} \quad (II-58)$$

with

$$\gamma_o / \tau_o = (K'^2 + K''^2)^{1/2} \quad (II-59)$$

$$\delta = \tan^{-1} (K''/K') \quad (II-60)$$

The lag angle δ specifies the degree of viscoelasticity. If $\delta = \pi/2$, the material is purely viscous; if $\delta = 0$, the material is purely elastic.

Energy dissipation per unit volume in the medium is given by:

$$\varphi = \int_0^t \sigma \frac{\partial \epsilon}{\partial t} dt = \text{imag} \left[\int \tau \frac{\partial \gamma}{\partial t} dt \right] \quad (\text{II-61a})$$

By inserting into the integral, the expressions involving δ ,

$$\varphi = \tau_0 \gamma_0 \sin \delta \quad (\text{II-61b})$$

However, a further complication of δ is that it depends upon ω , as suggested by (II-60). If $K''(i\omega) = 1/i\omega\eta$ and $K' = 1/E$, then for large ω , $\delta > 0$ and the response is glassy (elastic). For small ω , $\delta > \pi/2$ and the response is viscous. In general, an arbitrary input will have a spectral, or time distribution, which indicates that for most materials the high frequency component waves (rapid times) will propagate elastically and instantaneously. The high speed wave will be attenuated only after a duration when the dashpots have time to activate. After a while, all the dashpots relax and no further additional attenuation is possible. In experiments of pulses propagating through long viscoelastic rods, the pulse has been shown to be broadened by this interaction.

The beautifully simple way of describing the stress-strain behavior of linear viscoelastic media by using the lag angle arguments is useful for comparison of response of real solids to model solids (See Figure II-6). Note that for solid polystyrene and polyethylene plastics, the response is relatively flat over the entire spectral range. The rate sensitivity present in their high density foams should be in the limit, that of the solid specimens.

To further illustrate the method of linearizing the stress-strain equation to solve stress problems in viscoelastic theory, one may utilize the solution to a stress problem of a rod semi-infinitely long. The uniaxial stress-strain equation is written as

$$\frac{\partial \sigma}{\partial x} = \rho \frac{\partial^2 u}{\partial t^2} \quad (\text{II-62})$$

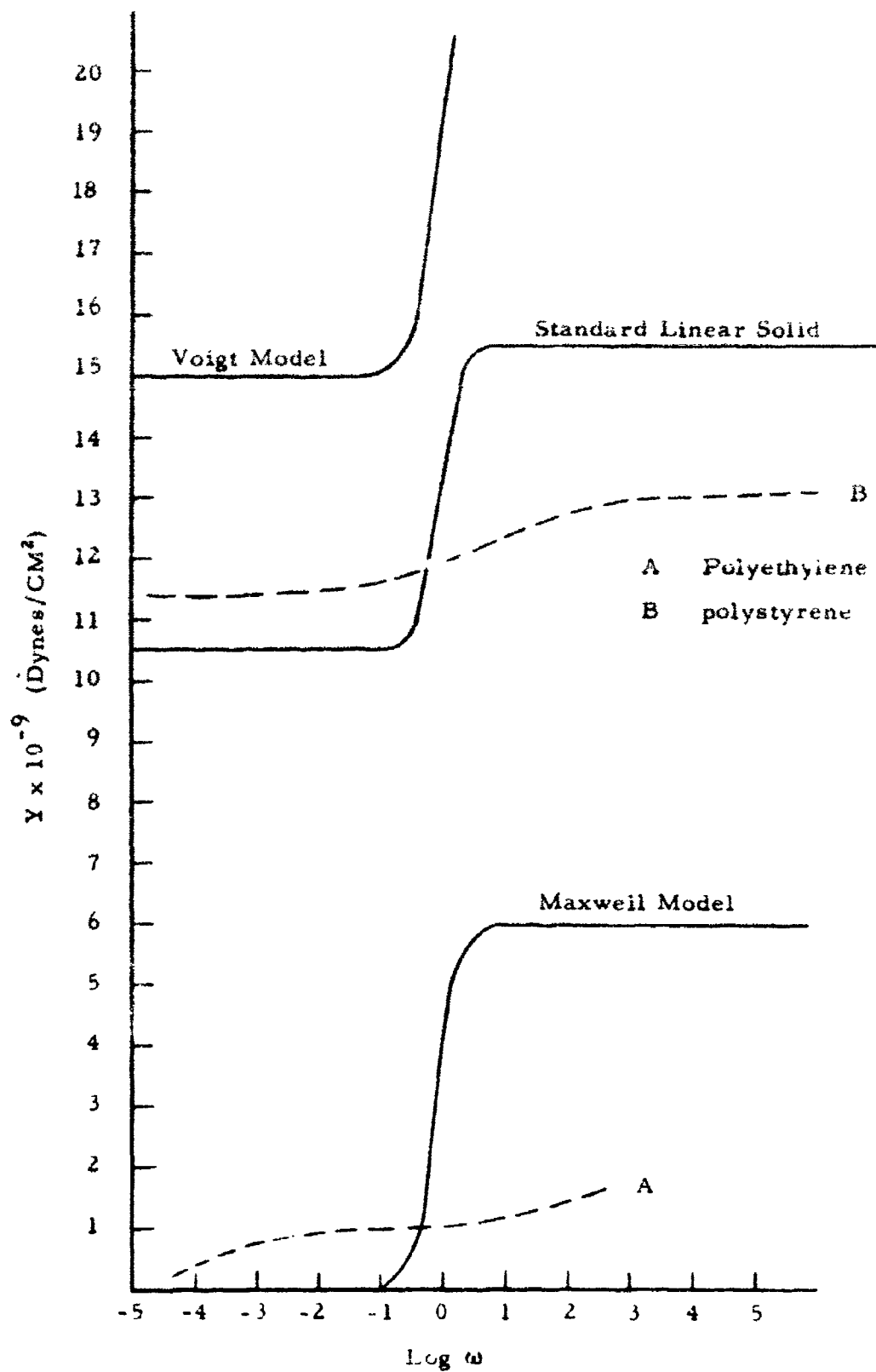


Figure II-6 - Comparison between Response of Model Solids and Measured Values of Real Polymers

where

σ = uniaxial stress

ρ = mass density of V. E. material

u = displacement in the x direction.

Under LaPlace transformation, (II-62) becomes

$$\frac{\partial \bar{\sigma}(i\omega)}{\partial x} = \rho (i\omega)^2 \bar{u}(i\omega) \quad (\text{II-63})$$

where the bar over the parameter indicates the frequency transform.

The one-dimensional stress strain relationship already discussed is

$$P\sigma = Q\epsilon \quad (\text{II-64})$$

where

$$Q/P = E(i\omega)$$

Transforming (II-64) yields

$$\bar{\sigma} = Q/P \bar{\epsilon} = Q/P \frac{d\bar{u}}{dx} = E \frac{d\bar{u}}{dx} \quad (\text{II-65})$$

Substituting (II-65) into (II-63) yields for (II-63)

$$E \frac{d^2 \bar{u}}{dx^2} = \rho (i\omega)^2 \bar{u} \quad (\text{II-66})$$

which has a solution of the form

$$\bar{u}(i\omega) = Ae^{-i\omega x/c(i\omega)} \quad (\text{II-67})$$

where

$$c(i\omega) = \sqrt{E(i\omega)/\rho}$$

$\bar{\sigma}(i\omega)$ could have been solved just as well. By transformation, the desired solution $u(x, t)$ can be obtained. It is important to understand that $E(i\omega)$ will involve several terms for most models. By the choice of models, or specification of $E(i\omega)$ the transform of \bar{u} or $\bar{\sigma}$ would yield different responses.

A classical example is the calculation of $\sigma(x, t)$ for a Maxwellian semi-infinite rod when subjected to an impulse $VH(t)$ at $x = 0$. The initial conditions are

$$\sigma(x, 0) = 0$$

$$\sigma(\infty, t) = 0$$

$$\dot{u}(x, 0) = 0 \quad \dot{u}(0, t) = VH(t)$$

Equation (II-66) can be differentiated with respect to x and rewritten as

$$c^2(i\omega) \frac{\partial^2 \bar{\sigma}}{\partial x^2} - \bar{\sigma} = 0 \quad (\text{II-68})$$

The transformation of (II-68) yields

$$c^2(p) \frac{d^2 \bar{\sigma}}{dx^2} - p^2 \bar{\sigma} = 0 \quad (\text{II-69})$$

where $p = i\omega$

A solution to (II-69) is,

$$\bar{\sigma} = Ae^{-px/c(p)} + Be^{px/c(p)} \quad (\text{II-70})$$

The boundary condition, $\bar{\sigma}(\infty) = 0$, is satisfied if $B = 0$. Since

$$\frac{d\bar{\sigma}}{dx} = -p \bar{\mu} \quad (\text{II-71})$$

$$A = -\rho c p \bar{\mu}(0, p) = \frac{-\rho c V}{p} \quad (\text{II-72})$$

Substituting A in (II-70),

$$\bar{\sigma}(x, p) = \frac{-\rho c V}{p} e^{-px/c(p)} \quad (\text{II-73})$$

Then, by transformation to the time domain,

$$\sigma(x, t) = \int_0^\infty dp \frac{c\rho}{p} V e^{-px/c(p)}$$

If $c(p) = \text{constant}$, which is the case of a pure elastic response,

$$\sigma(x, t) = -c\rho VH(t-x/c) = -c\rho V \begin{cases} 0; & x/c > t \\ 1; & x/c < t \end{cases} \quad (\text{II-74})$$

The interpretation of $c(p) = \text{constant}$ in this problem is that for an elastic system the rod sees no stress at any point, x , until the time $t = x/c$. The compression stress afterwards remains constant. If the stress-strain relationship is Maxwellian, the constant, c , is replaced by

$$c(p) = \frac{c_0 p}{\sqrt{p^2 + E/\eta} p}$$

then

$$\bar{\sigma}(x, p) = \frac{-c \rho V}{\sqrt{p^2 + E/\eta p}} \exp \left[-\frac{x}{c} \sqrt{p^2 + \frac{E}{\eta} p} \right] \quad (\text{II-75})$$

The transform of $\bar{\sigma}$ is

$$\sigma(x, t) = -V \rho c e^{-\frac{Et}{2\eta}} I_0 \left(\frac{E}{2\eta} \sqrt{t^2 - x^2/c^2} \right) H(t-x/c) \quad (\text{II-76})$$

where $I_0(z)$ is the Bessel function of zero order and imaginary argument. This result was first published by Lee & Kanter.⁽²⁹⁾

Letting

$$\beta = \frac{x E}{c \eta}, \quad \tau = \frac{t E}{\eta}, \quad \sigma^s(x, t) = -V \rho c H(t-x/c)$$

$$\frac{\sigma}{\sigma^s} = e^{-\tau/2} I_0 \left(\frac{1}{2} \sqrt{\tau^2 - \beta^2} \right) \quad (\text{II-77})$$

where σ^s is the pure elastic stress solution ($c(p) = \text{constant}$).

$e^{-\tau/2} I_0 \left(\frac{1}{2} \sqrt{\tau^2 - \beta^2} \right)$ is the attenuation function due to the Maxwellian response. At long times the stress becomes attenuated no further. Figure II-7 represents the functional behavior of (II-77).

If the standard linear model solid had been chosen, a similar solution would have followed.

The viscoelastic solutions to the rod problem has been restricted to a semi-infinite length above but may be evaluated for a finite length, l . The correction involves a step-wise superposition of the reflected pressures (stresses) from the stress-free end. The solution is of the form

$$\sigma(x, t) = \sigma_0(x, t) - \sigma_0(2l - x, t) + \sigma_0(2l + x, t) - \sigma_0(4l - x, t) + \dots \quad (\text{II-78})$$

where $\sigma_0(x, t)$ is the solution given in (II-77). This has been pointed out by Nowacki,⁽¹⁸⁾ p. 103

The corrections for a finite length then in principle are possible. The conclusion is that if $c(p)$ can be established by experimental methods, then by choice of a geometry and boundary conditions whose purely elastic solution is available the viscoelastic $\sigma(x, t)$ is solvable.

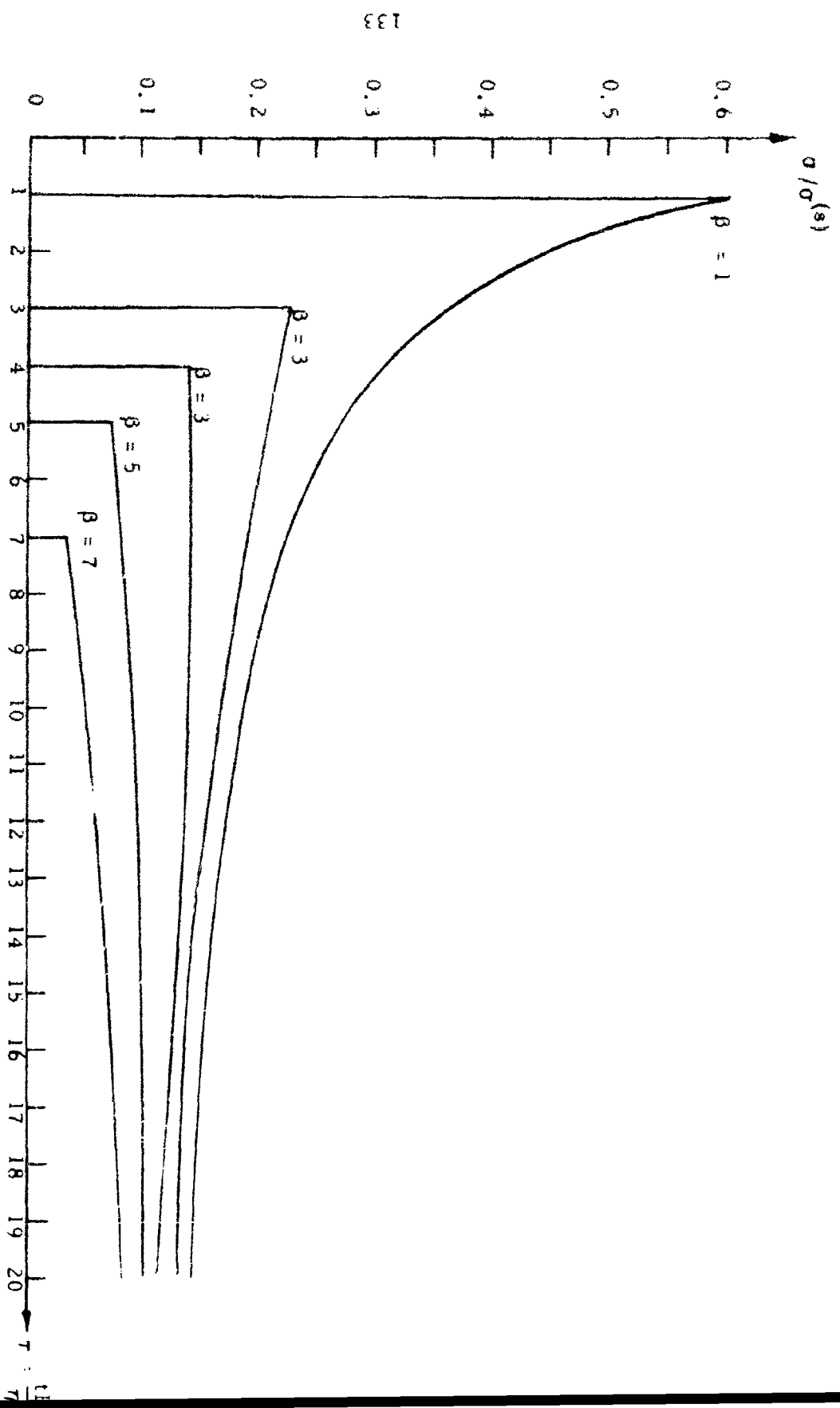


Figure II-7 - Wave Propagation In Finite Rods of Viscoelastic Material

APPENDIX III

Summary of Nuclear Weapons Characteristics

1. Blast Wave Characteristics - There are numerous treatments of the description of a nuclear fission release or explosion. The discussion here is not meant to be an exhaustive repository of blast characteristics but simply a collection of a few pertinent curves from S. Glasstone, ⁽¹¹⁾ for the convenience of describing the loading on an above ground structure. There are two incident pressures in the mechanical blast or shock wave; peak overpressure, which is transient in nature and dynamic or wind pressure, which persists over a somewhat longer period of time. The magnitudes of each of the pressures are functions of distance from the detonation point and time of travel. The duration of a blast wave at a given location depends upon the energy of the burst and the distance from the blast point.

At the surface of any obstacle, more dense than air, in the path of these waves there will be a reflection of the blast wave. The magnitude of the reflected overpressure varies with the strength of the incident overpressure wave and the angle at which the wave front strikes the surface. At any point on the surface, the reflected overpressure is the shock felt by the body. Hence the reflected overpressure is important in loading calculations.

The blast properties of an ideal shock front or blast wave are derived from the Rankine-Hugoniot conditions based on conservation of mass energy and momentum at the shock front. These conditions with the equation of state for air yield the required relations involving the shock velocity, the particle or wind velocity, overpressure, dynamic pressure, and density of air behind the shock front. All the pertinent equations are listed in Table III-1. The significance of the ideal equations are that for the majority of conditions, they give a precise description of the blast behavior and permit the computation of the loading on exposed structures. Figure III-1 is a plot of the blast wave characteristics in terms of the peak overpressure. Figure III-2 through III-4

TABLE III-1
RANKINE-HUGONOT EQUATIONS

| | |
|-------------------------------|---|
| Shock Velocity, U | $U = C_o \left[\left(1 + \frac{\gamma+1}{2\gamma} \right) p/P_o \right]^{1/2}$ |
| U_{air} | $U = C_o \left[1 + 6 p/7 P_o \right]^{1/2}$ |
| Wind Velocity, u | $u = \frac{C_o p}{\gamma P_o} \left(1 + \frac{\gamma+1}{2\gamma} \frac{p}{P_o} \right)^{-1/2}$ |
| u_{air} | $u = \frac{5p}{7P_o} \frac{C_o}{\left(1 + \frac{6p}{7P_o} \right)^{1/2}}$ |
| Density shocked air, ρ | $\rho_{\text{air}} = \rho_o \left[\frac{2\gamma P_o + (\gamma+1)p}{2\gamma P_o + (\gamma-1)p} \right]$ |
| | $\rho_{\text{air}} = \rho_o \left[\frac{7 + 6p/P_o}{7 + p/P_o} \right]$ |
| Dynamic Pressure, q | $q = \frac{1}{2} \rho u^2$ |
| | $q_{\text{air}} = \frac{5}{2} \frac{p^2}{(7 P_o + p)}$ |
| Reflected Overpressure, p_r | $P_r = 2 p + (\gamma+1) q$ |
| | $P_r = 2 p \left[\frac{7 P_o + 4p}{7 P_o + p} \right]$ |

C_o = Ambient speed of sound in unshocked air

γ = Ratio of specific heats

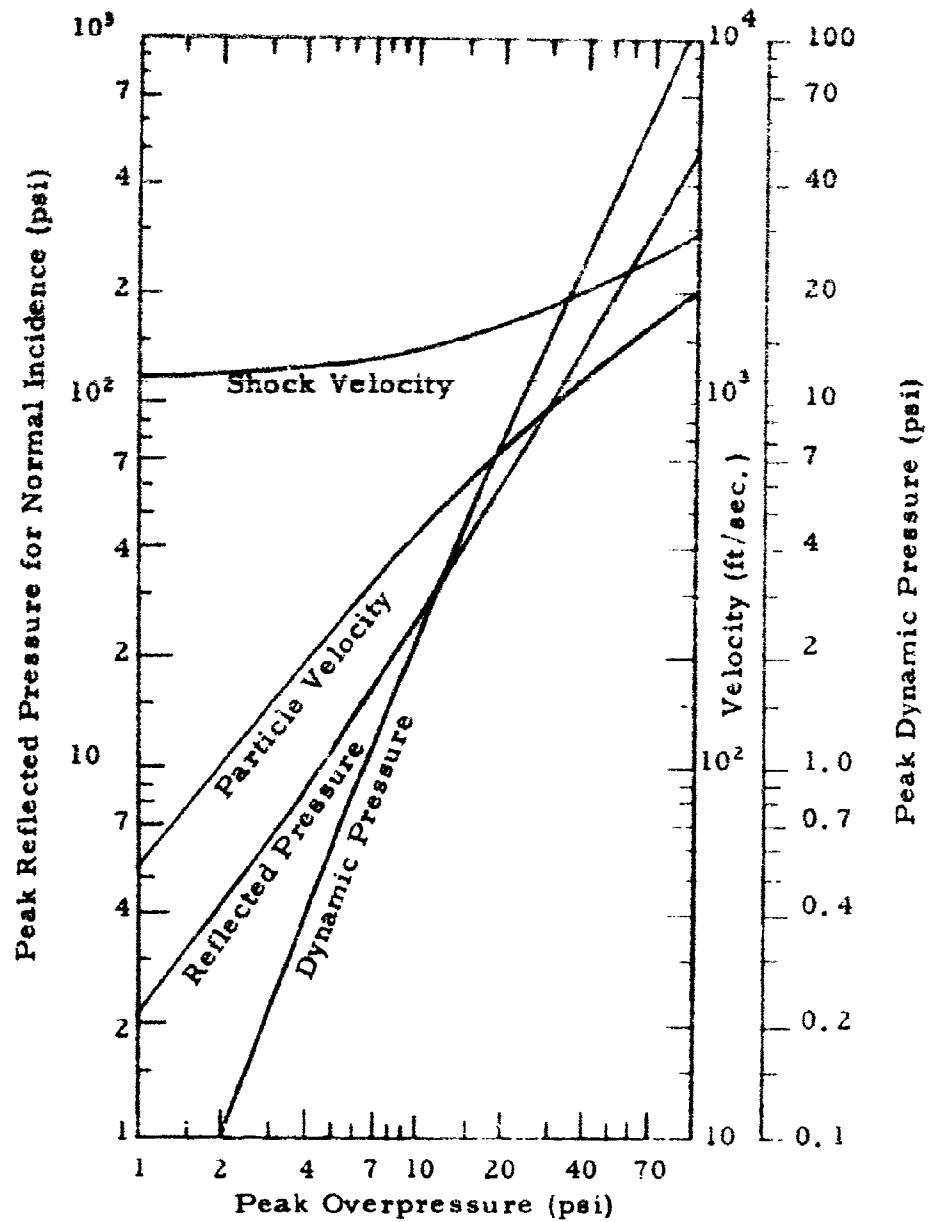


Figure III-1 - Blast Characteristics vs Peak Overpressure

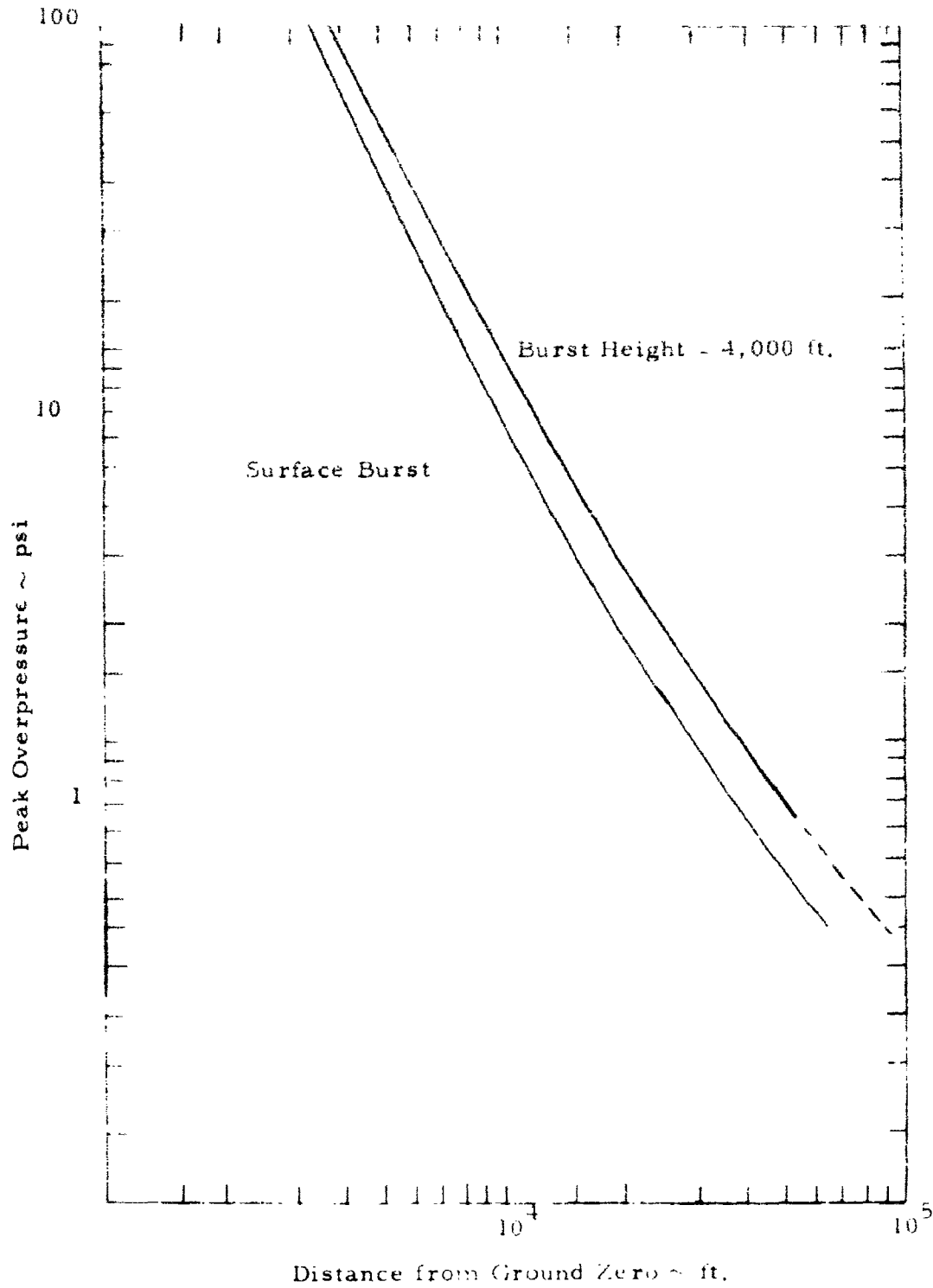


Figure III-2 - Peak Overpressure on the Ground vs Distance from Ground Zero

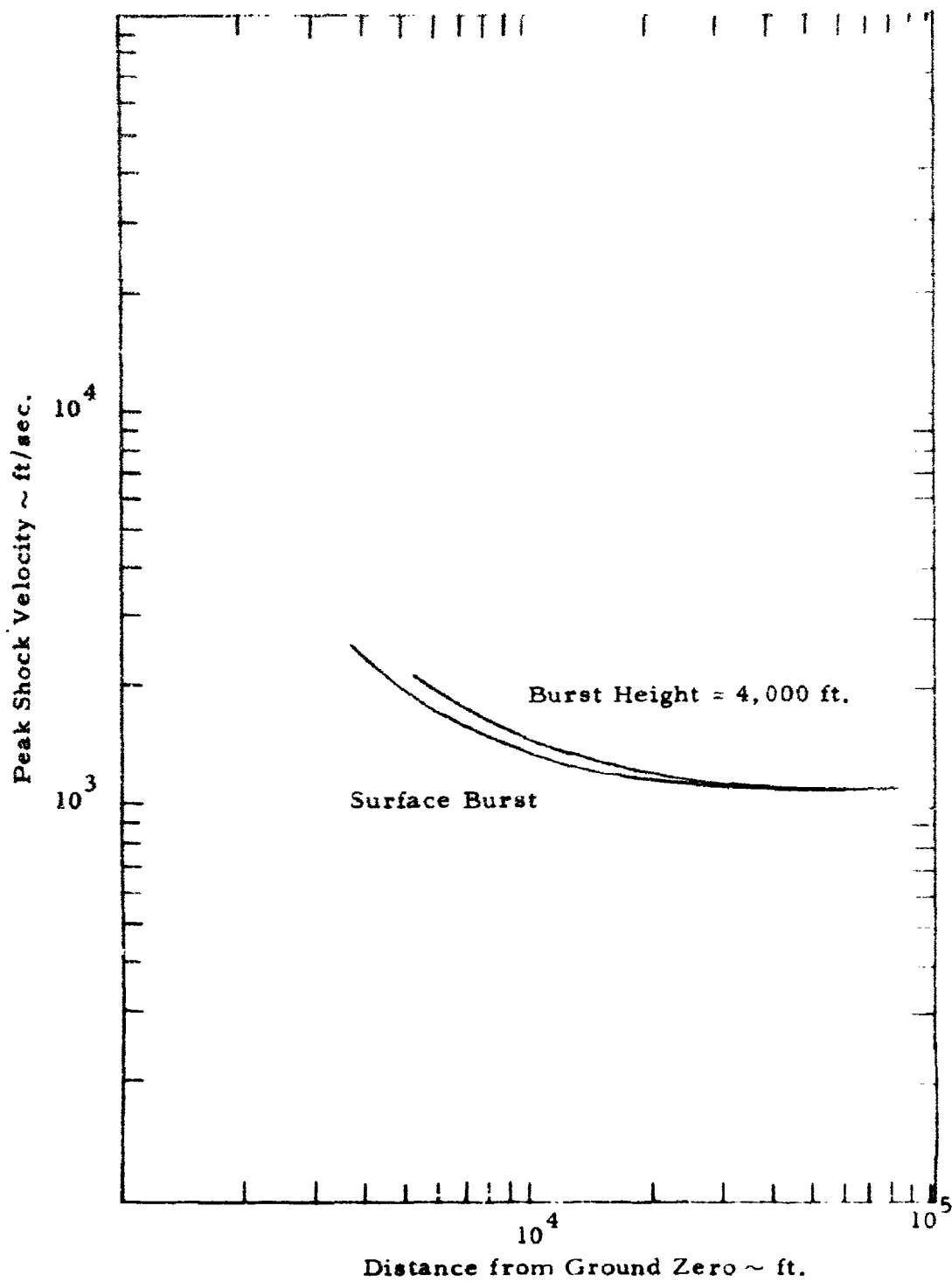


Figure III-3 - Peak Shock Velocity vs Distance from Ground Zero

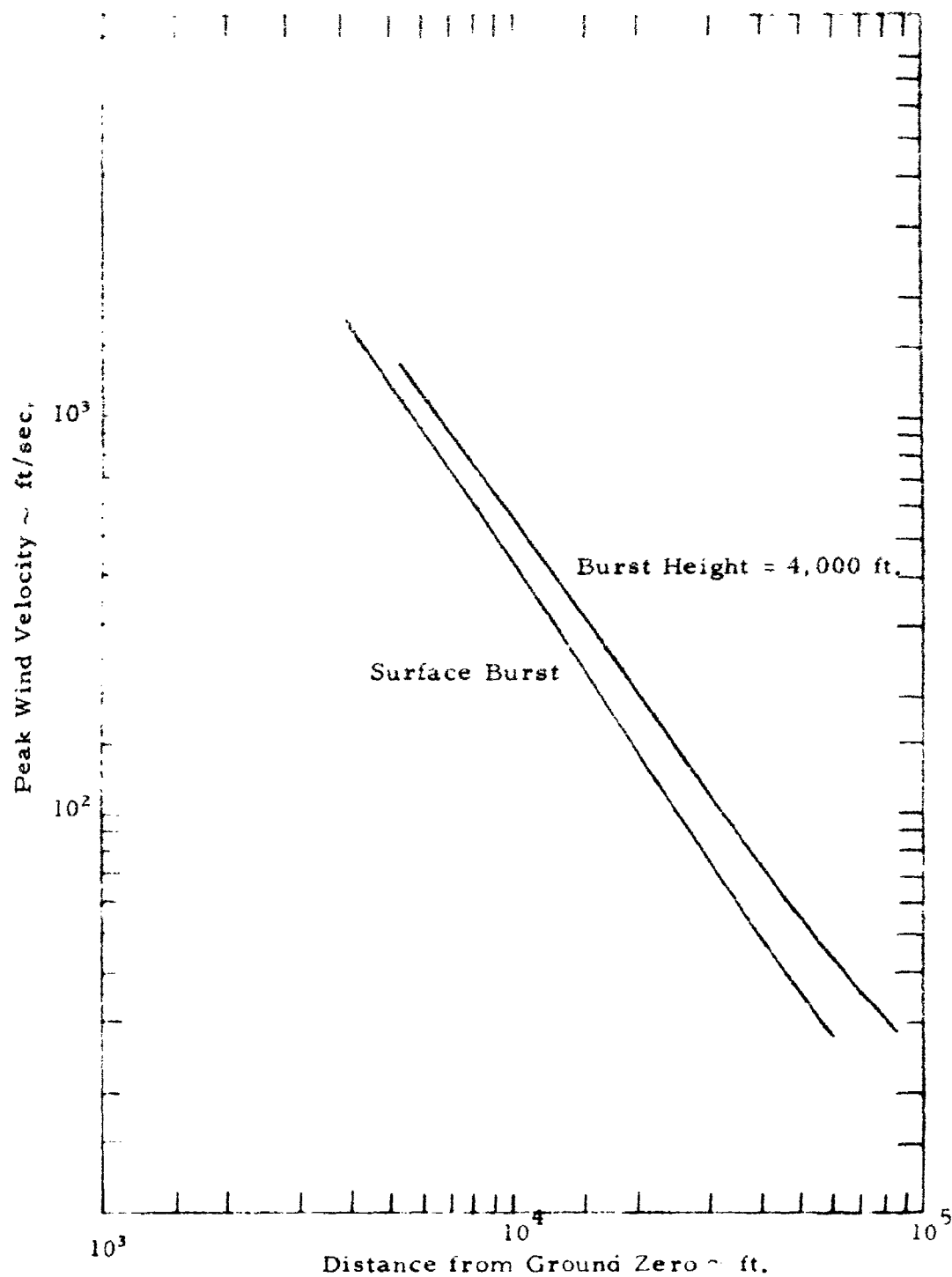


Figure III-4 - Peak Wind Velocity vs Distance From Ground Zero

describe the variation of the blast parameters with distance from ground zero for bursts of the 1 MT size. Figure III-5 shows the importance of incidence angle on reflected overpressure. Furthermore, the pressures are known to decrease at a given place with time according to the empirical exponential laws which are described in Figures III-6 and III-7. The positive phase duration is given in Figures III-8 and III-9 for various distances from ground zero, and also in Figure III-10 as a function of peak overpressure. Note that at higher weapon yields the duration is longer.

The total yield of a nuclear bomb for an atmospheric burst is distributed in blast or shock, thermal radiation, and nuclear radiation. The time integrated quantity of energy from a 1 megaton burst is about 10^{15} calories. About fifty percent of this energy comes off as blast and shock. Its angular distribution of shock energy is difficult to assess but at large distances, isotropic distribution is a useful approximation. The integrated energy density contained in the positive duration of the blast wave is given exactly by

$$E = \int_0^{t_t} p(t) U(t) dt + \int_0^{t_t} q(t) u(t) dt \quad (\text{III-1})$$

The integrals are both complicated and non-closed, due to the time functions in the integral. By graphical approximations or simplifying the time functions, the expression for E may be reduced. Suppose one chooses to solve for the case where $p(0) = 75$ psi and $t_t = 1.5$ sec., by approximation or simplification techniques, one can reduce (III-1) to

$$E = .26 p(0) U(0) + .045 q(0) u(0) \quad (\text{III-2})$$

Thus, setting

$$p(0) = 75 \text{ psi}$$

$$U(0) = 2500 \text{ ft./sec.}$$

$$q(0) = 75 \text{ psi}$$

$$u(0) = 1800 \text{ ft./sec.}$$

Substitution into (III-2), the appropriate values yield $E = 7.7 \times 10^6 \frac{\text{ft-lb}}{\text{ft}^2}$

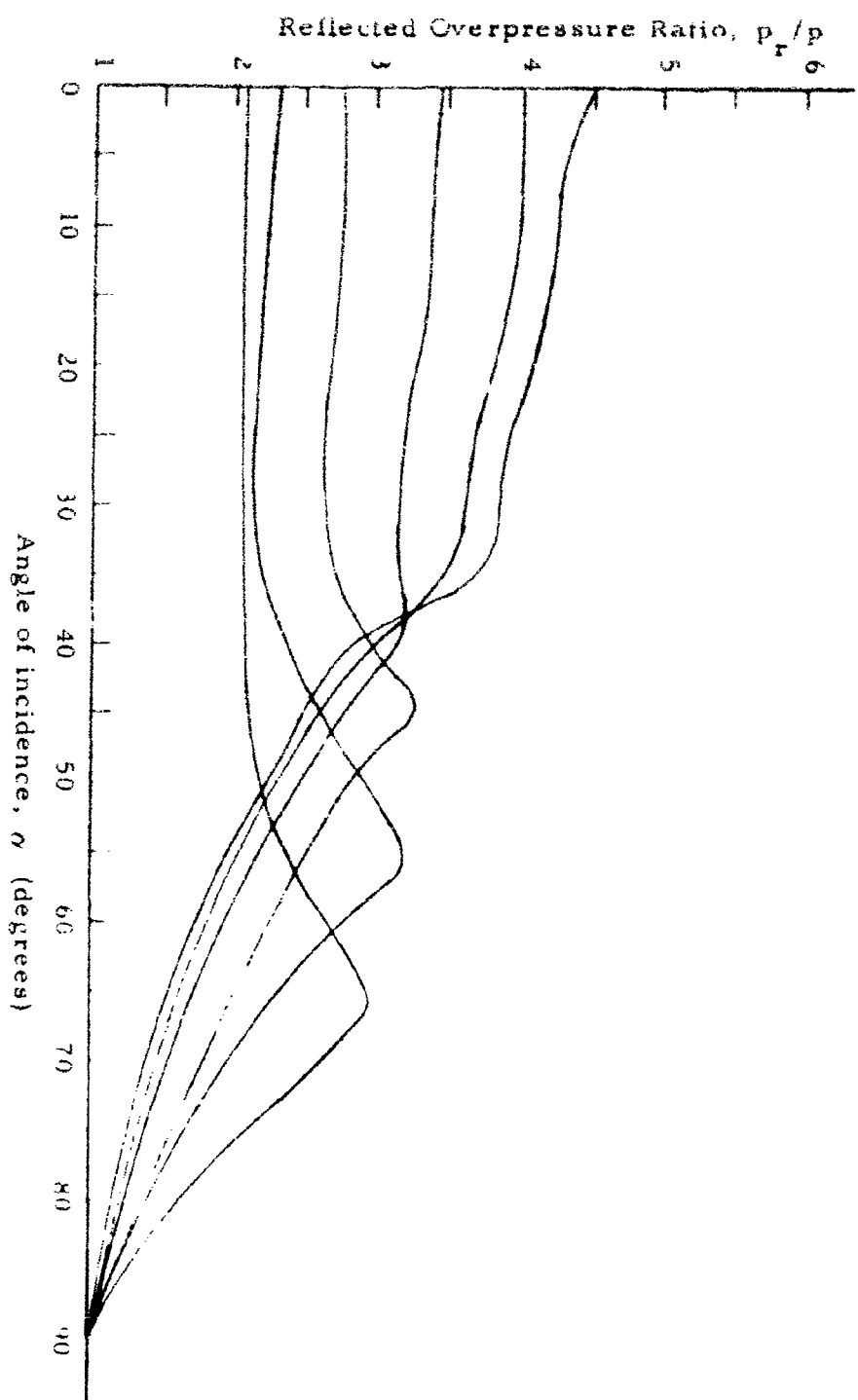


Figure III-5 - Reflected Overpressure Ratio vs Angle of Incidence

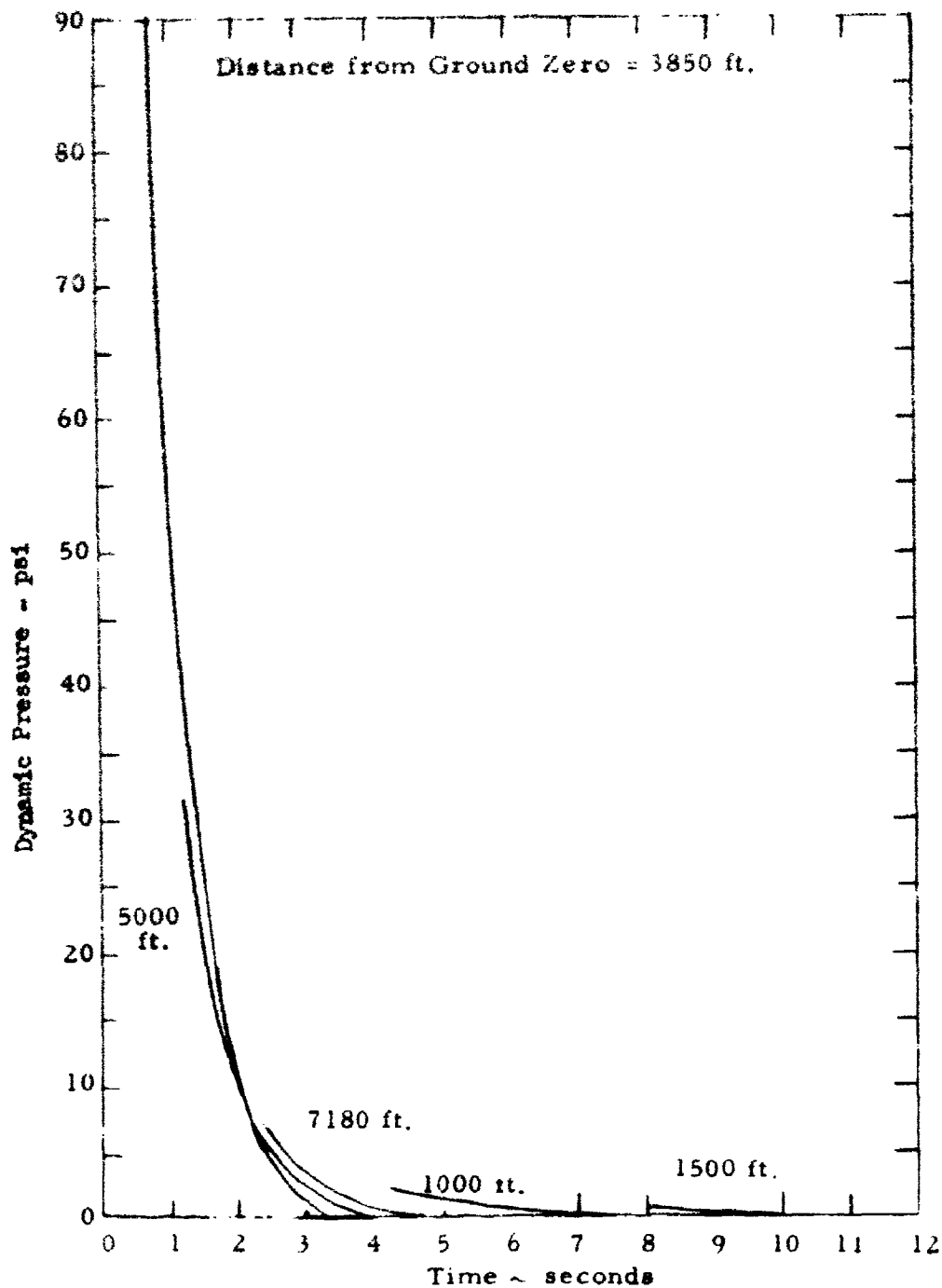
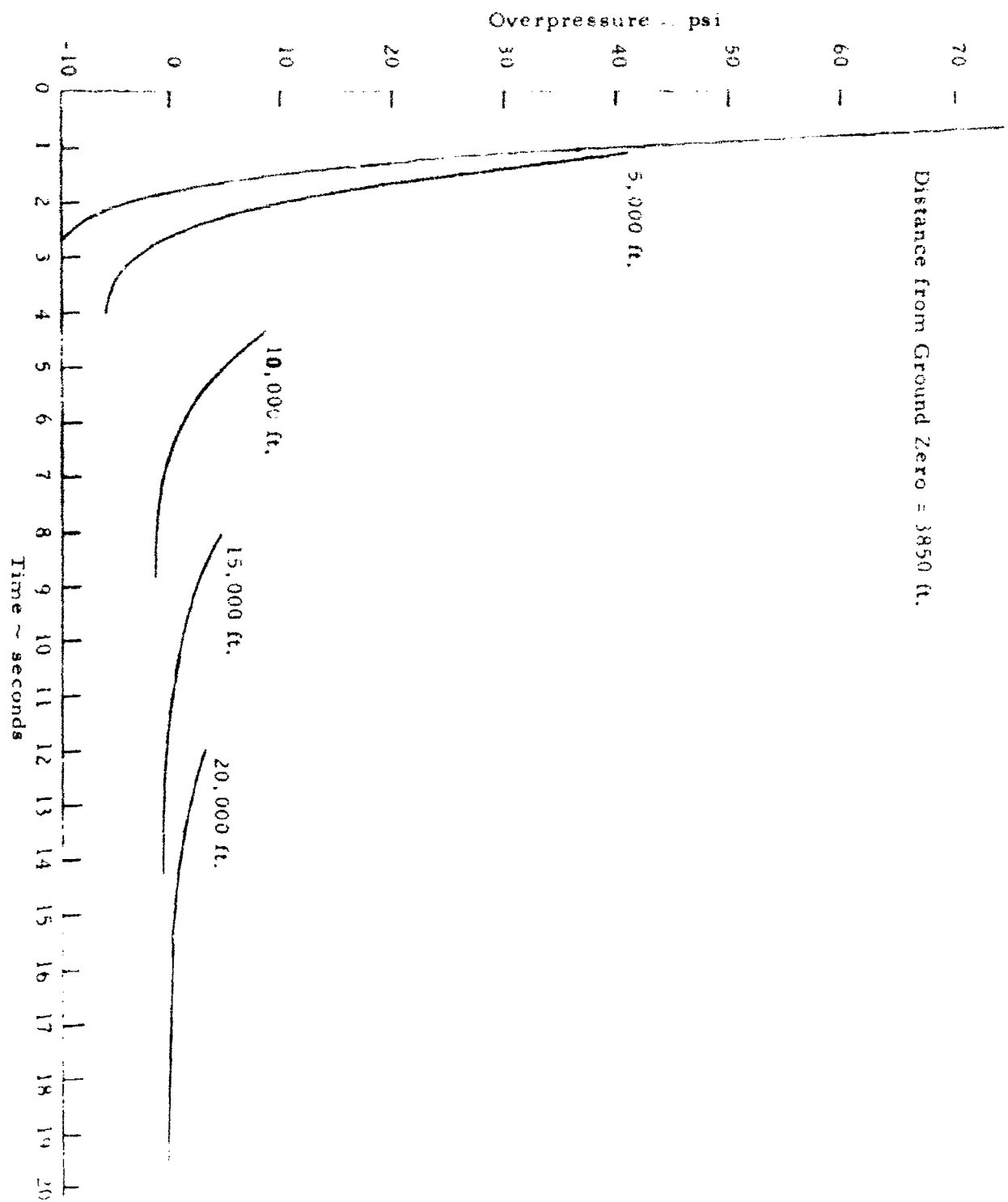


Figure III-6 - Decay Curves of Dynamic Pressure Surface Burst



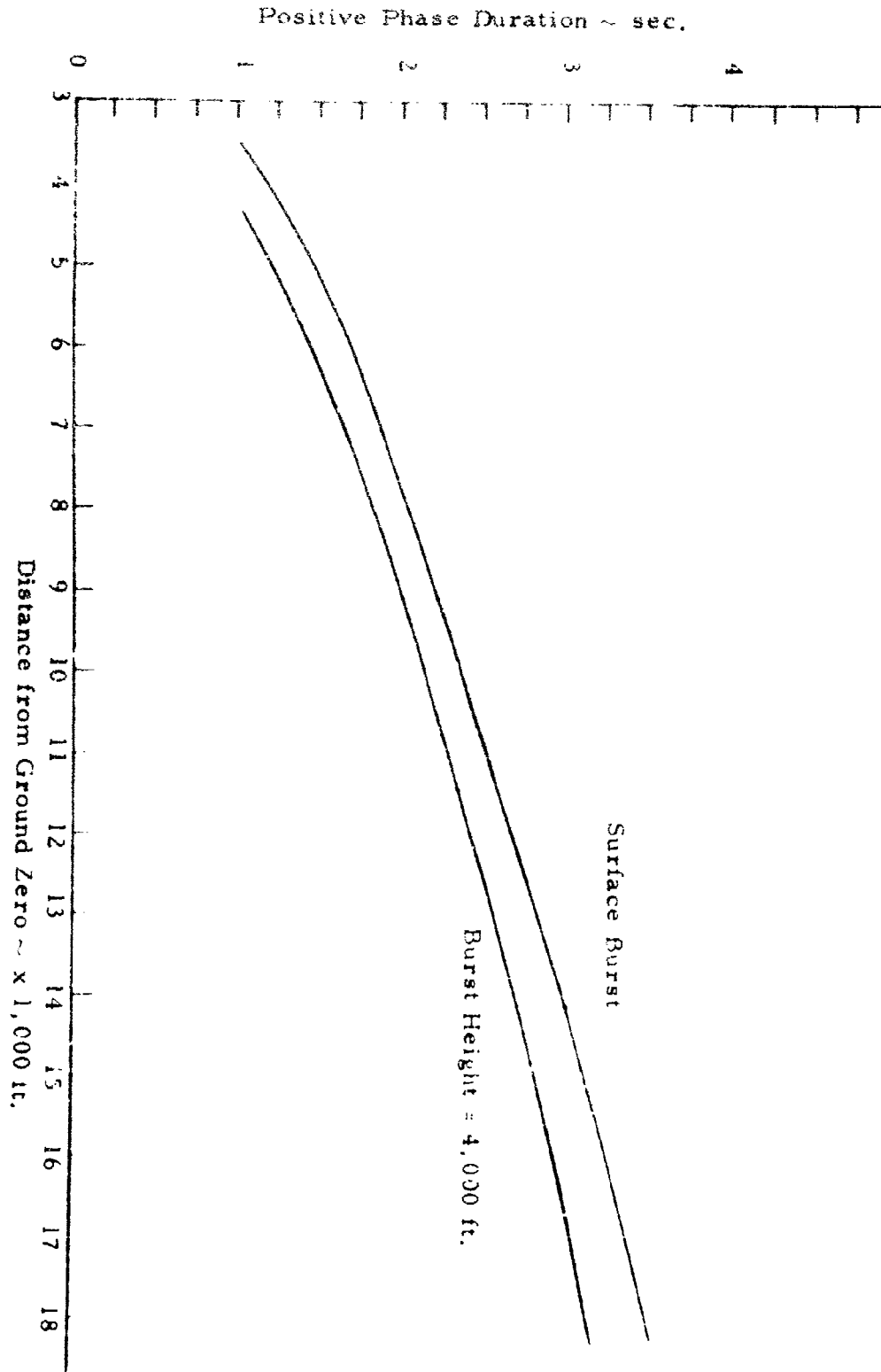


Figure III-8 - Positive Phase Duration on the Ground of Overpressure

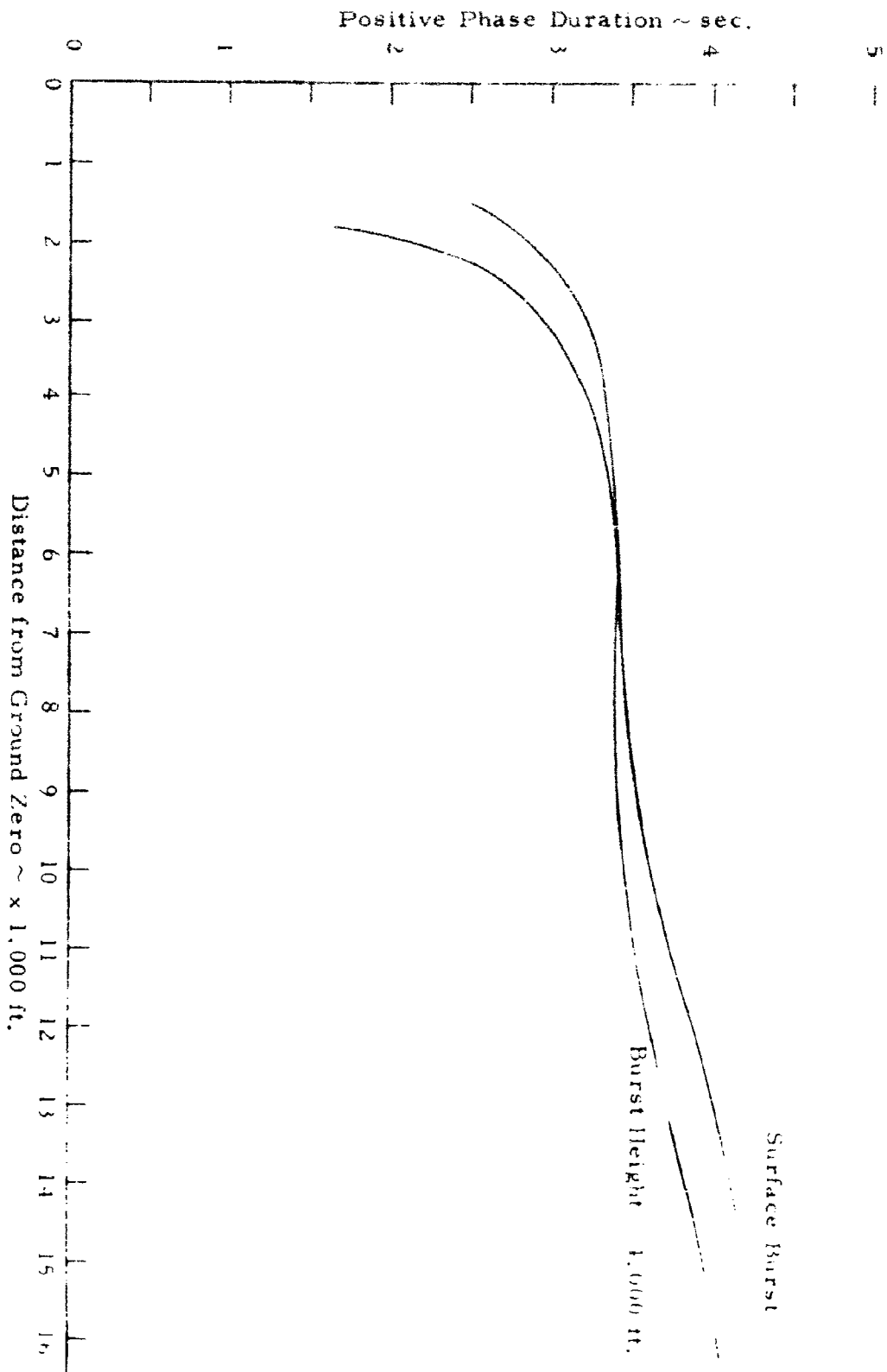


Figure III-9 - Positive Phase Duration on the Ground of Dynamic Pressure

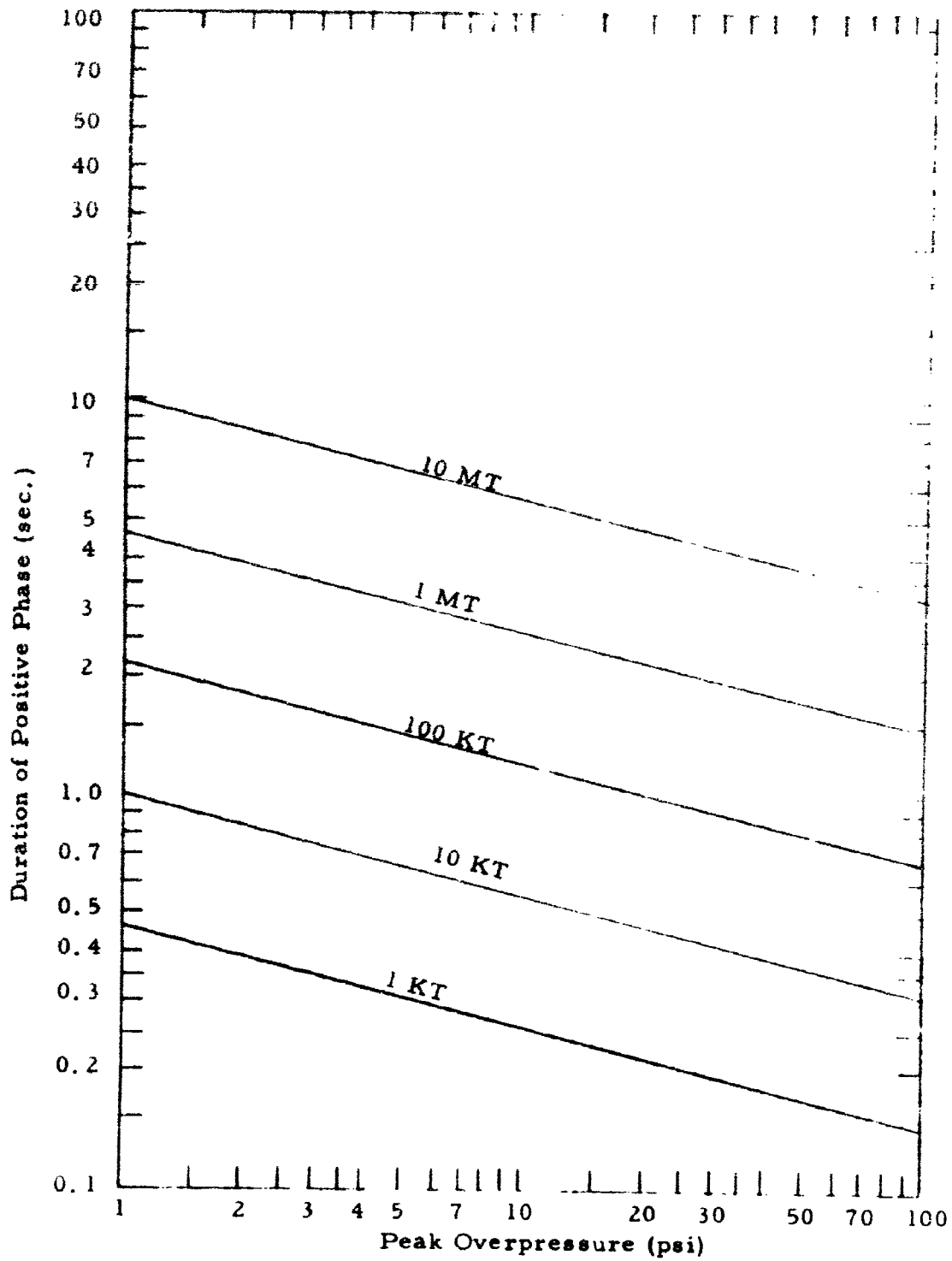


Figure III-10 - Duration of Positive Phase - Typical Air Burst

By assuming an isotropic distribution one would obtain

$$E = \frac{3 \times 10^{15} \text{ ft-lb.}}{4 \pi (4,000 \text{ ft})^2} = 1.5 \times 10^7 \frac{\text{ft-lb}}{\text{ft}^2}$$

which is several times as large as the approximate integral solution.

The usefulness of this computation is that it shows how tremendously energetic the blast wave is. Figure III-11 shows approximately how blast energy density computed by approximate integral solutions is expected to vary with incident peak overpressure.

2. Thermal Radiation Characteristics - The normal procedure in describing the thermal radiation from a nuclear blast is to estimate the average temperature of the fireball which is assumed to be of blackbody distribution. For a blackbody, the distribution of radiant energy is a function of photon frequency and temperature given by:

$$E_{\lambda} = \frac{8}{\lambda^5} \frac{hc}{e^{hc/KT} - 1} \quad (\text{III-3})$$

where

- c = velocity light
- h = Planck's constant
- K = Boltzmann's gas constant
- T = absolute temperature
- $E_{\lambda} d\lambda$ = energy density, energy per unit volume in wavelength interval, λ to $\lambda + d\lambda$.

The rate of energy from the "blackbody" fireball which is on the order of several thousand degrees Kelvin is given by:

$$J_{\lambda} = \frac{c}{4} E_{\lambda} \quad (\text{III-4})$$

The interesting consideration is the wavelength where the blackbody distribution peaks, given by the relationship

$$\lambda_m = \frac{2.9 \times 10^7}{T} \quad (\text{angstrom} - ^\circ\text{K}) \quad (\text{III-5})$$

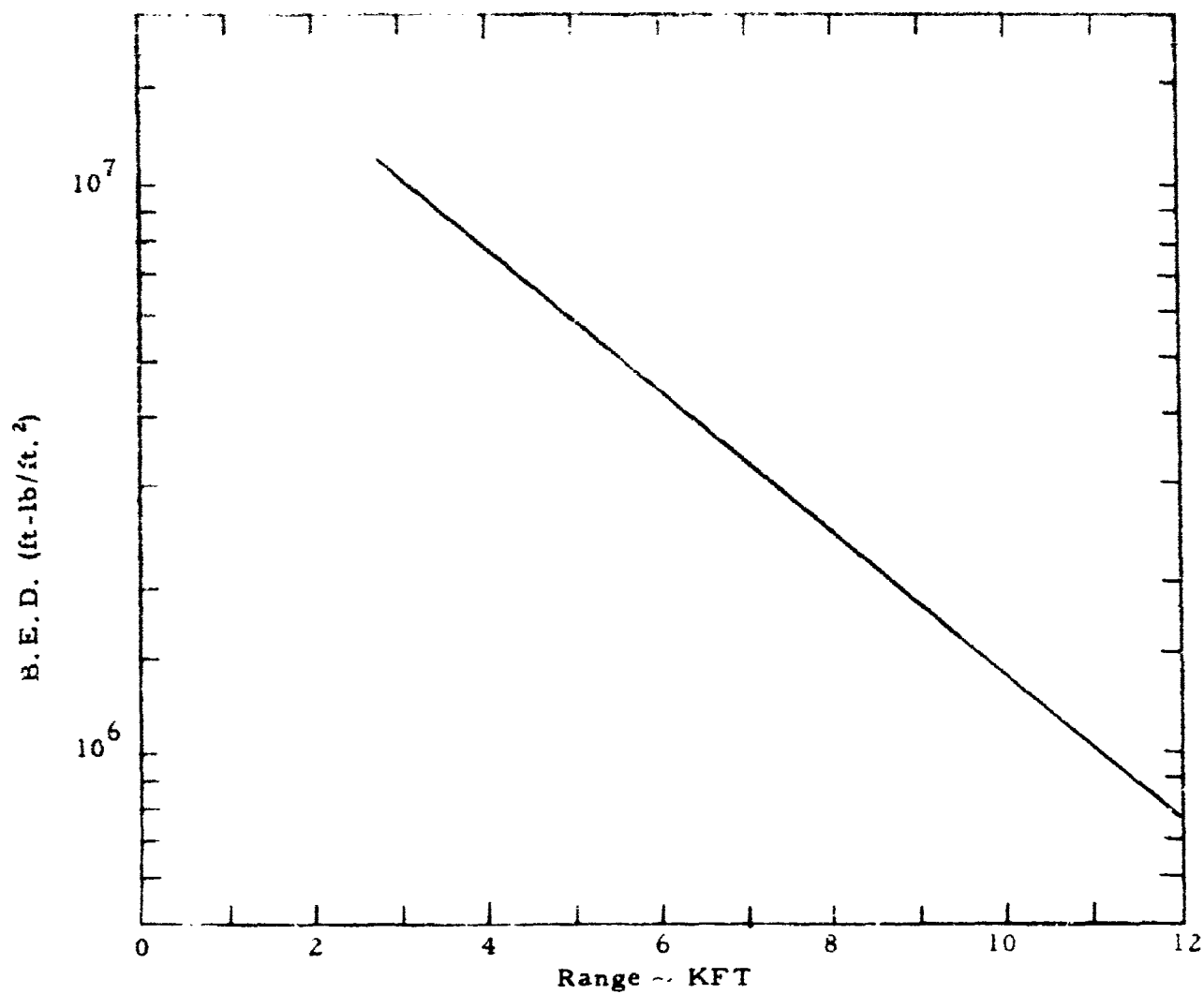


Figure III-11 - Blast Energy Density vs Range

Figure III-12 is a plot of the spectral energy density for a 6,000°K source. Note that most of the energy is located in the visible domain. Note further that the spectrum is finite over the entire spectral range but falls off rapidly at the X-ray and far infra-red extremities. The temperature of the fireball will depend upon the state of the air present where the bomb detonation occurs but the bulk energy features for low altitude bursts (less than 100,000 feet) will not be greatly different.

The total radiant energy per square centimeter per second from a blackbody fireball is taken to obey the Stefan-Boltzmann law,

$$J = 1.4 \times 10^{-12} T^4 \left(\frac{\text{cal}}{\text{cm}^2 \text{sec}^\circ \text{K}^4} \right) = \int_0^\infty J_\lambda d\lambda \quad (\text{III-6})$$

The rate of energy leaving a fireball of radius R in feet is given by

$$P = 1.6 \times 10^{-8} T^4 R^2 \frac{\text{cal}}{\text{sec}} \quad (\text{III-7})$$

The energy, however, is emitted in two pulses, the first pulse being highly peaked but of short duration ($\sim 1\%$ of total energy), and the second being peaked at t_{max} but considerably broader. The maximum power which one observes at t_{max} obeys the law,

$$P_{\text{max}} = 4W^{1/2} \text{ kilotons/second} \quad (\text{III-8})$$

where W is the yield of the bomb in kilotons. The value of t_{max} is given approximately by

$$t_{\text{max}} = .032 W^{1/2} \text{ seconds} \quad (\text{III-9})$$

The total amount of thermal energy emitted by the fireball in any air burst up to any specified time can be obtained from the area under the Power vs Time curve. The total thermal energy of a bomb is usually about 33%. Hence,

$$E_{\text{tot}} (\text{kilotons}) = \frac{1}{3} W \quad (\text{III-10})$$

The thermal energy received, i.e., the radiant exposure, at any distance D from the explosion, is given by

$$Q = \frac{E_{\text{total}}}{4D^2} e^{-KD} \quad (\text{III-11})$$

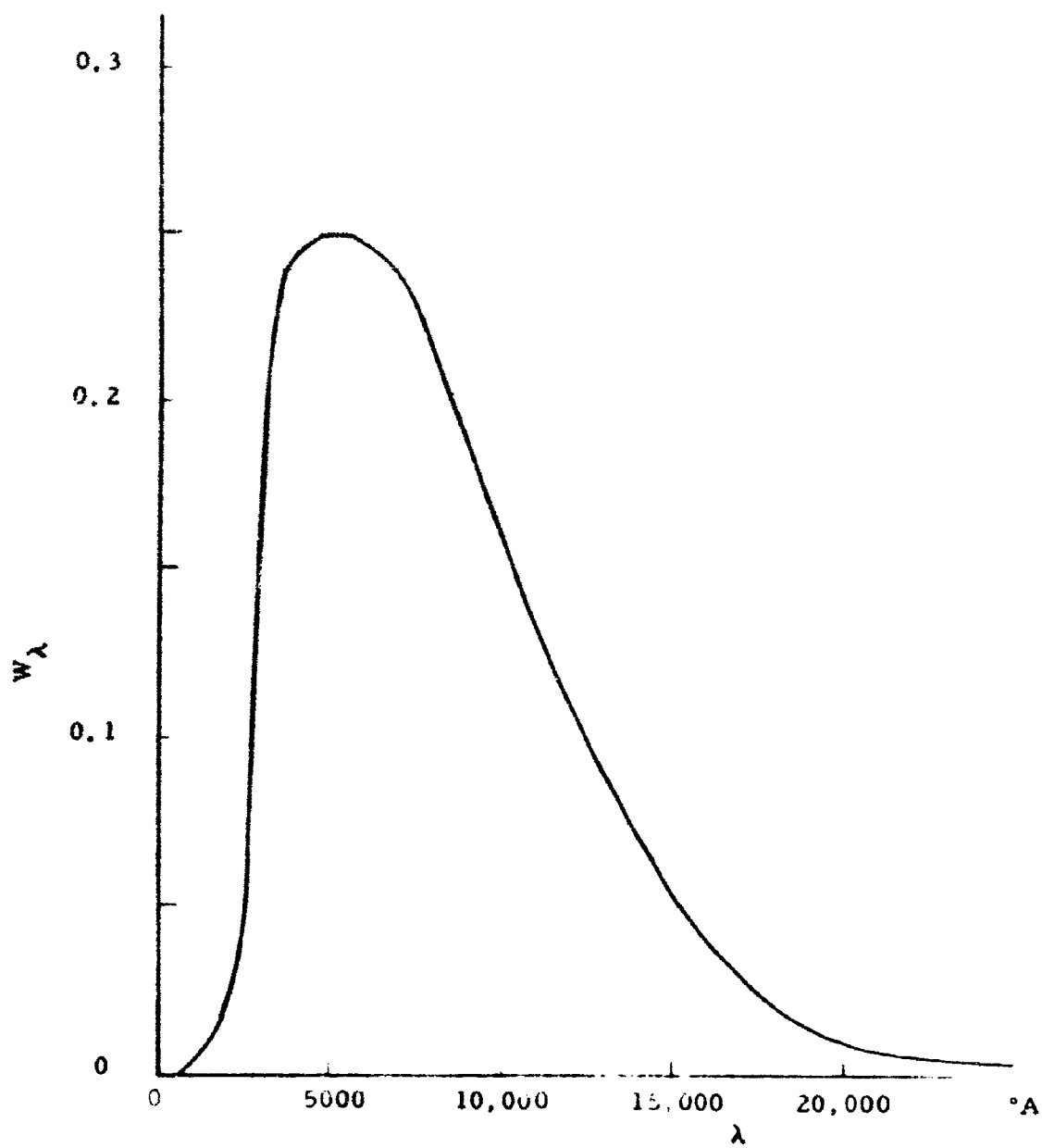


Figure III-12 - 6,000° Black Body Distribution

where t^{-KD} is the thermal energy transmittance of the atmosphere. The transmittance is also a function of atmospheric conditions, and the spectral content of the thermal blast wave.

In general, many initial conditions affecting a blast and its environment are possible. For this reason, the effort here is simply to present the curves, Figures III-13 to Figure III-19, which are representative of the expected thermal characteristics of a typical 1 MT air burst detonation under clear visibility conditions. The data for the curves have all been taken from "Effects of Nuclear Weapons".

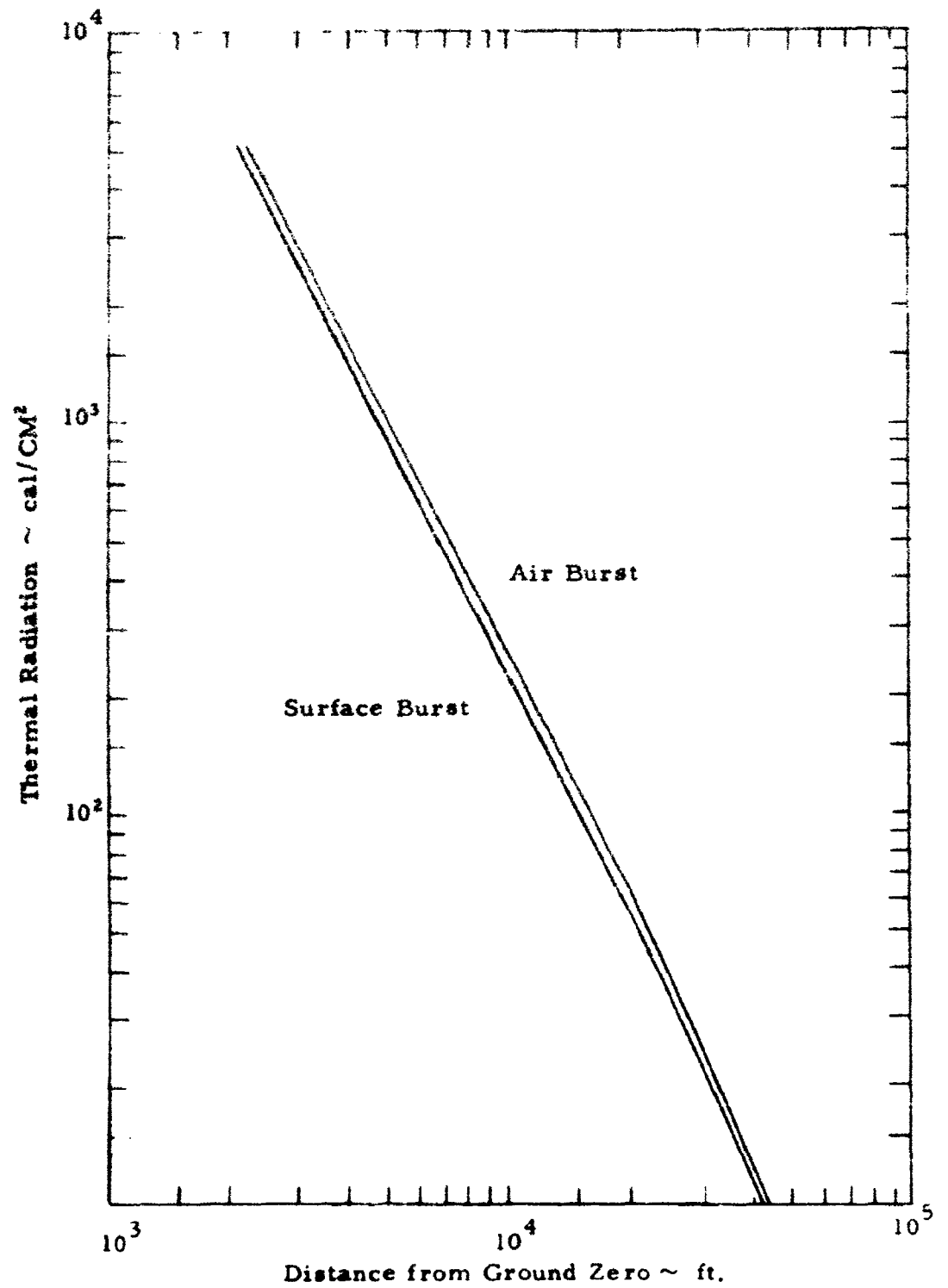


Figure III-13 - Total Thermal Radiation Dose vs Distance from Ground Zero

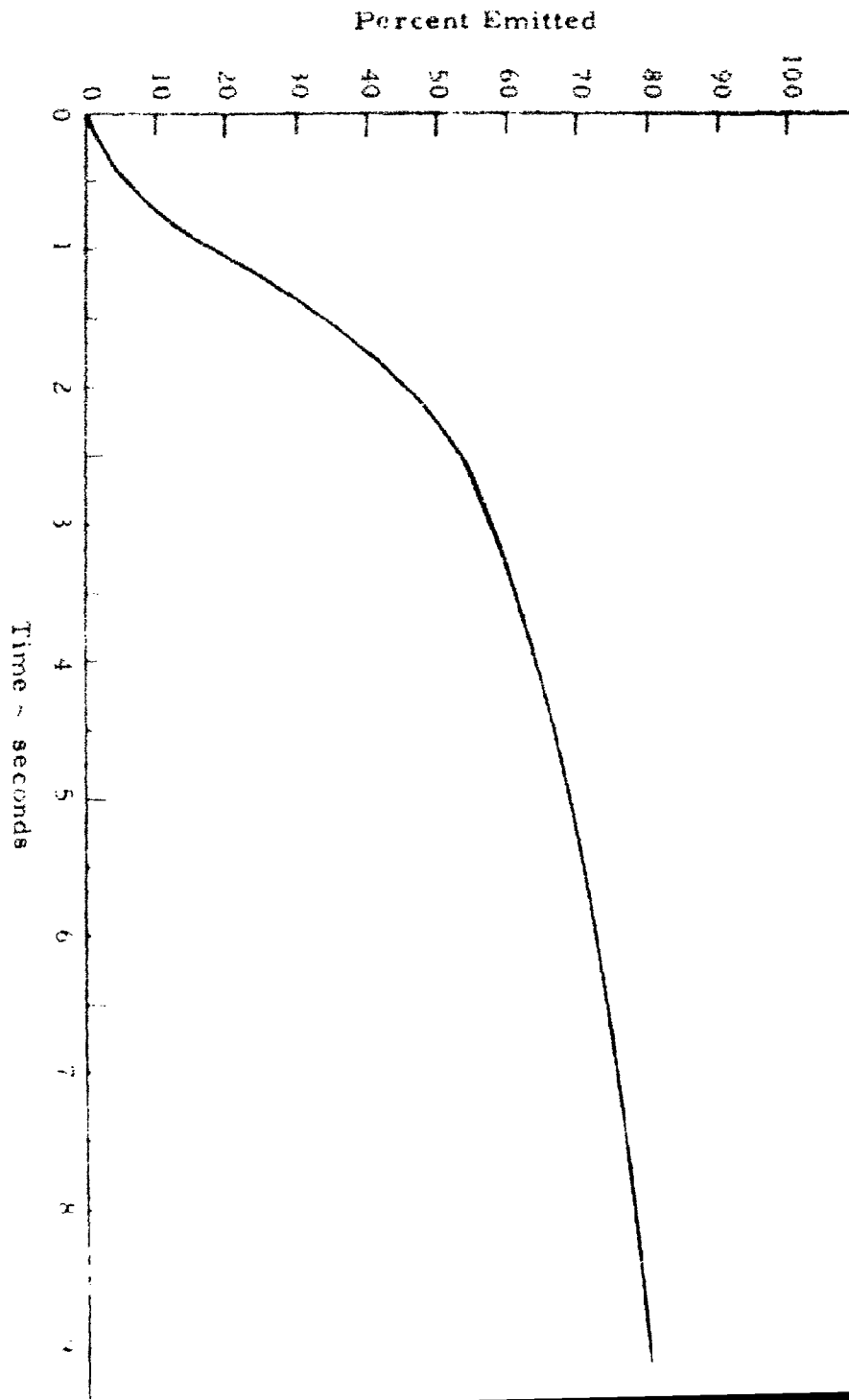


Figure III-14 - Percent of Thermal Radiation Emitted

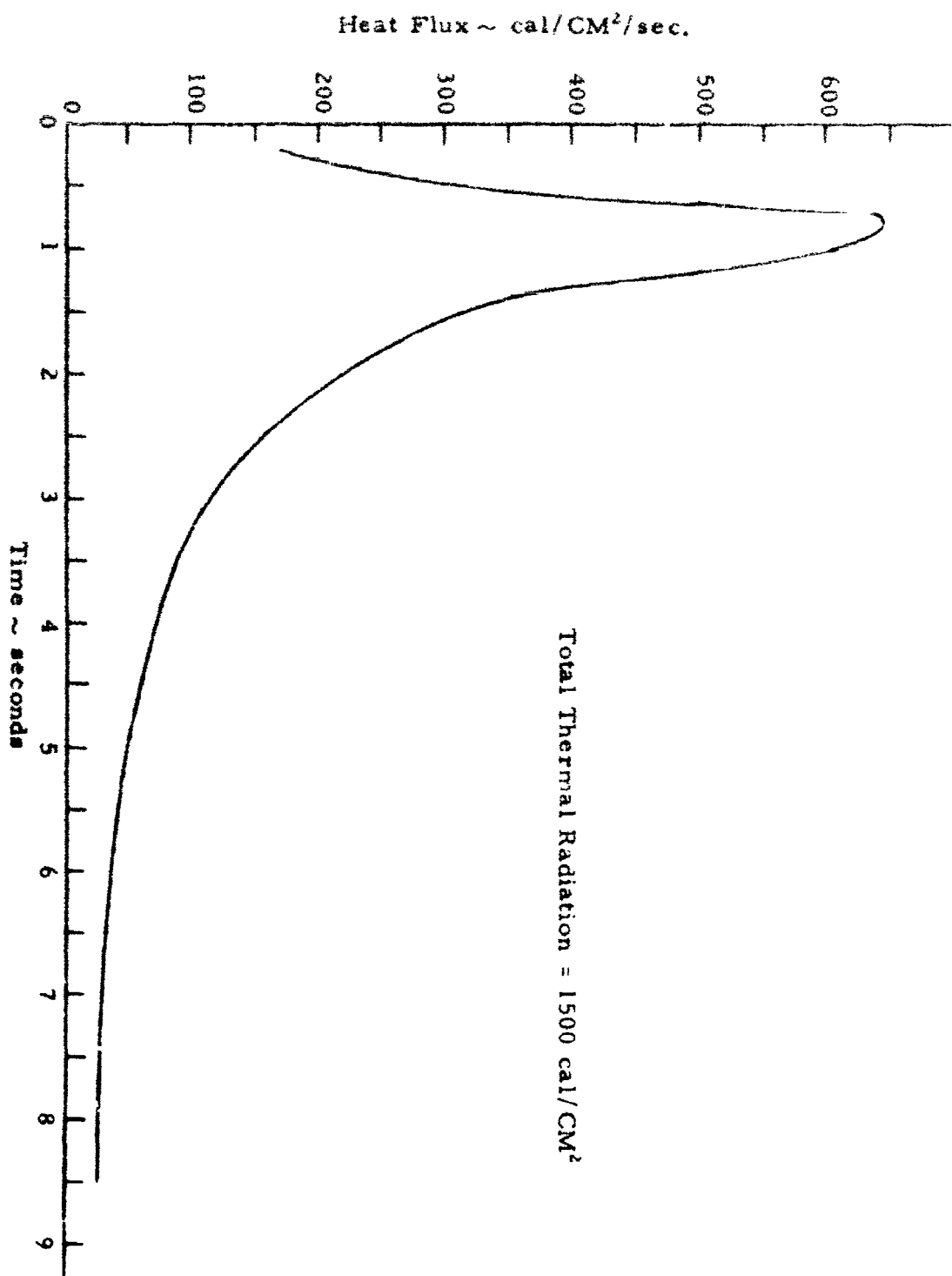


Figure III-15 - Heat Flux Surface Burst 3, 850 ft. from Ground Zero

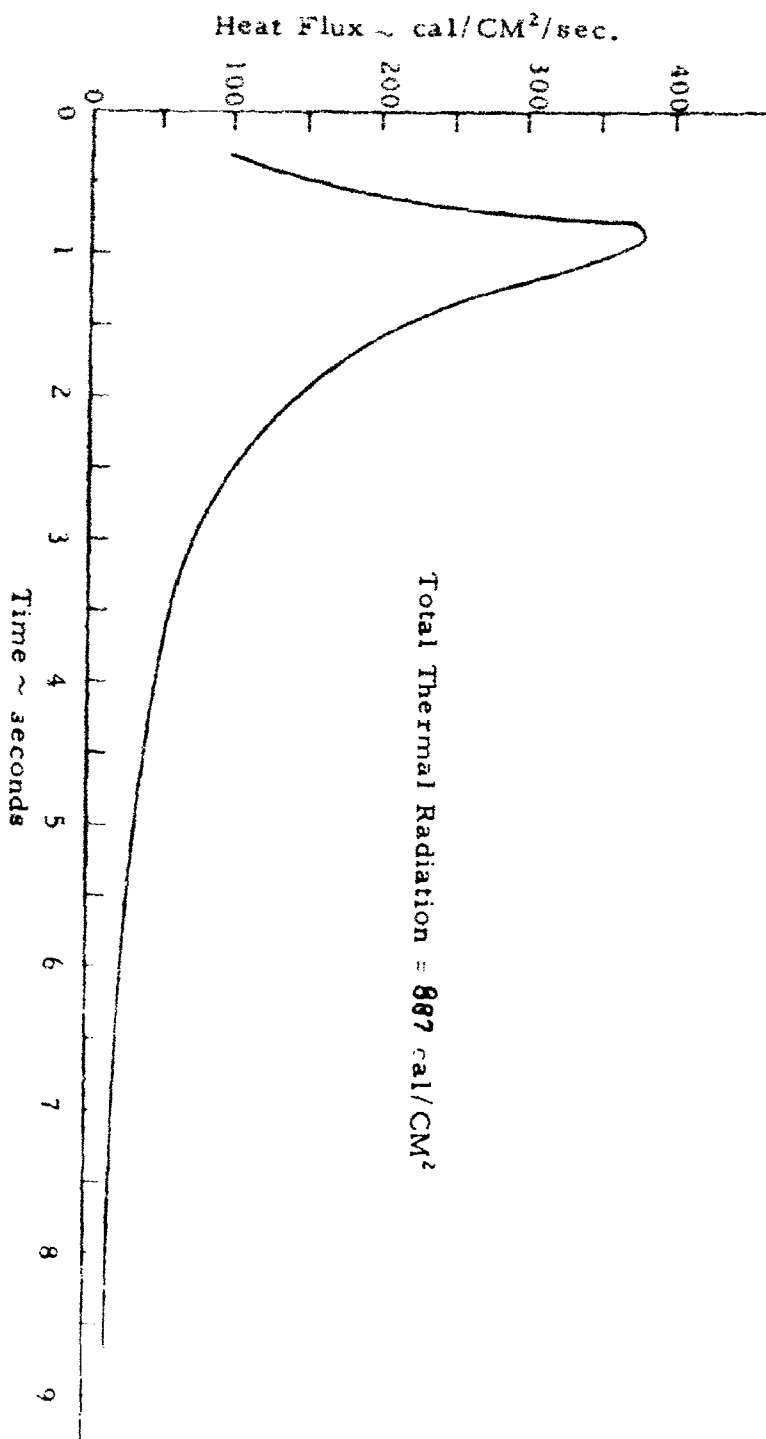


Figure III-16 - Heat Flux Surface Burst 5,000 ft. from Ground Zero

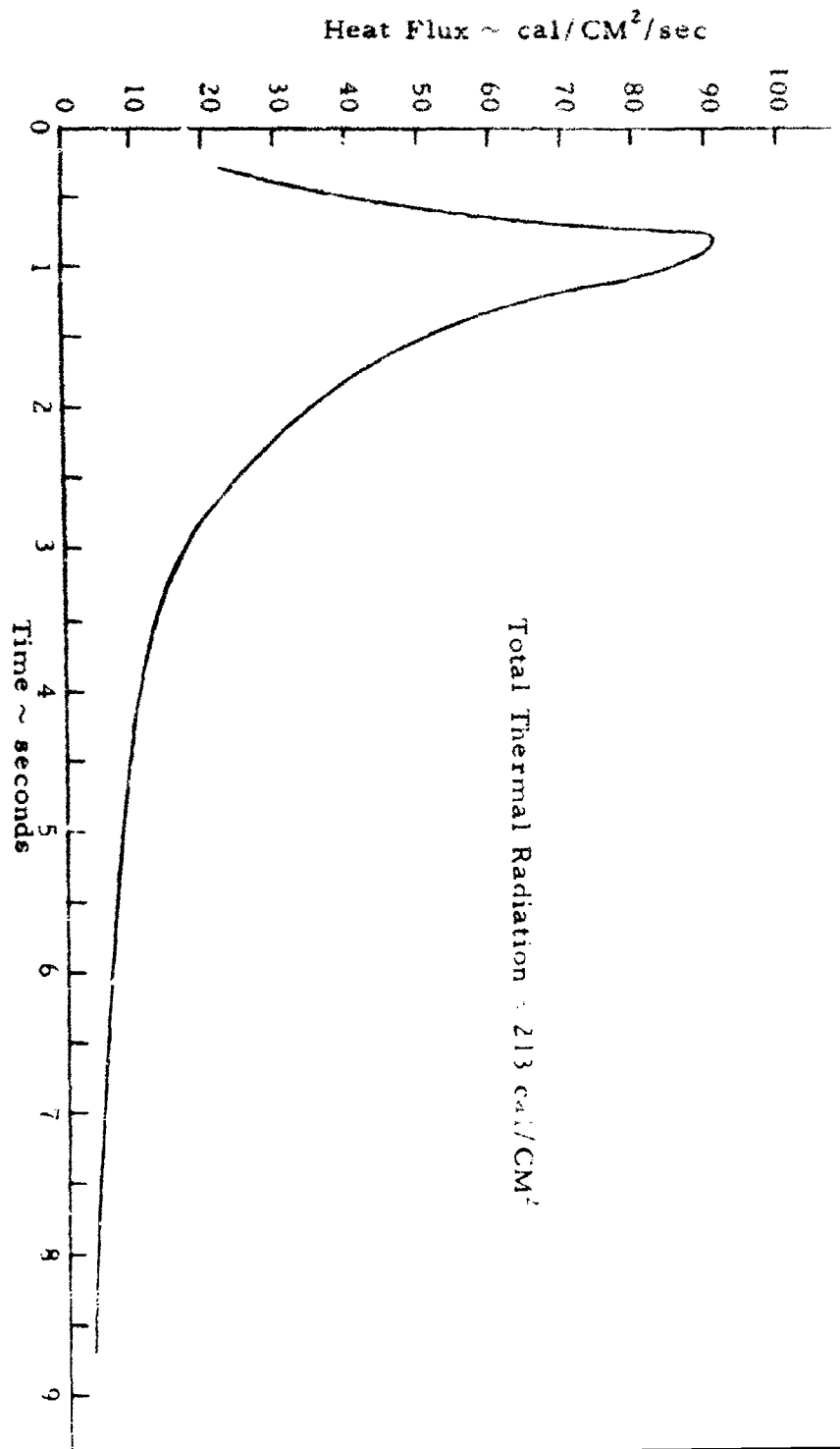


Figure III-17 - Heat Flux Surface Burst 10,000 ft. from Ground Zero

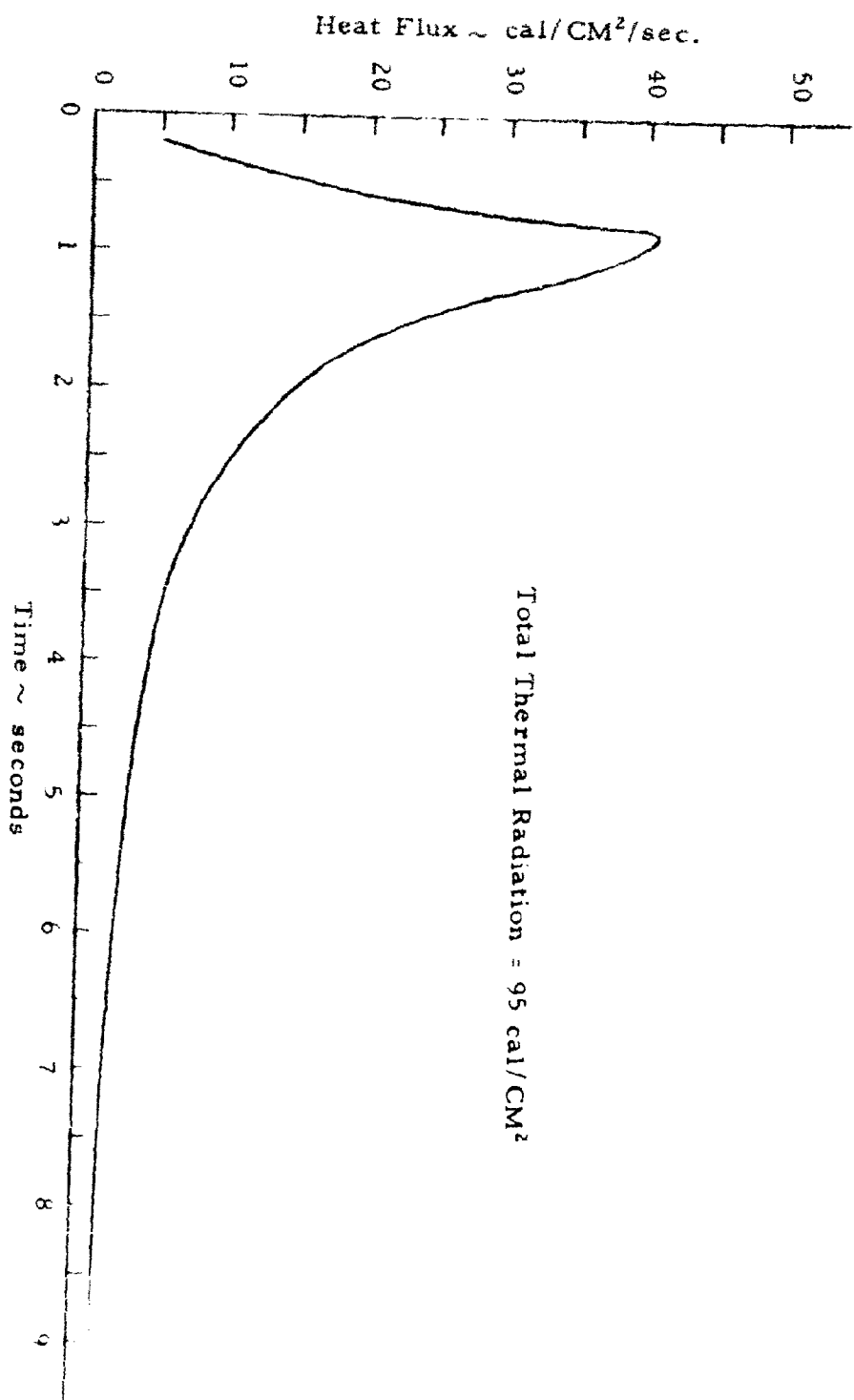


Figure III-18 - Heat Flux Surface Burst 15,000 ft. from Ground Zero

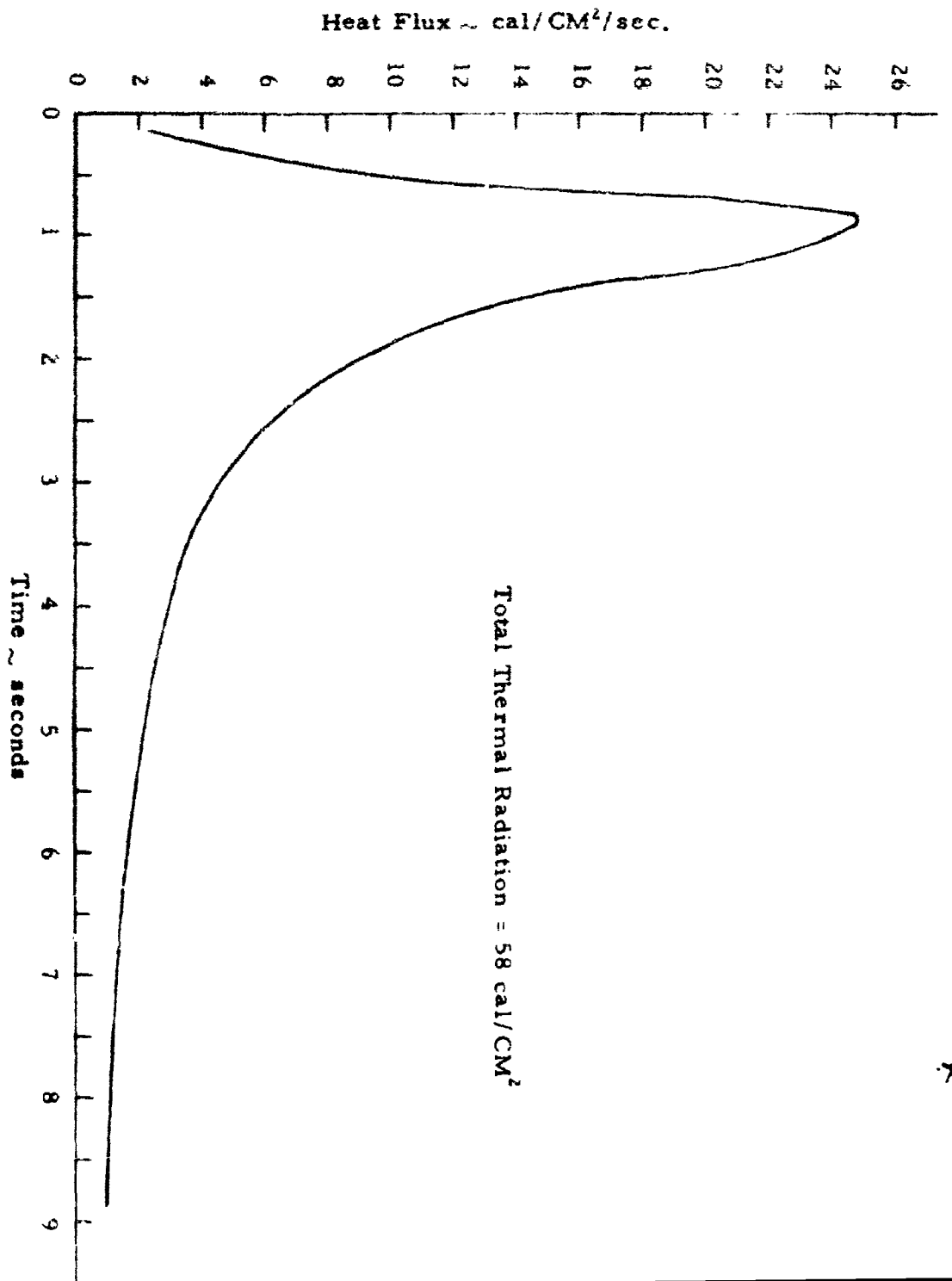


Figure III-19 - Heat Flux Surface Burst 20,000 ft. from Ground Zero

APPENDIX IV

STRESS-STRAIN DATA ON POLYMER FOAMS

The contents of this section are not an exhaustive survey of all data on polymeric foams but, rather, a compact account of what has been observed by the plastics industries on the somewhat important ones, i.e., polystyrene and polyurethane. Figures IV-1 through IV-6 describe the published mechanical and electrical data for polyurethane in its rigid or semi-rigid modes. Figures IV-7 through IV-9 apply to polystyrene rigid foam. Table IV-1 summarizes all the material constants for polyurethane and polystyrene. The restriction to these polymers is based upon the assumption that they now appear to be most suitable for foam hardening applications. Figure IV-10 indicates the relative energy absorption of various foams.

TABLE IV-1

| | <u>Polystyrene</u> | <u>Polyurethane</u> |
|--|--------------------|-----------------------|
| Density (pcf) | 2-15 | 2-35 |
| Compressive Strength (psi) | 20-200 | 10-1000 |
| Ultimate Compressive (psi) | 27-270 | 100-1000 |
| Tensile Strength (psi) | 48-480 | 20-700 |
| Dielectric Constant | 1.02-1.45 | 1.03-1.55 |
| Modulus of Elasticity | up to 10^4 | up to 2×10^4 |
| Loss Tangent | .0005 | .0006 |
| Temperature Applicability | up to 160° F | up to 215° F |
| Energy Absorption (in-lb/lb.) at 50% Strain | 6000-8000 | 2000 |

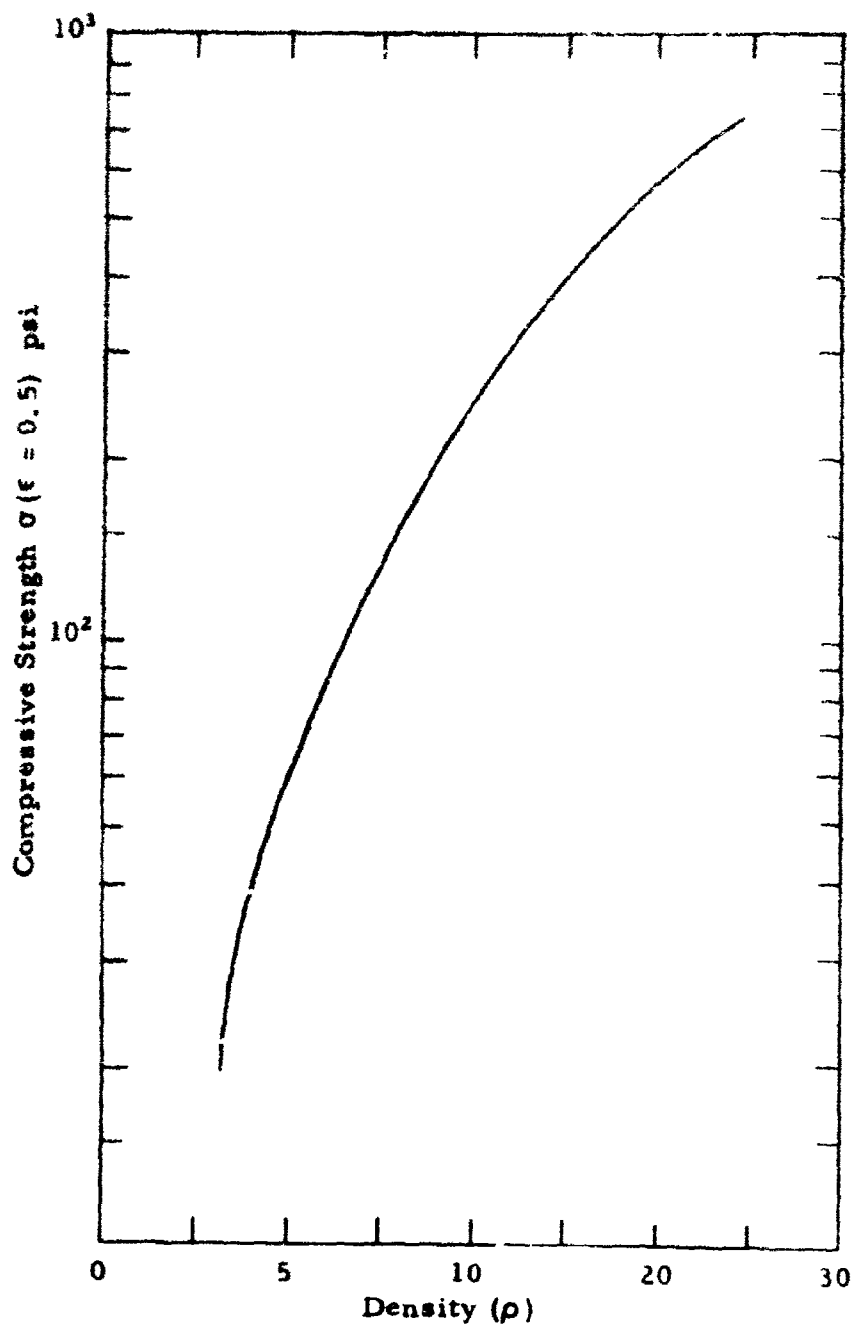


Figure IV-1 - Polyurethane Compressive Strength
 σ ($\epsilon = 0.5$) vs ρ Room Temperature
(Semi-rigid)

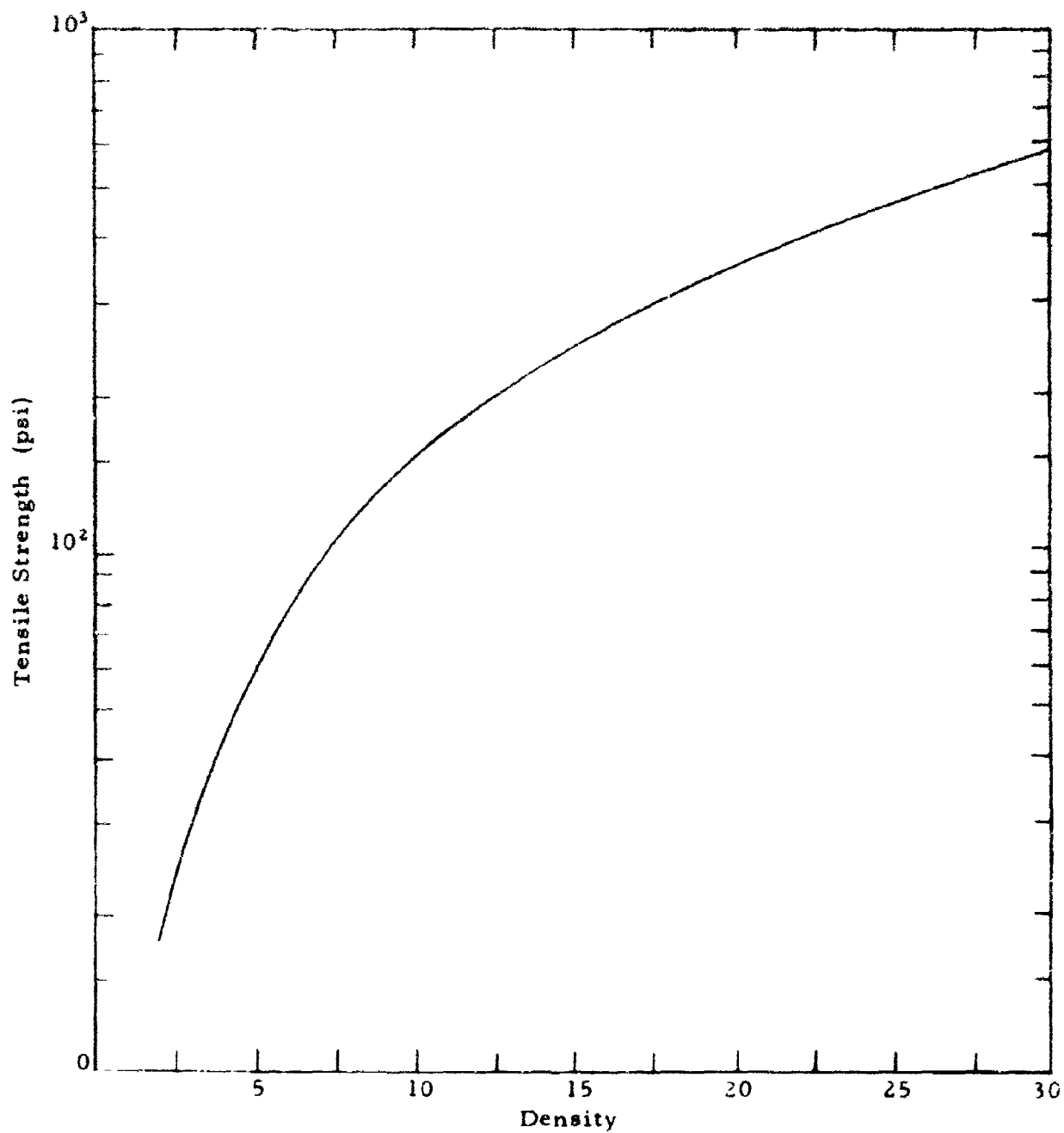


Figure IV-2 - Polyurethane Tensile Strength at Room Temperature
vs Density (Semi-Rigid)

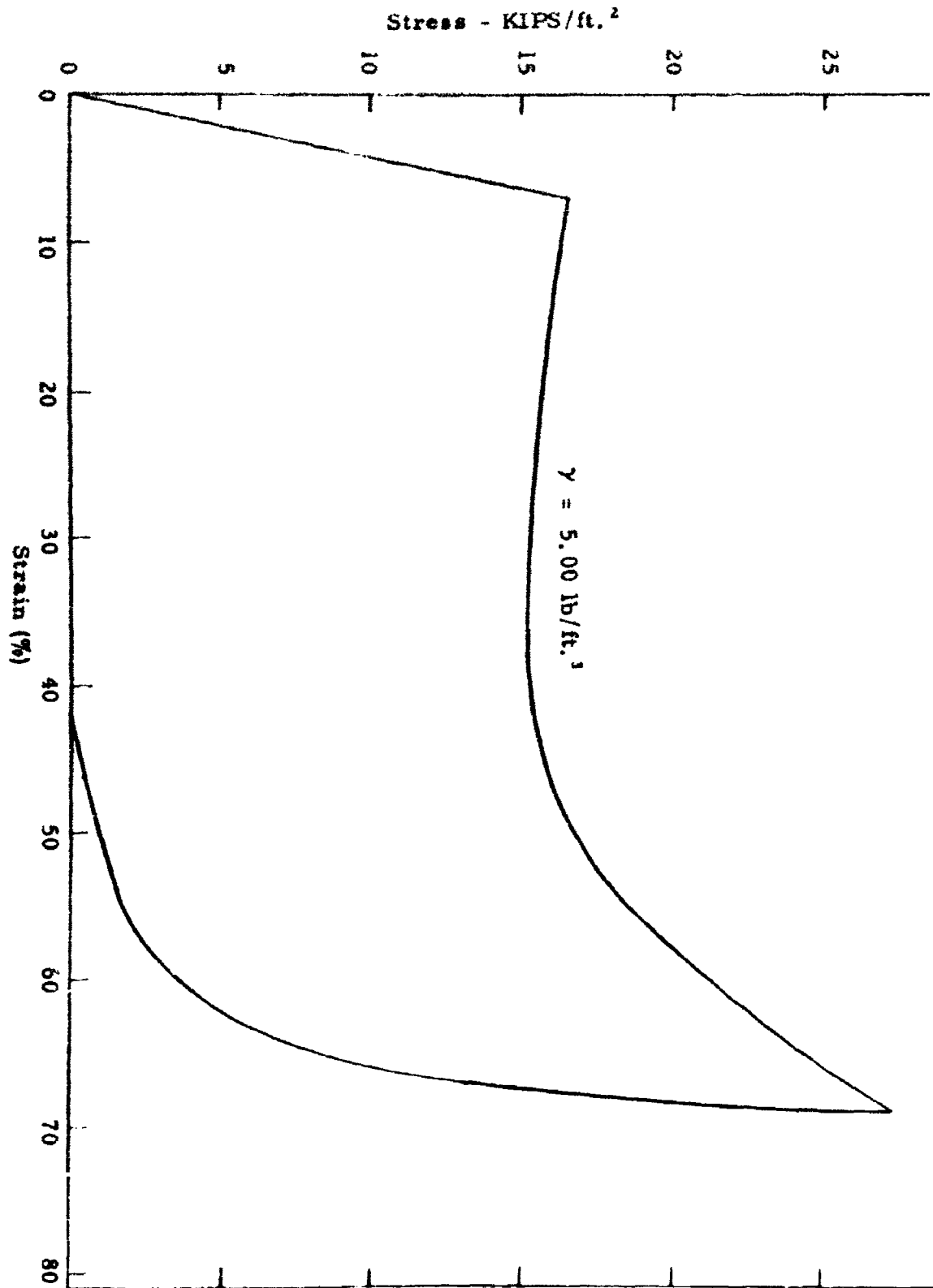


Figure IV-3 - Foamed Polyurethane Stress - Strain Curve

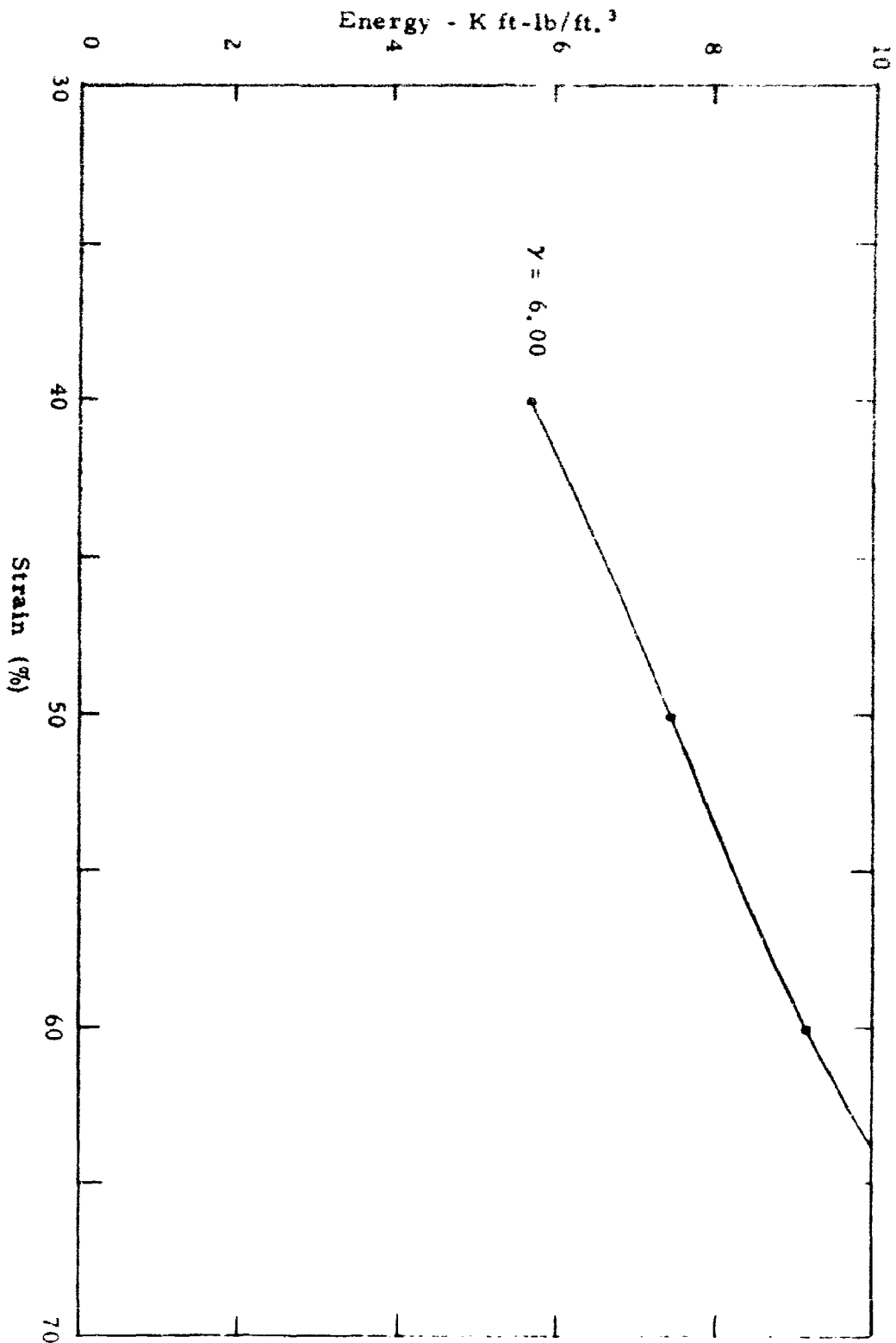
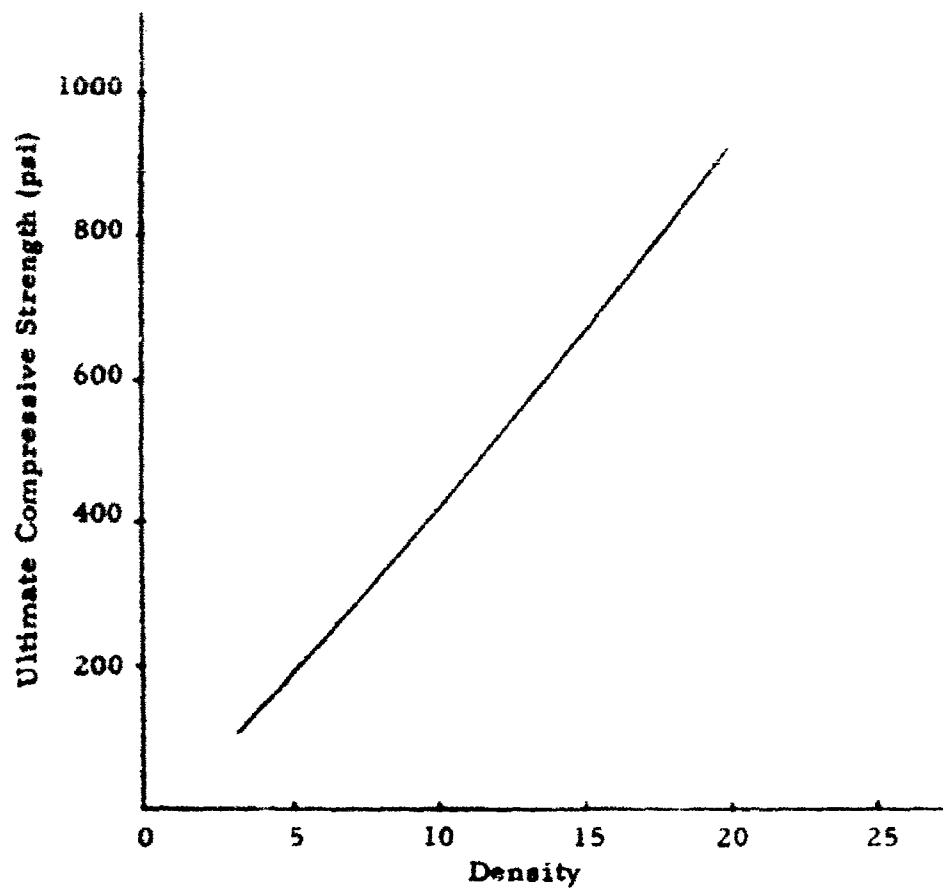


Figure IV-4 - Energy Absorption vs Strain of Foamed Polyurethane (lbs/ft.³)



**Figure IV-5 - Ultimate Compressive Strength vs Density
Rigid Polyurethane at Room Temperature**

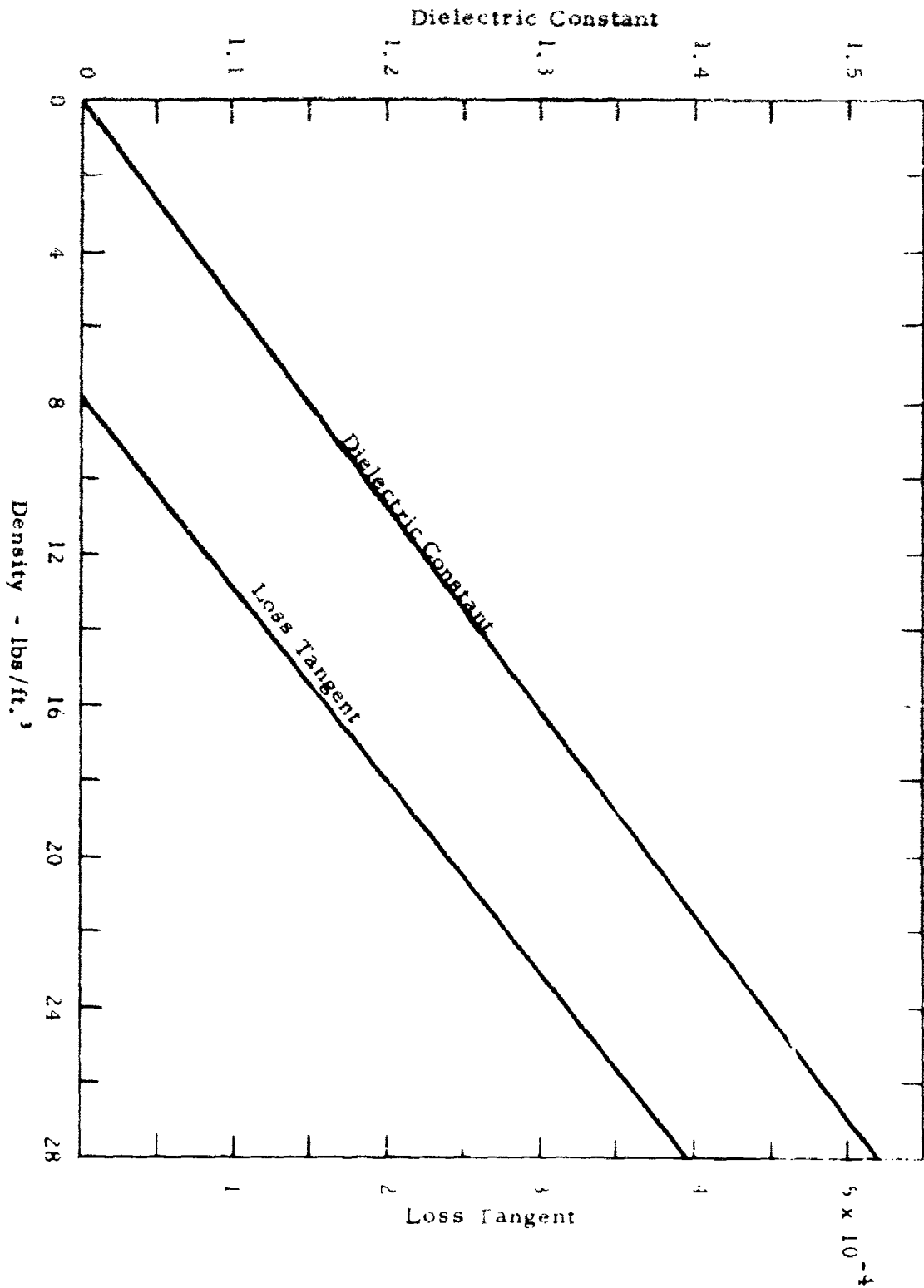


Figure IV-6 - X-Band Dielectric Measurements - Polyurethane Foam at Room Temperature

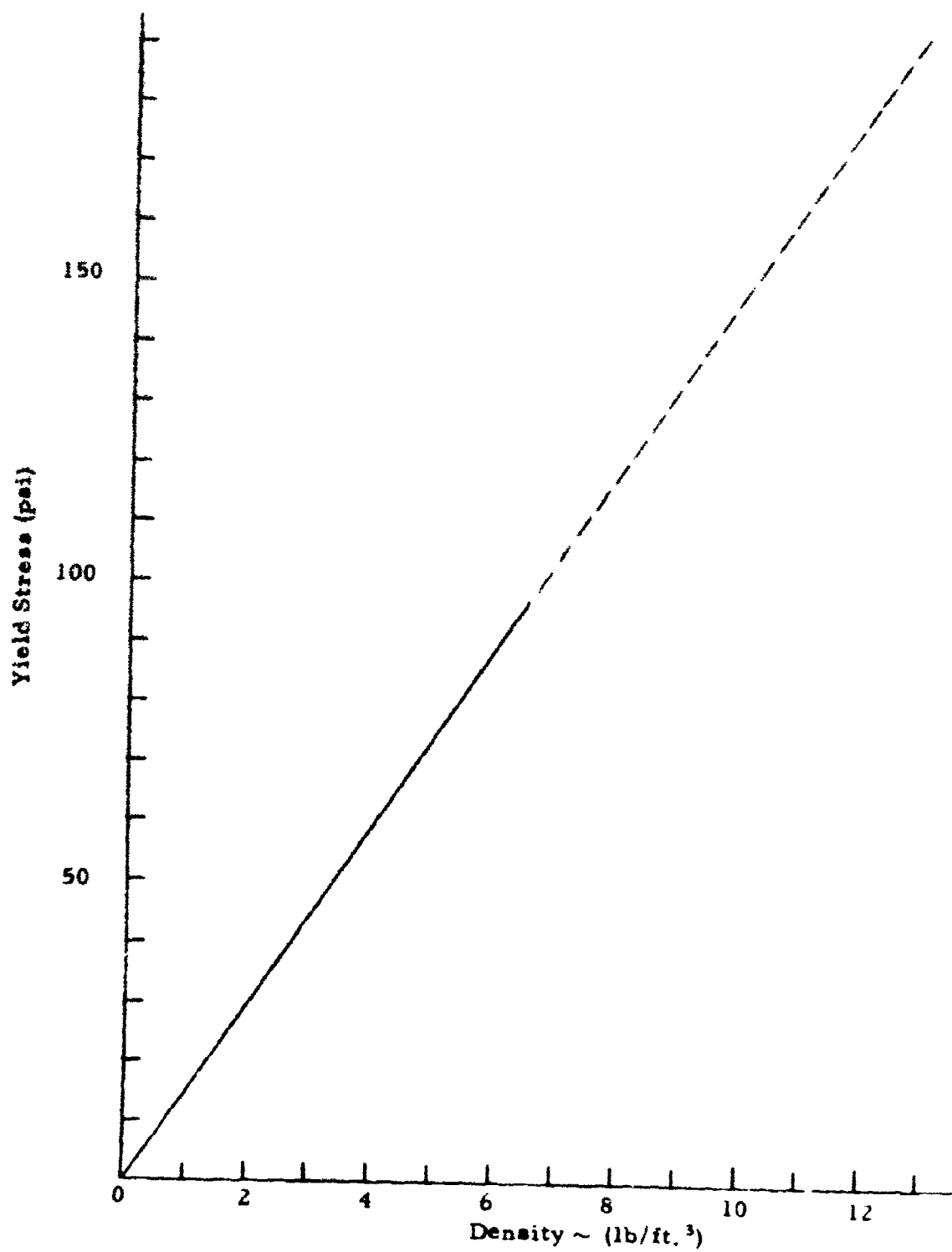


Figure IV-7 - Yield Stress vs Density - Polystyrene Foam

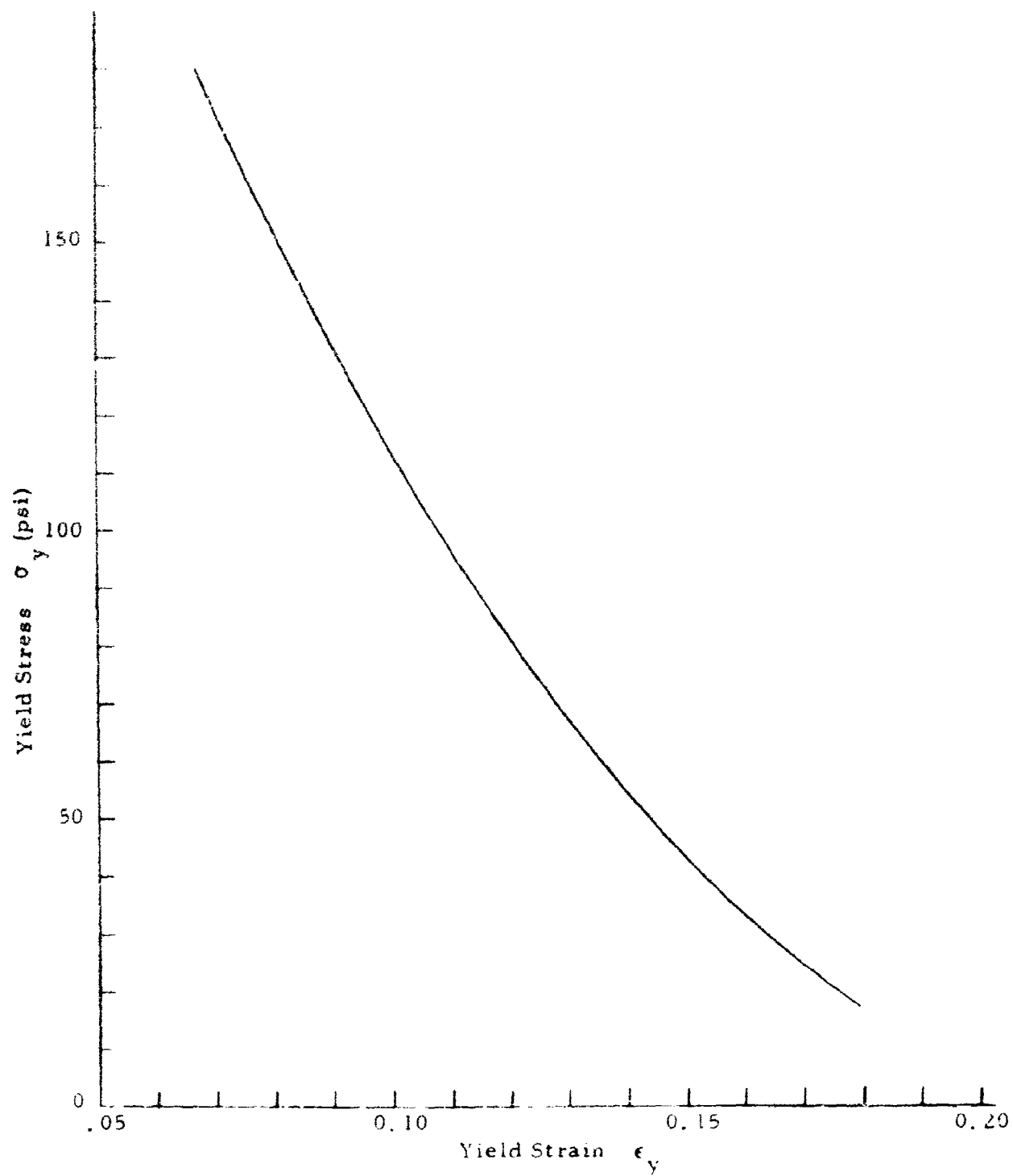


Figure IV-8 - Yield Stress vs Yield Strain - Polystyrene Foam

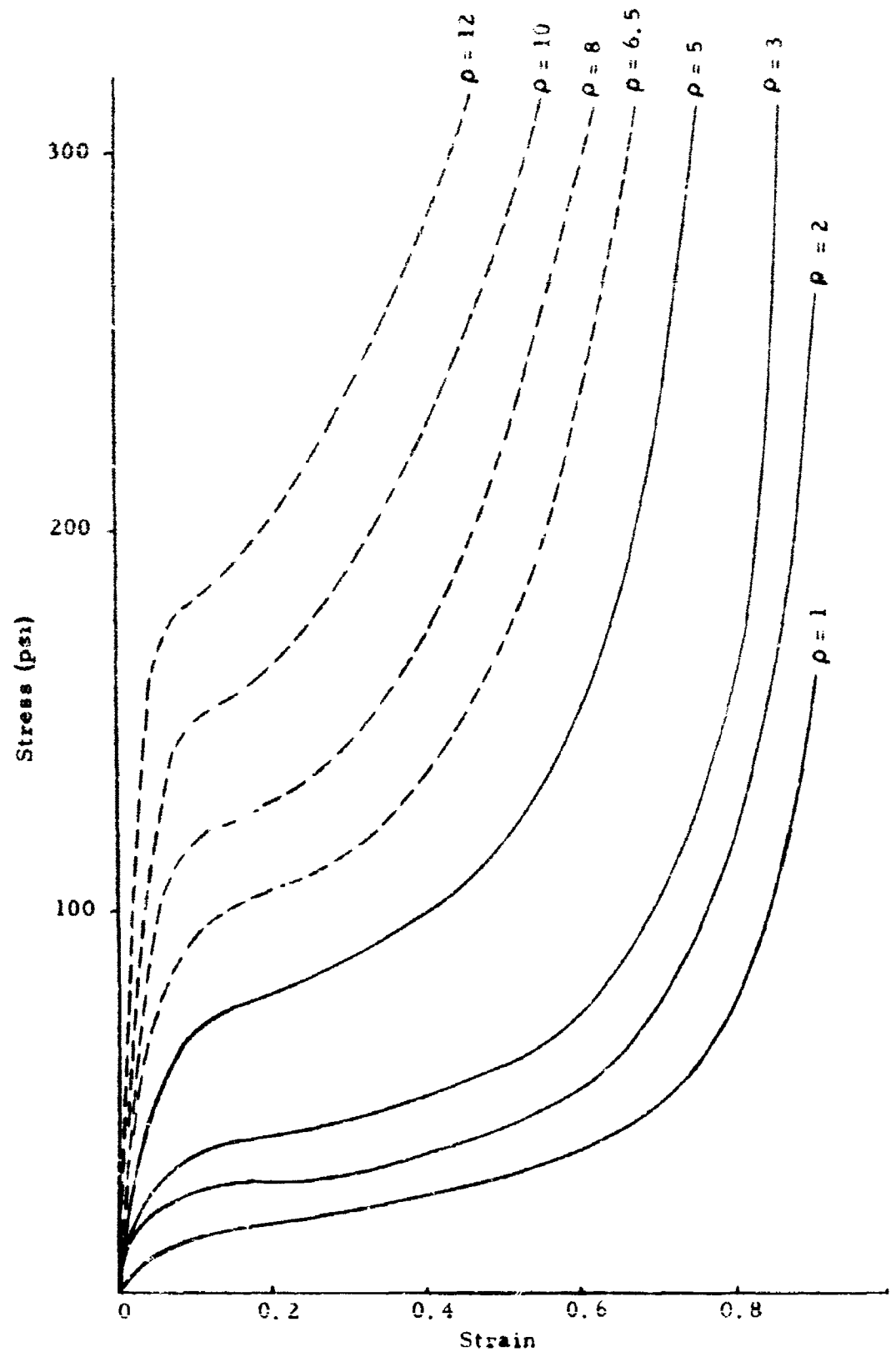


Figure IV-9 - Stress vs Strain Polystyrene Foam
 (ρ = density in pcf)

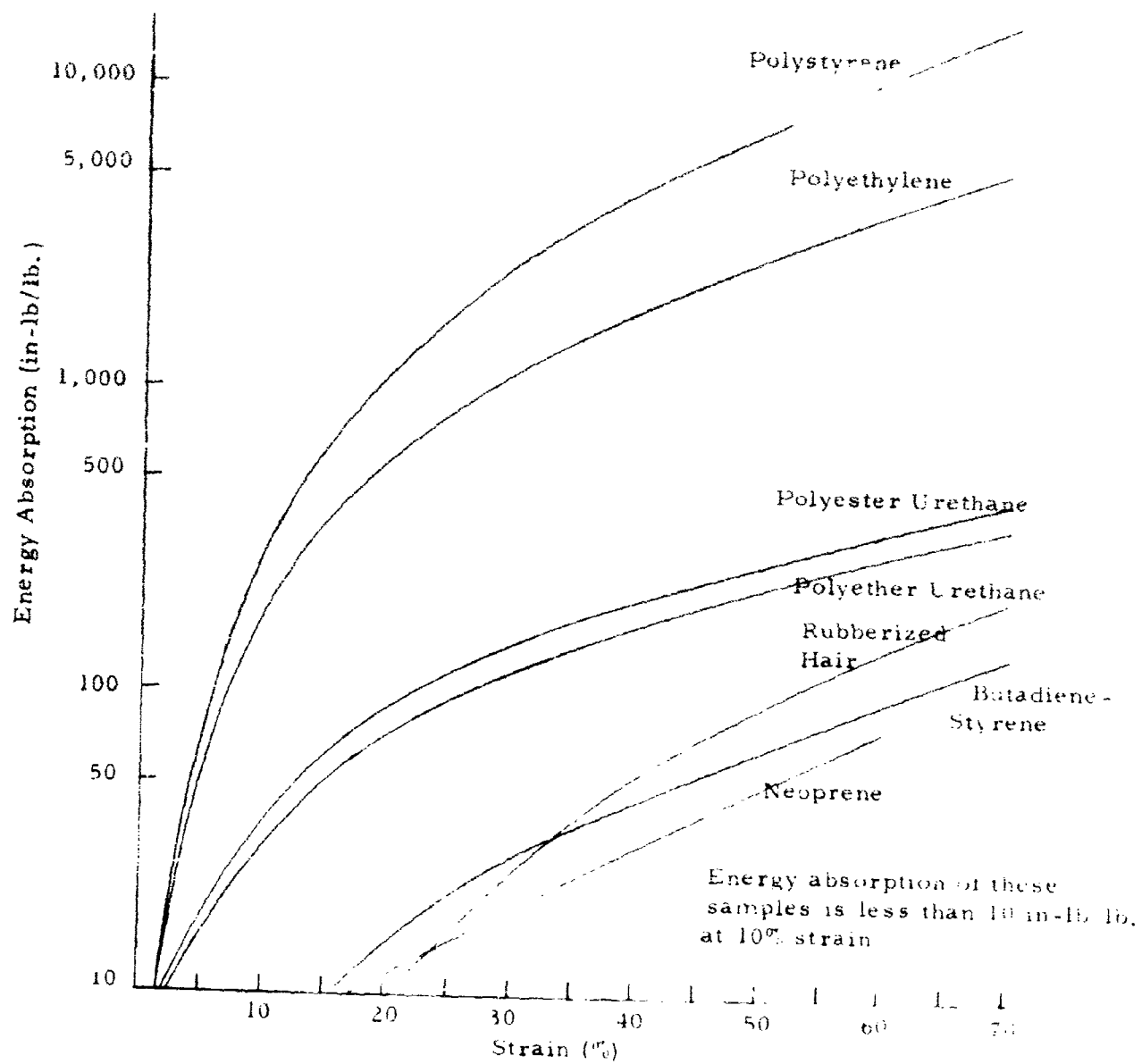


Figure IV-10 - Energy Absorption vs Strain Various Foam Materials

APPENDIX V

STRESS ANALYSIS COMPUTATIONS

1. INTRODUCTION

This appendix presents the results of a simplified stress analysis on a protective dome structure for a hardened antenna site. Three sets of approximations were used to determine the general feasibility of a foamed-plastic structure for use in the reflection region at 75 psi free field overpressure. The results of the analysis are not conclusive because many simplifying assumptions were made, but the study does indicate a potential for further study.

The analysis was done in three steps. Each step represents a different approximate method of analysis. In the first approximation, a dome was tentatively designed on the basis of a uniform pressure field of intensity equal to the sum of the maximum values of incident overpressure and dynamic wind overpressure. The results of the analysis established a trial value for the thickness of the shell required for the dome.

The second approximation applied criteria of elastic stability to the shell to determine a second trial thickness for the shell. The results of this trial were compared with those of the first trial.

The third approximation involved a rough dynamic analysis of the shell defined by the first and second approximations. The greater (more conservative) thickness was used in this analysis.

The three approximations indicate reasonable (i.e., order of magnitude) agreement with each other. The criterion of elastic stability was the governing one for this analysis. Generalization of these results to a viscoelastic medium is not warranted without additional study.

2. FIRST APPROXIMATION

The first approximate solution consists of solving a simplified static model to determine a trial shell thickness. The simplified model consists of:

- a. A uniform pressure distribution over the surface of the shell.

- b. A uniform, homogeneous and isotropic hemispherical shell supported on and restrained by a rigid foundation.

The pressure distribution is determined for this model by the following method:

$$p = p_{so} + q_{so} \quad (V-1)$$

where

- p = model overpressure (lbs/in.²)
 p_{so} = free field (side-on) overpressure (lbs/in.²)
 q_{so} = maximum dynamic overpressure due to blast wind (lbs/in.²)

Reference 30 gives the following approximate relationship for q_{so} , (Equation 11.7, page 255.)

$$q_{so} = 14.7 \left[\frac{\frac{5}{14} \left(\frac{p_{so}}{14.7} \right)^2}{1 + \frac{1}{7} \left(\frac{p_{so}}{14.7} \right)} \right] \quad (V-2)$$

Numerically, at $p_{so} = 75$ psi,

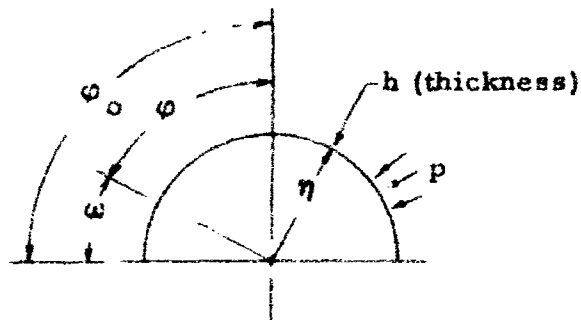
$$q_{so} = 79.047 \text{ lbs/in.}^2 \quad (V-2a)$$

Hence, the total loading pressure p is given by

$$\begin{aligned} p &= 75 + 79.047 \\ &\approx 154 \text{ lbs/in.}^2 \end{aligned} \quad (V-2b)$$

The loads introduced into the shell are found by the method of Reference 31, Section 49, page 163 ff.

In this method, the shell is considered first to deform freely (i.e., without edge restraints) as a membrane. Edge loads and moments are applied to the edge of the shell to satisfy the boundary conditions imposed by the foundations. Bending stresses and direct stresses caused by the edge loads and moments are superposed on the membrane stresses to determine the total stress pattern. The shell solution will be made in terms of thickness h . The required thickness will be found from material allowable stresses.



For this model, the following values are assumed:

r = middle surface radius = 600 in.

ϕ_0 = included half-angle = $\pi/2$ rad.

E = Young's Modulus = 10,000 lbs/in.²

μ = Poisson's Ratio = 0.15

p = external pressure = 154 lbs/in.²

2.1 Stress Deflection Calculations

2.1.1 Membrane Forces

$$N_m = T_m = \frac{pr}{2} \quad (V-3)$$

N_m = tangential normal force (lbs/in. of arc)

T_m = meridional normal force (lbs/in. of arc)

$$N_M = T_m = \frac{(154)(600)}{2} \quad (V-3a)$$

$$= 46,200 \text{ lbs/in.}$$

2.1.2 Membrane Deflection (at base)

$$u_o = \frac{r \sin(\phi_0 - \omega)}{Eh} [N_m - \mu T_m] \quad (V-4)$$

where u_o = horizontal deflection (in). Substitution of numerical values yields:

$$\begin{aligned}
 u_o &= \frac{r \sin(\frac{\pi}{2} - 0)}{E h} [46,200 - (0.15)(46,200)] \\
 &= 3.927 \times 10^4 \frac{r}{E h}
 \end{aligned} \tag{V-4a}$$

2.1.3 Deflection Due to Summed Forces and Moments

a. Deflection:

$$u = \frac{r \sin(\phi_o - \omega)}{E h} N \tag{V-5}$$

$$N = C \frac{\lambda e^{-\lambda \omega}}{\sqrt{\sin(\phi_o - \omega)}} [\cos(\lambda \omega + \psi) - \sin(\lambda \omega + \psi)] \tag{V-6}$$

b. Constants:

$$\lambda = \left[3(1 - \mu^2) \frac{r^2}{h^2} \right]^{1/4} \tag{V-7}$$

Numerically,

$$\begin{aligned}
 \lambda &= \left[3(1 - (0.15)^2) \frac{(600)^2}{h^2} \right]^{1/4} \\
 \lambda &= 32.05 \left(\frac{1}{\sqrt{h}} \right)
 \end{aligned} \tag{V-7a}$$

The constant ψ is determined from the boundary conditions $\theta = 0$ for $\omega = 0$, where

$$\theta = \frac{2\lambda^2}{Eh} C \frac{e^{-\lambda \omega}}{\sqrt{\sin(\phi_o - \omega)}} \cos(\lambda \omega + \psi) \tag{V-8}$$

since

$$\frac{2\lambda^2}{Eh} \neq 0$$

and

$$\frac{e^{-\lambda \omega}}{\sqrt{\sin(\phi_o - \omega)}} \neq 0,$$

then either

$$C = 0$$

or

$$\cos (\lambda \omega + \psi) = 0.$$

If $C = 0$, the trivial solution results. Therefore,

$$\cos (\lambda \omega + \psi) = \cos (0 + \psi) = 0$$

or

$$\psi = \pi / 2 \quad (V-9)$$

The constant C is found from the boundary condition on u . From (V-5) and (V-6),

$$u = \left[\frac{r \sin (\varphi_0 - \omega)}{E h} \right] C \frac{\lambda e^{-\lambda \omega}}{\sqrt{\sin (\varphi_0 - \omega)}} \left[\cos (\lambda \omega + \psi) - \sin (\lambda \omega + \psi) \right] \quad (V-10)$$

for $\omega = 0$, $\varphi_0 = \frac{\pi}{2}$ and $\psi = \frac{\pi}{2}$:

$$\sin (\varphi_0 - \omega) = \sin \left(\frac{\pi}{2} - 0 \right) = 1.00$$

$$e^{-\lambda \omega} = e^0 = 1.00$$

$$\cos (\lambda \omega + \psi) = \cos \left(0 + \frac{\pi}{2} \right) = 0.00$$

$$\sin (\lambda \omega + \psi) = \sin \left(0 + \frac{\pi}{2} \right) = 1.00$$

Hence,

$$u = \frac{r}{E h} C \lambda = u_0 \quad (V-11)$$

or

$$C = \frac{E h}{r \lambda} \left[\frac{r}{E h} (39.270) \right] \quad (V-12)$$

which numerically yields,

$$C = 1225.273 \sqrt{h} \text{ lbs/in.} \quad (V-12a)$$

2.1.4 Forces and Moments at Various Elevations

The equations for normal forces and bending moments are:

$$Q = C e^{-\lambda \omega} \frac{1}{\sqrt{\sin (\varphi_0 - \omega)}} \sin (\lambda \omega + \psi) \quad (V-13)$$

$$N = C \lambda e^{-\lambda \omega} \frac{1}{\sqrt{\sin (\varphi_0 - \omega)}} \left[\cos (\lambda \omega + \psi) - \sin (\lambda \omega + \psi) \right] \quad (V-14)$$

$$T = - Q \cot (\varphi_o - \omega) \quad (V-15)$$

or

$$T = - C e^{-\lambda \omega} \frac{\cot (\varphi_o - \omega)}{\sqrt{\sin (\varphi_o - \omega)}} \sin (\lambda \omega + \psi) \quad (V-16)$$

$$M_1 = \frac{r}{2\lambda} C e^{-\lambda \omega} \frac{1}{\sin (\varphi_o - \omega)} \left[\cos (\lambda \omega + \psi) + \sin (\lambda \omega + \psi) \right] \quad (V-17)$$

$$M_2 = \mu M_1 \quad (V-18)$$

Each of these can be expressed in terms of a constant and some functions of the angle ω . Thus,

$$N = K_1 \left[(F_1) \left(\frac{1}{F_3} \right) (F_7) \right] \quad (V-19)$$

$$T = K_2 \left[(F_1) \left(\frac{1}{F_3} \right) (F_5) \right] \quad (V-20)$$

$$M_1 = K_3 \left[(F_1) \left(\frac{1}{F_3} \right) (F_4) \right] \quad (V-21)$$

$$M_2 = K_4 \left[(F_1) \left(\frac{1}{F_3} \right) (F_4) \right] \quad (V-22)$$

where

$$K_1 = C \lambda \quad (V-23)$$

$$K_2 = -C \quad (V-24)$$

$$K_3 = \frac{2r}{\lambda} C \quad (V-25)$$

$$K_4 = \mu \frac{2r}{\lambda} C \quad (V-26)$$

and

$$F_1 = e^{-\lambda \omega} \quad (V-27)$$

$$F_3 = \sqrt{\sin (\varphi_o - \omega)} \quad (V-28)$$

$$F_4 = \cos (\lambda \omega + \psi) + \sin (\lambda \omega + \psi) \quad (V-29)$$

$$F_5 = \cos (\lambda \omega + \psi) - \sin (\lambda \omega + \psi) \quad (V-30)$$

$$F_7 = \cot (\varphi_o - \omega) \quad (V-31)$$

2.1.5 Stresses

The final stress system in the shell is found by superposing the results of the membrane analysis and the bending analysis. Hence,

$$N_{TOT} = N_m + N \quad (V-32)$$

$$T_{TOT} = T_m + T \quad (V-33)$$

$$M_{1TOT} = M_1 \quad (V-34)$$

$$M_{2TOT} = M_2 \quad (V-35)$$

and

$$\sigma_N = \frac{N_{TOT}}{h} \quad (V-36)$$

$$\sigma_T = \frac{T_{TOT}}{h} \quad (V-37)$$

$$\sigma_{M_1} = \frac{M_1}{6h^2} \quad (V-38)$$

$$\sigma_{M_2} = \frac{M_2}{6h^2} \quad (V-39)$$

2.1.6 Numerical Results

For the base of the shell, $\omega = 0$, the numerical constants for equations (V-37) through (V-39) can be determined:

$$F_1 = e^0 = 1.0$$

$$F_3 = \sqrt{\sin\left(\frac{\pi}{2} - 0\right)} = 1.0$$

$$F_4 = \cos\left(0 + \frac{\pi}{2}\right) + \sin\left(0 + \frac{\pi}{2}\right) = 1.0$$

$$F_5 = \cos\left(0 + \frac{\pi}{2}\right) - \sin\left(0 + \frac{\pi}{2}\right) = -1.0$$

$$F_7 = \cot\left(\frac{\pi}{2}\right) = 0$$

and

$$N = C\lambda (1.0) \left(\frac{1}{1.0}\right)(0) = 0$$

$$T = -C (1.0) \left(\frac{1}{1.0} \right) (-1.0)$$

$$= 1225.273 \sqrt{h} \text{ lbs/in.}$$

$$M_1 = \frac{2r}{\lambda} C (1.0) \left(\frac{1}{1.0} \right) (1.0)$$

$$= \frac{2(600)}{32.05/\sqrt{h}} (1225.273 \sqrt{h})$$

$$= 45,875.446 h \text{ in. lbs/in.}$$

$$M_2 = \mu M_1$$

$$= (0.15)(45,875.446 h)$$

$$= 6,881.317 h \text{ in. lbs/in.}$$

$$N_m = T_m = 46,200 \text{ lbs/in.}$$

Hence,

$$\sigma_N = \frac{46,200 + 0}{h}$$

$$= \frac{46,200}{h} \text{ lbs/in.}^2$$

$$\sigma_T = \frac{46,200 + 1225.273 \sqrt{h}}{h} \text{ lbs/in.}^2$$

$$\sigma_{M_1} = \frac{45,875.446 h}{6h^2}$$

$$= \frac{7645.9}{h} \text{ lbs/in.}^2$$

$$\sigma_{M_2} = \frac{6,881.317 h}{6h^2}$$

$$\sigma_{M_2} = \frac{1,146.9}{h} \text{ lbs/in.}^2$$

The maximum stress occurs for

$$\sigma = \frac{46,200 + 1225.273 \sqrt{h} + 7645.9}{h}$$

Letting $a = \sqrt{h}$

$$\sigma = \frac{53,845.9 + 1225.273 a}{a^2}$$

Assuming an allowable maximum stress of $\sigma_a = 800 \text{ lbs/in.}^2$

$$a^2 = \frac{1}{800} [51,845.9 + 1225.271 a]$$

$$= 67.307 + 1.532 a$$

or

$$a^2 - 1.532 a - 67.307 = 0$$

from whence,

$$a = 9.006$$

This means that a required thickness, h , is obtained from

$$a^2 = h = (9.006)^2 = 81.108 \text{ in.}$$

3. SECOND APPROXIMATION

The second approximation is based on a shell which will resist buckling under the assumed uniform external pressure model.

The trial thickness obtained by the buckling analysis will be compared with the thickness obtained by the first approximation. A trial thickness, taken as the greater of the two approximations, will be used to solve the dynamic model.

3.1 Buckling of Thin Shell

Tsien and Von Karman have found for a hemispherical shell that the critical buckling stress is given by:

$$\sigma_{\text{crit}} = \frac{1}{3\sqrt{5}(1-\mu^2)} \frac{Eh}{R} \quad (\text{V-40})$$

For the shell in question (h based on steady pressure $p_{so} + q_{so} = 154 \text{ lbs/in.}^2$)

$$\sigma_{\text{crit}} = 204 \text{ lbs/in.}^2 \quad (\text{V-40a})$$

The membrane stress, σ_m , is given by

$$\sigma_m = \frac{pr}{2t} = \frac{(154)(600)}{2(81)} = 570.37 \text{ lbs/in.}^2 \quad (\text{V-41})$$

If $h = 120 \text{ in.}$

$$\sigma_{\text{cr}} = \frac{120}{81} (204) = 302 \text{ lbs/in.}^2 \quad (\text{V-41a})$$

$$\sigma_m = \frac{81}{120} (570) = 384 \text{ lbs/in.}^2 \quad (\text{V-41b})$$

If $h = 127$ in.

$$\sigma_{cr} = \frac{127}{81} (204) = 319.87 \text{ lbs/in.}^2 \quad (\text{V-41c})$$

$$\sigma_m = \frac{81}{127} (570) = 363.66 \text{ lbs/in.}^2 \quad (\text{V-41d})$$

If $h = 140$ in.

$$\sigma_{cr} = \frac{140}{81} (204) = 352.5 \text{ lbs/in.}^2 \quad (\text{V-41e})$$

$$\sigma_m = \frac{81}{140} (570) = 330.0 \text{ lbs/in.}^2 \quad (\text{V-41f})$$

So, a thickness, h , of 140 in. is considered to be the result of this approximation.

4. THIRD APPROXIMATION

The third approximation is based on the reflected overpressure transient pulse and the dynamic characteristics of the dome. An equivalent static load will be determined for comparison with assumed static load used in the preceding approximations.

4.1 Natural Frequency of Dome

The natural frequency of the hemispherical dome is found by application of the Rayleigh energy method. The method is outlined in Ref. (32), Chapter 12.

4.2 Potential Energy

The potential energy of the vibrating system is stored in strain energy within the shell. Considering a symmetrical dome, the strain energy of bending in a unit "beam" can be found in a manner similar to that used in the static case.

$$E_p = 2 \left[\frac{1}{2} D \int_0^{\pi/2} (M_1 + M_2) \frac{d^2 z}{d\omega^2} d\omega \right] \quad (\text{V-42})$$

where

E_p = strain energy (in. lbs.)

D = shell stiffness

$$D = \frac{Eh^3}{12(1-\mu^2)}$$

M_1 = meridional bending moment (in. lbs.)

M_2 = tangential bending moment (in. lbs.)

z = radial deflection (in.)

From previous work,

$$M_2 = \mu M_1$$

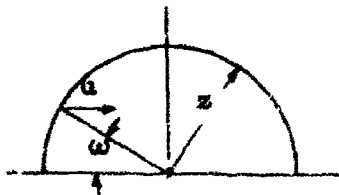
$$M_1 = \frac{r}{2\lambda} C \frac{e^{-\lambda \omega}}{\sqrt{\sin(\varphi_0 - \omega)}} \left[\cos(\lambda \omega + \phi) + \sin(\lambda \omega + \phi) \right] \quad (V-44)$$

where

$$\varphi_0 = \pi/2, \text{ and}$$

$$\phi = \pi/2$$

The constant C was previously expressed in terms of the external pressure loading. For this analysis, C can be defined geometrically. Observe that



$$u = z \cos \omega \quad (V-45)$$

But

$$u = \frac{r}{Eh} C \lambda \quad (V-46)$$

or

$$C = \frac{Eh}{r\lambda} (z \cos \omega) \quad (V-47)$$

where

$$M_1 = \left(\frac{r}{2\lambda} \right) \left(\frac{Eh}{r^2} \right) (z \cos \omega) \frac{e^{-\lambda \omega}}{\sqrt{\sin(\phi_0 - \omega)}} \left[\cos(\lambda \omega + \psi) + \sin(\lambda \omega + \psi) \right] \quad (V-48)$$

and

$$E_p = D(1 + \mu) \left(\frac{Eh}{2\lambda} \right) \int_0^{\pi/2} z \cos \omega \frac{e^{-\lambda \omega}}{\sqrt{\sin(\phi_0 - \omega)}} \left[\cos(\lambda \omega + \psi) + \sin(\lambda \omega + \psi) \right] \frac{d^2 z}{d\omega^2} d\omega \quad (V-49)$$

Putting in $\phi = \pi/2$ and $\psi = \pi/2$, and simplifying gives

$$E_p = D(1 + \mu) \left(\frac{Eh}{2\lambda} \right) \int_0^{\pi/2} e^{-\lambda \omega} (\cos \omega)^{1/2} (\cos \lambda \omega - \sin \lambda \omega) z \frac{d^2 z}{d\omega^2} d\omega \quad (V-50)$$

4.4.3 Kinetic Energy

The kinetic energy stored in the system can be found by means of

$$E_k = 2 \left[\frac{1}{2} \int_0^{\pi/2} \rho h (z\Omega)^2 d\omega \right] \quad (V-51)$$

where

E_k = kinetic energy

ρ = density (lbs/in.³)

Ω = circular frequency (rad/sec.)

4.4.4 Deflection Curve

The assumed deflection curve, $z = z_0 z(\omega)$ must satisfy the boundary conditions. These are:

a. at $\omega = 0$, deflection $z = 0$

slope $z' = 0$

b. at $\omega = \pi/2$, deflection $z = z_0$

slope $z' = 0$

The function

$$z(\omega) = \frac{z_0}{2} \left[1 - \cos(2\omega) \right] \quad (V-52)$$

satisfies these conditions. Also, the first and second derivatives

$$\frac{dz}{d\omega} = z_0 \sin(2\omega) \quad (V-53)$$

$$\frac{d^2 z}{d\omega^2} = 2 z_0 \cos(2\omega) \quad (V-54)$$

The potential energy is then

$$E_p = \left\{ \frac{D}{2\lambda} \right\} (Eh z_0^2 (1 + \mu)) \int_0^{\pi/2} e^{-\lambda \omega} (\cos \omega)^{1/2} (\cos \lambda \omega - \sin \lambda \omega) (\cos 2\omega)(1 - \cos 2\omega) d\omega \quad (V-55)$$

and the kinetic energy is

$$E_k = \frac{1}{2} \rho h z_0^2 \Omega^2 \int_0^{\pi/2} \cos^2 2\omega d\omega \quad (V-56)$$

By Rayleigh's method,

$$E_{p_{\max}} = E_{k_{\max}} \quad (V-57)$$

and the natural circular frequency Ω can be found by equating the two expressions after integration.

By Rayleigh's Principle, the frequency obtained by this method cannot be less than the fundamental natural frequency. Hence, the period of vibration found by this method cannot be greater than the fundamental natural period.

The integration of the expression for E_p can be performed by expanding the terms in power series. For the purposes of this preliminary study, a simplified expression for the fundamental natural frequency, from Lord Rayleigh,⁽³⁴⁾ will be used as an approximation. In the symbols used previously, Ω can be found from

$$\Omega^2 = \left(\frac{g}{p} \right) \left(\frac{E}{2(1 + \mu)} \right) \frac{h^2}{r} \quad (4.279) \quad (V-58)$$

which numerically is found by proper substitution:

$$\Omega^2 = \left(\frac{386}{16} \right) (1728) \left(\frac{10,000}{2(1 + 0.15)} \right) \left(\frac{(140)^2}{(600)^4} \right) (4.279)$$

$$\Omega^2 = 59.828 \text{ rad}^2/\text{sec}^2 \quad (\text{V-58a})$$

or

$$\Omega = 7.734 \text{ rad/sec.} \quad (\text{V-58b})$$

The natural period τ of this model is

$$\tau = 2\pi \left(\frac{1}{\Omega}\right) \quad (\text{V-59})$$

or

$$\tau = 0.813 \text{ sec.} \quad (\text{V-59a})$$

4.4.5 Reflected Overpressure Transient

The reflected overpressure acts as a transient dynamic load pulse. In the elastic range, the loads on the shell can be considered separately. The reflected overpressure transient will be treated as a triangular impulsive load.

Curves of Figure 7.12, Ref. (30), gives values of the dynamic load factor as a function of the ratio C_T ,

$$C_T = \frac{T}{\tau} \quad (\text{V-60})$$

where

T = load pulse duration.

Taking the pulse duration as equal to the clearing time, t_c

$$T = t_c = \frac{3r}{C_{\text{refl}}} \quad (\text{V-61})$$

where

C_{refl} = velocity of sound in reflected overpressure region (ft/sec.)

$\approx 1973 \text{ ft/sec.}$ (Figure 11.21, Ref. 30)

r = dome height (ft.)

Numerically,

$$t_c = \frac{3(50)}{1973} = 0.076 \text{ sec.} \quad (\text{V-61a})$$

and

$$C_T = 0.0935 \quad (\text{V-61b})$$

From the curves of Figure 7.12, Ref. 10, the maximum dynamic load factor for a triangular load and $C_T = 0.1$ is

$$DLF \approx 0.3 \quad (V-62)$$

where the dynamic load factor is the increase in static load due to the dynamic character of the load.

The reflected overpressure load is a function of the angle ω . The total load, P , on the dome behind the blast front due to reflected overpressure is shown below, assuming uniform reflected overpressure behind the blast front.

| ω | $P_r(\text{psi})$ | area(in ²) | $P(\text{lbs})$ |
|----------|-------------------|------------------------|----------------------|
| 0 | 330 | 0 | 0 |
| 30 | 289 | 151,550 | 47.738×10^6 |
| 45 | 180 | 331,260 | 59.627 |
| 60 | 128 | 565,490 | 72.383 |
| 90 | 75 | 1,130,970 | 84.823 |

Taking the maximum value $P = 84.823 \times 10^6$ and applying the dynamic load factor, $DLF = 0.3$, the equivalent static load is

$$P = 110.270 \times 10^6 \text{ lbs.} \quad (V-63)$$

The static load capability of the dome based on the buckling criteria of the second static approximation is

$$P = 154 (2\pi r^2) \quad (V-64)$$

$$= 348.318 \times 10^6 \quad (V-64a)$$

which is greater than the equivalent static load due to the reflected overpressure transient.

5. NOMENCLATURE USED IN APPENDIX V

| | |
|-------|---|
| N_m | Tangential normal membrane force |
| T_m | Meridional normal membrane force |
| N | Tangential force due to bending and shear loading |
| T | Meridional force due to bending and shear loading |
| r | Middle surface radius |

| | |
|---------------|--|
| h | Shell thickness |
| M_1 | Meridional bending moment |
| M_2 | Tangential bending moment |
| ω | Latitude angle |
| E | Modulus of elasticity |
| ϕ | $\phi_0 - \omega$ |
| C | Constant of integration |
| ψ | Constant of integration |
| μ | Horizontal deflection |
| μ_0 | Horizontal deflection at base |
| μ | Poisson's ratio |
| Q | Horizontal shear force |
| N_{TOT} | $N + N_m$ |
| T_{TOT} | $T + T_m$ |
| σ_N | $\frac{N_{TOT}}{h}$ |
| P | Total overpressure or external pressure |
| P_{so} | field free overpressure |
| q_{so} | Dynamic overpressure |
| θ | $\frac{z\lambda^2}{Eh} C \frac{e^{-\lambda\omega}}{\sqrt{\sin(\phi_0 - \omega)}} \cos(\lambda\omega + \psi)$ |
| σ_a | Maximum allowable stress from uniaxial yield stress data |
| σ_{cr} | Critical stress from configuration stress distribution |
| σ_m | Membrane stress |
| z | Radial deflection |
| D | Shell stiffness |
| E_p | Potential energy |
| E_k | Kinetic energy |

| | |
|------------|--|
| ρ | Density |
| Ω | Circular frequency |
| τ | Natural period |
| T | Load pulse duration |
| t_c | Clearing time |
| C_{refl} | Velocity of sound in reflected overpressure region |
| DLF | Dynamic load factor |

Convenience Functions:

$$\begin{aligned}
 K_1 &= C\lambda \\
 K_2 &= -C \\
 K_3 &= \frac{2\dot{r}}{\lambda} C \\
 K_4 &= \mu \frac{2r}{\lambda} C \\
 F_1 &= e^{-\lambda \omega} \\
 F_3 &= \sqrt{\sin(\varphi_0 - \omega)} \\
 F_4 &= \cos(\lambda \omega + \psi) + \sin(\lambda \omega + \psi) \\
 F_5 &= \cos(\lambda \omega + \psi) - \sin(\lambda \omega + \psi) \\
 F_7 &= \cot(\varphi_0 - \omega) \\
 \sigma_N &= N_{TOT}/L \\
 \sigma_T &= T_{TOT}/L \\
 \sigma_{M_1} &= M_1/6h^2 \\
 \sigma_{M_2} &= M_2/6h^2 \\
 a &= \sqrt{h} \\
 C_T &= T/\tau \\
 \lambda &= \left[3(1 - \mu^2) \frac{r^2}{h^2} \right]^{1/4}
 \end{aligned}$$

APPENDIX VI
THERMAL ABLATION DATA

I. SUMMARY

The curves VI-1 and VI-2 give the relationship between the heat flux, power input and distance from the quartz lamps used in the ablation tests of polyethylene foam. The calibration tests are summarized in Table VI-1. The heat of ablation calculations are summarized in Table VI-2. Figures VI-3 through VI-10 show the temperature time plots of the measured temperature of ablation.

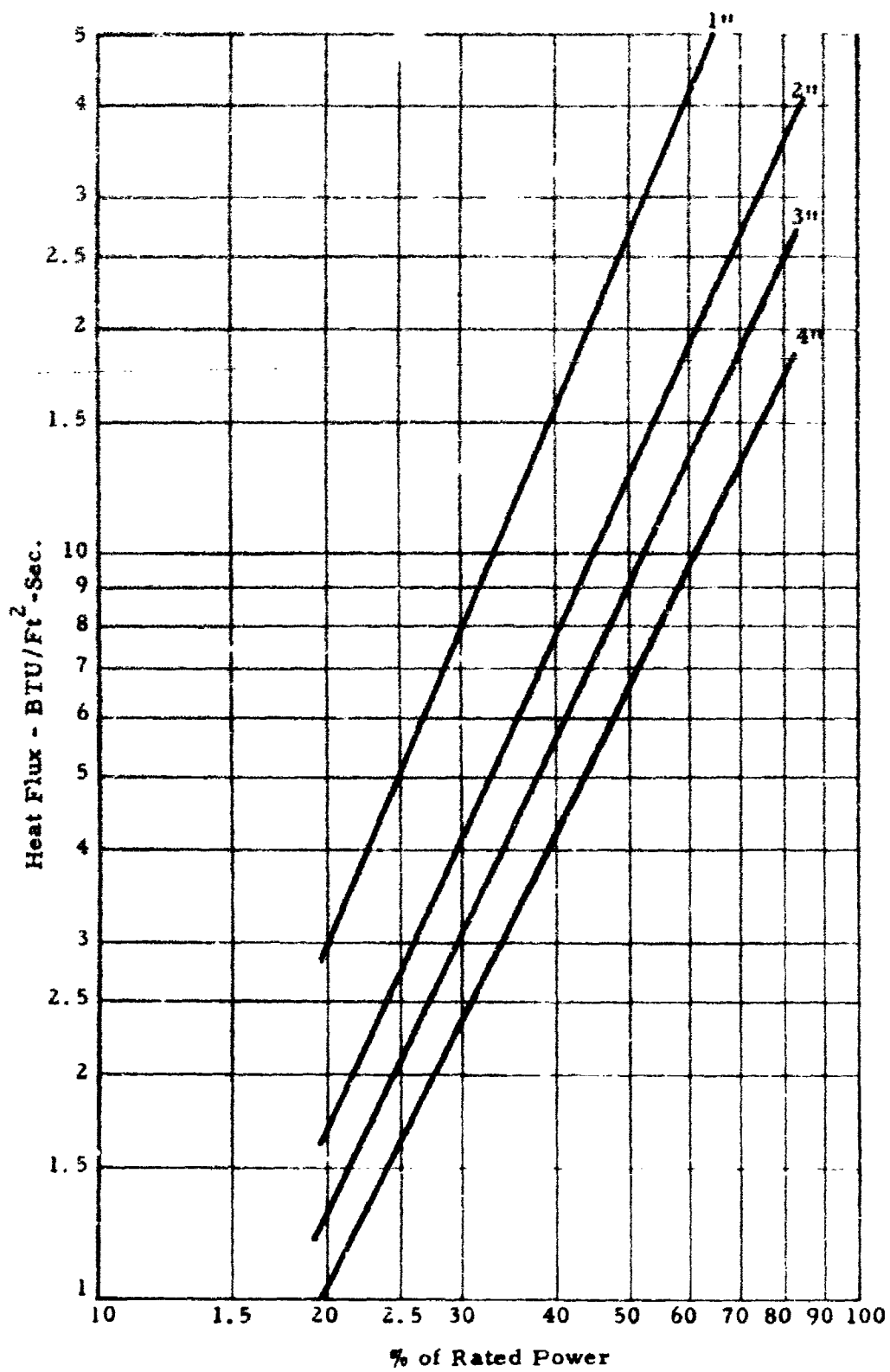


Figure VI-1

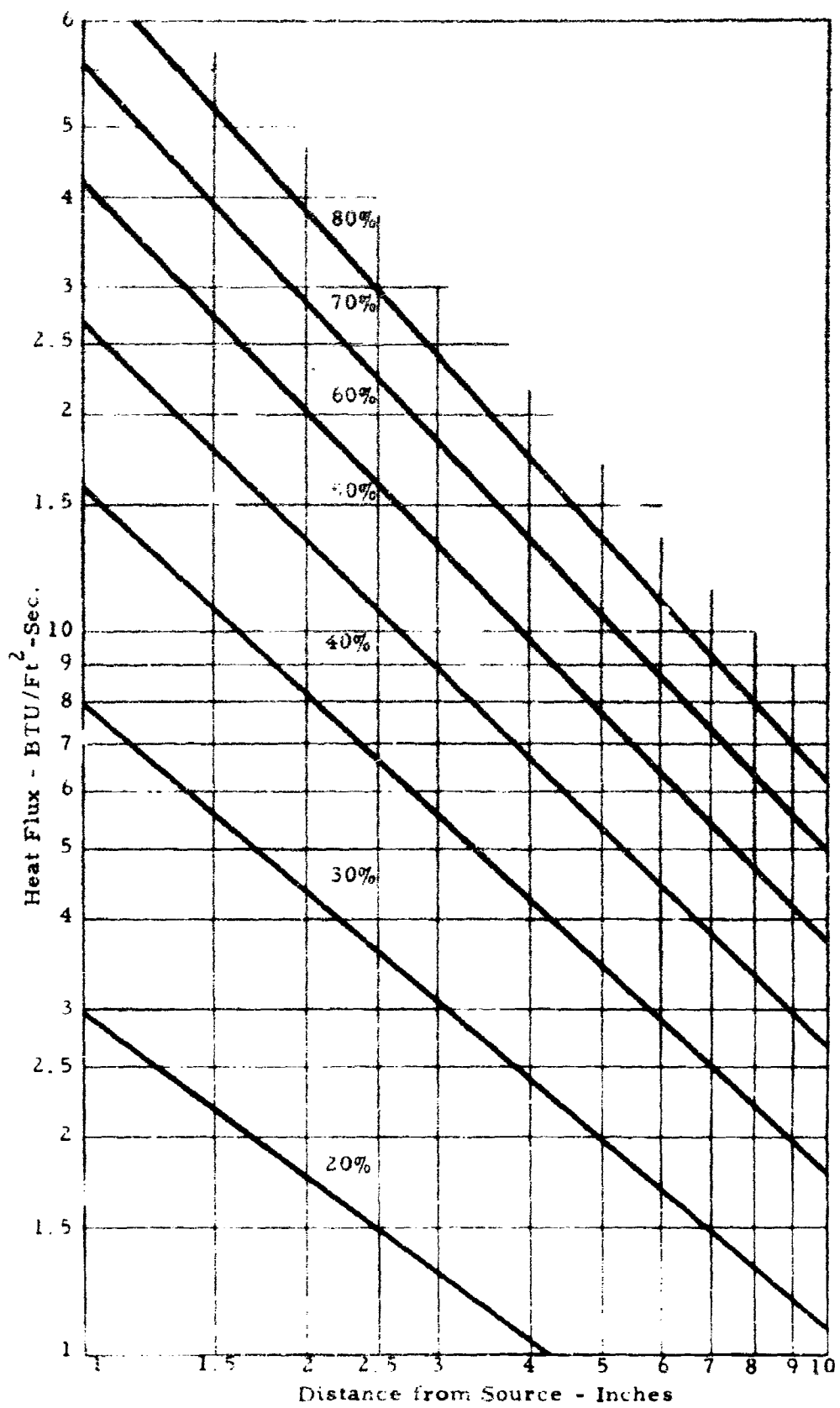


Figure VI - 2

TABLE VI-1

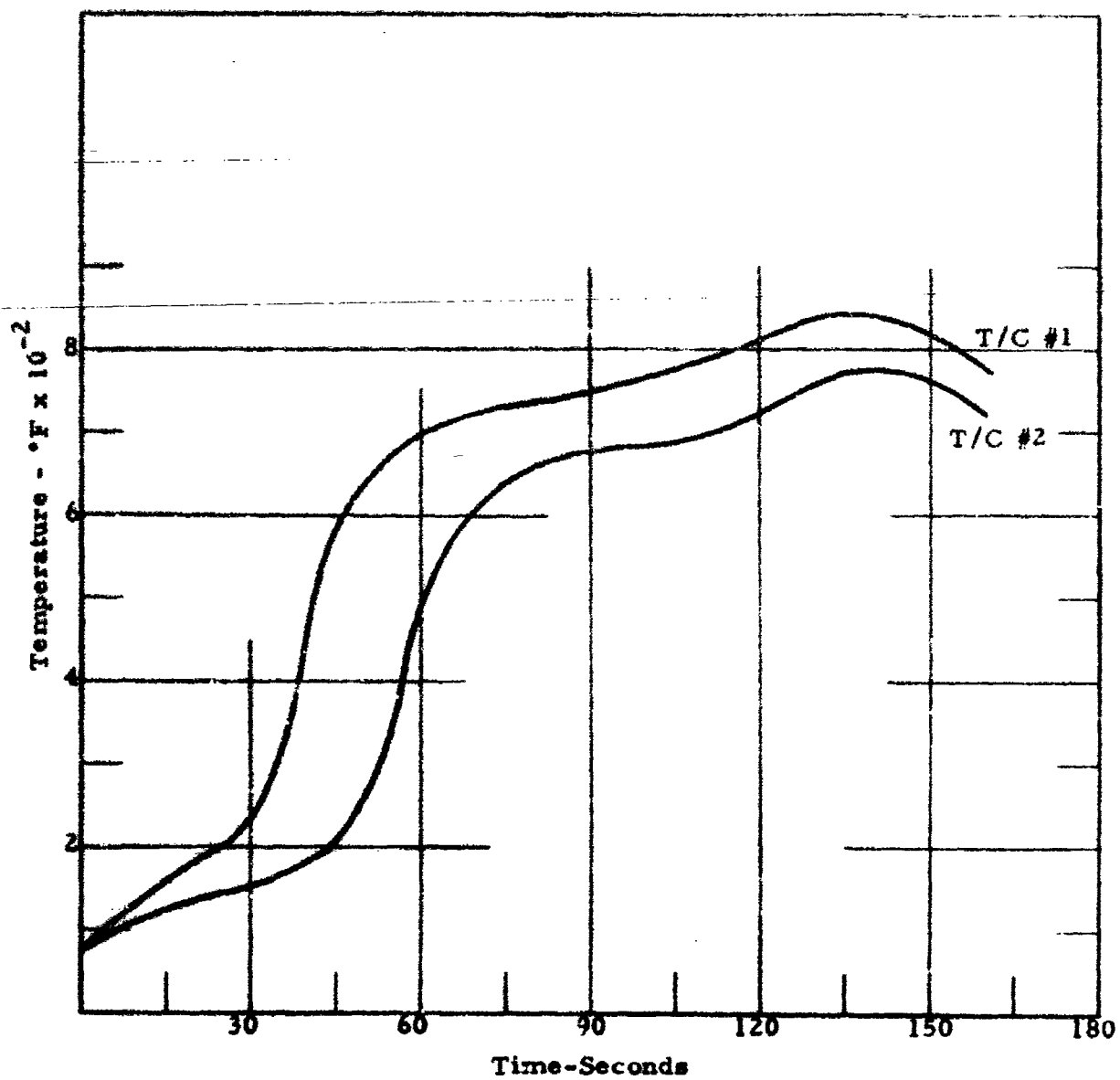
Results of Facility Calibration Tests

| Distance from Lamps | Power Input % | Equilibrium Temp. -°F. | Incident Heat Flux BTU/ft. ² -sec. | Cal/cm ² -sec. |
|------------------------|------------------|---------------------------|--|---------------------------|
| 1" | 40 | 1950 | 16.0 | 4.34 |
| 2" | 40 | 1550 | 7.8 | 2.11 |
| 3" | 40 | 1400 | 5.7 | 1.54 |
| 4" | 40 | 1275 | 4.3 | 1.17 |
| 1" | 30 | 1625 | 9.0 | 2.44 |
| 2" | 30 | 1260 | 4.1 | 1.11 |
| 3" | 30 | 1140 | 3.2 | 0.87 |
| 4" | 30 | 1040 | 2.4 | 0.65 |
| 1" | 20 | 1120 | 3.6 | 0.81 |
| 2" | 20 | 920 | 1.7 | 0.46 |
| 3" | 20 | 825 | 1.3 | 0.35 |
| 4" | 20 | 760 | 1.05 | 0.28 |

TABLE VI-2

Test Results - Heat of Ablation

| Sample No. | Weight gms | Distance from Source- inches | Power Setting % | Initial Heat Flux BTU/ft. ² - sec. | | Time to Ablate sec. | | Total Heat BTU | Heat of Ablation BTU/lb. | Cal/gm | Remarks |
|------------|------------|------------------------------|-----------------|---|----|---------------------|-------|----------------|--------------------------|-------------|---------|
| | | | | 1" | 2" | | | | | | |
| 1 | 18.7 | 1 | 20 | 3.0 | 40 | 140 | 26.5 | 642 | 357 | No Ignition | |
| 2 | 18.6 | 1 | 30 | 8.0 | 23 | 53 | 26.7 | 652 | 362 | No Ignition | |
| 3a | 18.6 | 1 | 40 | 16.0 | 18 | 37 | 37.32 | 918 | 510 | Ignition | |
| 4 | 18.3 | 1 | 60 | 42.5 | 11 | 24 | 58.31 | 1442 | 803 | Ignition | |
| 5 | 18.3 | 1 | 80 | 85.0 | 7 | 17 | 75.43 | 1840 | 1038 | Ignition | |
| 6a | 18.3 | 2 | 40 | 8.3 | 23 | 47 | 30.49 | 755 | 421 | Ignition | |
| 8 | 18.3 | 3 | 30 | 3.1 | 42 | 92 | 24.78 | 613 | 341 | No Ignition | |
| 9 | 18.3 | 3 | 60 | 13.3 | 25 | 32 | 35.4 | 876 | 487 | Ignition | |



Thermocouple Time - Temperature Record
Sample #1

Figure VI-3

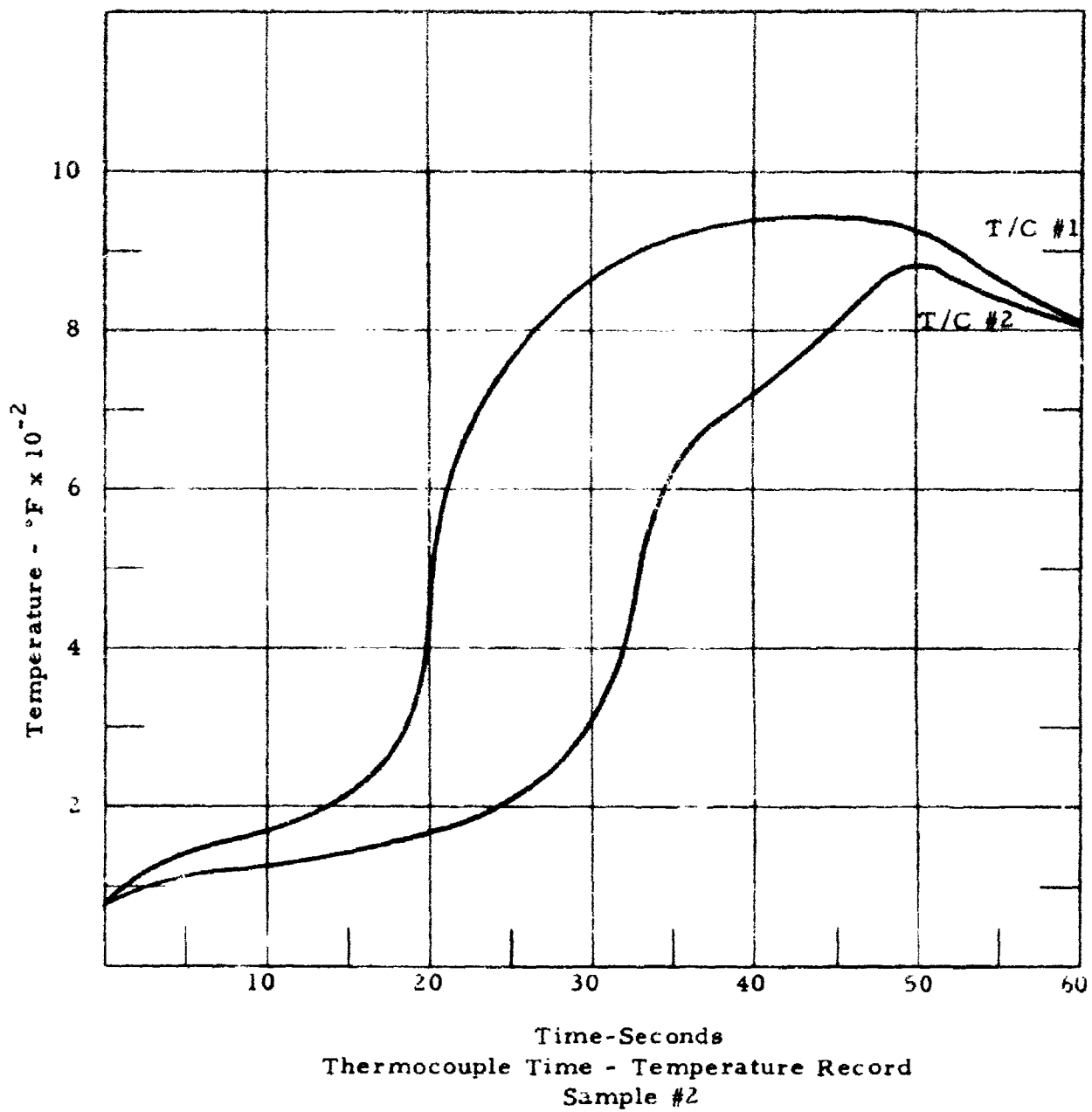
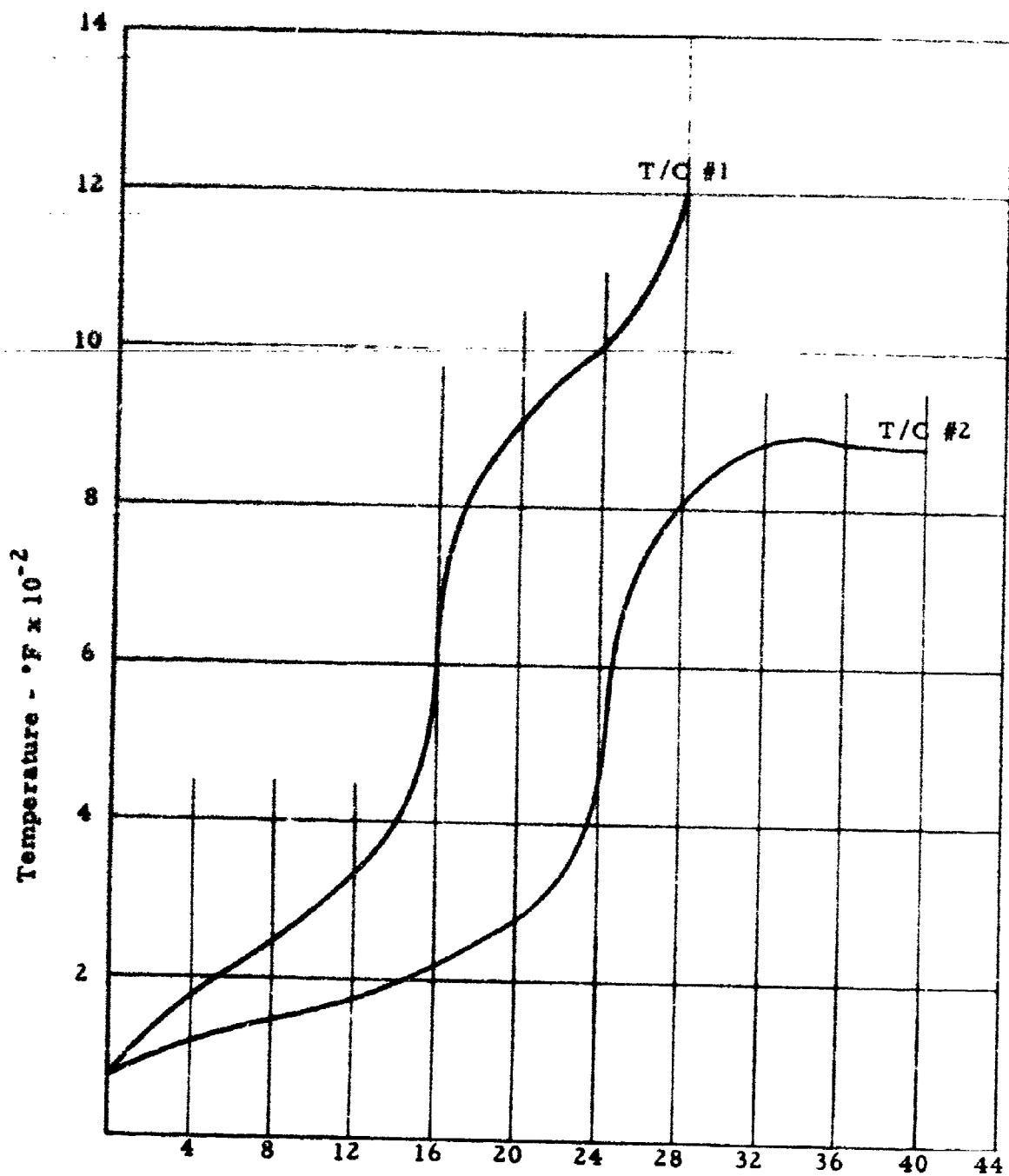
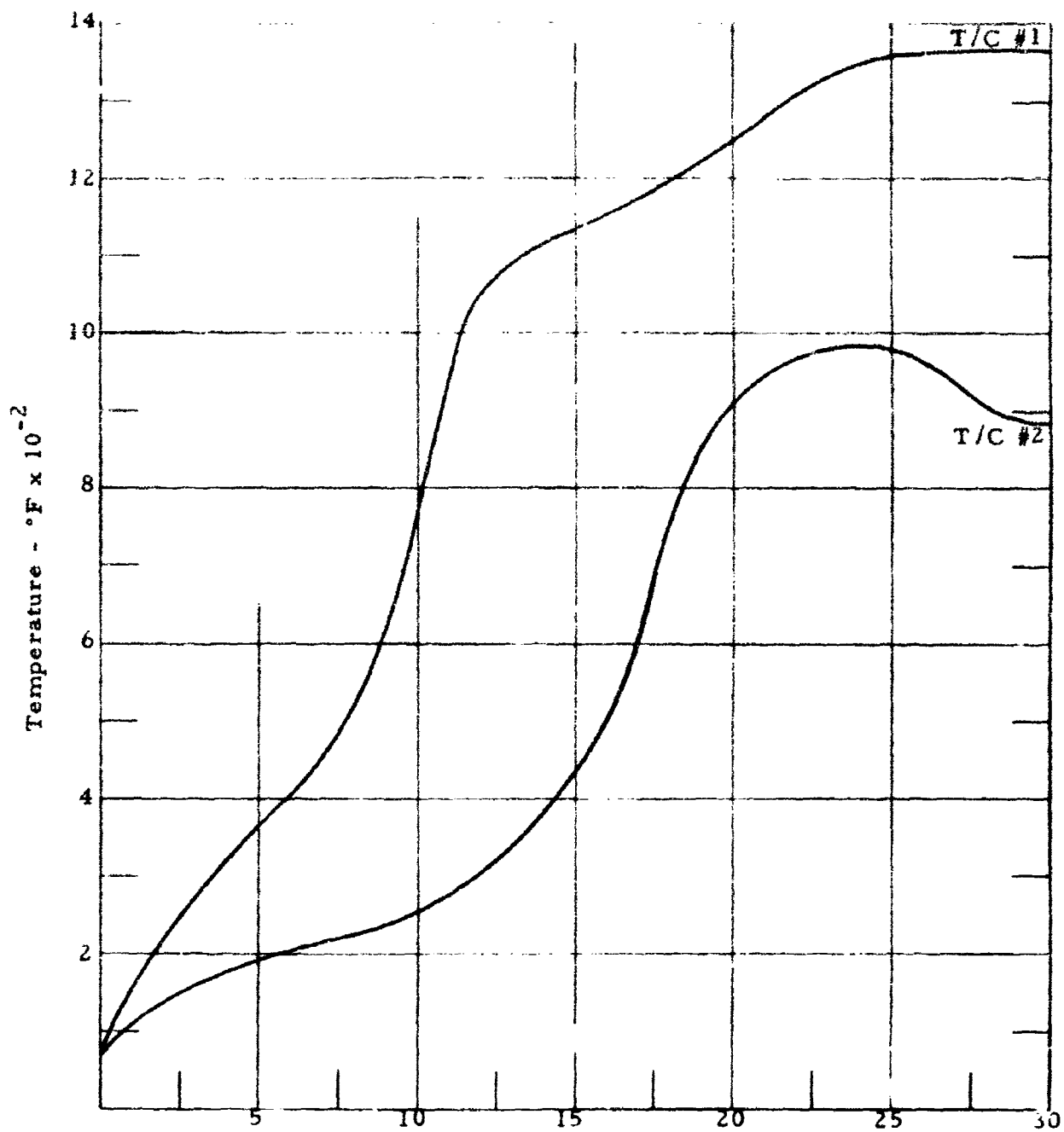


Figure VI-4



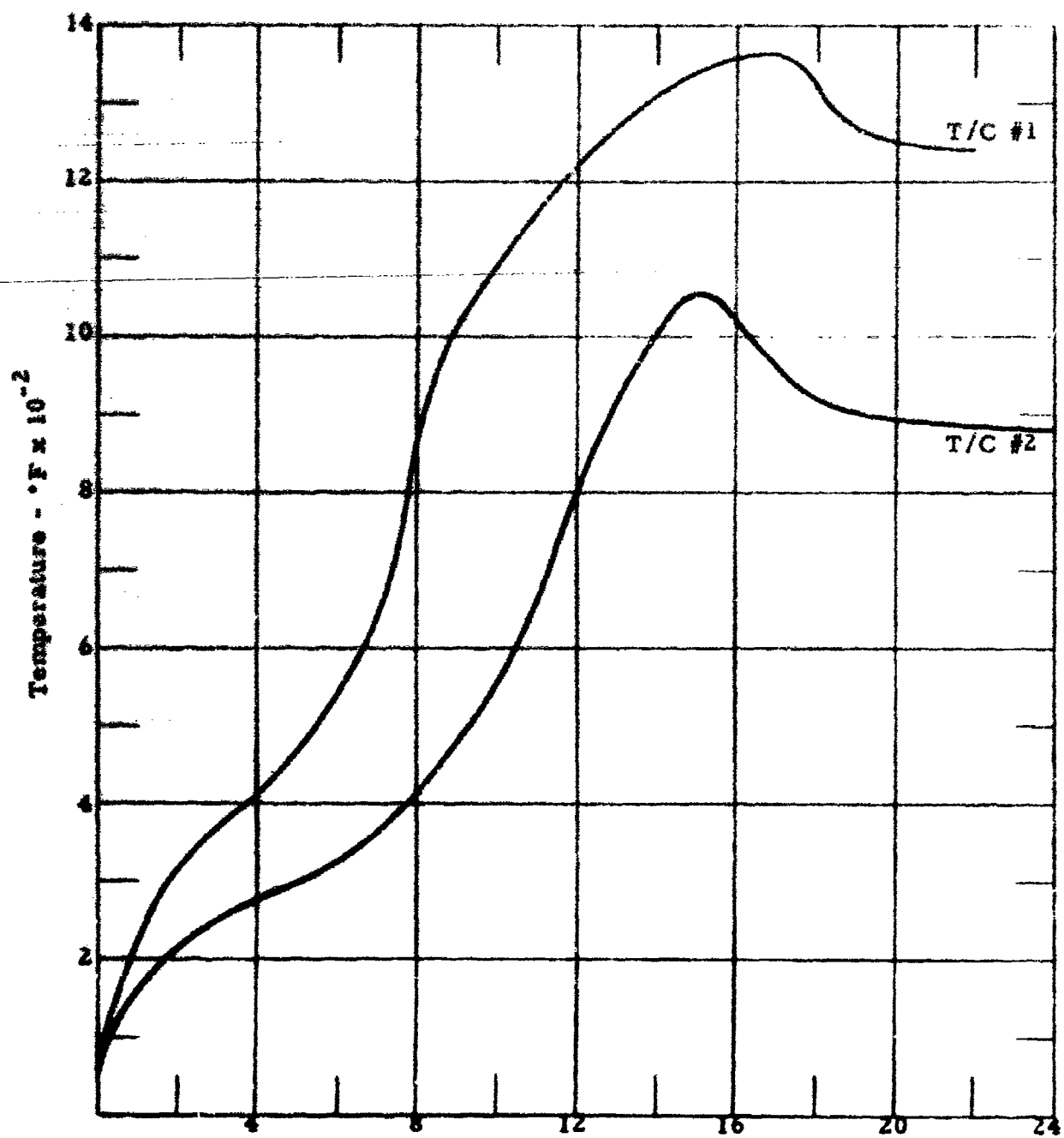
Time-Seconds
Thermocouple Time - Temperature Record
Sample #3a

Figure VI-5



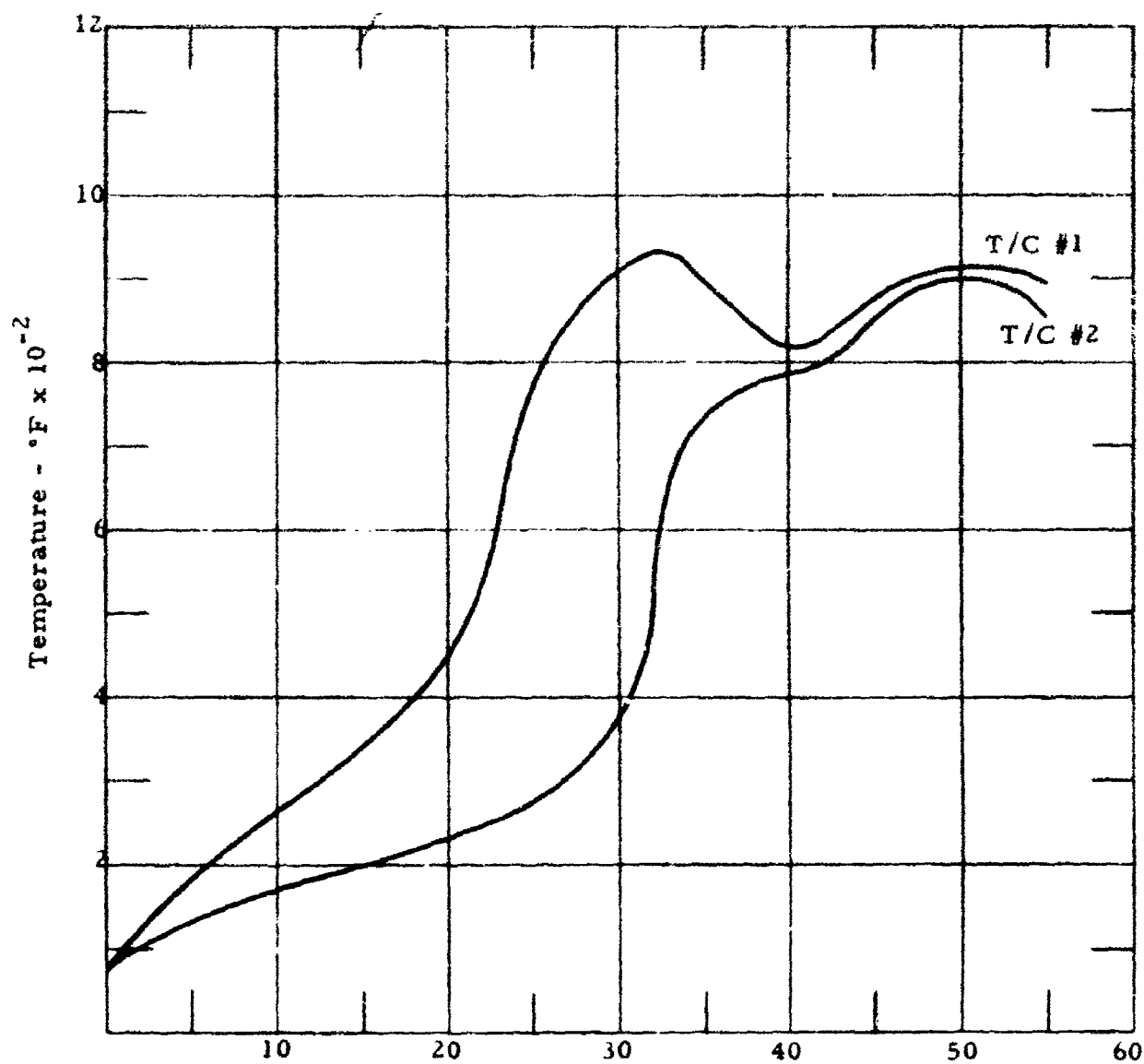
Time-Seconds
Thermocouple Time - Temperature Record
Sample #4

Figure VI-6



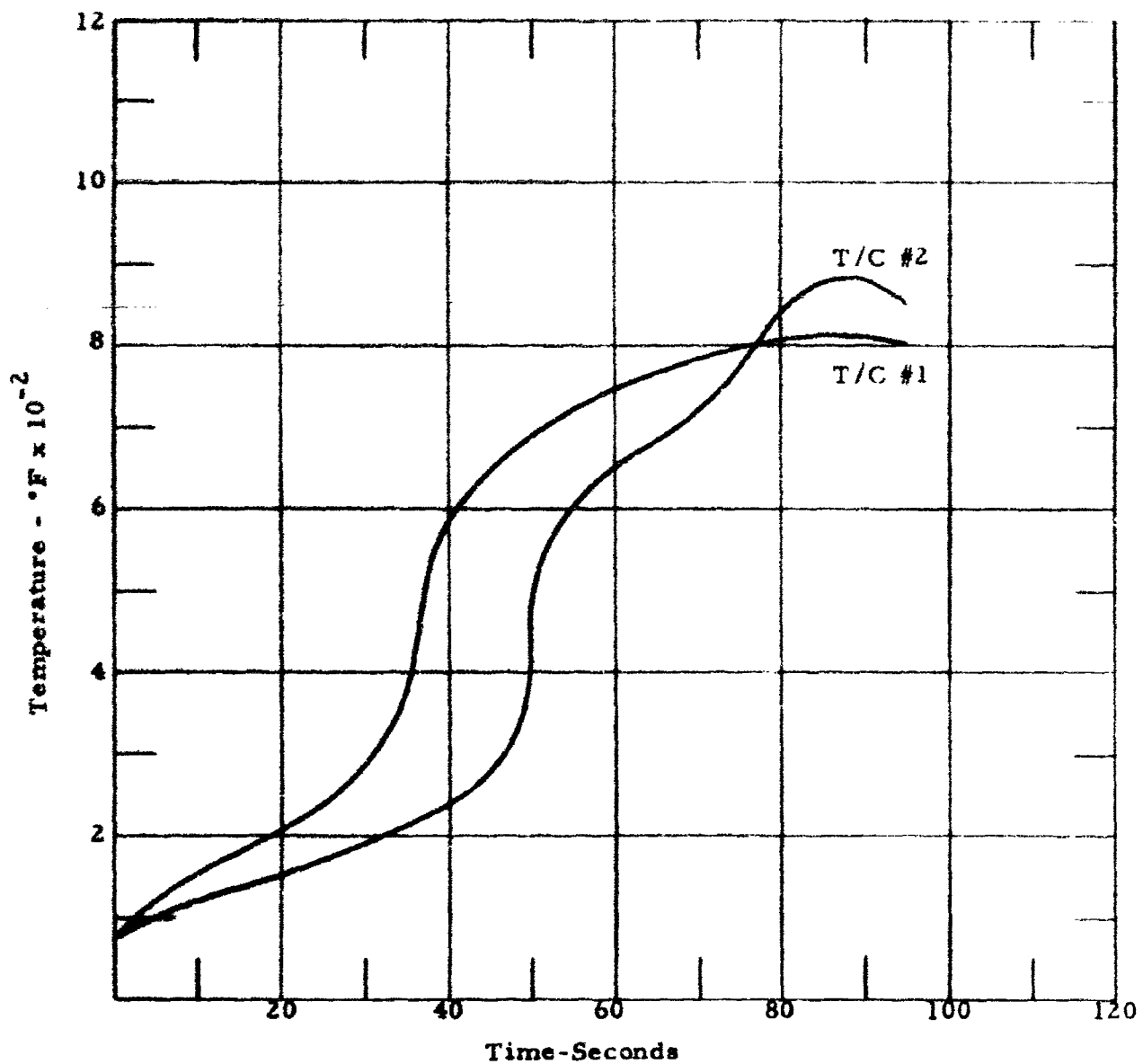
Time-Seconds
Thermocouple Time - Temperature Record
Sample #5

Figure VI-7



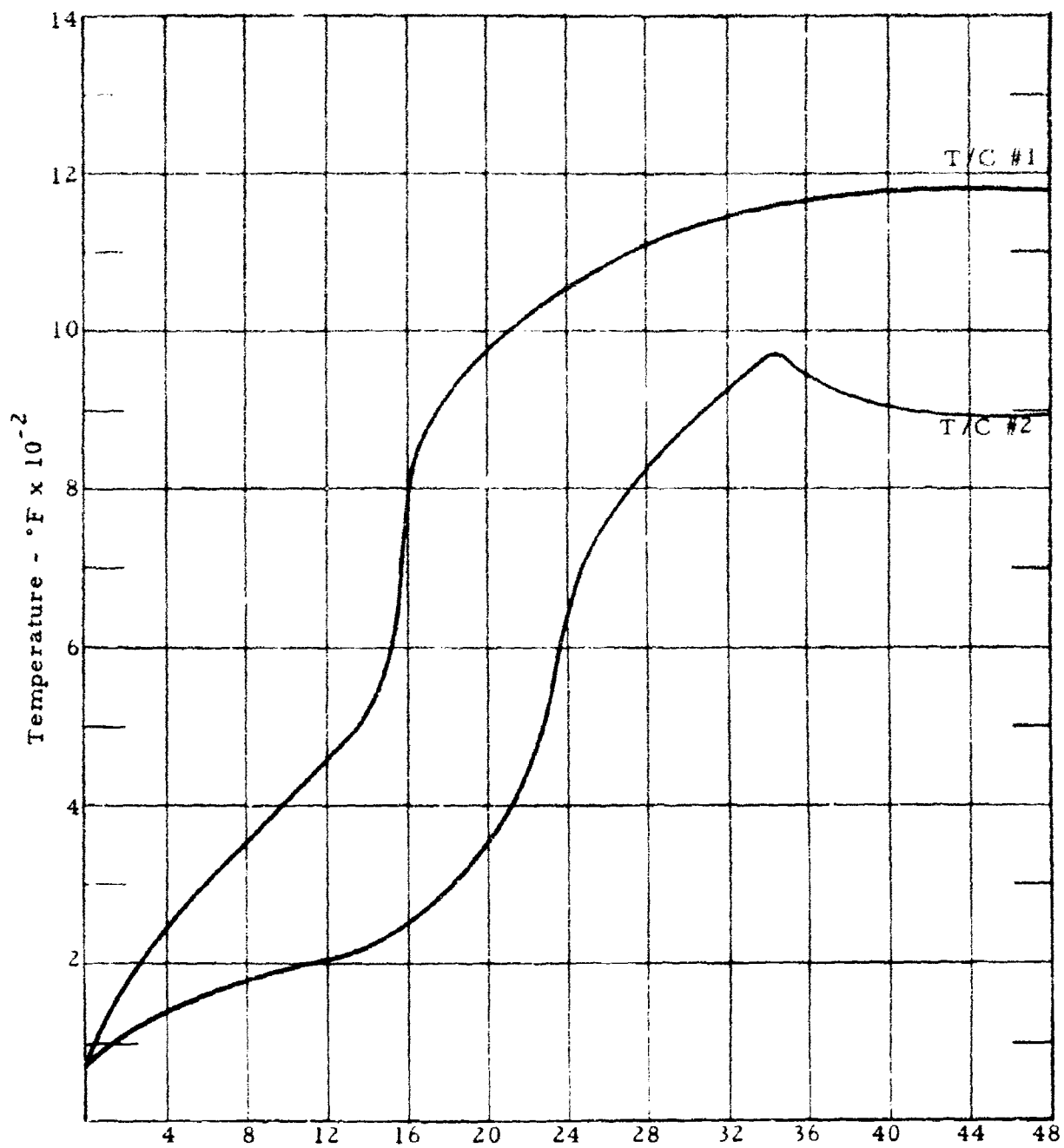
Time-Seconds
Thermocouple Time - Temperature Record
Sample #6a

Figure VI-8



Time-Seconds
Thermocouple Time - Temperature Record
Sample #8

Figure VI-9



Time-Seconds
Thermocouple Time - Temperature Record
Sample #9

Figure VI-10

APPENDIX VII

MEASUREMENTS OF THE DIELECTRIC CONSTANTS OF FOAMED PLASTICS

1. INTRODUCTION

This appendix describes the theory of measurement, procedure and sample calculations of low-loss dielectric constants of foamed plastics. The parameters of interest are the real and the imaginary components which constitute the complex dielectric constant, ϵ^* . The loss tangent, which is many times used to indicate the losses in signal propagation throughout the dielectric medium is given by $\tan \delta = \epsilon''/\epsilon'$ where ϵ' is the real (usually called dielectric constant) and ϵ'' the imaginary component of the complex, dielectric constant ϵ^* . The exponential factor, α , can be calculated directly from the loss tangent when the real dielectric constant and frequency are given. The relationship is well established in the theory of dielectric waves in nonmagnetic mediums:

$$\frac{1}{\alpha} = \frac{\lambda}{\pi \tan \delta \sqrt{\frac{\epsilon'}{\epsilon_0}}} \quad (\text{VII} - 1)$$

where ϵ_0 is the dielectric constant of a vacuum, and λ is the wavelength of the electromagnetic radiation in the medium.

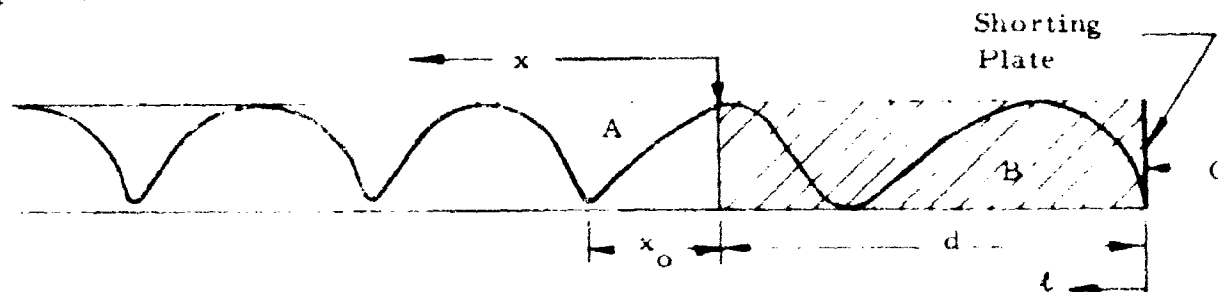
The importance of the dielectric measurements is that all the electrical characteristics of a system utilizing the subject medium are determined in terms of the dielectric parameters. The theory of measurement, the procedure and analytical techniques, charts or aids given in this appendix have been redacted from A. VonHippel's "Dielectrics and Waves", Wiley, 1954, and "Dielectric Materials and Applications", Wiley, 1954, a companion edition to the first text. These texts are written very vividly and it would be very difficult to improve on the presentation of the material. Justification for the formulas used in this appendix will then be referenced freely to the above texts without presenting the formal proofs which are to be found in VonHippel's texts. The dielectric data on the foamed plastic were taken jointly, but independently, at both the Aeronca Manufacturing

Corporation, Middletown, Ohio, and the Melpar Corporation, Falls Church, Virginia.

2. THEORY OF MEASUREMENT OF DIELECTRICS IN SHORTED HOLLOW RECTANGULAR WAVEGUIDES

The dielectric constants of nonmagnetic low-loss materials are measured by setting up standing waves in a hollow, rectangular waveguide through reflections from a shorting section. A stabilized klystron oscillator of a prescribed frequency radiates monochromatic radiation into one end of the hollow guide and it is reflected from the shorting metallic plate at the other end. The standing waves are measured by a slotted line probe traveling along the slot parallel to the guide axis. A dielectric sample is inserted into the closed end of the guide opposite the transmitter and adjacent to the short. The sample is cut to fit into the guide rather snugly. Its length, d , is chosen to be about three-quarter guide wavelengths long, which is possible only when the value of dielectric constant and free space wavelength are known approximately. It is also essential that the faces be perpendicular to the guide axis.

Consider the waveguide transmission line, shown below, consisting of three mediums. Medium Number A will be considered a lossless medium with a dielectric constant relative to that of free space (i.e., $\epsilon_r^* = 1$), Medium Number B is some dielectric material having a complex dielectric constant $\epsilon^* = \epsilon' + j\epsilon''$ where ϵ' is the relative dielectric constant of the material and ϵ'' is the loss factor of the material. The loss tangent is the ratio ϵ''/ϵ' or $\tan \delta = \epsilon''/\epsilon'$; Medium Number C is considered as a perfect short circuit.



the nearest minimums to be valid.

Using (VII-14) in (VII-10), one obtains

$$Z(0) = Z_1 \left[\frac{\frac{E_{\min}}{E_{\max}} - j \tan \frac{2\pi x_0}{\lambda_1}}{1 - j \frac{E_{\min}}{E_{\max}} \tan \frac{2\pi x_0}{\lambda_1}} \right] \quad (\text{VII-15})$$

The terminating impedance, $Z(0)$, can, therefore, be determined experimentally by measurements on the standing wave pattern in Medium A. Since one wants to obtain properties of Medium B for measurements in Medium A, one utilizes the Equations (VII-3) and (VII-15), i.e.,

$$Z(0) = Z_2 \tan \lambda_2 d$$

$$Z(0) = Z_1 \left[\frac{\frac{E_{\min}}{E_{\max}} - j \tan \frac{2\pi x_0}{\lambda_1}}{1 - j \frac{E_{\min}}{E_{\max}} \tan \frac{2\pi x_0}{\lambda_1}} \right]$$

Z_1 and Z_2 are characteristic impedances for Mediums B and C (shorting plate). Since for nonmagnetic substances it can be shown (see "Dielectric and Waves", page 75) that

$$Z_1 \lambda_1 = Z_2 \lambda_2 \quad (\text{VII-16})$$

Equation (VII-3) can be written with the substitution of (VII-16) as

$$Z(0) = \frac{Z_1 \lambda_1 d}{\lambda_2 d} \tanh \lambda_2 d \quad (\text{VII-17})$$

Since Medium A is lossless, $\gamma_1 = j\beta = j\frac{2\pi}{\lambda_1}$. Then, one can derive γ_2 from the measured quantities by the expression

$$\frac{\tanh \gamma_2 d}{\gamma_2 d} = \frac{-j\lambda_1}{2\pi d} \left[\frac{\frac{E_{\min}}{E_{\max}} - j \tan \frac{2\pi x_0}{\lambda_1}}{1 - j \frac{E_{\min}}{E_{\max}} \tan \frac{2\pi x_0}{\lambda_1}} \right] \quad (\text{VII-18})$$

which also can be written

$$\frac{\tanh \gamma_2 d}{\gamma_2 d} = C e^{j\zeta} \quad (\text{VII-19})$$

The function $C e^{j\zeta}$ is found by measuring the thickness d of the sample, the wavelength λ_1 in the air filled section, the inverse VSWR, or $\frac{E_{\min}}{E_{\max}}$ and the distance x_0 of the first minimum. Then, the function $\gamma_2 d = T e^{j\tau}$ is determined from charts of the function

$$\frac{\tanh T e^{j\tau}}{T e^{j\tau}} = C e^{j\zeta}$$

From the characteristic propagation factor, γ_2 , one can determine the complex dielectric constant of Medium B from the relationship

$$\epsilon_r^* = \frac{\epsilon^*}{\epsilon_0} = \frac{\epsilon'}{\epsilon_0} - j \frac{\epsilon''}{\epsilon_0} = \frac{\left(\frac{1}{\lambda_c}\right)^2 - \left(\frac{\gamma_2}{2\pi}\right)^2}{\left(\frac{1}{\lambda_c}\right)^2 + \left(\frac{1}{\lambda_1}\right)^2} \quad (\text{VII-20})$$

where λ_c is the cutoff wavelength for the fundamental TE_{10} mode of operation in the waveguide, ϵ_0 is the dielectric constant of air, and λ_1 is the air-filled guide wavelength, (VII-20) is derived from the treatment of electromagnetic fields in waveguides (Ref. Section 22, "Dielectrics and Waves"). Equation (VII-20) is the sought-after relationship which can be determined from the shorted waveguide experimental approach.

3. METHOD AND PROCEDURE

The shorted waveguide method of dielectric measurements described herein is perhaps the best known and most universally employed. It may be crude or accurate, depending upon the equipment and discernment observed in the experiment. The experimental setup is shown schematically in Figure VII-1. The standing wave is measured in air above the dielectric sample of thickness, d , as shown in Figure VII-2. The terminating impedance $Z(0)$ of the air guide is found by measuring the inverse VSWR and the distance x_0 of the first minimum from the dielectric boundary. Since the detector would be overloaded and the field distribution disturbed if

E_{\max} were measured directly, the ratio $\frac{E_{\min}}{E_{\max}}$, or the inverse VSWR, is usually found by measuring the distance Δx between the two positions where the current in the detector doubles its minimum value (see Figure VII-2).

For a detector of "square law" response and high VSWR (VSWR > 100:1), the relationship between Δx and $\frac{E_{\min}}{E_{\max}}$ is given by

$$\frac{E_{\min}}{E_{\max}} = \pi \frac{\Delta x}{\lambda_1} \quad (\text{VII-21})$$

where λ_1 is the guide wavelength in the air space. The quantity, λ_1 , can be determined by measuring the distance between two successive minima. For low-loss samples, the waveguide walls between the minimum and the sample boundary may be appreciable. The loss in the empty guide is determined by a measurement of Δx_e taken at a distance d_e from the shorting plate. With the sample in the guide, a value $\Delta x'$ is subtracted from the measured value, Δx , to correct for these losses. The correction is

$\Delta x_e \frac{d'}{d_e}$ so that

$$\Delta x_{\text{corrected}} = \Delta x_{\text{measured}} - \frac{d'}{d_e} \Delta x_e \quad (\text{VII-22})$$

where d' is the distance from the dielectric air interface to the null position, and d_e is the distance from the measured inverse VSWR to the shorting plate in the empty guide. Figure VII-3 is a sketch of typical standing patterns and the measured observables in each situation.

The distance, x_{o1} , from the dielectric air interface to the first minimum is determined from measured null positions in both the empty and dielectric filled guide. Using Figure VII-3, it is easy seen that

$$x_o = d_N - d' - d \quad (\text{VII-23})$$

where d_N is the distance from the shorting plate to the measured null position. Having measured λ_1 , Δx_e , and x_o , the determination of ϵ^* , the complex dielectric constant, can be computed from the formulas of

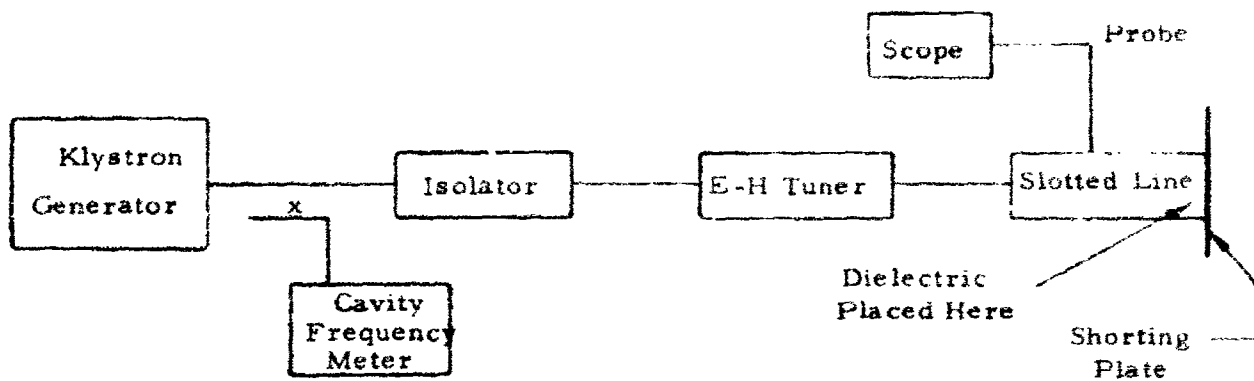


Figure VII-1 - X-Band Dielectrometer Circuit

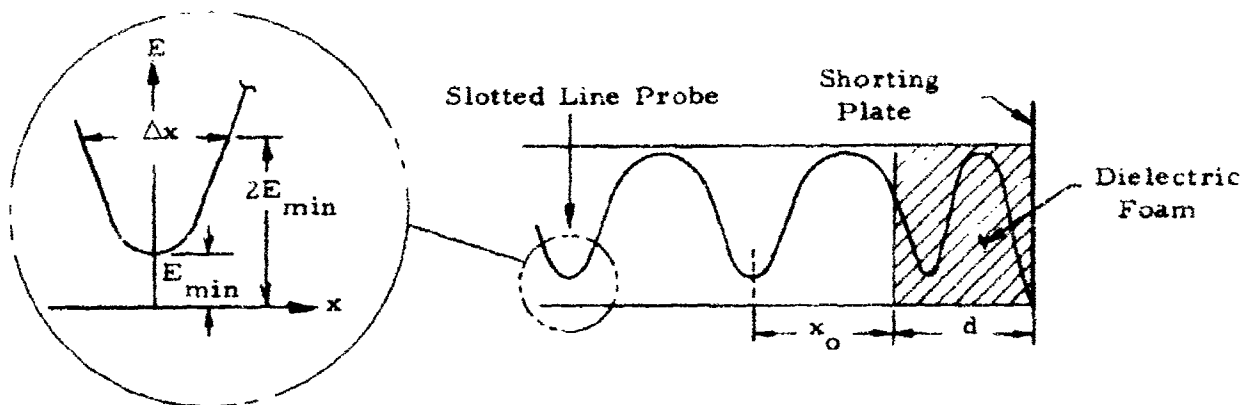


Figure VII-2 - VSWR Measurement

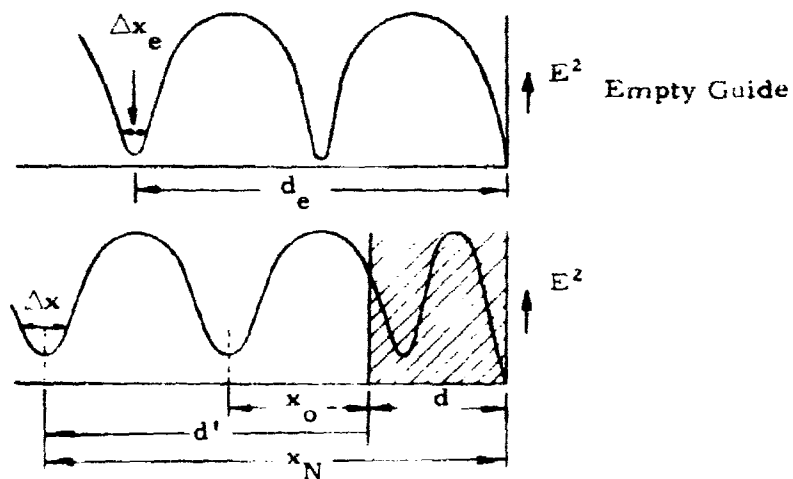


Figure VII-3 - Standing Wave Patterns

Section VII. 2. The free space wavelength, λ_o , the guide wavelength, λ_1 , and the cutoff wavelength, λ_c , are determined by the usual formulas:

$$\lambda_o = \frac{C}{f} \quad (\text{VII-24})$$

$$\lambda_1 = \frac{\lambda_o}{\sqrt{\epsilon_r - \left(\frac{\lambda_o}{\lambda_c}\right)^2}} \quad (\text{VII-25})$$

and

$$\lambda_c = 2a \text{ (TE}_{10} \text{ mode)} \quad (\text{VII-26})$$

where

- a is the width of the guide,
- f is the klystron tuned frequency,
- ϵ_r is the relative dielectric constant of the dielectric in the guide, and
- C is the speed of light in a vacuum.

The procedure for measuring the complex dielectric constant of a solid foam sample at X-band frequency (10 kmc) was as follows:

- a. Sample preparation - the sample was cut into a bar of length approximately three-quarter guide wavelengths long, where λ_1 was determined from VII-25 by estimating ϵ_r to be about 1.02. The free space wavelength was determined by VII-24. The frontal area of the sample bar was slightly less than that of the guide for a snug fit. The sample length was measured as accurately as possible.
- b. Empty guide measurements - with the setup shown in Figure VII-1, the klystron is tuned to peak at 10 kmc with square wave modulation set to 1,000 cps. The slotted line probe is tuned and adjusted for the maximum null position. The E-H tuner adjustment then permits fine tuning for a minimum square-wave pattern on the scope. With repeated adjustments on the slotted line and E-H tuner, the slotted line probe is centered at a maximum null point, or minimum square-wave pattern on the scope. This distance from this null to the shorting plate is measured

and recorded as d_e . The slotted line is then moved along the guide on both sides of the null to the position of twice the minimum power. This measurement requires care and stability from the klystron generator. This measurement is recorded as Δx_e . The distances between two nulls should also be measured to determine $\lambda_1/2$.

- c. Sample in guide measurements - with the sample placed inside the guide, the same procedure of (b) is followed, except that the null to be measured should be, if at all possible, the very first null; i.e., the one adjacent to the dielectric sample. Since this was not possible because of the limitations of the slotted line, the null position, x_N , had to be measured and the number of that null from the dielectric interface determined from λ_1 and d , the length of the sample.

4. DIELECTRIC DATA AND CALCULATIONS

4.1 Experimental Tabulated Data

| Parameter (units) | Polystyrene Foam | Polyethylene Foam | Measuring Device |
|----------------------|---------------------|----------------------|---------------------------|
| density (pcf) | 2 | 1 | - |
| f_o (kmc) | 10 | 10 | cavity frequency meter |
| λ_o (in.) | 1.18 | 1.18 | calculated |
| λ_1 (in.) | 1.563 | 1.566 | S.L. * micrometer gage |
| λ_c (in.) | 1.800 | 1.80 | calculated |
| x_N (in.) | 3.881 | 8.020 | S.L. micrometer gage |
| x_o (in.) | .3741 | .334 | S.L. micrometer gage |
| d (in.) | 1.163 | 1.19 | vernier caliper |
| Δx (in.) | .0024 | .0038 | S.L. micrometer gage |
| Δx_e (in.) | .0020 | .0030 | S.L. micrometer gage |

| Parameter (units) | Polystyrene Foam | Polyethylene Foam | Measuring Device |
|----------------------|---------------------|----------------------|--------------------------|
| d' (in.) | 2.718 | 2.686 | S. L. micrometer gage |
| d_e (in.) | 3.9065 | 3.918 | S. L. micrometer gage |

*S. L. ~ slotted line

The measurement accuracy of the slotted line micrometer gage was to the nearest thousandth-of-an-inch. The ten thousandths could be estimated but was doubtful.

4.2 Calculated Results of ϵ^*

The calculated values of ϵ^* for polystyrene foam (2 pcf) and polyethylene foam (1 pcf) are tabulated below. ϵ_0 was assumed to be unity.

4.2.1 Polystyrene Foam

$$\epsilon^* = 1.028 - .00025 j \text{ (relative complex dielectric constant)}$$

$$\epsilon' = 1.028 \text{ (relative dielectric constant)}$$

$$\epsilon'' = .00025 \text{ (relative loss factor)}$$

$$\tan \delta = \frac{\epsilon''}{\epsilon'} \approx .00025 \text{ (loss tangent)}$$

4.2.2 Polyethylene Foam

$$\epsilon^* = 1.04 - .0004 j \text{ (relative complex dielectric constant)}$$

$$\epsilon' = 1.04 \text{ (relative dielectric constant)}$$

$$\epsilon'' = .0004 \text{ (relative loss factor)}$$

$$\tan \delta \approx .0004 \text{ (loss tangent)}$$

4.2.3 Sample Calculation

The calculation for polystyrene only is given as follows:

Using equation (VII-18)

$$\frac{\tanh \gamma_2 c}{\gamma_2 d} = \frac{-j \lambda_1}{2 \pi d} \left[\frac{\frac{E_{\min}}{E_{\max}} - j \tan \frac{2 \pi x_0}{\lambda_1}}{1 - j \frac{E_{\min}}{E_{\max}} \tan \frac{2 \pi x_0}{\lambda_1}} \right]$$

where

$$\lambda_1 = 1.5626''$$

$$d = 1.163''$$

$$x_o = .3741''$$

$$\frac{E_{\min}}{E_{\max}} = \frac{\pi \Delta x_c}{\lambda_1} = \frac{\pi}{\lambda_1} \left(\Delta x - \frac{d'}{d_e} \Delta x_e \right)$$

$$d' = 2.718''$$

$$d_e = 3.9065''$$

$$\Delta x_e = .0020''$$

$$\Delta x = .0024''$$

Therefore, substitution of numerical values into (VII-18) yields:

$$\frac{\tanh \gamma_2 d}{\gamma_2 d} = \frac{-j(1.5626)}{2(3.14)(1.163)} \left[\frac{3.14}{1.5626} \left(.0024 - \frac{(2.718)(.002)}{3.9065} \right) - j \tan \frac{2(3.14)(3.741)}{1.5626} \right]$$

$$\frac{\tanh \gamma_2 d}{\gamma_2 d} = -.2138 j \left[\frac{.002 - 14.99j}{1 - .0304 j} \right] = \frac{-3.205 - .004 j}{1 - .0304 j}$$

This reduces to

$$\frac{\tanh \gamma_2 d}{\gamma_2 d} = -3.202 - .0978 j$$

which defines a vector of length 3.204 and oriented in space at the angle $181^\circ 45'$. This may be rewritten as:

$$\frac{\tanh \gamma_2 d}{\gamma_2 d} = 3.204 / 181^\circ 45'$$

The functional relationship

$$\frac{\tanh \gamma_2 d}{\gamma_2 d} = \frac{\tanh T / \tau}{T / \tau} = \frac{1}{C} / -\zeta$$

is plotted on charts in VonHippel's "Dielectric Materials and Applications". The value of $\gamma_2 d$ or T / τ may be read directly from such charts. Figures VII-4, VII-5 and VII-6 are charts obtained from VonHippel's text for the range where $1/C = .312$ and $\zeta = 178.25^\circ$. The vector $3.204 / 181.45^\circ$ may be considered as a rotation of 360° of the vector $3.204 / -178.25^\circ$. This permits the use of the charts, Figures VII-4 through VII-6. However, there are several possible solutions to the transcendental equation. Using the charts of Figures VII-4, VII-5 and VII-6, there are three solutions for $\frac{1}{C} = .312$ and $\zeta = 178.25^\circ$. They are:

$$T / \tau = \gamma_2 d = 1.7475 / 89.8^\circ \quad (\text{Figure VII-4})$$

$$T / \tau = \gamma_2 d = 4.784 / 89.9^\circ \quad (\text{Figure VII-5})$$

$$T / \tau = \gamma_2 d = 7.90 / 89.9^\circ \quad (\text{Figure VII-6})$$

With the solution for $\gamma_2 d$, the complex dielectric constant can now be determined from Equation (VII-20).

$$\epsilon_r^* = \epsilon' - j\epsilon'' = \frac{\left(\frac{1}{\lambda_c}\right)^2 - \left(\frac{\gamma_2 d}{2\pi d}\right)^2}{\left(\frac{1}{\lambda_c}\right)^2 + \left(\frac{1}{\lambda_1}\right)^2}$$

$$\epsilon_o = 1.0$$

$$\lambda_c = 1.8 \text{ in.}$$

$$\lambda_1 = 1.5626 \text{ in.}$$

$$\gamma_2 d = T / \tau = T e^{j\tau} = T(\cos \tau + j \sin \tau)$$

$$(\text{Case a}) \quad \gamma_2 d = 1.7475 / 89.8^\circ = 1.7477 (\cos 89.8^\circ + j \sin 89.8^\circ)$$

$$\gamma_2 d = .0040 + 1.747 j$$

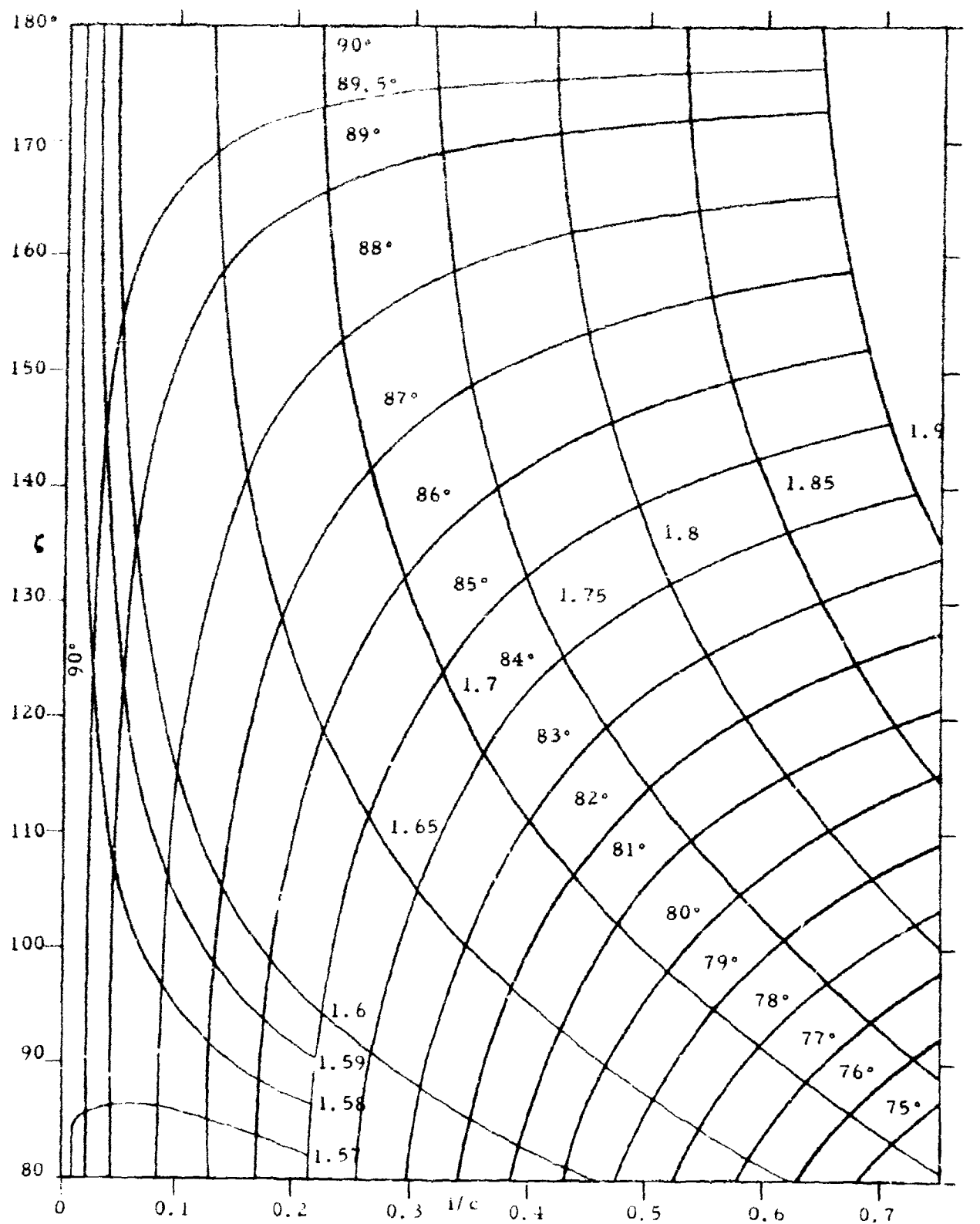
$$(\text{Case b}) \quad \gamma_2 d = 4.74 / 89.9^\circ = 4.74 (\cos 89.9^\circ + j \sin 89.9^\circ)$$

$$\gamma_2 d = .008 + 4.74 j$$

$$(\text{Case c}) \quad \gamma_2 d = 7.90 / 89.9^\circ = 7.90 (\cos 89.9^\circ + j \sin 89.9^\circ)$$

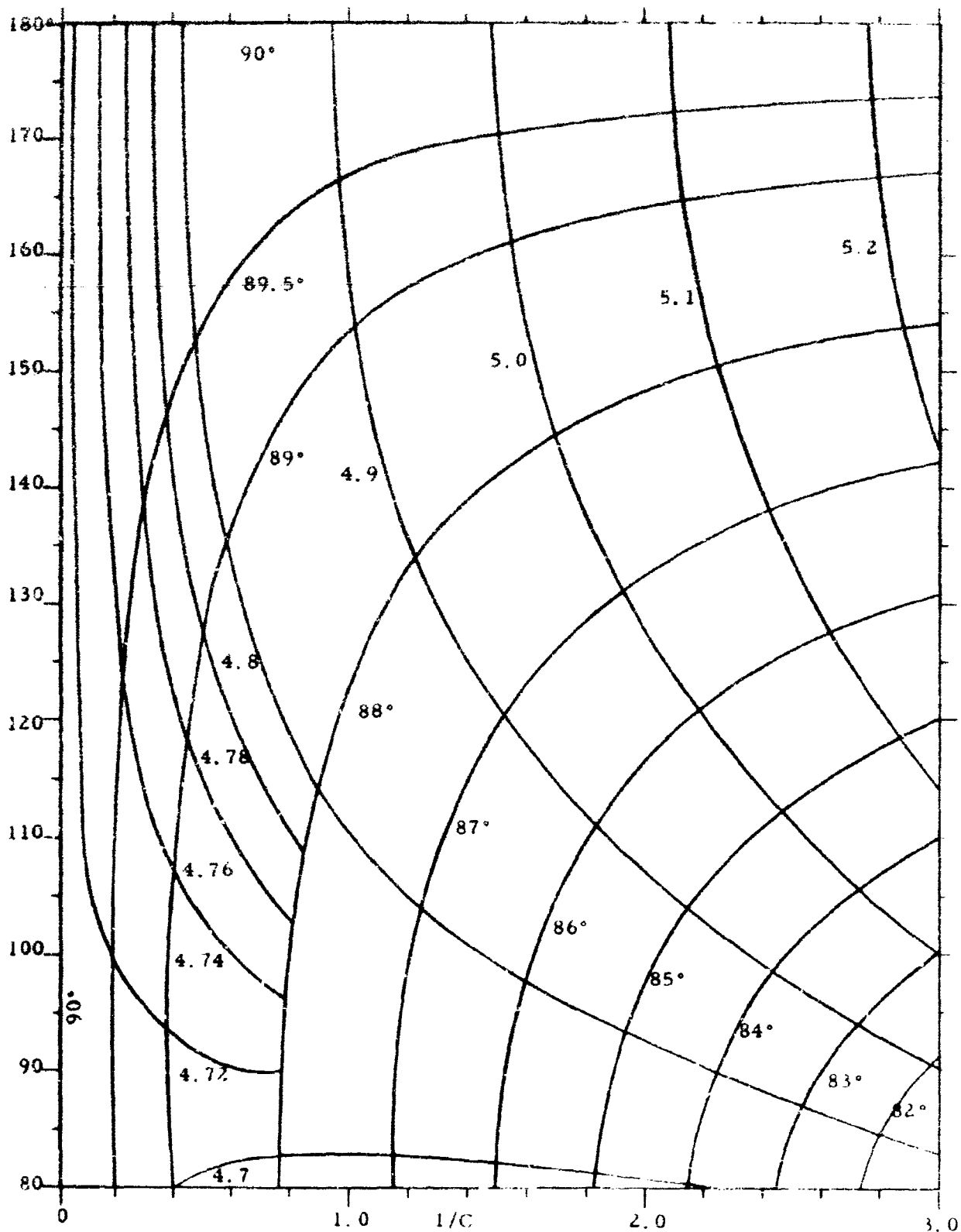
$$\gamma_2 d = .0139 + 7.90 j$$

Trying Case a in Equation (VII-20)



$\frac{\tanh \tau / \tau}{\tau / \tau} = \frac{1}{C}$ Part A, τ , 0 to 2.0; τ , 70° to 90°; Part B, $1/C$, 0 to 0.75;
 ζ , 80° to 180°

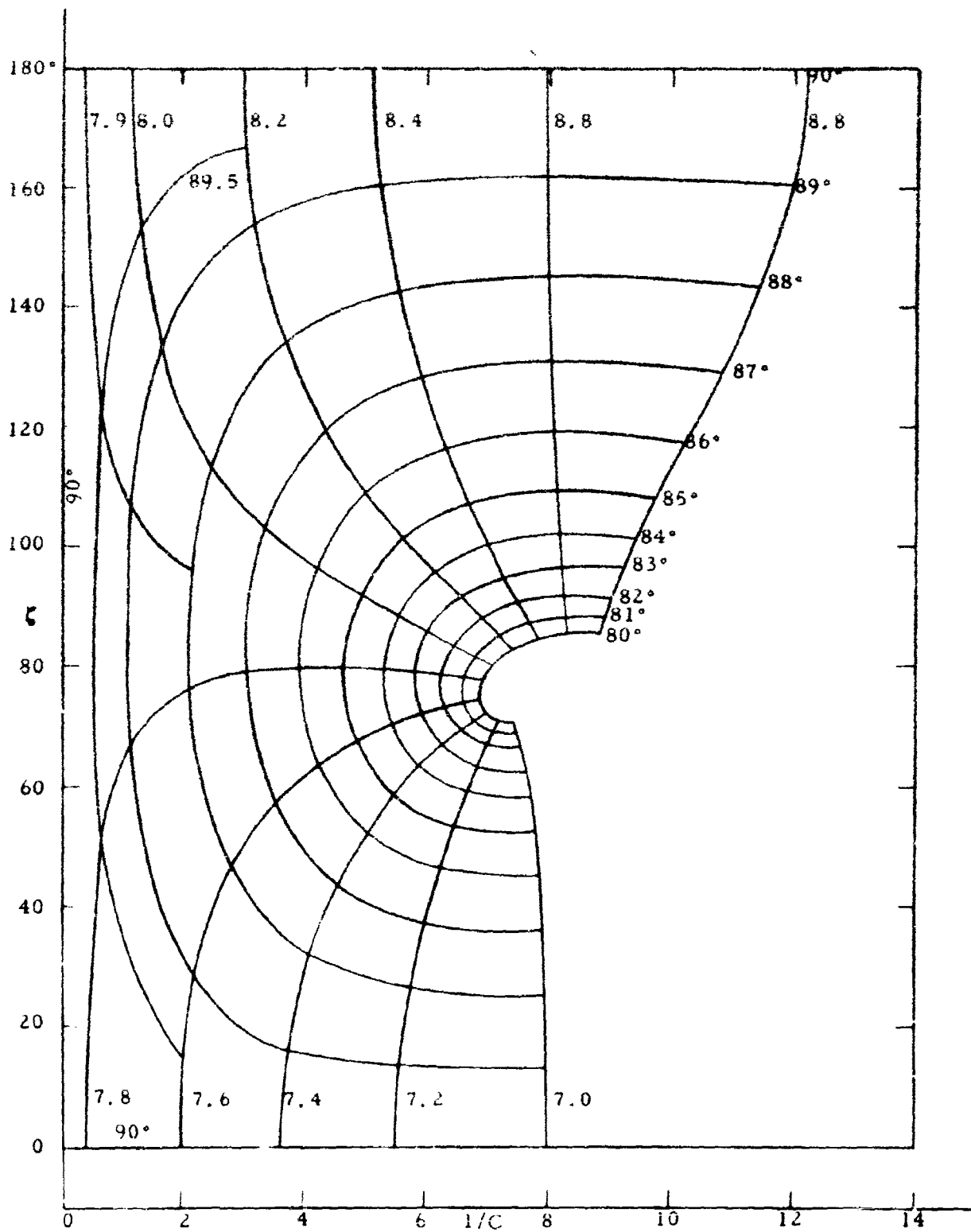
Figure VII-4



$\frac{\tanh T / \tau}{T / \tau} = \frac{1}{C} \frac{1}{\zeta}$, T , 4.0 to 5.4; τ , 70° to 90°; Part B, $1/C$, 0 to 3.0;

ζ , 80° to 100°

Figure VII-5



$\frac{\tanh T / \tau}{T / \tau} = \frac{1}{C} \quad T, 7.0 \text{ to } 8.8, \tau, 80^\circ \text{ to } 90^\circ; 1/C, 0 \text{ to } 13; \zeta, 0^\circ \text{ to } 180^\circ$

Figure VII-6

$$\epsilon_r^* = \epsilon' - j\epsilon'' = \frac{\left(\frac{1}{1.8}\right)^2 - \frac{(3.04 + j1.747)^2}{2(3.14)(1.163)}}{\left(\frac{1}{1.8}\right)^2 + \left(\frac{1}{1.563}\right)^2}$$

$$\epsilon_r^* = .509 - .000371 j$$

$$\tan \delta = \frac{.00037}{.509} \approx .00073$$

This is an impossible solution since $\epsilon' = 1$ for a vacuum.

Trying Case b in Equation (VII-20)

$$\epsilon_r^* = \epsilon' - j\epsilon'' = \frac{\left(\frac{1}{1.8}\right)^2 - \frac{(.008 + 4.74 j)^2}{2(3.14)(1.163)}}{\left(\frac{1}{1.8}\right)^2 + \left(\frac{1}{1.563}\right)^2}$$

$$\epsilon_r^* = 1.028 - .00025 j$$

$$\tan \delta = \frac{.00025}{1.028} \approx .00025$$

Trying Case c in Equation (VII-20)

$$\epsilon_r^* = \epsilon' - j\epsilon'' = \frac{\left(\frac{1}{1.8}\right)^2 - \frac{(.014 + 7.90 j)^2}{2(3.14)(1.163)}}{\left(\frac{1}{1.8}\right)^2 - \left(\frac{1}{1.563}\right)^2}$$

$$\epsilon_r^* = 2.04 - .0057 j$$

$$\tan \delta = \frac{.0057}{2.04} \approx .0028$$

This solution is not realistic since the material dielectric constant is known to be near unity, therefore, Case b is the desired solution.

5. REMARKS

The difficulty with standing wave experiments to measure dielectrics with the low constants that are characteristic of foamed plastics is achieving the accuracy in the inverse VSWR measurement. The dielectric losses in the dielectric are so low that wall losses, or shorting plate losses, etc., that is, things normally neglected in most experiments, are no longer insignificant. Consequently, the accuracy of measurement must be at least

good enough to eliminate these interferences. It is very likely in our experiment that the micrometer dial gage of the slotted line was not accurate enough for high precision measurements of the loss tangent. The loss tangent was proportional to the measured value of Δx , the separation between the half-minimum points on either side of a null but Δx could only be read to .001 in. accurately with our gage. The fourth place, i. e., 000x, was estimated, and hence was doubtful. The loss tangent for polystyrene was measured by the same technique but with a more accurate micrometer gage by the Melpar Corporation, and was indeed observed to be .00005. Their value was some five times smaller than the observed result of this study. The only difference, however, was the accuracy of the slotted line micrometer gages used in the experiments. Ultra accuracy is achieved by a resonant cavity technique where the loss is measured by the change in frequency bandwidth. This can be read as accurately as $1/10^6$.

Sources of error in this experiment to be noted are:

- a. Lack of frequency stability in the klystron tuning.
- b. Dial gage accuracy.
- c. Calibration accuracy of the -3 db point on the VSWR meter.
- d. Length measurements of the sample.
- e. Short circuit perturbations due to the shorting plate.

However, it is believed that (b) was the principal source of error in the experimental technique.

APPENDIX VII

BORESIGHT SHIFT ANALYSIS

1. ANALYSIS

The method of approximating the boresight shift, α , of a parabolic reflector antenna system due to a phase distorting medium, which causes a known phase front across the reflector aperture, is to compare to the known phase front a phase front of the same slope across the boresight axis. This phase variation has a functional relationship to the boresight shift.

A careful study of Figure VIII-1 immediately suggests that the inter-connecting link between the resultant phase front across the antenna aperture and the boresight shift angle, α , is the apparent feed displacement distance, δ . If, in Figure VIII-1, the reflecting surface BOB' were a flat plane with \overline{OP} normal to that surface, then, according to Snell's laws of reflection, the angle of reflection, α , is equal to the angle of incidence, θ . However, for paraboloidal surfaces, extensive measurements have revealed that for small incident angles (θ), ratio of the reflected to the incident angle, α/θ , is slightly less than unity and a function of the ratio, f/D , of the focal length, f , to the diameter, D , of the paraboloid (Ref. 37). This function is known as the beam factor (B.F.).

Using Snell's law and adding the beam factor, the boresight shift equation is given by:

$$\alpha = \text{B.F. } \theta$$

or, in terms of the feed displacement, δ ,

$$\alpha = \text{B.F. } \tan^{-1} \frac{\delta}{f} \quad (\text{VIII-1})$$

The phase front resulting from the feed displacement can be determined by considering the parabolic reflector as an array of isotropic point radiators whose phase relationship is dependent upon the phase of the incident energy. If the incident energy originates with a spherical wave-front from the focal point, then the resultant wave-front reradiated from

the parabolic surface is a plane normal to the axis of the parabola. Referring to Figure VIII-1, the distance from the focal point, P, to the parabolic surface is given by:

$$\rho = \sqrt{(y)^2 + (f - x)^2} \quad (\text{VIII-2})$$

A spherical wave-front originating at point P will produce a plane wave-front across the parabolic aperture normal to the parabola axis. If the spherical wave-front origin is displaced an arbitrary distance, δ , from the parabola focal point, P, to a point, P', such that P' remains the same distance, f, away from the parabola vertex, then the resultant wave-front reradiated from the parabola is determined by the path difference between ρ and ρ' (referenced to a plane normal to the parabola axis). This difference is given by:

$$\rho - \rho' = \sqrt{(y)^2 + \left(f - \frac{y^2}{4f}\right)^2} - \sqrt{(y - \delta)^2 + \left[f - \frac{(y - \delta)^2}{4f}\right]^2} \quad (\text{VIII-3})$$

where $\frac{y^2}{4f} = x$ is the equation of the parabola.

By selecting the proper value for δ and finding $\rho - \rho'$ from equation (VIII-3), the slope across the boresight axis of a known phase front may be duplicated. The value obtained for δ may then be used in equation (VIII-1) to solve for the boresight shift angle (α). This method of calculating the boresight shift angle does have some inherent error since the refraction due to the interface of the interferring medium is not considered and only the slope at the point where the phase front crosses the parabola axis is considered. In the case of the antenna study of this report, both of these errors are small due to the very small amount of refraction produced by the encapsulating foamed plastic and due to the near linear phase front in the vicinity of the parabola axis produced by the encapsulation material.

2. CALCULATIONS

From Figure 16 of Section 3.8.4, it is noted that the phase front slope at the parabolic axis due to the encapsulation is 192° across the antenna aperture. A value of δ must be selected such that for the parameters of the test configuration, equation (VIII-3) yields the same phase front slope. If a value of 0.4 inches is selected for δ and the other parameters of the

test configuration are $y = \pm 36$ inches, $f = 27.5$ inches, $\lambda_0 = 0.9833$ inches, the value of ρ (equation VIII-2) is:

$$\rho = \sqrt{(36)^2 + \left[27.5 - \frac{(36)^2}{4 \times 27.5}\right]^2} = 39.2818 \text{ inches}$$

The maximum phase lead across the reflector aperture occurs when y is positive. Solving for ρ' of equation (VIII-3),

$$\rho' = \sqrt{(35.6)^2 + \left[27.5 - \frac{(35.6)^2}{4 \times 27.5}\right]^2} = 39.0088 \text{ inches}$$

Therefore, equation VIII-3 becomes:

$$\rho - \rho' = 39.2818'' - 39.0088'' = 0.2730 \text{ inches}$$

In terms of wavelength,

$$\rho - \rho' = 0.2776 \lambda_0$$

and in terms of degrees phase lead,

$$\rho - \rho' = 99.9^\circ$$

The maximum phase lag across the reflector aperture occurs when y is negative. Solving for ρ' of equation (VIII-3),

$$\rho' = \sqrt{(36.4)^2 + \left[27.5 - \frac{(36.4)^2}{4 \times 27.5}\right]^2} = 39.5451 \text{ inches}$$

Equation (VIII-3) becomes,

$$\rho - \rho' = -0.2633 \text{ inches}$$

or, in terms of degrees,

$$\rho - \rho' = -96.4^\circ$$

The total phase front slope across the antenna aperture due to a fixed displacement of $\delta = 0.4$ inches is the sum of the phase lead and the phase lag, or 196.3° . This phase front slope very closely approximates the calculated phase front slope produced by the foamed plastic encapsulation of 192° .

Substituting $\delta = 0.4$ inches, B.F. = 0.85 (obtained from reference 37 for a focal length to diameter ratio (f/D) of 0.382) and $f = 27.5$ inches (focal length of parabola) into equation (VIII-1), and solving for the bore-sight shift angle (α),

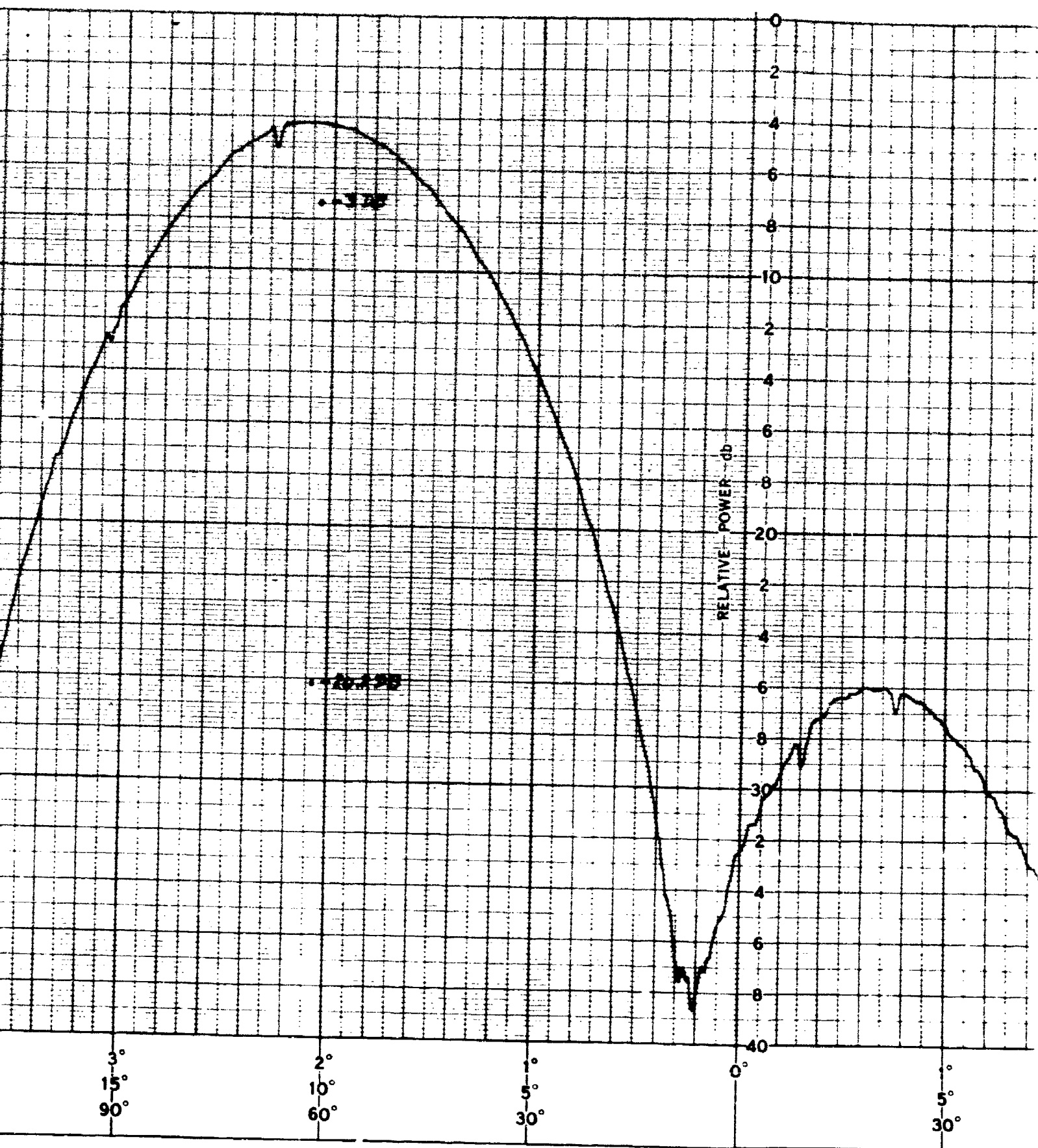
$$\alpha = .85 \tan^{-1} \frac{.4}{27.5} = .707^\circ$$

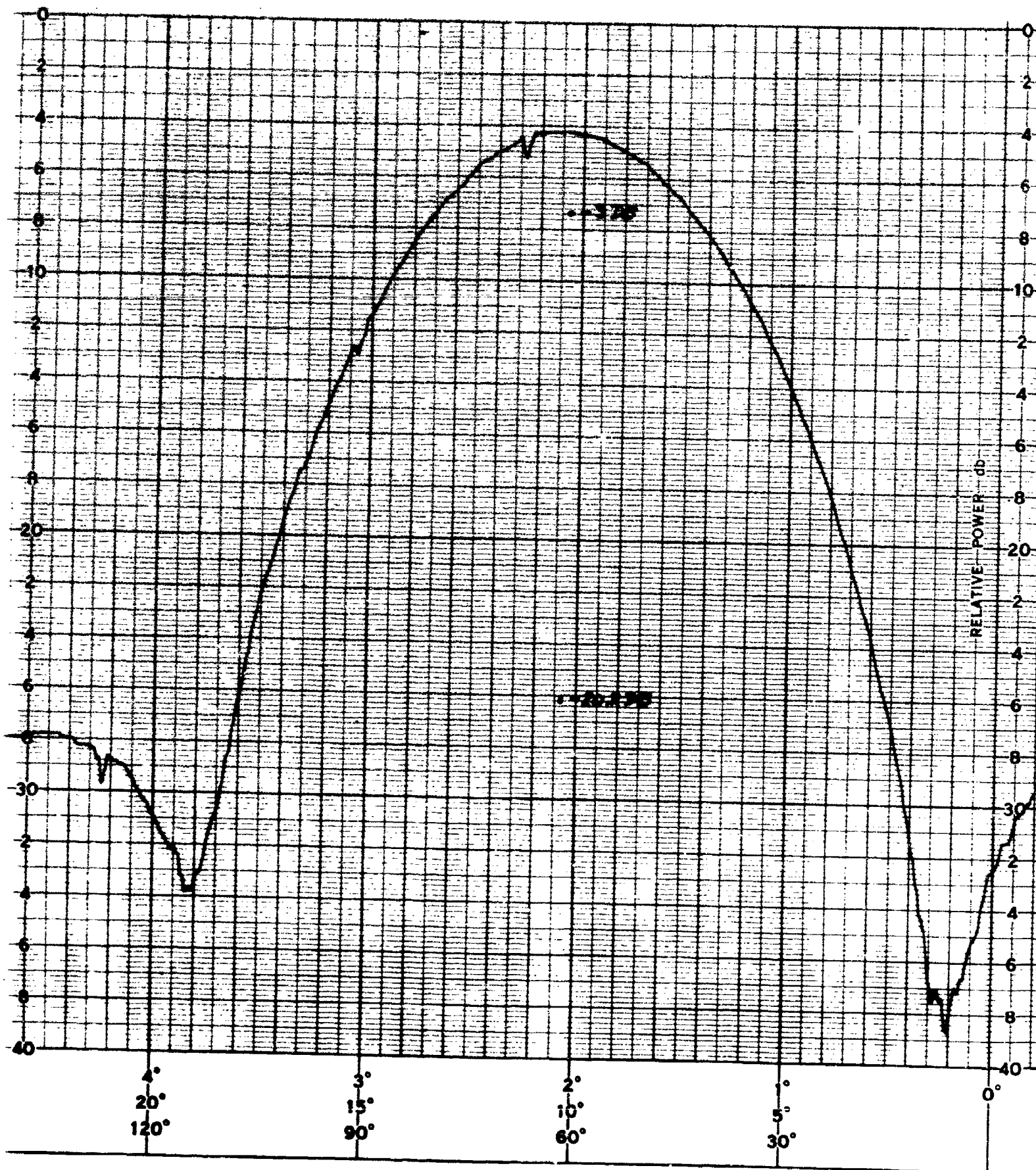
APPENDIX IX

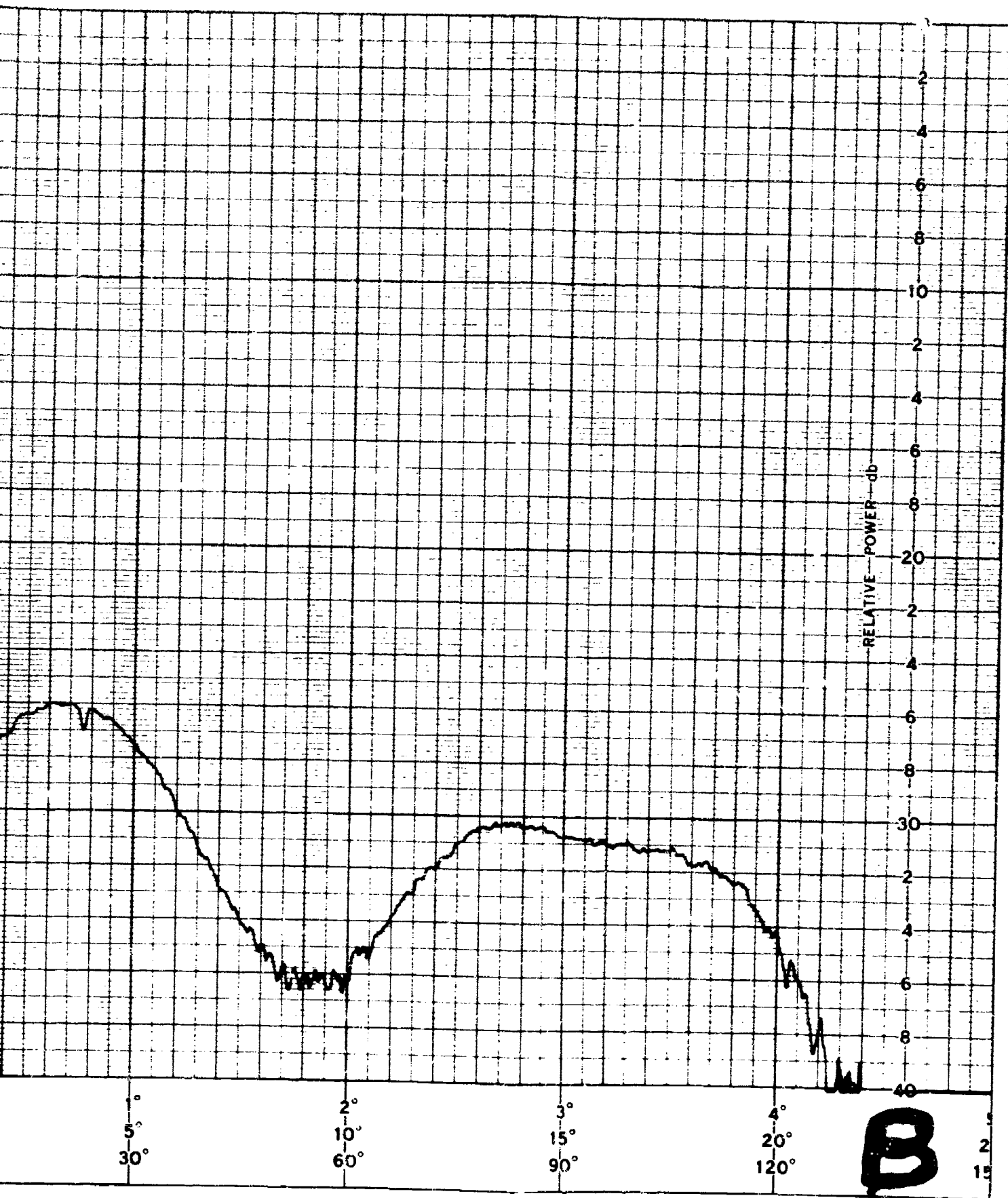
ENCAPSULATED ANTENNA PATTERN DATA

This appendix contains the raw data or patterns of the power distribution characteristics of the scale model antenna measured with and without encapsulating foam. The purpose of these tests was to demonstrate the effects of a low density encapsulating foam plastic on the electrical efficiency of a scale model antenna. The results tabulated in Section 3.8.7.3 of this report were reduced from these patterns. Patterns 5.3.1 through 5.3.5 represent the power distribution without encapsulating foam and patterns 5.4.1 through 5.4.5 the power distribution with encapsulating foam. Pattern 5.5 shows the measured boresight shift due to the presence of encapsulating foam. The details of the measurement procedure and philosophy have been described in Section 3.8.7. The legend of the pattern plots indicates the condition of the test.

FIGURE IX-1







PATTERN NO. 5.3.2 DATE 5/64

PROJECT

ENGINEER

REMARKS

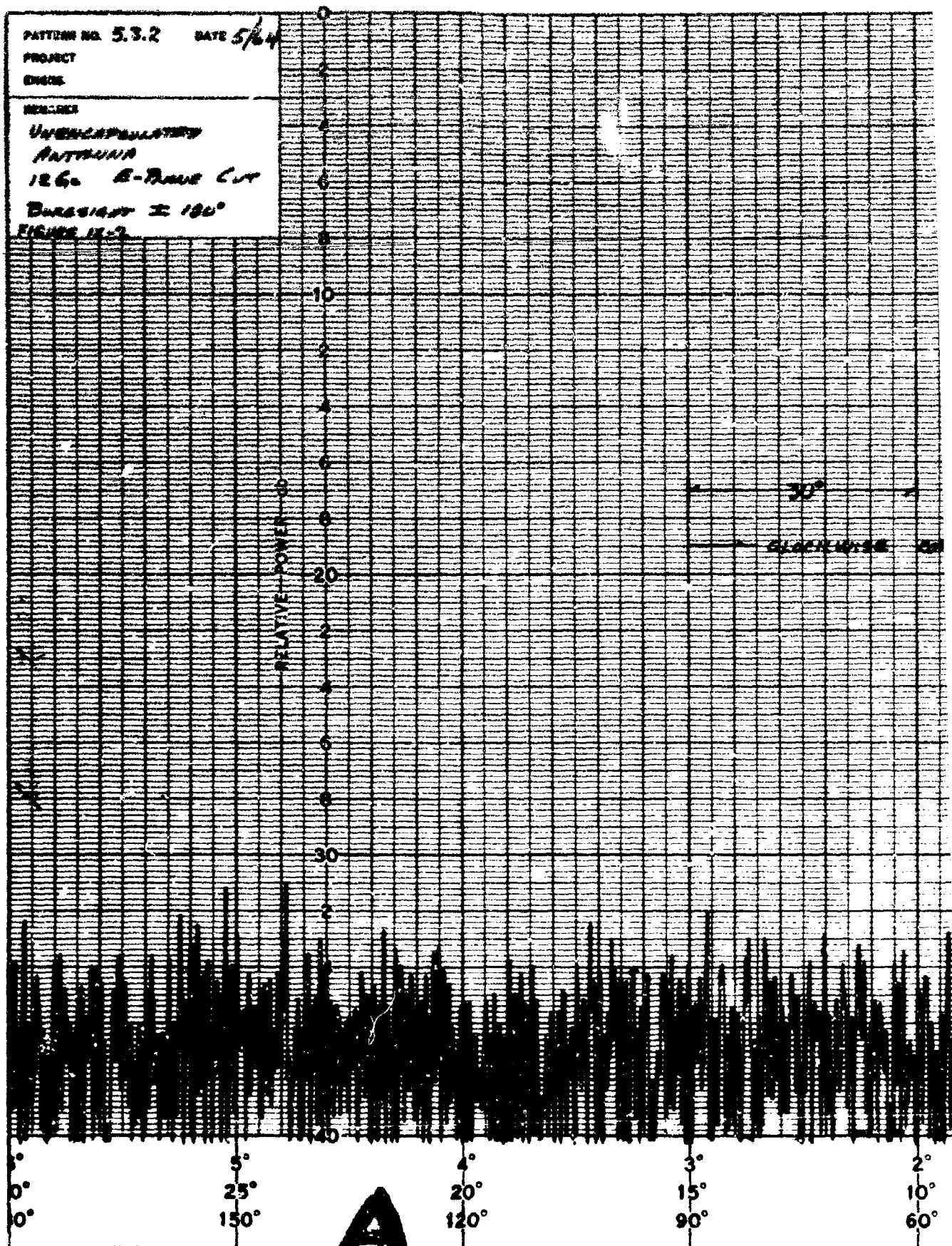
UNENCAPULATED

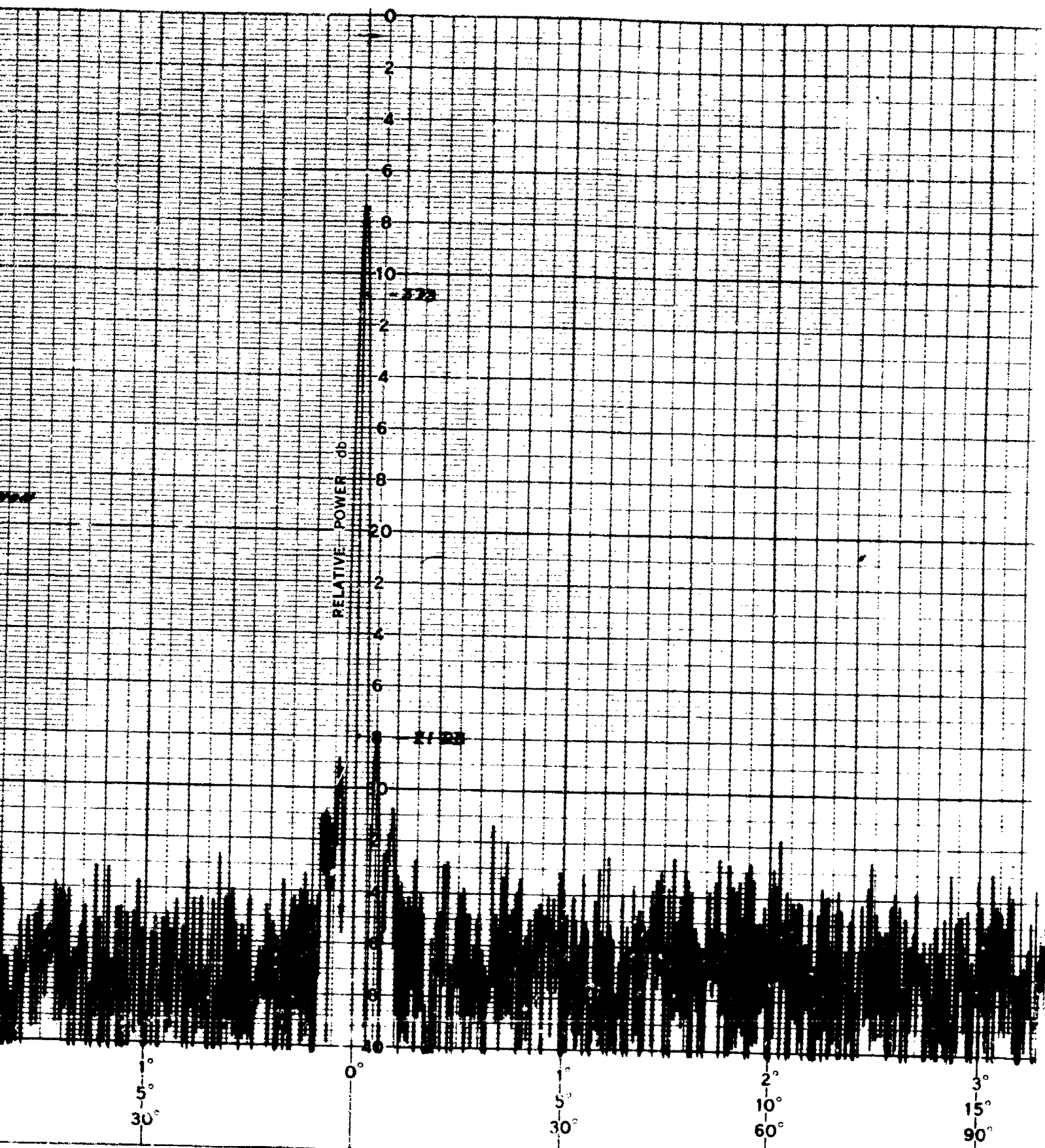
ANTENNA

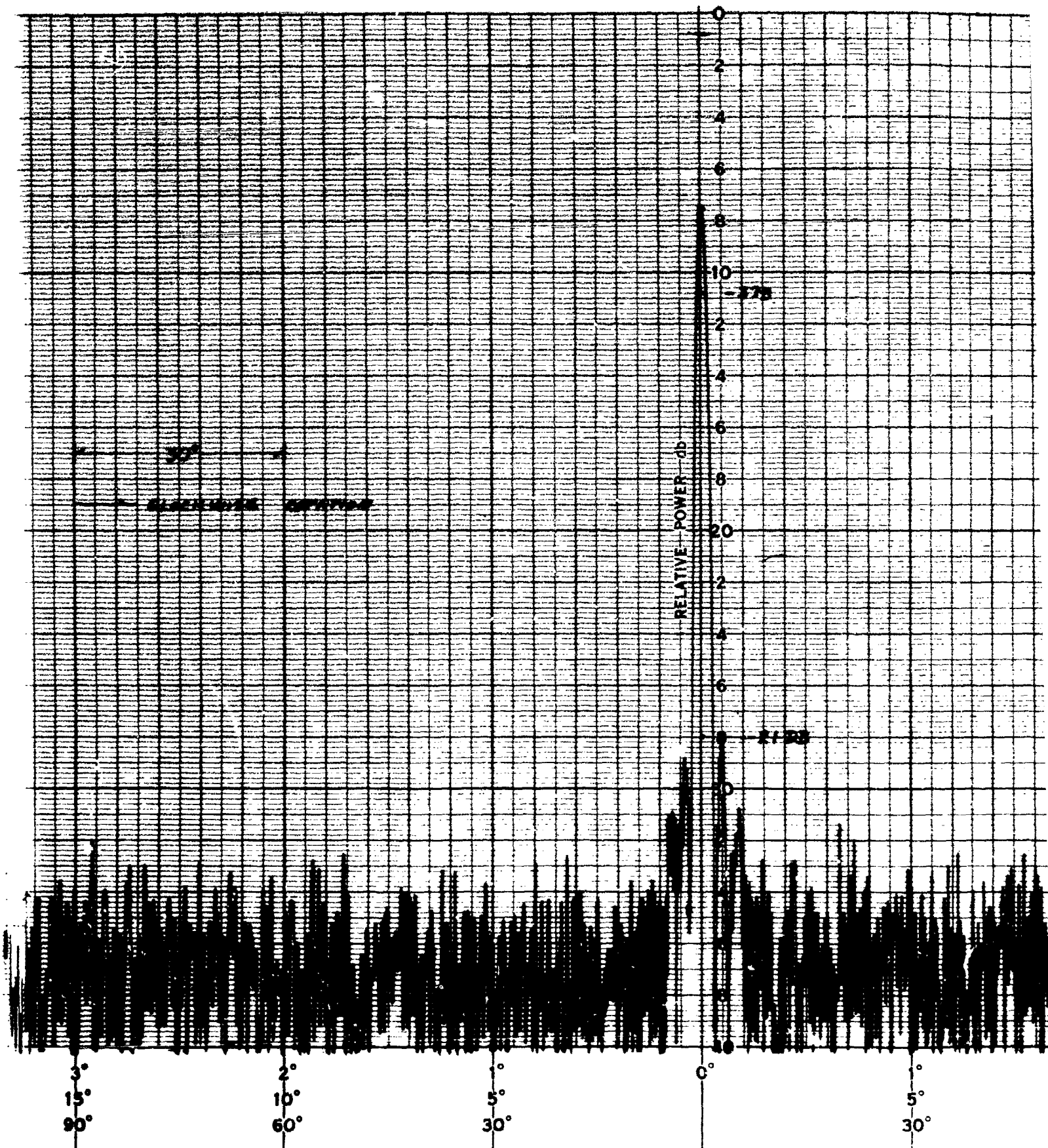
1260 B-BAND CUT

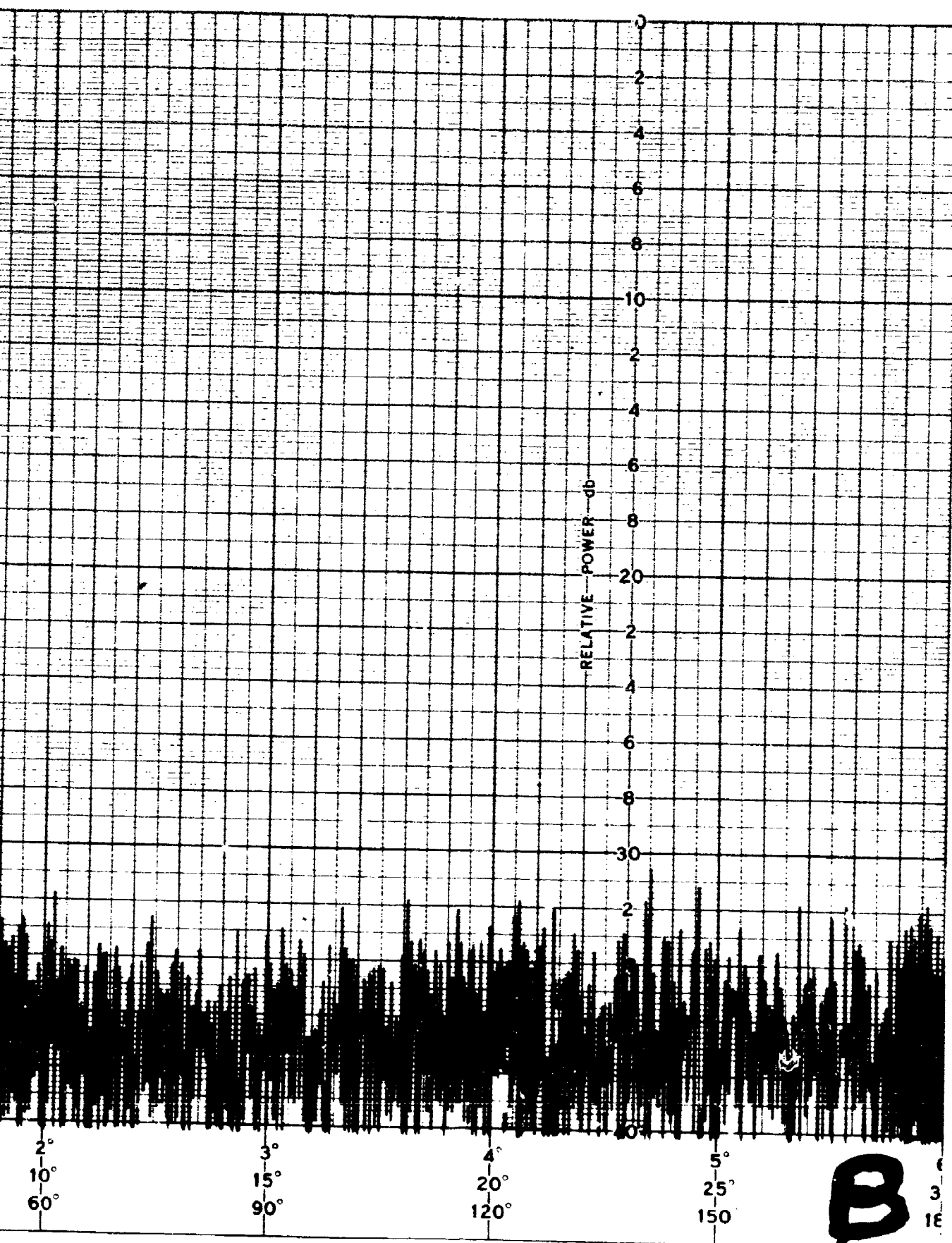
BURSTING $\pm 180^\circ$

FIGURE 12-2





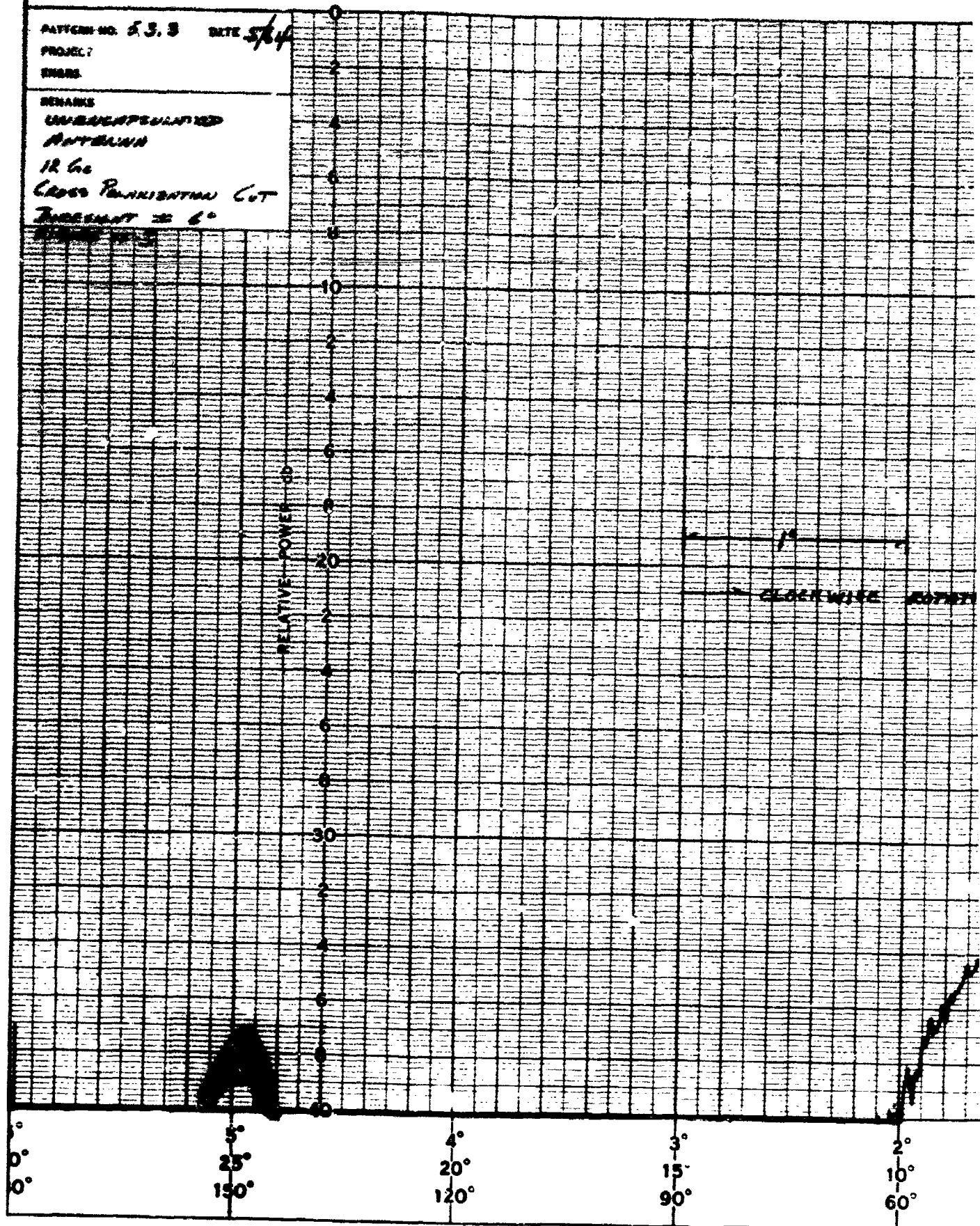


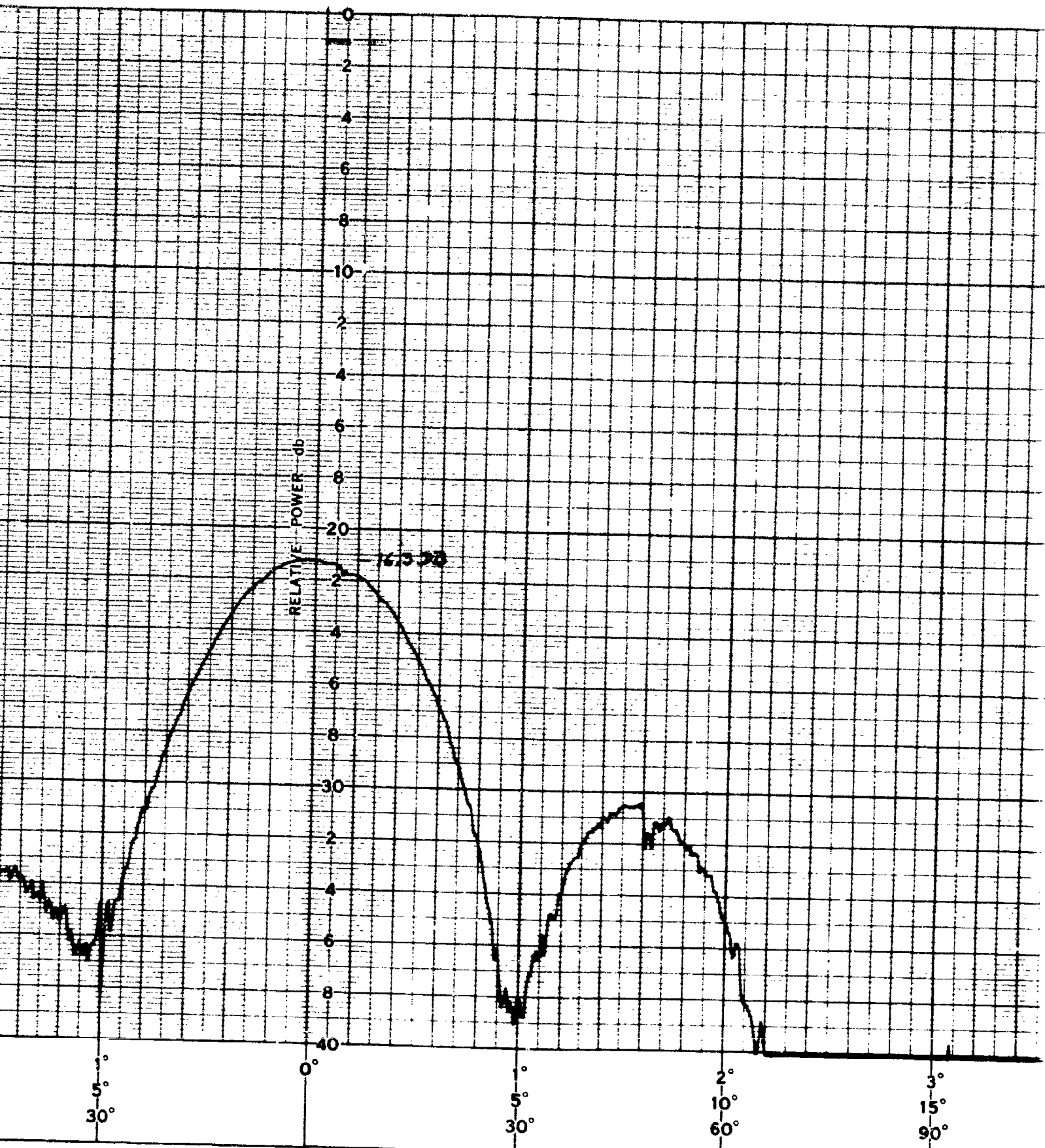


PATTERN NO. 53.3 DATE 5/4

PROJECT
ENGINEER

REMARKS
UNREPRESENTED
ANTENNA
12 G6
CROSS POLARIZATION CUT
TOLERANCE $\pm 6^\circ$





CLOCKWISE ROTATION

RELATIVE POWER db

16.538

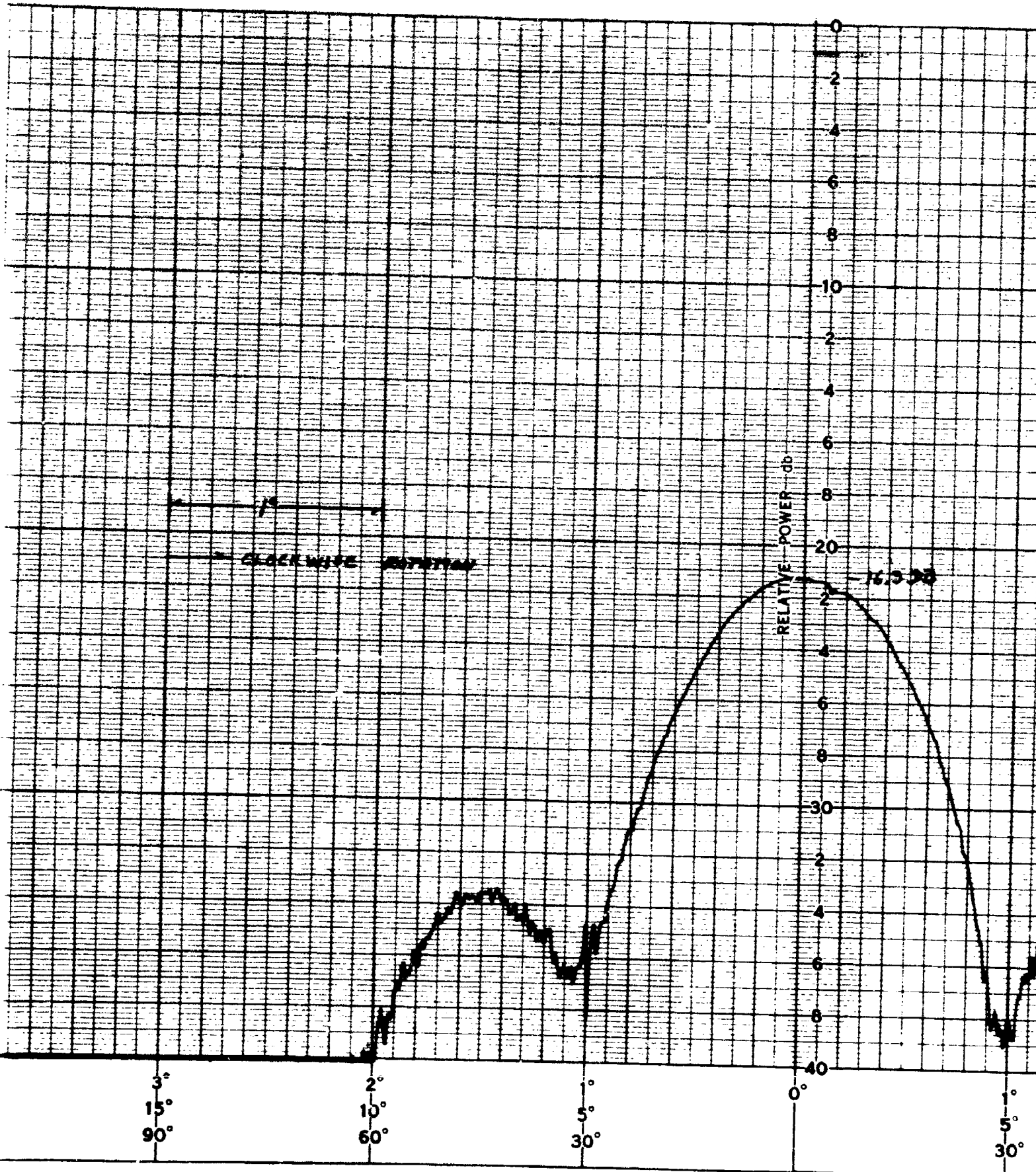
3°
15°
90°

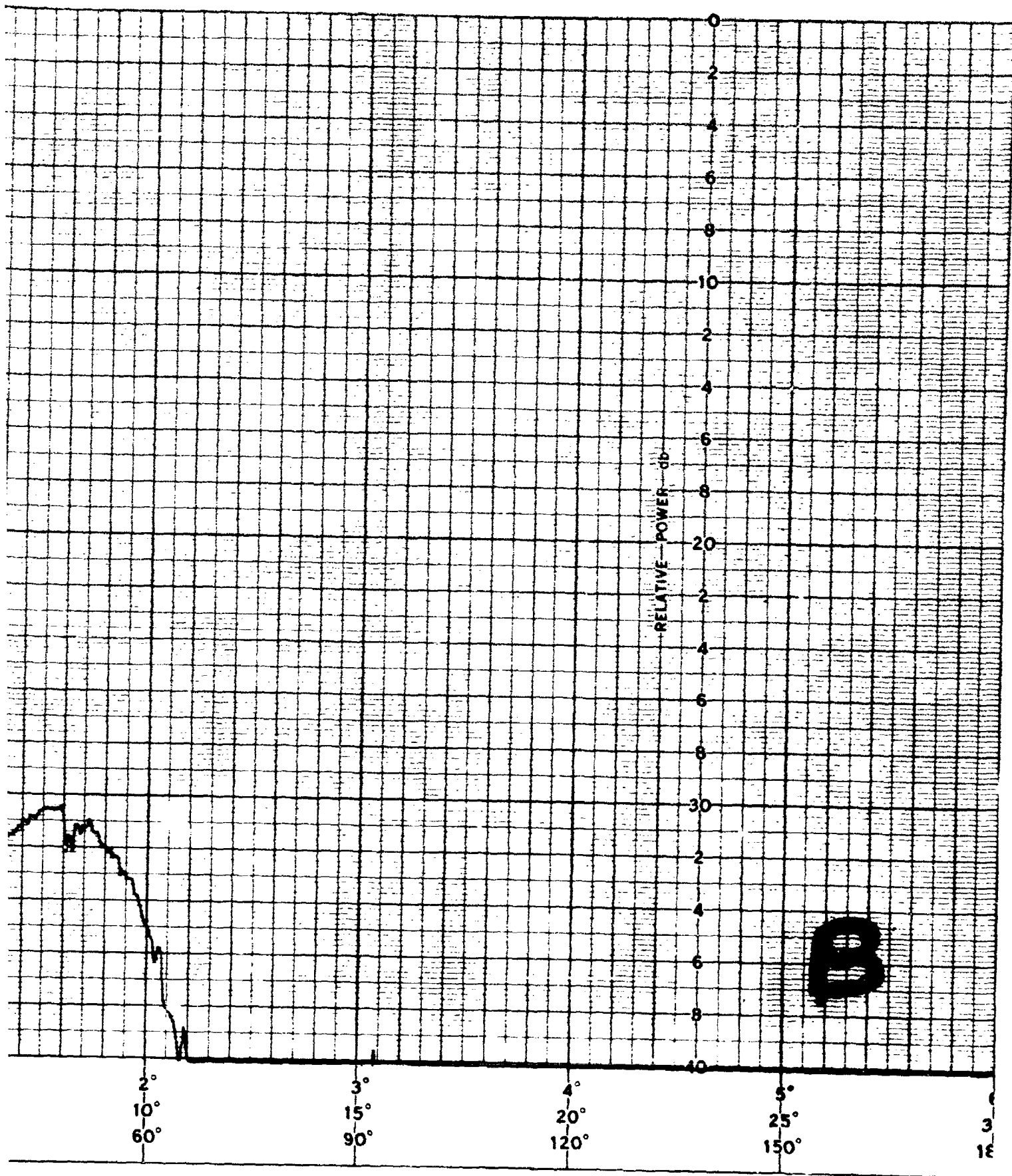
2°
10°
60°

1°
5°
30°

0°

1°
5°
30°

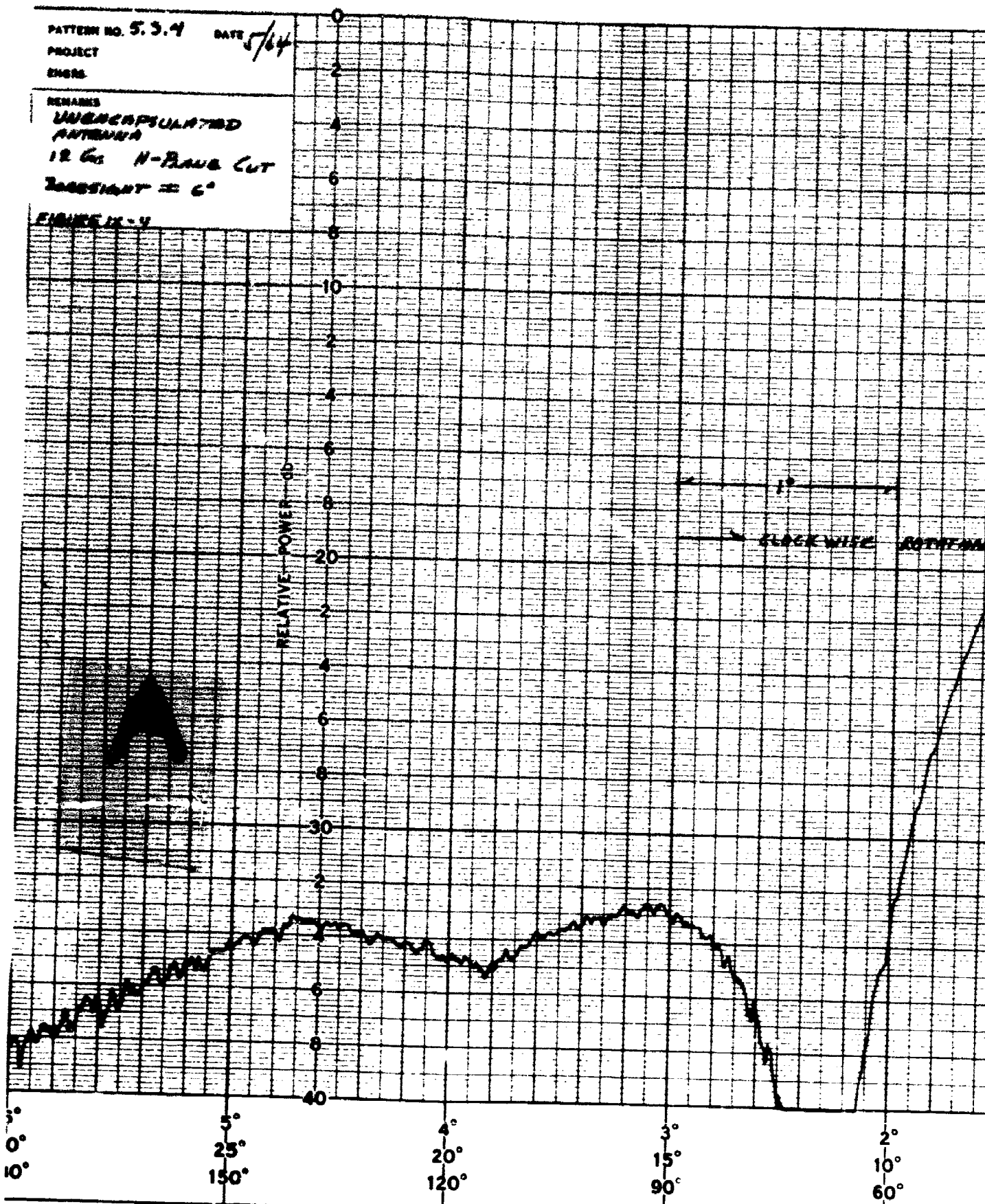


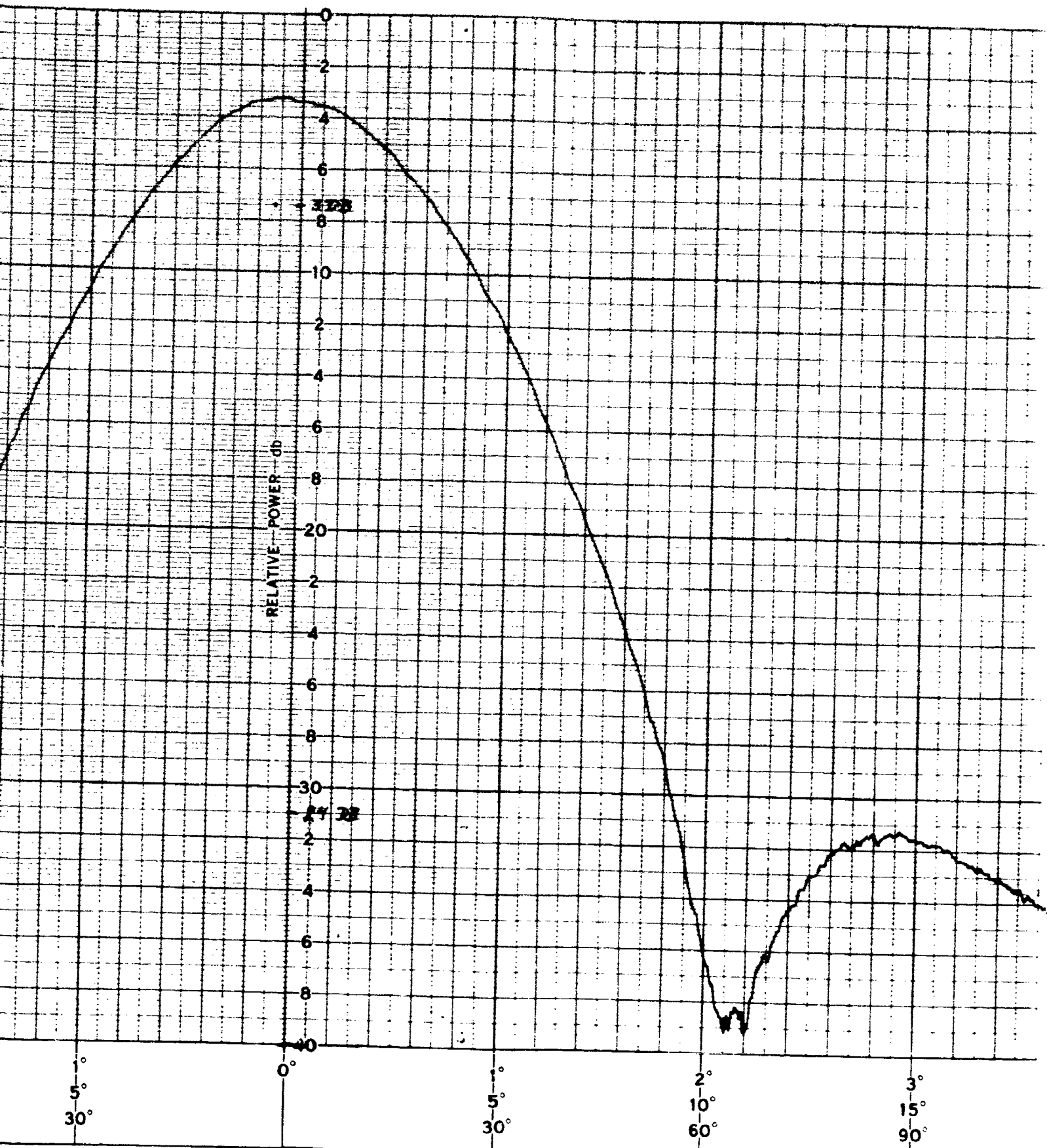


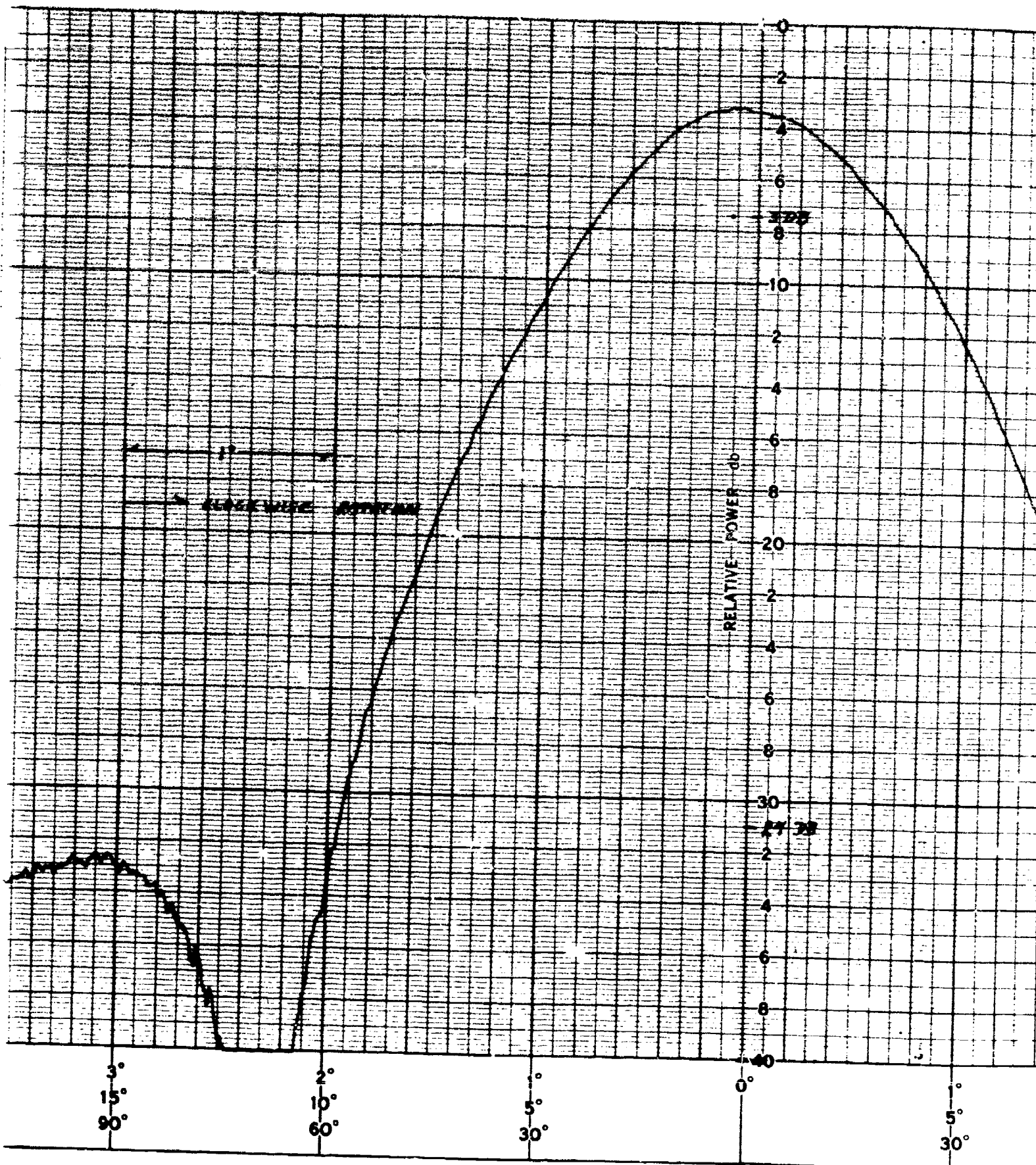
PATTERN NO. 5.3.4 DATE 5/64
PROJECT
ENGINEER

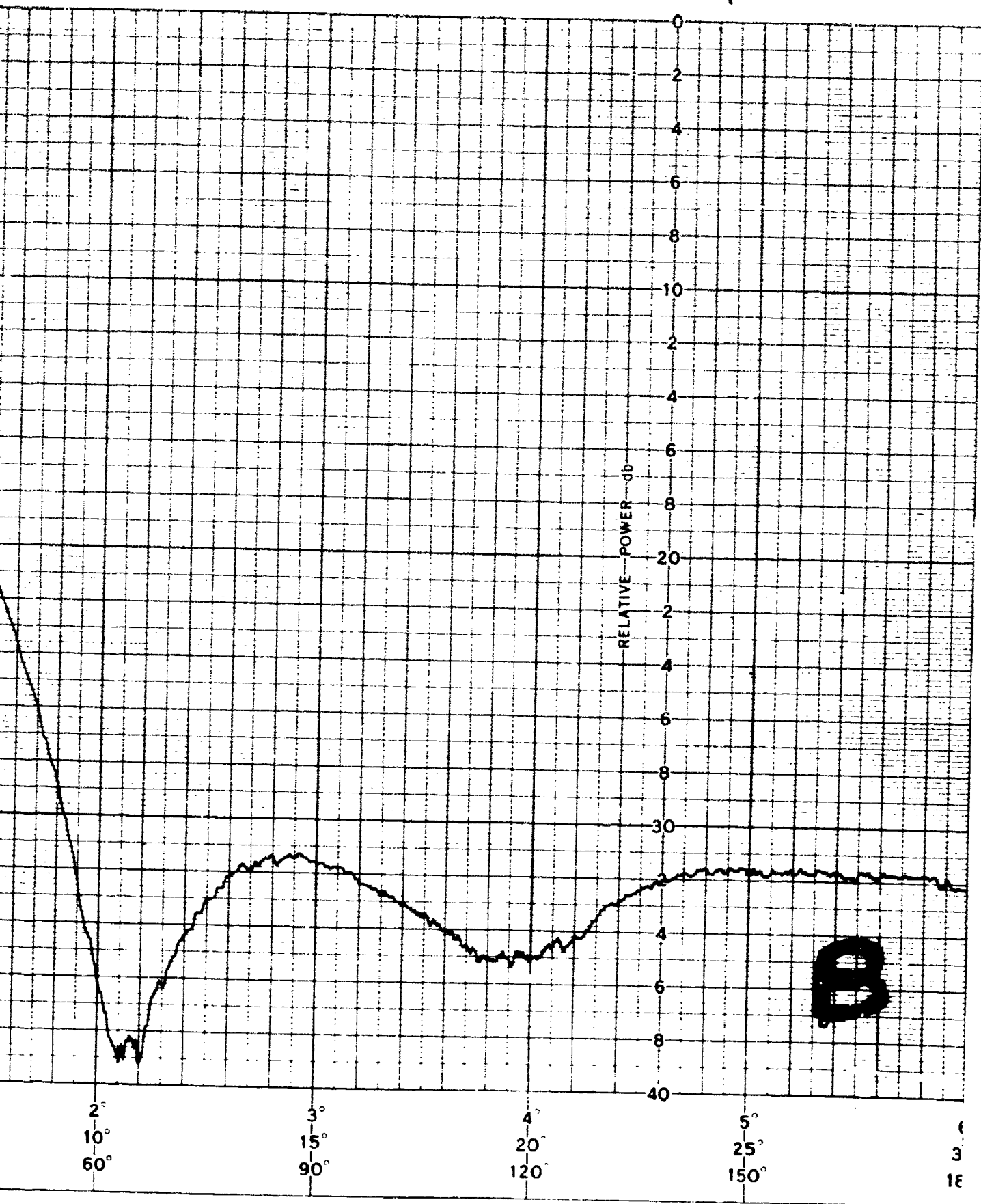
REMARKS
UNENCAPSULATED
ANTENNA
12 GS H-BAND CUT
ELEVATION = 6°

FIGURE 12-4









PATTERN NO. 5.3.5 DATE 5/64

PROJECT

ENGNS

REMARKS

UNENCAP SQUARED

ANTENNA

12.6C H-PARA CUT

BORISANT I 180°

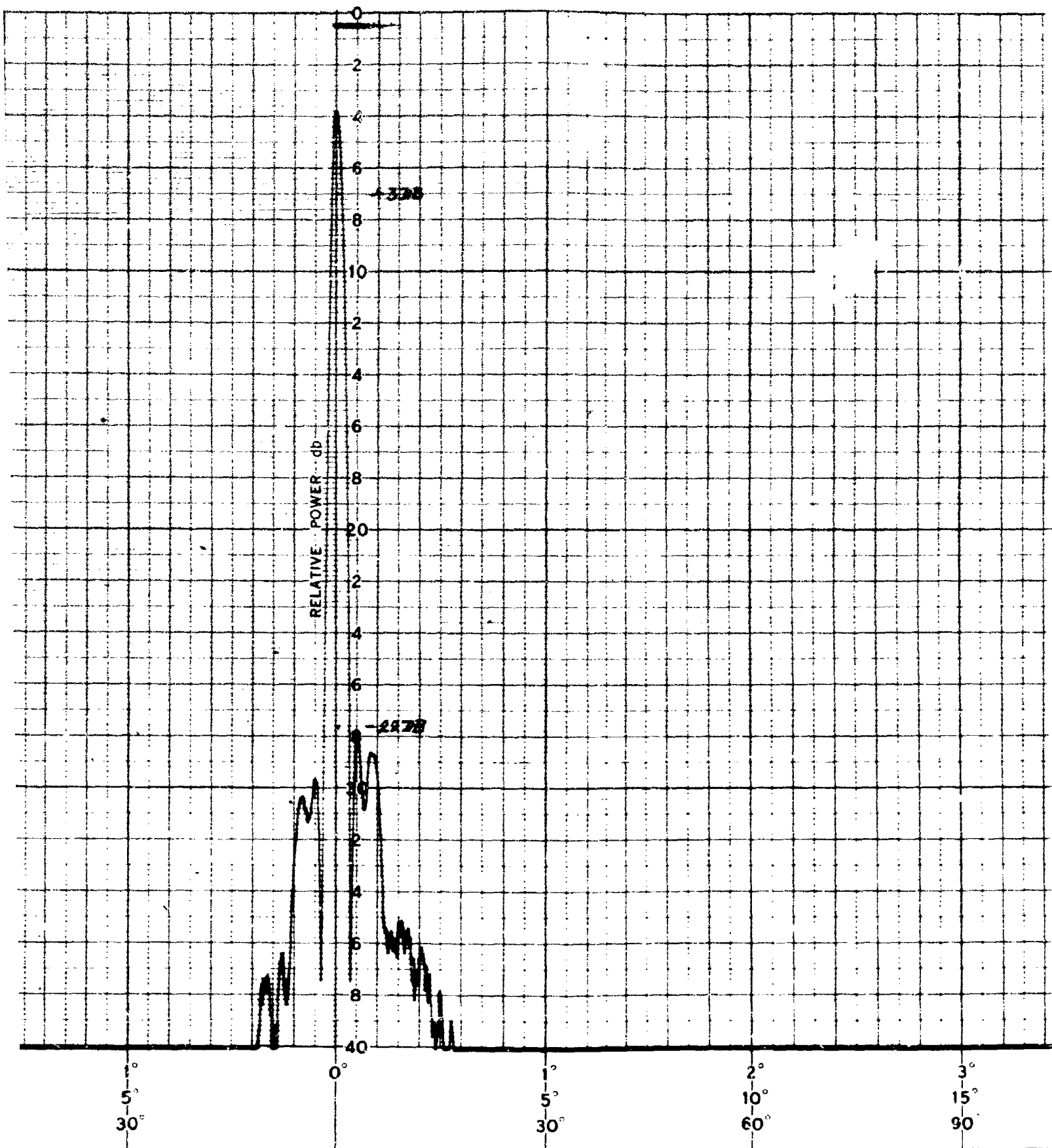
FIGURE 12-5

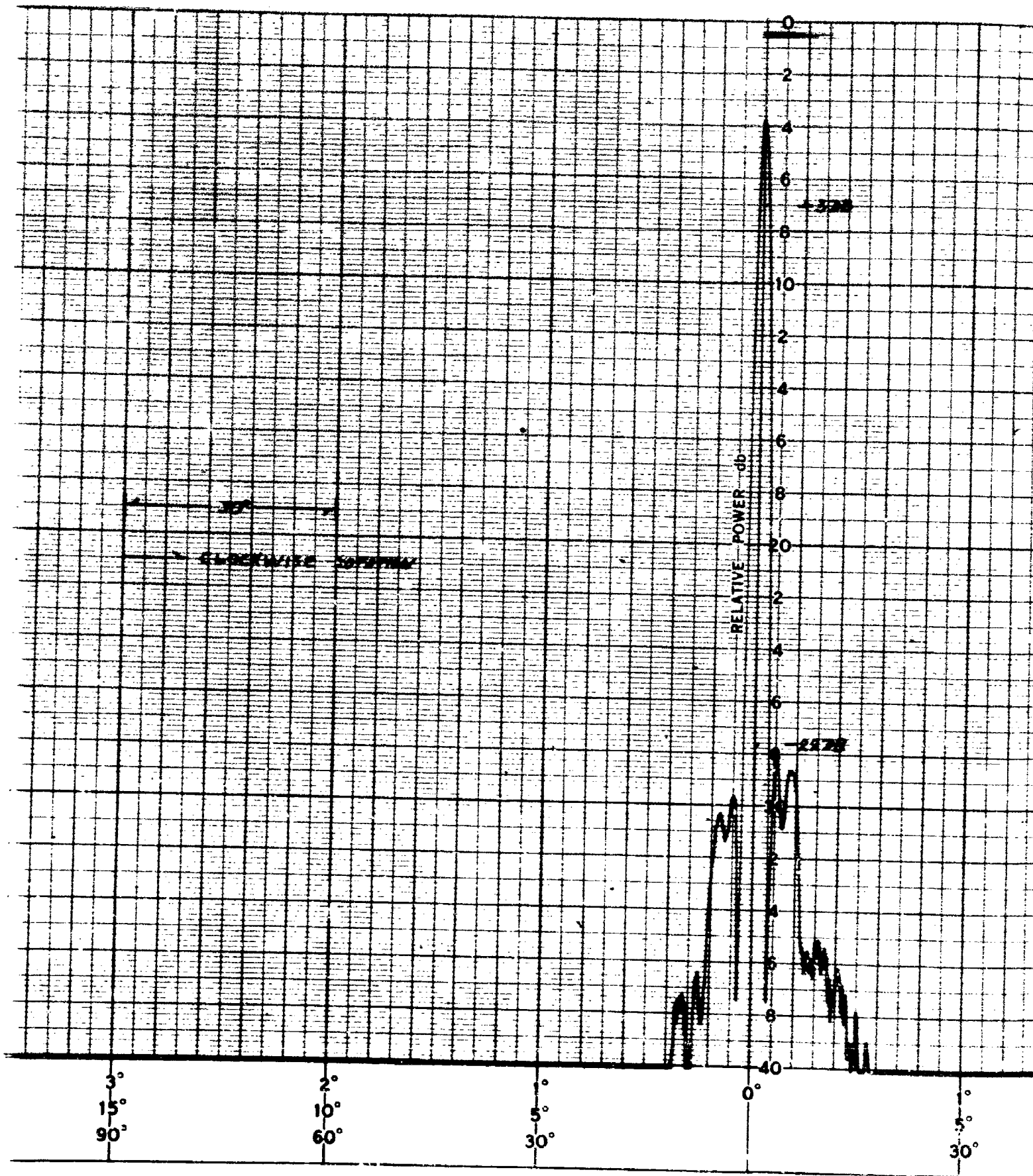
RELATIVE POWER (dB)

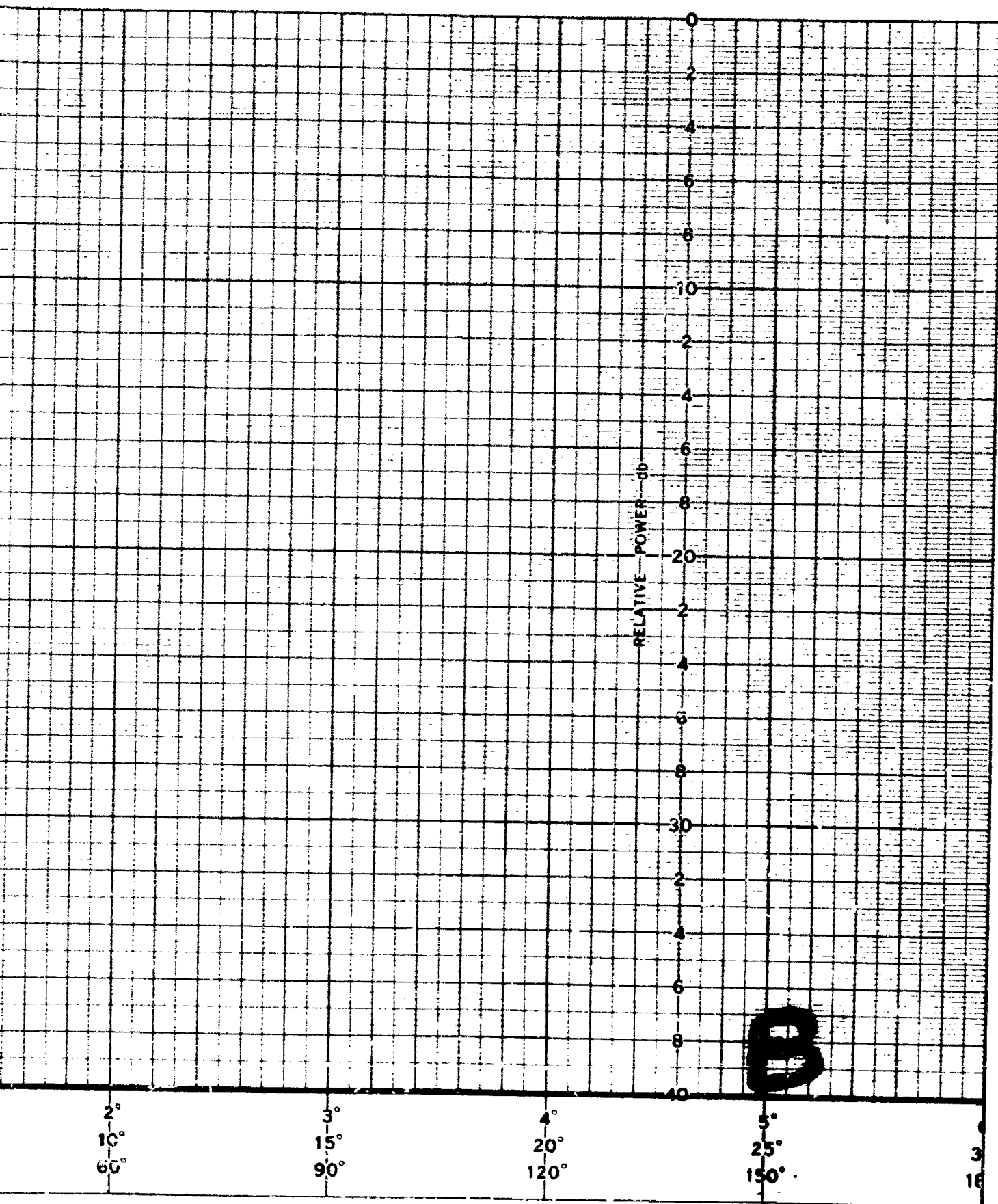
30°

CLOCKWISE ROTATION

5° 25° 150° 4° 20° 120° 3° 15° 90° 2° 10° 60°







PATTERN NO. 5.4.1 DATE 5/64

PROJECT

ENGINEER

REMARKS

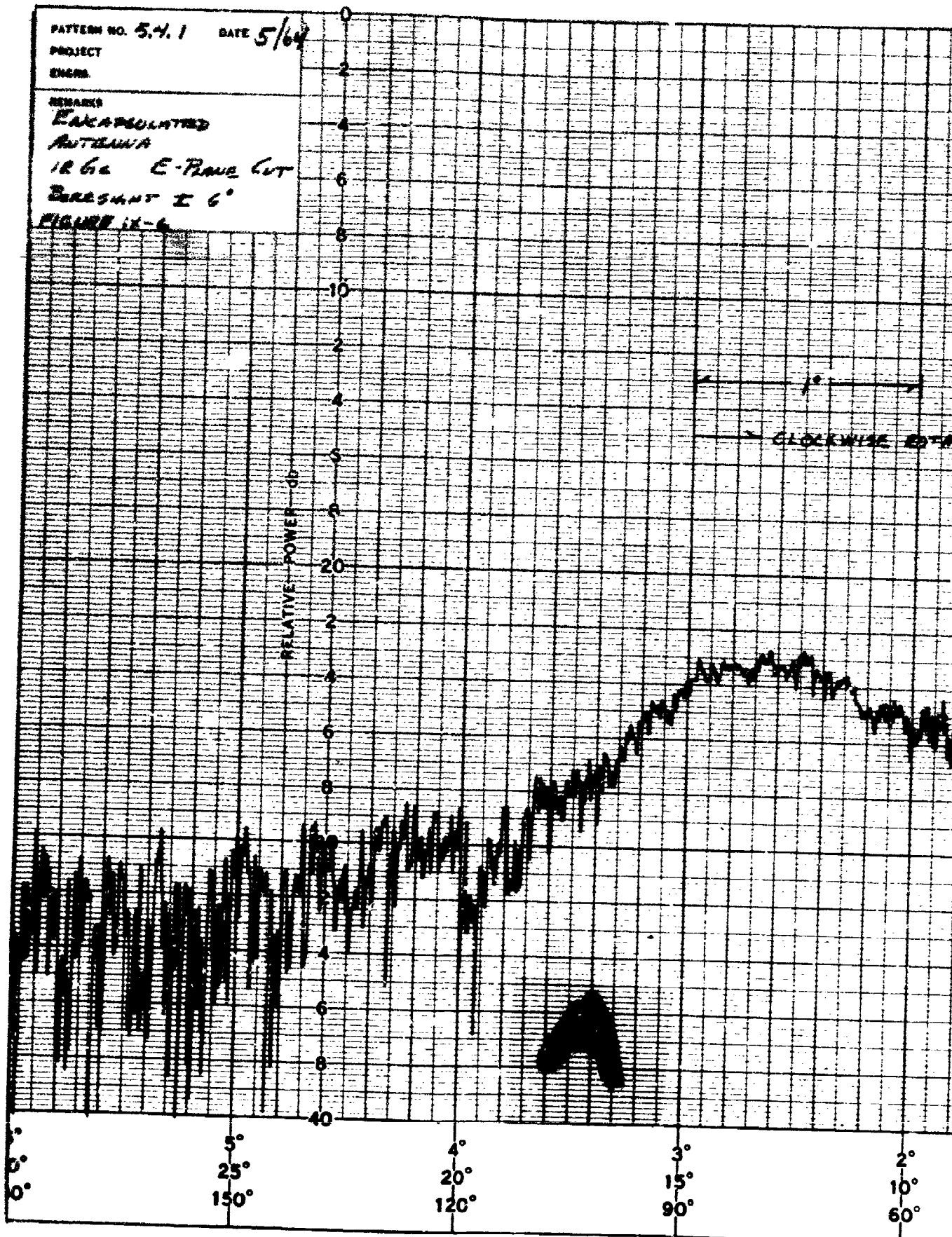
EXCERPTED

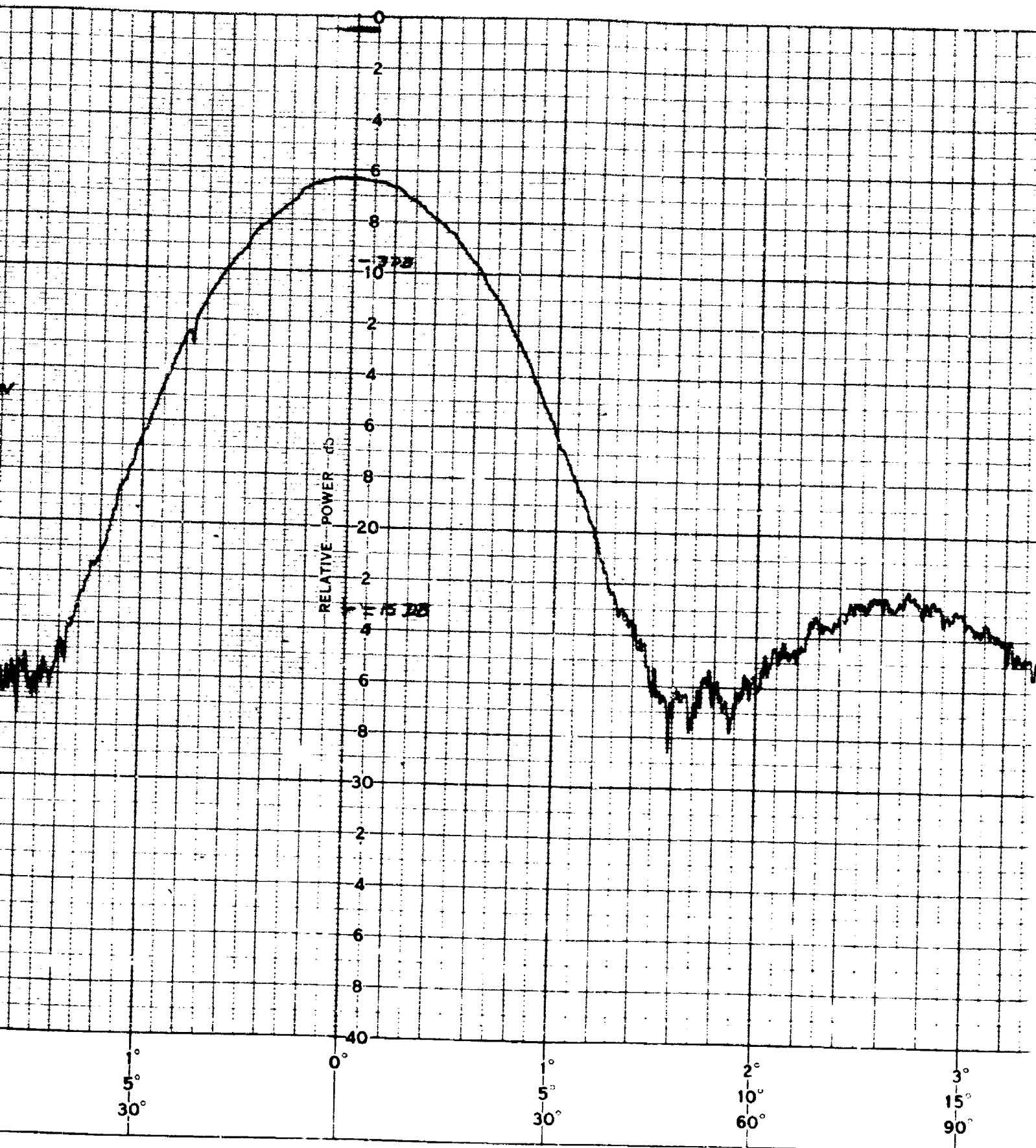
ANTENNA

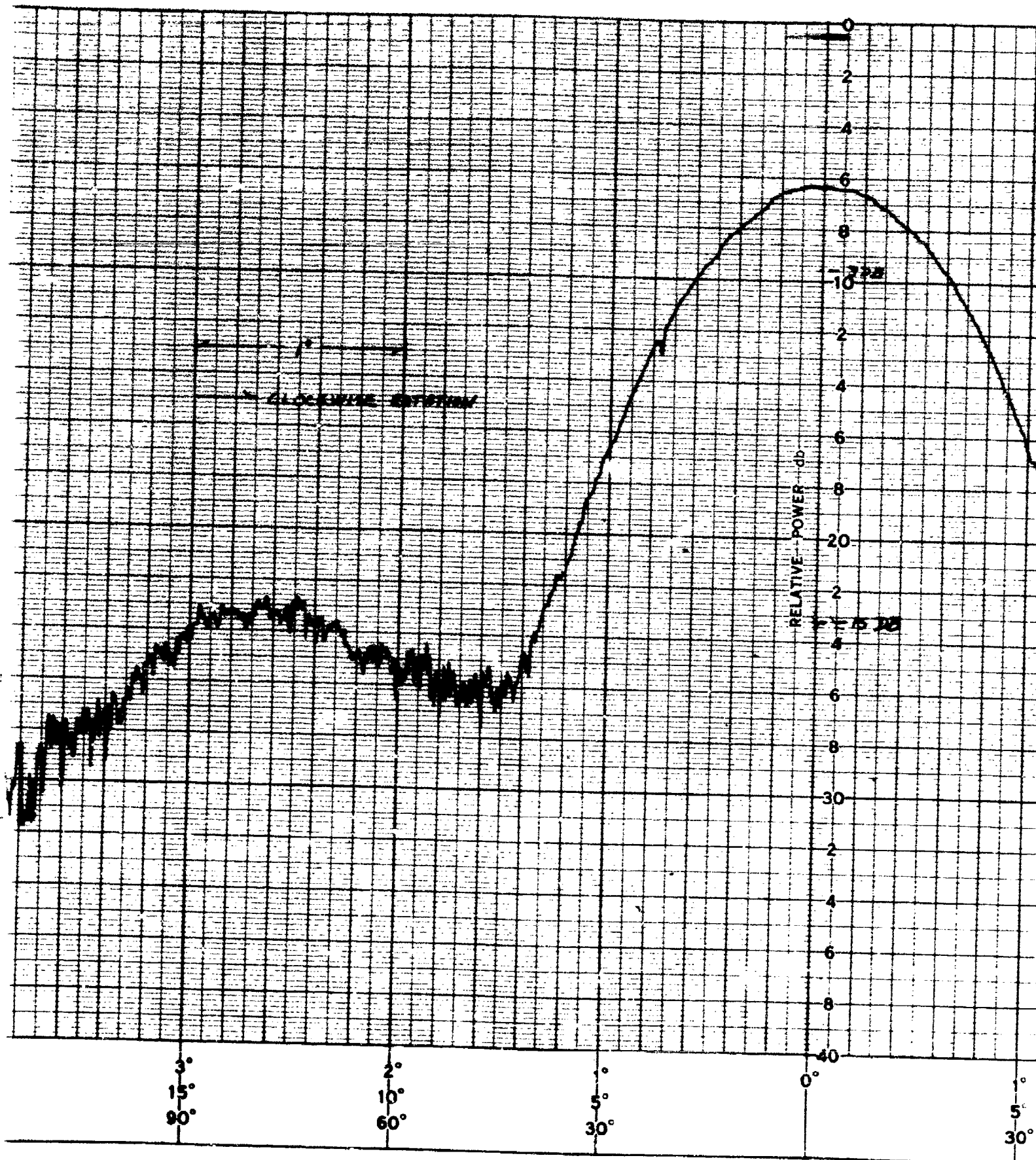
1862 E-PLANE CUT

REMARKS I 6'

FIGURE IX-6







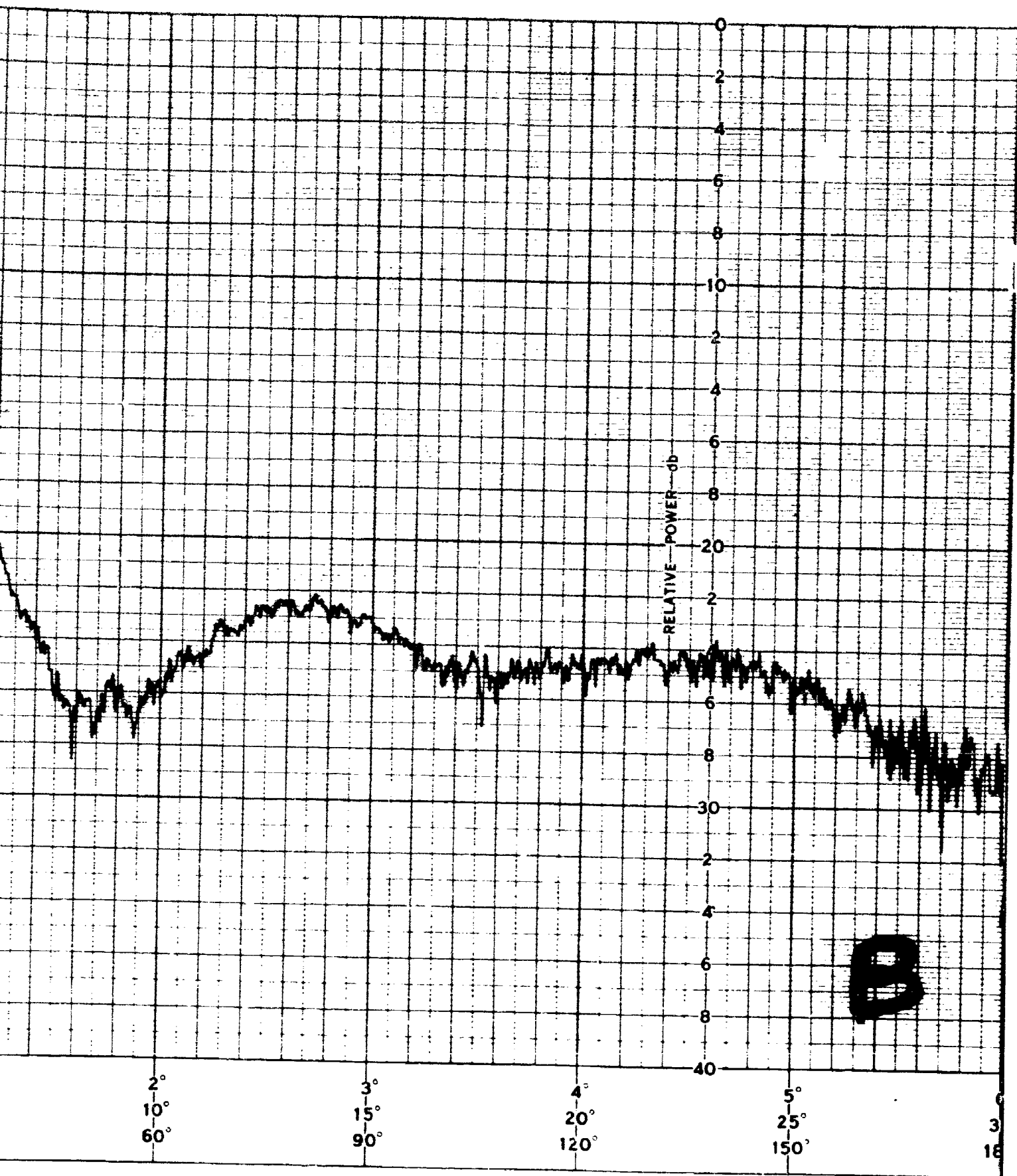
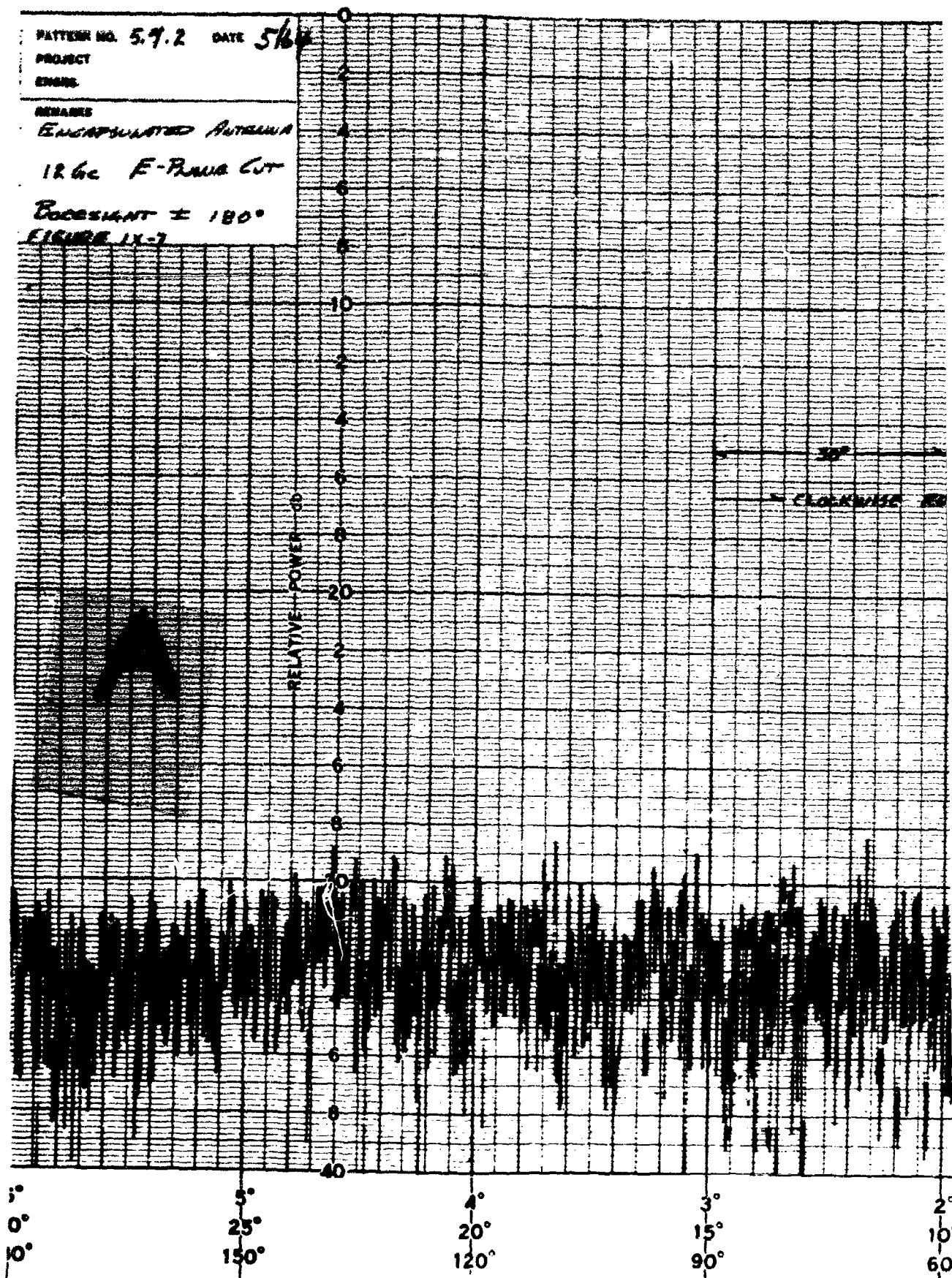
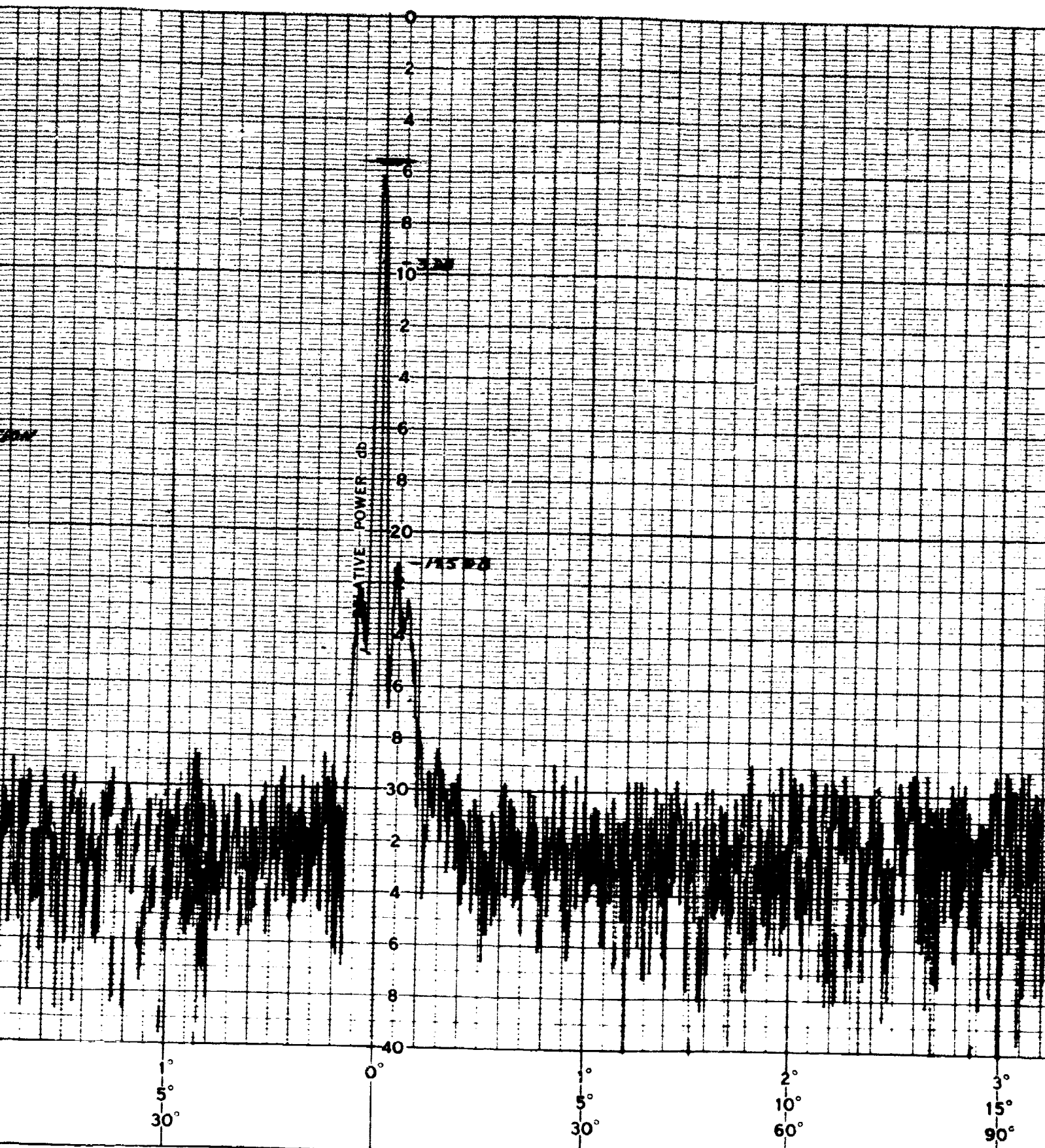
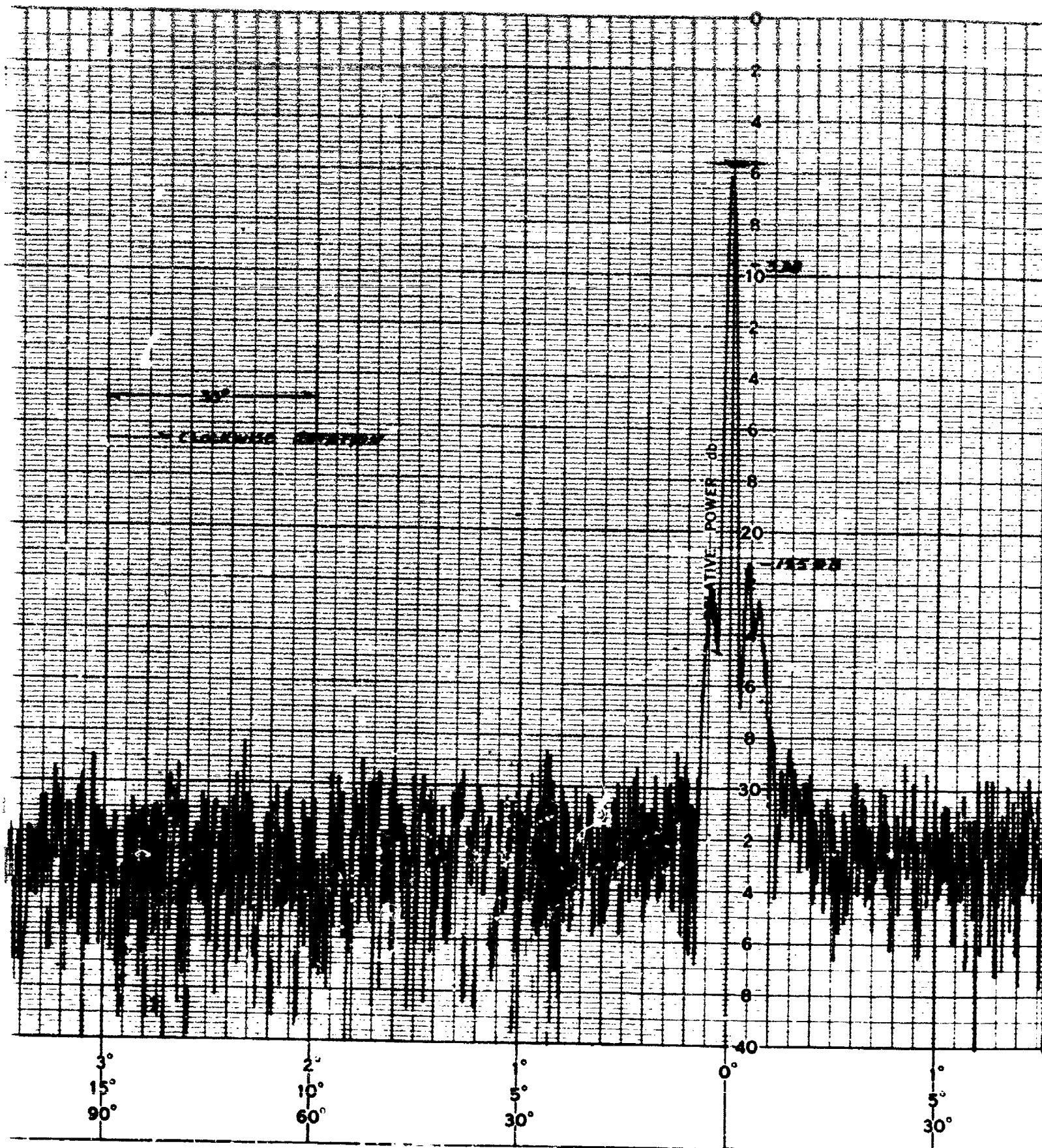
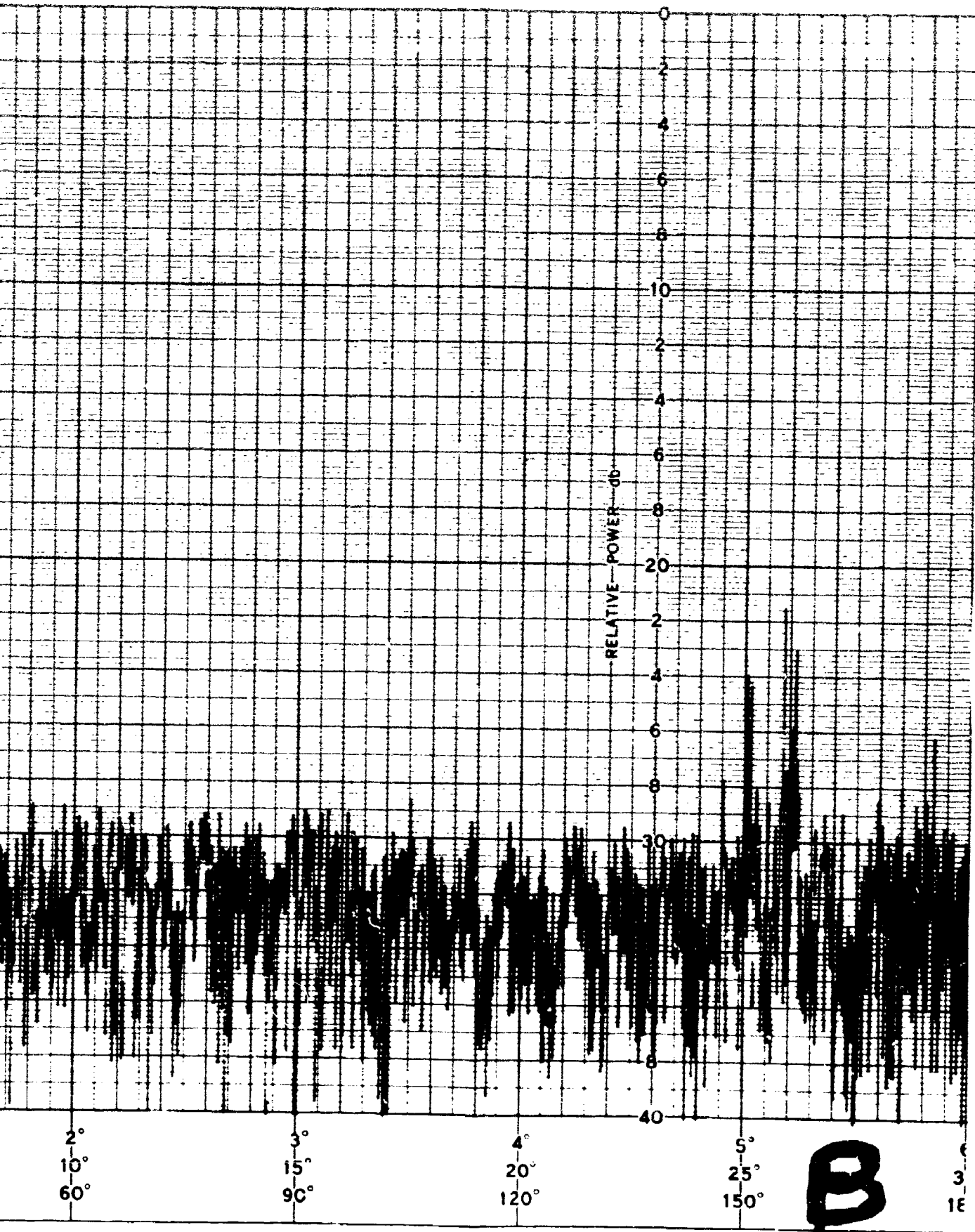


FIGURE IX-7









PATTERN NO 54.3 DATE 5/64

PROJECT

ENGR

REMARKS

ENCAPSULATED ANTENNA

18 66

CROSS POLARIZATION CUT

BORESIGHT $\pm 6^\circ$

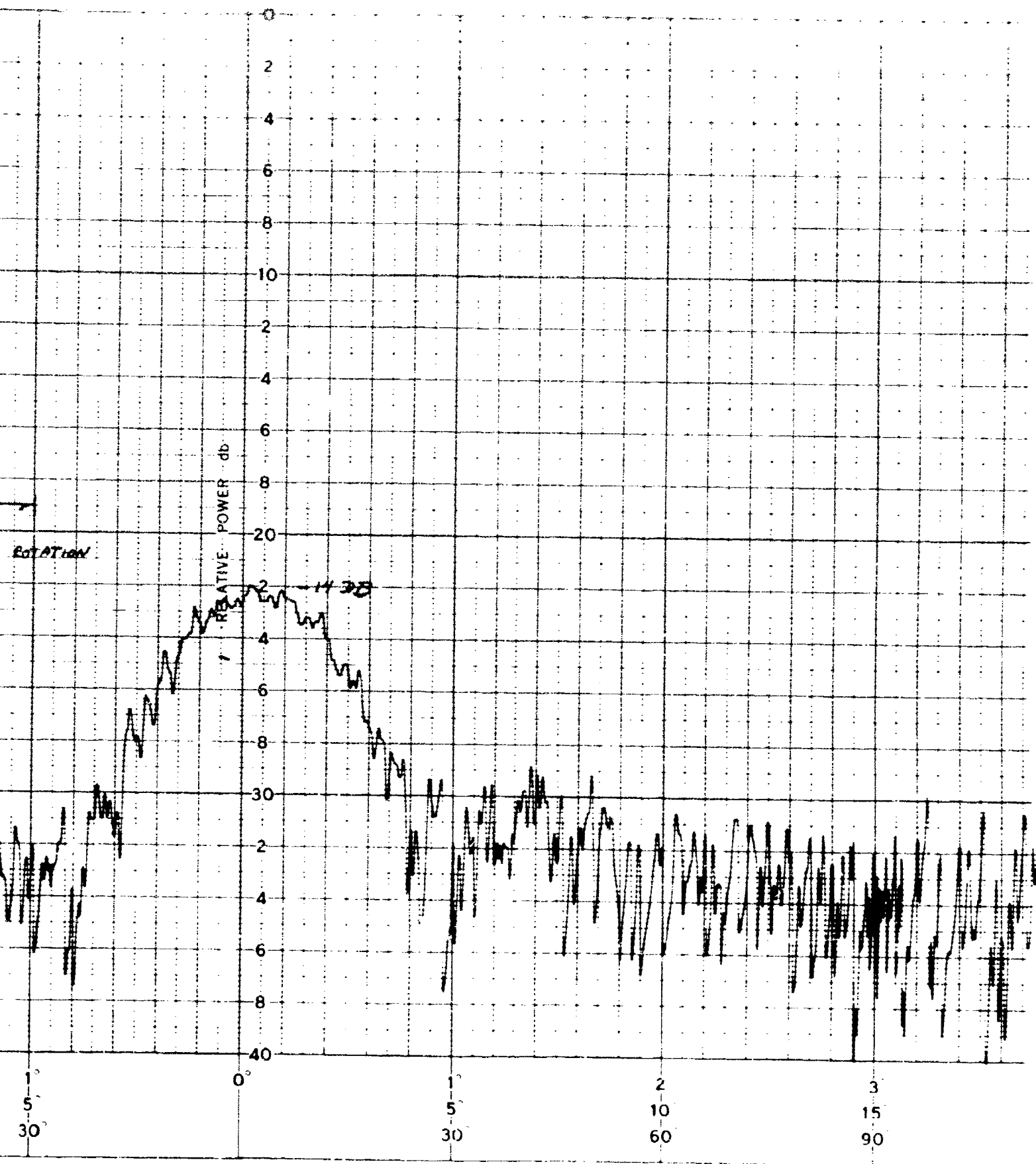
FIGURE 14-9

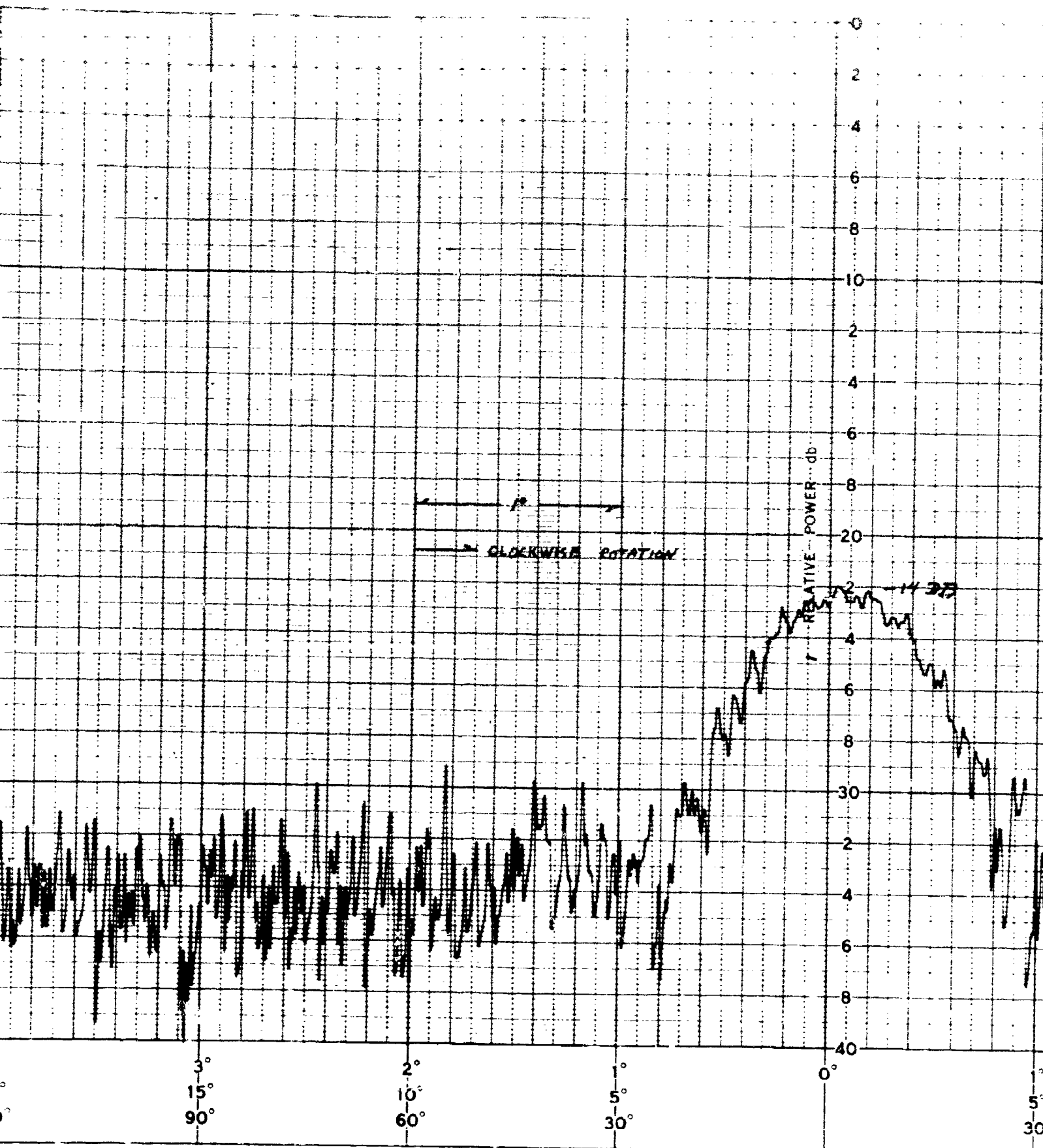
RELATIVE POWER - db

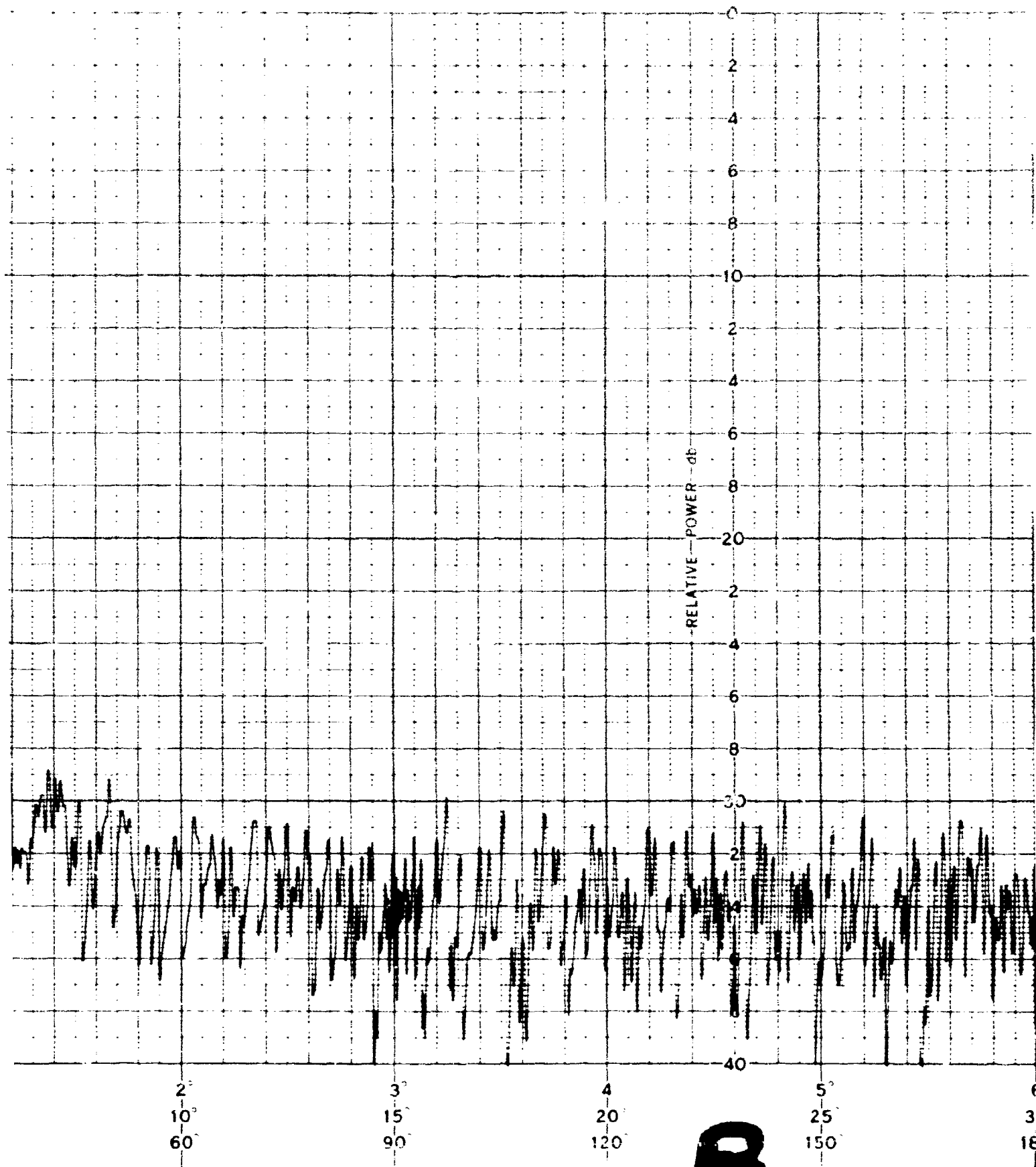
CLOCKWISE

5° 0° 10° 15° 20° 25° 30° 35° 40° 45° 50° 55° 60° 65° 70° 75° 80° 85° 90° 95° 100° 105° 110° 115° 120° 125° 130° 135° 140° 145° 150°

A







DATE: 5-9-64

PROJECT:

ENCLOSURE

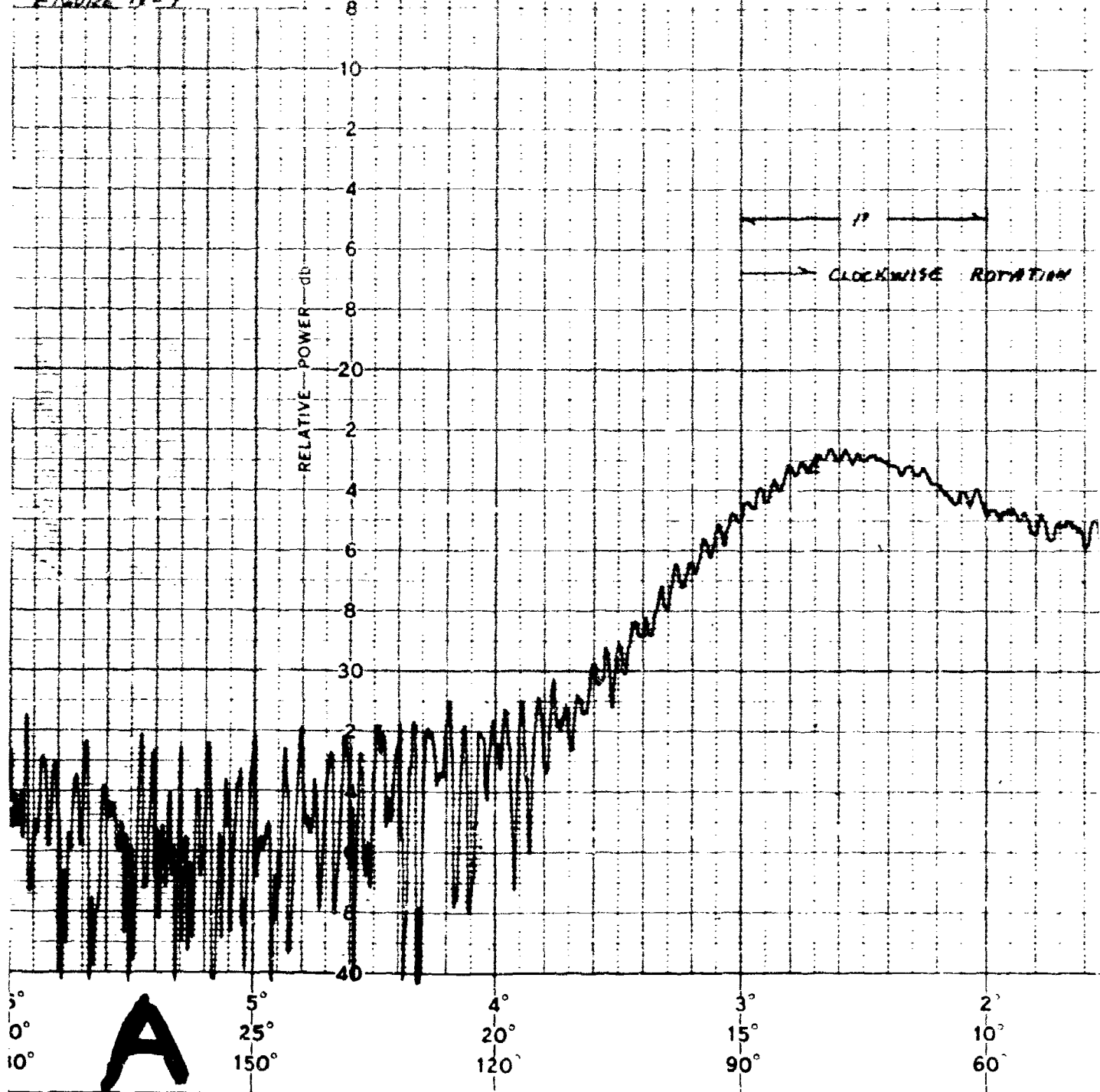
REMARKS:

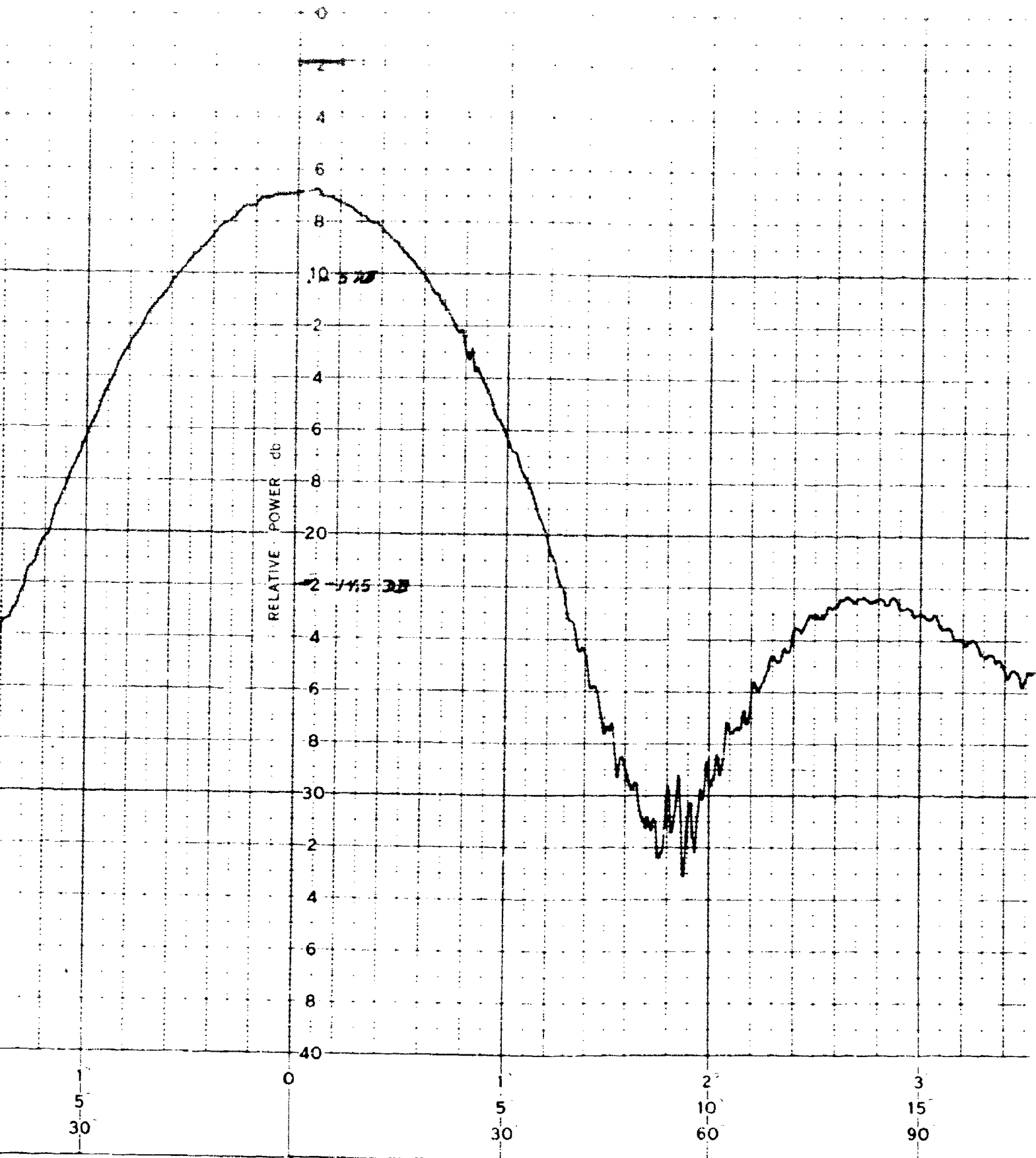
ENCAPSULATED
ANTENNA

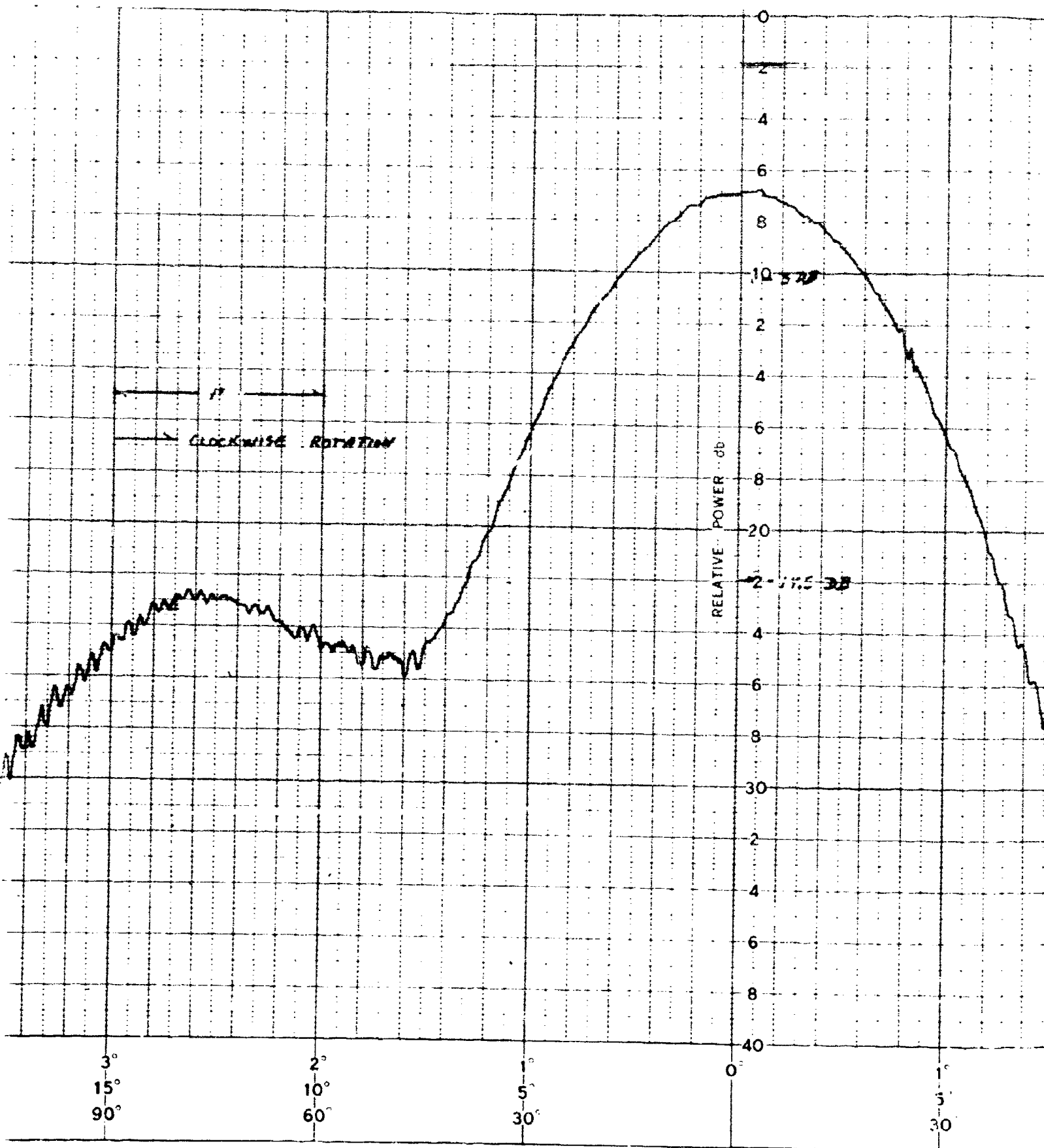
12.6 GHz H-Plane Cut

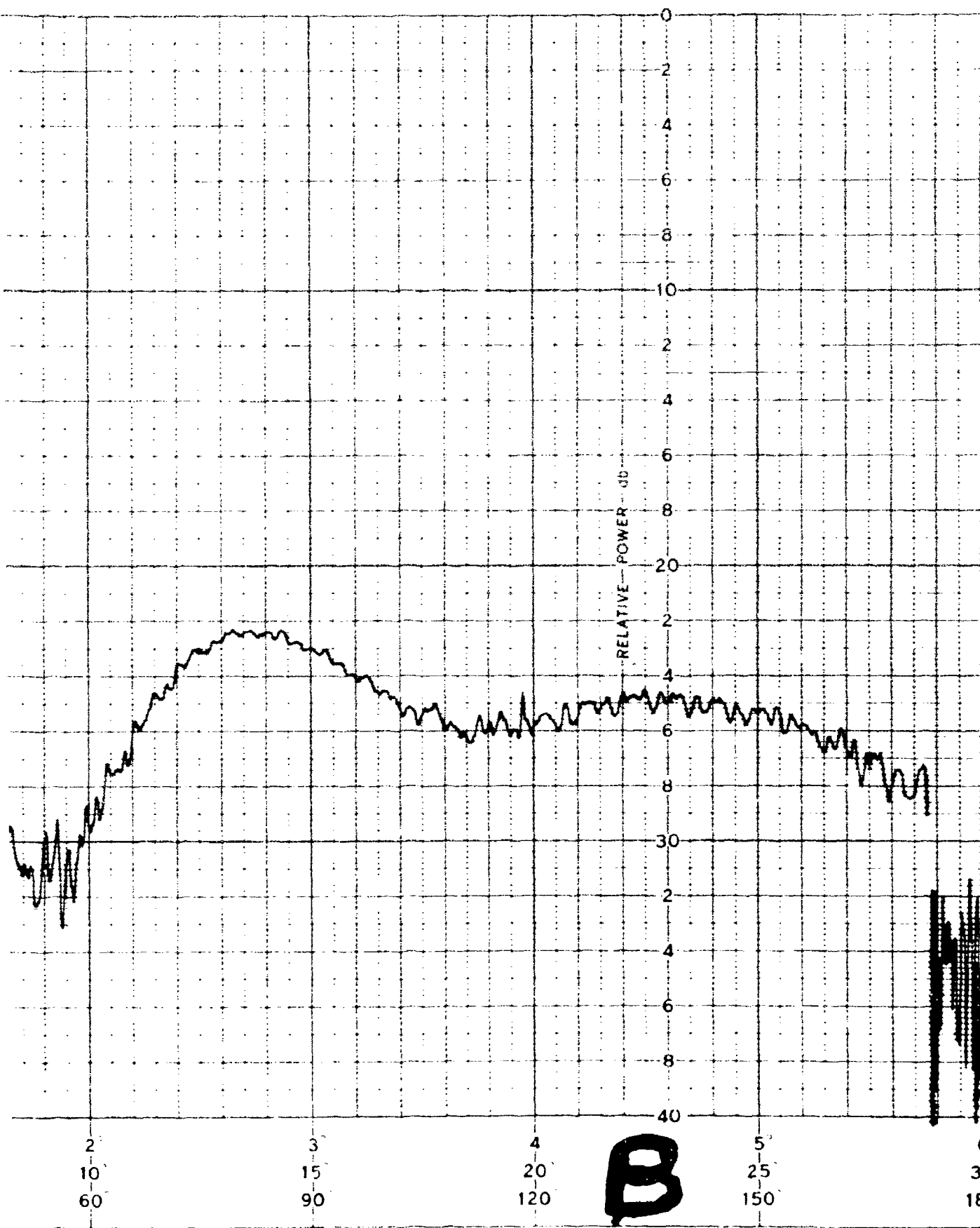
BORESIGHT $\pm 6^\circ$

FIGURE IX-9









PATTERN NO 5.4.5 DATE 5/64

PROJECT

ENGERS

REMARKS

ENCAPSULATED ANTENNA

12 GC H-PLANE CUT

PORESKINT $\pm 180^\circ$

FIGURE 1X-10

RELATIVE POWER - dB

5°
0°
10°

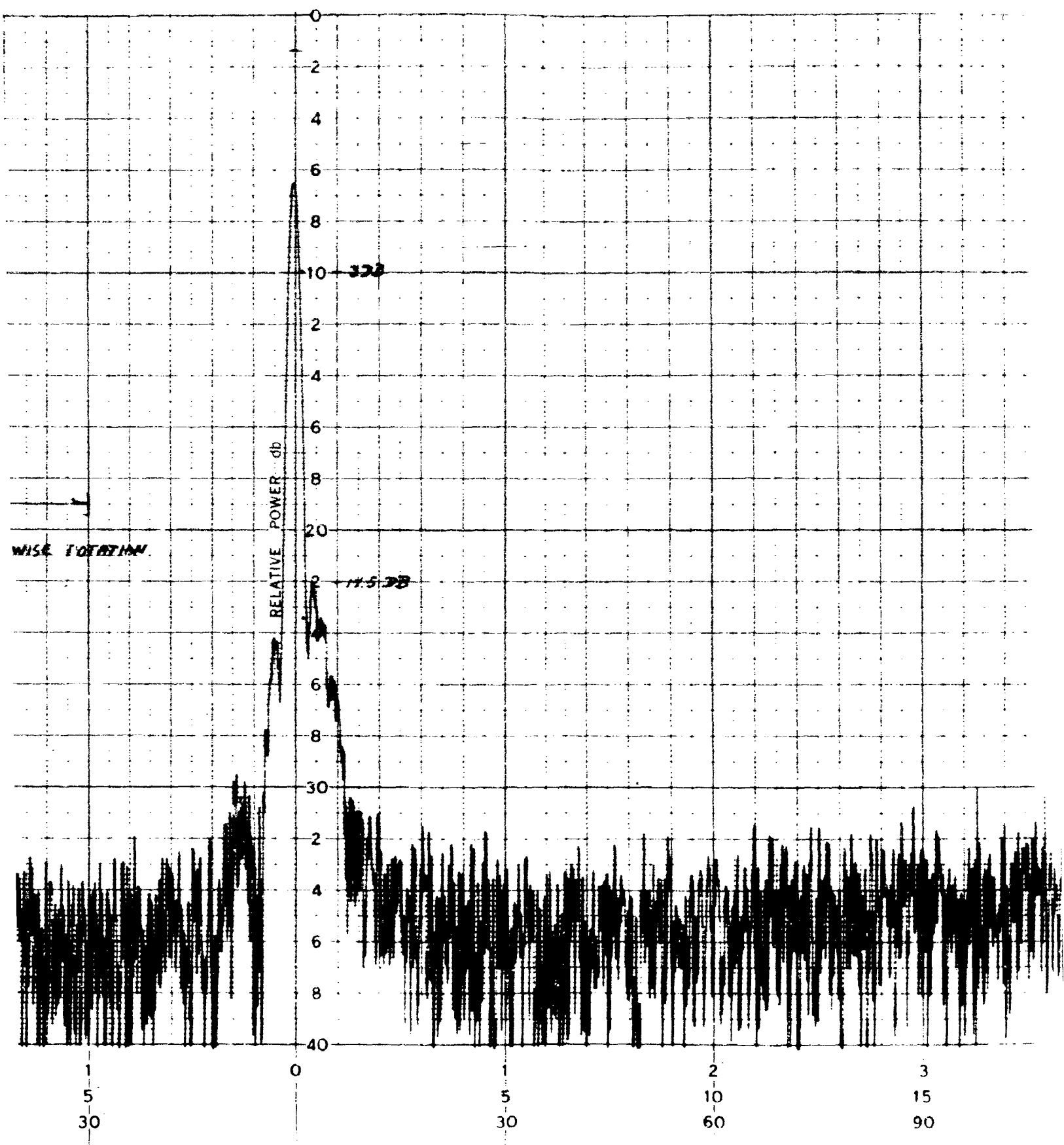
A

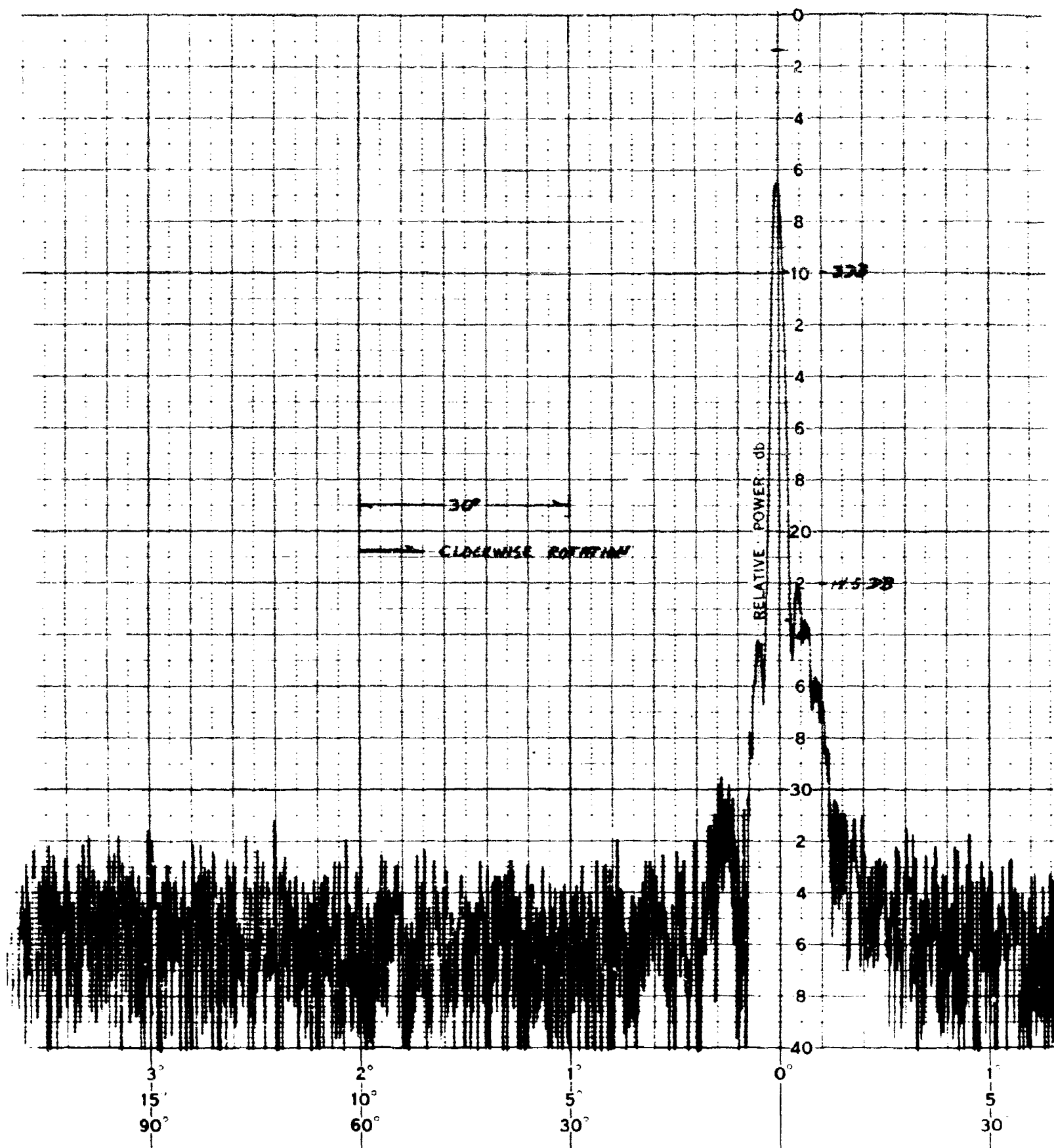
5°
25°
150°

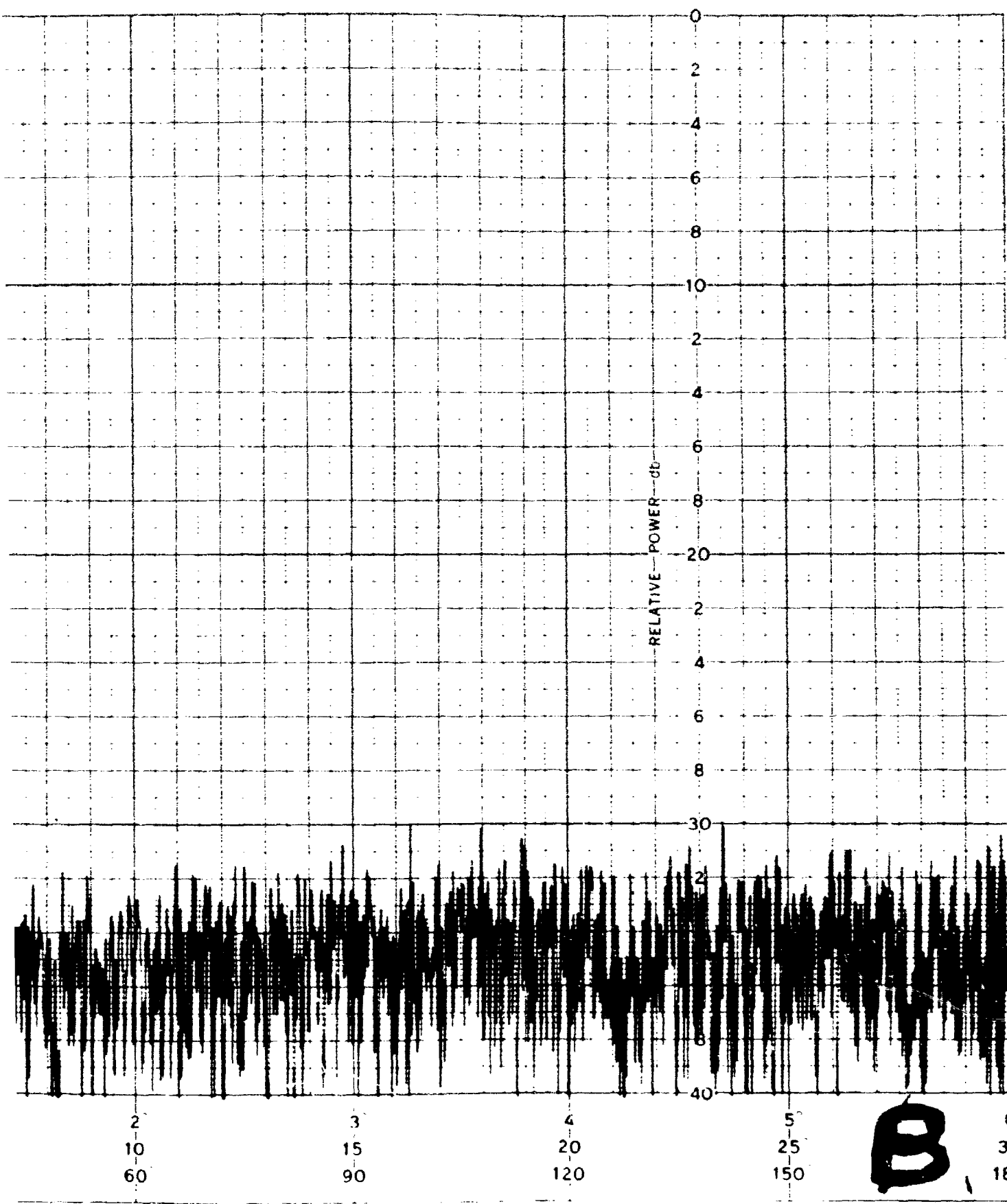
4°
20°
120°

3°
15°
90°

2°
10°
60°







PATTERN NO. 5.5

DATE 5/64

PROJECT

ENGRS

REMARKS

BORESIGHT SHIFT

126° E-PLANE CUT

BORESIGHT $\pm 6^\circ$

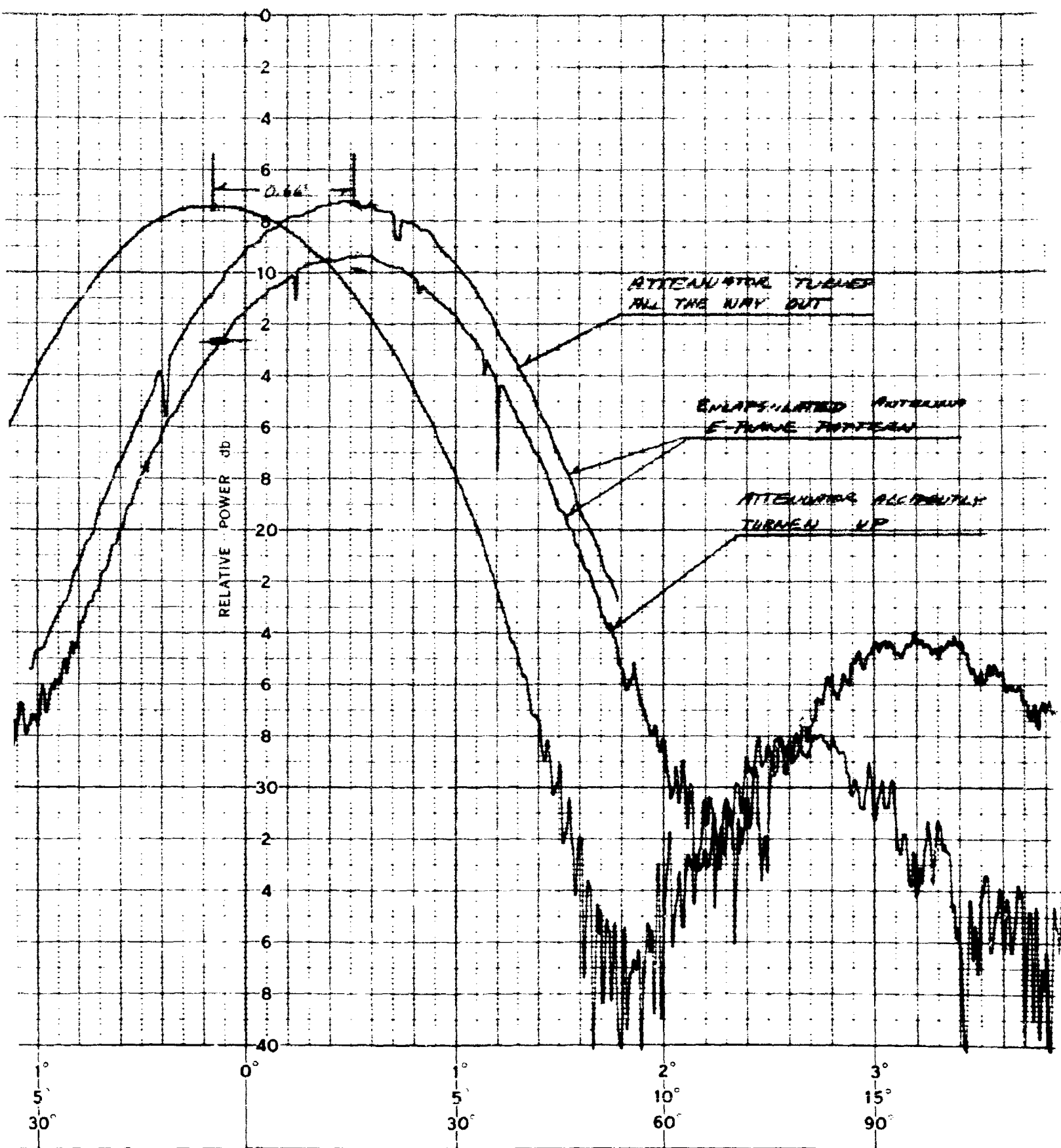
FIGURE 12-11

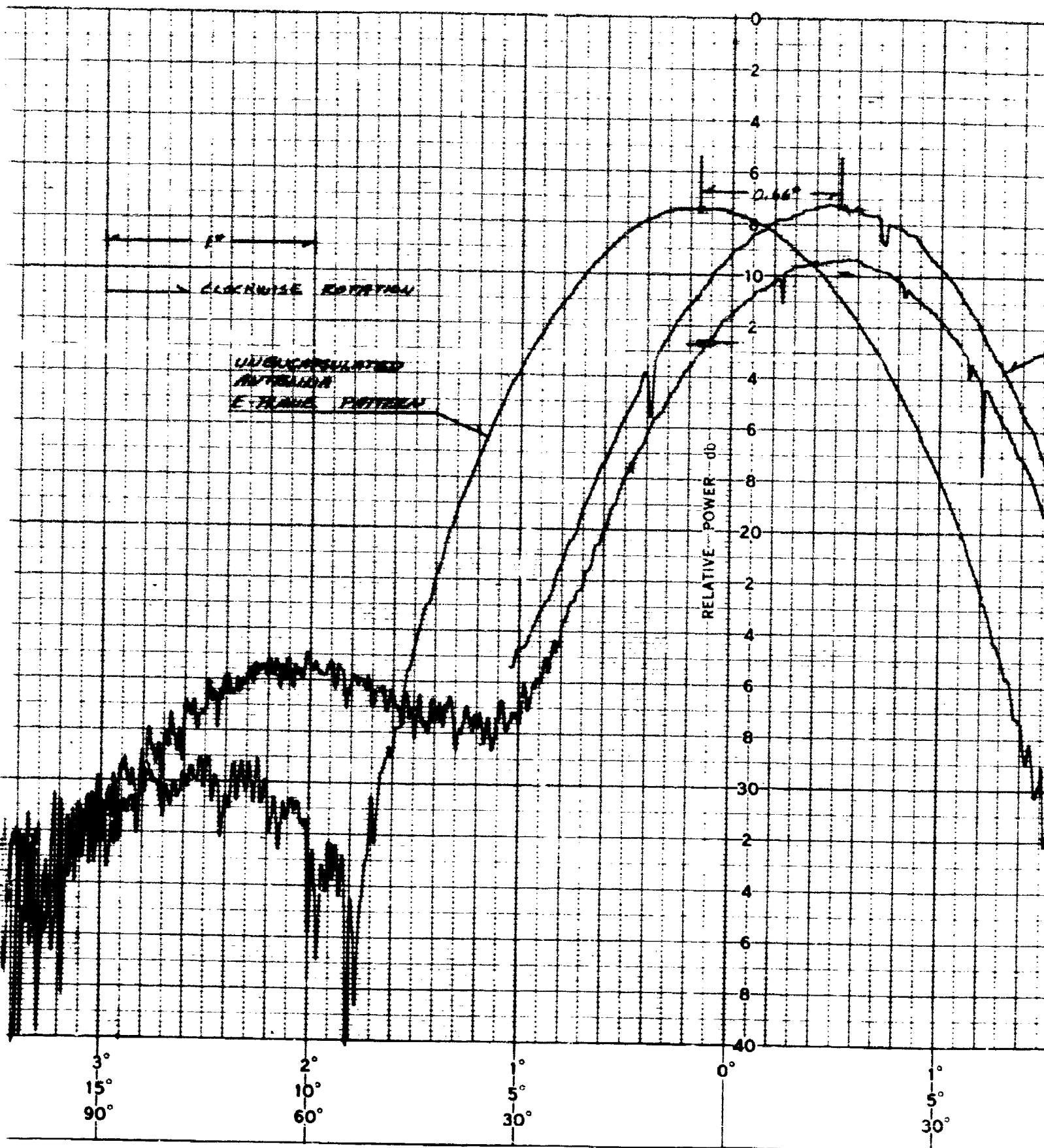
RELATIVE POWER - db

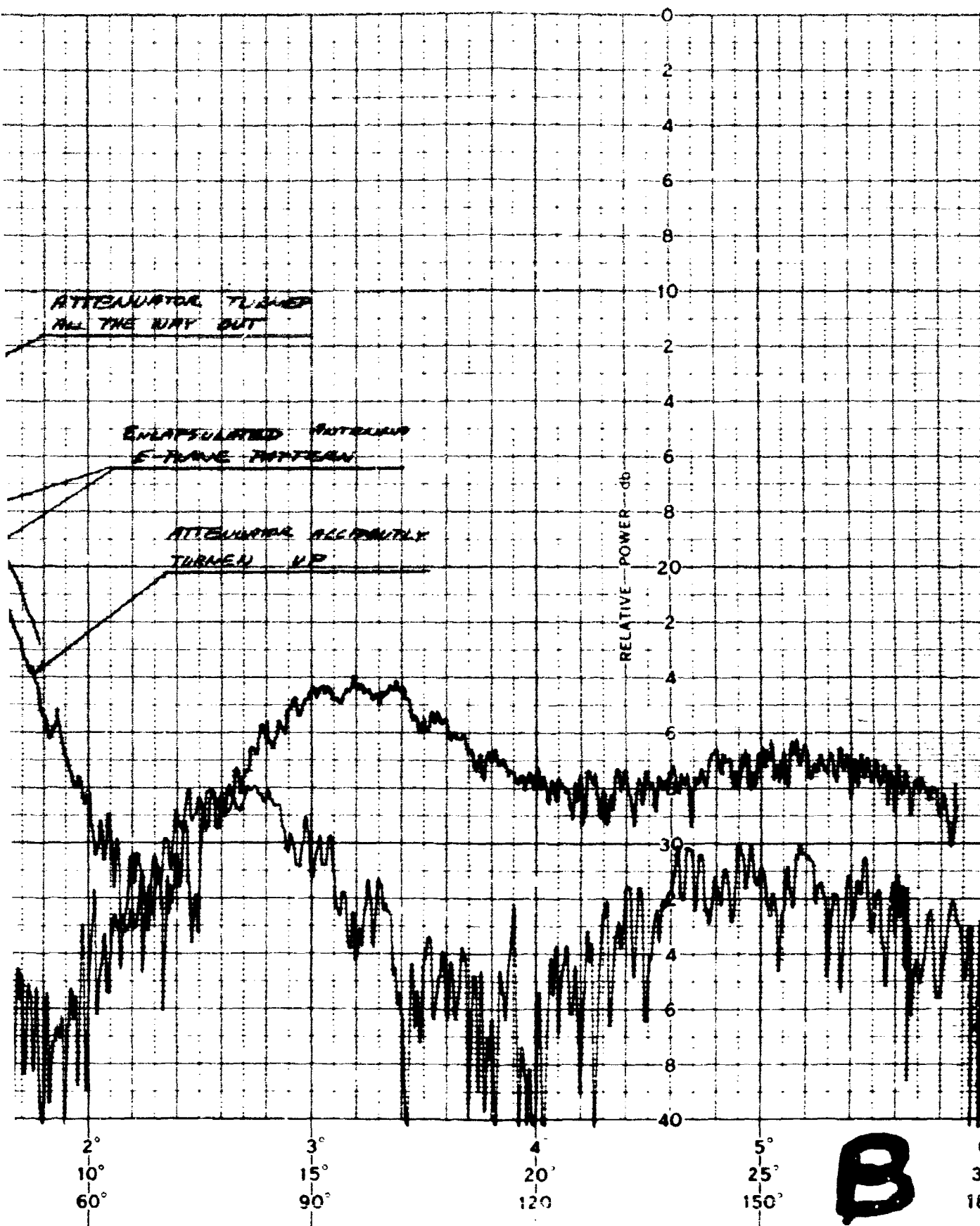
CLOCKWISE ROTATION

UNCALIBRATED
ANTENNA
E-PLANE PATTERN

0° 0° 0° 5° 25° 150° 4° 20° 120° 3° 15° 90° 2° 10° 60°







Security Classification

DOCUMENT CONTROL DATA - R&D

(Security classification of title, body of abstract and indexing annotation must be entered when the overall report is classified)

| | | | |
|--|--|--|-----------------------|
| 1. ORIGINATING ACTIVITY (Corporate author) AEC Research Corp. Washington, D.C. | | 2a. REPORT SECURITY CLASSIFICATION UNCLASSIFIED | |
| | | 2b. GROUP 6 | |
| 3. REPORT TITLE Feasibility of Foam Plastic Techniques for Hardening Above Ground Radome | | | |
| 4. DESCRIPTIVE NOTES (Type of report and inclusive dates) Final Report 1 Jul 1963 - 31 May 1964 | | | |
| 5. AUTHOR(S) (Last name, first name, initial) Jennings, R. R. Smith, B. B. | | | |
| 6. REPORT DATE October 1964 | | 7a. TOTAL NO. OF PAGES 243 | 7b. NO. OF REFS 37 |
| 8a. CONTRACT OR GRANT NO. AR 30(602)-3123 | | 9a. ORIGINATOR'S REPORT NUMBER(S) DA 693 | |
| b. PROJECT NO. 557 | | | |
| c. 557001 | | 9b. OTHER REPORT NO(S) (Any other numbers that may be assigned this report) RADC-TDR-64-363 | |
| 10. AVAILABILITY/LIMITATION NOTICES Qualified requesters may obtain copies of this report from DDC. Refer to OLC. | | | |
| 11. SUPPLEMENTARY NOTES N/A | | 12. SPONSORING MILITARY ACTIVITY Development Engineering Branch Rome Air Development Center Research and Technology Division Air Force Systems Command, GAOB, NY | |
| 13. ABSTRACT <p>The investigation reported here was directed toward the determination of the feasibility of hardening above ground antenna installations, at the 75 psi free-field overpressure range for a one megaton nuclear burst, by means of pseudo-encapsulation with a foam plastic radome.</p> <p>The problem was to determine if a foam plastic protection system could be designed to permit antenna survival to the blast, and if that design would permit efficient electrical transmission characteristics before and after the detonation occurred.</p> <p>The overall survival problem was approached by treating the effects of the individual environments on foam plastic separately. Conclusions from the investigation of the effects of a nuclear detonation on the selected foam plastics are summarized as follows:</p> <ol style="list-style-type: none"> 1. The nuclear radiation will have a negligible effect on the dielectric and mechanical properties. 2. Thermal radiation produces considerable physical changes in all foam plastic materials through ablation, burning and melting. The electrical properties of most foam plastics are affected as a result of charred | | | |

UNCLASSIFIED

Security Classification

| | | | | | | | |
|---|-----------|--------|----|--------|----|--------|----|
| 14 | KEY WORDS | LINK A | | LINK B | | LINK C | |
| | | ROLE | WT | ROLE | WT | ROLE | WT |
| Hardened Antenna Techniques Antennas Survival Plastics | | | | | | | |

INSTRUCTIONS

1. **ORIGINATING ACTIVITY:** Enter the name and address of the contractor, subcontractor, grantee, Department of Defense activity or other organization (*corporate author*) issuing the report.

2a. **REPORT SECURITY CLASSIFICATION:** Enter the overall security classification of the report. Indicate whether "Restricted Data" is included. Marking is to be in accordance with appropriate security regulations.

2b. **GROUP:** Automatic downgrading is specified in DoD Directive 5200.10 and Armed Forces Industrial Manual. Enter the group number. Also, when applicable, show that optional markings have been used for Group 3 and Group 4 as authorized.

3. **REPORT TITLE:** Enter the complete report title in all capital letters. Titles in all cases should be unclassified. If a meaningful title cannot be selected without classification, show title classification in all capitals in parenthesis immediately following the title.

4. **DESCRIPTIVE NOTES:** If appropriate, enter the type of report, e.g., interim, progress, summary, annual, or final. Give the inclusive dates when a specific reporting period is covered.

5. **AUTHOR(S):** Enter the name(s) of author(s) as shown on or in the report. Enter last name, first name, middle initial. If military, show rank and branch of service. The name of the principal author is an absolute minimum requirement.

6. **REPORT DATE:** Enter the date of the report as day, month, year, or month, year. If more than one date appears on the report, use date of publication.

7a. **TOTAL NUMBER OF PAGES:** The total page count should follow normal pagination procedures, i.e., enter the number of pages containing information.

7b. **NUMBER OF REFERENCES:** Enter the total number of references cited in the report.

8a. **CONTRACT OR GRANT NUMBER:** If appropriate, enter the applicable number of the contract or grant under which the report was written.

8b, 8c, & 8d. **PROJECT NUMBER:** Enter the appropriate military department identification, such as project number, subproject number, system numbers, task number, etc.

9. **ORIGINATOR'S REPORT NUMBER(S):** Enter the official report number by which the document will be identified and controlled by the originating activity. This number must be unique to this report.

9b. **OTHER REPORT NUMBER(S):** If the report has been assigned any other report numbers (*either by the originator or by the sponsor*), also enter this number(s).

10. **AVAILABILITY/LIMITATION NOTICES:** Enter any limitations on further dissemination of the report, other than those

imposed by security classification, using standard statements such as:

- (1) "Qualified requesters may obtain copies of this report from DDC."
- (2) "Foreign announcement and dissemination of this report by DDC is not authorized."
- (3) "U. S. Government agencies may obtain copies of this report directly from DDC. Other qualified DDC users shall request through _____."
- (4) "U. S. military agencies may obtain copies of this report directly from DDC. Other qualified users shall request through _____."
- (5) "All distribution of this report is controlled. Qualified DDC users shall request through _____."

If the report has been furnished to the Office of Technical Services, Department of Commerce, for sale to the public, indicate this fact and enter the price, if known.

11. **SUPPLEMENTARY NOTES:** Use for additional explanatory notes.

12. **SPONSORING MILITARY ACTIVITY:** Enter the name of the departmental project office or laboratory sponsoring (*paying for*) the research and development. Include address.

13. **ABSTRACT:** Enter an abstract giving a brief and factual summary of the document indicative of the report, even though it may also appear elsewhere in the body of the technical report. If additional space is required, a continuation sheet shall be attached.

It is highly desirable that the abstract of classified reports be unclassified. Each paragraph of the abstract shall end with an indication of the military security classification of the information in the paragraph, represented as (TS), (S), (C), or (U).

There is no limitation on the length of the abstract. However, the suggested length is from 150 to 225 words.

14. **KEY WORDS:** Key words are technically meaningful terms or short phrases that characterize a report and may be used as index entries for cataloging the report. Key words must be selected so that no security classification is required. Identifiers, such as equipment model designation, trade name, military project code name, geographic location, may be used as key words but will be followed by an indication of technical context. The assignment of links, rules, and weights is optional.

UNCLASSIFIED

Security Classification

13. ABSTRACT (con't):

composites on the residual surface. However, polyethylene foam laminate was concluded feasible.

3. Mechanical shock effects due to the blast overpressure wave was inconclusive due to inadequate test data on the stress-strain response of foams to dynamic loading. Conditional feasibility can be assured on the basis of anticipated foam plastic non-linear viscoelastic response.

The electrical transmission efficiency of a foam encapsulated scale model antenna was observed for a 6 ft. parabolic dish encapsulated with low density polystyrene foam. These tests indicate that phase errors are the main contributors to degradation of the pattern; and these should be eliminated if possible by a symmetrical assembly. The attenuation and reflection losses in low density foam were small. Boresight shift was observed and agreed well with the calculated value. The experimental tests indicate that electrical performance can be predicted for a full scale model.

A program to acquire high energy, dynamic loading data on certain foam plastic materials such as polyethylene, polystyrene, and polyurethane seems warranted to complete the feasibility analysis for the foam plastic hardening concept.